Doctoral Dissertation
Doctoral Program in Civil and Environmental Engineering (39^{th}cycle)

Analysis of Glubam Joint Behavior and Truss Model Updating Based on Optimization Algorithms

By

Da Shi

Supervisor(s):
Prof. Giuseppe.Carlo.Marano, Supervisor
Prof. Cristoforo.Demartino; Prof. Yan.Xiao Co-Supervisor

Doctoral Examination Committee:
Prof. Tingju Zhu, Referee, Zhejiang University
Prof. Liangjiu Jia, Referee, Tongji University
Prof. Giuseppe Quaranta, Referee, Sapienza University of Rome
Prof. Amedeo Manuello Bertetto, Referee, Politecnico di Torino
Prof. Laura Sardone, Referee, Politecnico di Torino
Prof. Wenwen Huang, Referee, Zhejiang University
Prof. Yasutaka Narazaki, Referee, Zhejiang University
Prof. Jian Ma, Referee, Zhejiang Institute of Architectural Design

Politecnico di Torino
2025

Declaration

I hereby declare that, the contents and organization of this dissertation constitute my own original work and does not compromise in any way the rights of third parties, including those relating to the security of personal data.

Da Shi
2025

* This dissertation is presented in partial fulfillment of the requirements for **Ph.D. degree** in the Graduate School of Politecnico di Torino (ScuDo).

I would like to dedicate this thesis to my loving parents

Acknowledgements

Time flies, and my Ph.D. journey is now drawing to a close. At this meaningful moment, I would like to express my deepest gratitude to all those who have offered help and support throughout my doctoral studies.

First and foremost, I would like to express my heartfelt thanks to my doctoral supervisor, Professor Cristoforo Demartino. Since the very beginning of my Ph.D., Professor Demartino has profoundly influenced me with his rigorous academic attitude and diligent work ethic. He has always pursued precision in research and has guided his students with remarkable dedication and care. He not only provided clear direction for my research but also offered hands-on guidance in various aspects such as experimental design, coding, and manuscript preparation, from which I benefited immensely.

Professor Demartino consistently upheld a supportive and encouraging educational approach. During moments of self-doubt and even when I considered giving up, he was the one who continuously offered encouragement and helped me push forward. He also cared deeply about my mental well-being and often checked in to ensure I was managing the stress of doctoral life. Although we occasionally had disagreements during this journey, we always managed to resolve them quickly with mutual understanding and trust. He was not only my academic mentor but also a guiding figure in my life—someone I respect deeply and am truly grateful to. He is the person I am most thankful for during my Ph.D. Without his help, I would not be where I am today.

I would also like to sincerely thank my doctoral supervisor Professor Yan Xiao for his guidance and support during the final year of my Ph.D. After Professor Demartino's departure, I was able to continue my doctoral work under Professor Xiao's supervision through an arrangement made by the university and my personal preference. In fact, my Ph.D. journey started in 2020 when I first contacted Professor

Xiao via email, and it was through his recommendation that I had the opportunity to begin my research.

As an internationally renowned expert in bamboo structures, Professor Xiao has been my academic guide and mentor from the very beginning. Under his supervision, I gained in-depth knowledge of the latest developments in the field of bamboo structures, broadened my research perspectives, and benefited from his extensive academic experience. His support enabled me to transition smoothly and successfully complete my degree.

I am also deeply grateful to Professor Giuseppe Carlo Marano for his kind supervision and generous support during my two-year joint Ph.D. program in Italy. During my stay at Politecnico di Torino, Professor Marano provided abundant academic resources, a comfortable working environment, and a highly supportive research atmosphere. Under his guidance, I not only improved my research capabilities but also deepened my understanding of structural engineering. His professionalism and open-minded academic attitude made me feel welcomed and encouraged even in a foreign country.

My sincere thanks also go to the China Scholarship Council (CSC) for providing financial support, which enabled me to pursue this valuable international research experience and grow both academically and personally.

Finally, I would like to extend my heartfelt thanks to my parents and my girlfriend. Your unconditional love, understanding, and encouragement have been my greatest source of strength. You have always stood behind me, empowering me to persevere through every challenge.

With this, I express my sincere gratitude to all the teachers, family members, and friends who have supported me along the way.

ABSTRACT

Bamboo, as a naturally fast-growing renewable resource, is abundant in China and supported by a well-established industrial foundation, making it a crucial material for promoting green building development. Modern engineered bamboo structures are typically fabricated using industrialized processes with engineered bamboo-based panels as raw materials, which reduce environmental impact while enabling standardization and prefabrication of building components. These structures can effectively meet performance requirements in terms of safety, economy, and comfort. Glue-Laminated Bamboo (glubam), a representative type of engineered bamboo, features a high strength-to-weight ratio, low adhesive content, and stable physical and mechanical properties. As an innovative and sustainable construction material, glubam has shown great potential for application in modern structural engineering. Compared to traditional building materials such as timber and steel, glubam offers significant advantages in strength-to-weight performance, renewability, and environmental friendliness. Despite its excellent material properties, research on the hysteretic behavior of glubam structural joints and the seismic performance of glubam composite truss systems remains insufficient. Comprehensive design theories and reliable numerical modeling approaches are still lacking. Moreover, integrating artificial intelligence (AI) optimization algorithms into the seismic performance analysis of glubam structures represents a promising yet underexplored research direction.

In response to these challenges, this study systematically investigates the mechanical behavior of glubam joints and their corresponding truss assemblies under cyclic loading through a combination of experimental testing, numerical simulation, and AI-based optimization methods. The main research contents and findings are summarized as follows: First, according to relevant testing standards, two types of glubam joints and their corresponding planar truss and roof truss structures were subjected to quasi-static cyclic loading tests to evaluate their hysteretic behavior and failure modes. Based on the experimental observations, both high-fidelity three-dimensional finite element models and simplified low-fidelity hysteresis models were developed to capture the nonlinear mechanical responses of the two joint types. For the simplified models, two parametric hysteresis constitutive models were proposed to reproduce critical features observed under cyclic loading, such as pinching effects, asymmetry, and strength degradation. Three representative AI optimization algorithms—Genetic Algorithm (GA), Bayesian Inference (BI), and Neural Network (NN)—were introduced to perform parameter identification and model calibration, significantly improving the accuracy and generalizability of the models. Finally, using the calibrated hysteresis models, a macro-scale numerical model of the glubam truss structure was constructed by combining the joint models with beam-column elements. Structural-level model updating was then performed using AI algorithms, and the optimized model was used to analyze the structural response of glubam trusses under cyclic loading. The detailed research tasks and contributions of this study are summarized as follows:

This study first conducted axial monotonic and cyclic loading tests on two types of glubam joint connections with distinct configurations: the steel-insert glubam joint and the steel-plate clamped glubam joint. The fasteners used in these joints were designed with varying geometric dimensions. Through systematic experimentation, the mechanical behavior of both joint types under cyclic loading was comprehensively analyzed, including characteristics of their hysteresis curves, stiffness degradation patterns, energy dissipation capacity, and typical failure modes. The test results demonstrated that both types of glubam joints exhibited favorable hysteretic behavior and excellent energy dissipation performance. Their failure processes were primarily ductile in nature, indicating promising seismic resistance potential. In addition, the influence of geometric parameters of the fasteners on the mechanical performance of the joints was further investigated. It was found that these parameters significantly affect the joints' load-bearing capacity, initial stiffness, and energy dissipation efficiency.

Building upon the joint performance investigation, planar truss and roof truss systems were designed using the two connection types (steel-insert and steel-plate clamped) and subjected to quasi-static cyclic loading tests. The study systematically evaluated the global hysteretic performance, energy dissipation capacity, and seismic behavior of the two types of truss systems under cyclic loads. Test results indicated that glubam truss systems exhibited good deformation capacity and high energy dissipation efficiency, meeting the basic requirements of seismic design.

In the numerical simulation component of this study, high-fidelity three-dimensional finite element (FE) models were developed for both types of glubam joint configurations. A novel modeling approach was proposed by coupling the "element deletion method" with the Hill yield criterion, enabling simultaneous characterization of the orthotropic mechanical properties and crack propagation behavior of glubam. These constitutive mechanisms were implemented via a user-defined material subroutine (UMAT) in Abaqus and successfully applied to the high-fidelity 3D finite element model of the steel-insert glubam joint. The simulated load–displacement curves closely matched the experimental results, validating the model’s accuracy and reliability in capturing the nonlinear hysteretic response of the joints.

To enable more efficient simulation at the structural (macro) scale, two sets of low-fidelity simplified hysteretic models were further developed for the aforementioned joint configurations. These models innovatively combined multiple types of spring elements—each representing distinct mechanical behaviors such as ideal elastoplasticity, pinching, and gap characteristics—through series and parallel arrangements. This approach significantly reduced computational cost in structural analysis and facilitated subsequent parameter identification and model updating. The simplified hysteretic models systematically incorporated key nonlinear features observed during cyclic loading, including stiffness degradation, unloading stiffness recovery, strength deterioration, and energy dissipation. Comparison with experimental data demonstrated that the simulated load–displacement curves agreed closely with test results, confirming the proposed hysteretic models’ accuracy and engineering applicability.

To ensure that the numerical hysteresis models accurately capture the actual cyclic behavior of glubam joints, it is essential to identify and calibrate multiple key model parameters. However, due to the high dimensionality of these parameter sets, manual tuning is inefficient and often fails to yield stable and reliable results. To address this issue, this study incorporates three mainstream artificial intelligence (AI) optimization algorithms—Genetic Algorithm (GA), Bayesian Inference (BI), and Neural Networks (NN)—into the finite element (FE) simulation workflow, thereby establishing an intelligent parameter identification framework. By conducting a comparative analysis of the three algorithms in terms of accuracy, convergence speed, and robustness, the most suitable optimization strategy was selected. The resulting calibrated numerical hysteresis models exhibit both high accuracy and strong stability, and are capable of faithfully reproducing the cyclic behavior of the joints under repeated loading, providing a reliable basis for subsequent structural-level modeling. Building on this foundation, the calibrated simplified joint models were embedded into macro-scale glubam truss models, enabling simulation of the coupled behavior between the joints and the overall structural system. To further improve the predictive accuracy of the structural mo dels under realistic loading conditions, an advanced model updating procedure was implemented using optimization techniques. The updated models were validated through systematic comparisons between numerical simulations and experimental results, confirming the accuracy and practical value of the proposed model updating methodology.

The research findings demonstrate that glubam joints and their corresponding truss systems exhibit excellent energy dissipation capacity and mechanical stability under cyclic loading, highlighting their significant potential in seismic design and sustainable construction. This dissertation not only systematically uncovers the hysteresis evolution characteristics of glubam joints and truss systems but also proposes a comprehensive modeling and optimization framework—from constitutive joint modeling and parameter identification to structural-level model integration and updating. These contributions lay a solid theoretical and technical foundation for the engineering application of glubam-based structural systems in seismic design.

KEY WORDS: Glue laminated bamboo; Hysteresis behavior; Joint design; Truss structure; Parameter identification; Model updating

Contents

List of Figures

List of Tables

1 Introduction

1.1 Development of Bamboo Structures

Due to its growth characteristics, bamboo is primarily distributed in tropical, subtropical, and temperate regions, including countries and areas in South America, southern Africa, and Southeast Asia. China possesses abundant and widely distributed bamboo forest resources, accounting for approximately 19% of the global total, with a total area of about 6.01 million hectares. The provinces of Jiangxi, Fujian, Hunan, and Zhejiang are particularly rich in bamboo resources. As early as the Yuan Dynasty, China had compiled specialized treatises on bamboo. *Zhupu* (Treatise on Bamboo) by Li Kan documented common bamboo species and their growth cycle characteristics in detail, pointing out that bamboo can mature within 3 to 4 years, making it a high-quality, fast-growing natural material. This characteristic endows bamboo with significant potential as a sustainable engineering material. The scientific and rational development and utilization of bamboo resources—under strategies such as “replacing wood with bamboo” and “integrated use of bamboo and wood”—can help alleviate the imbalance between wood supply and demand, mitigate climate change, and promote the construction of a resource-efficient and environmentally friendly society.

As a structural material, the development of bamboo and the promotion of innovative bamboo-timber structural components are expected to become important breakthroughs in the field of civil engineering. From an engineering perspective, bamboo exhibits the following advantages: it has a high strength-to-weight ratio, although its strength decreases with increasing geometric dimensions. The tensile strength of a single bamboo fiber ranges from 1400 to 2700 MPa, while that of an individual bamboo strip is in the range of 95 to 200 MPa. However, bamboo also shows pronounced brittle behavior. Through rational structural design and optimized integration with other materials, bamboo demonstrates strong potential as a high-performance, eco-friendly building material. Currently, the application and research of bamboo in structural engineering are mainly focused on the following areas:

1. 2. 1 **Raw Bamboo Structures**

Bamboo has a long-standing history of use as a building material in China, South Asia, and South America[1]. Among the most representative species used in traditional raw bamboo construction are Phyllostachys edulis (commonly known as Moso bamboo) in China and Guadua bamboo in South America. These two species have served as the primary structural materials in traditional raw bamboo buildings.

Since the beginning of the 21st century, with increasing economic development and growing public concern over the environmental impacts of conventional industrial materials such as cement and steel, raw bamboo structures have achieved initial success in small-scale architectural applications. Notable examples include the “Bamboo House” of the Commune by the Great Wall designed by Kengo Kuma and the German Pavilion at the Shanghai World Expo. In bamboo-rich countries such as India[2] and Colombia[3], more systematic research has been carried out on raw bamboo structures based on local conditions. Colombia, in particular, has developed structural design codes specifically for round bamboo structures.

However, raw bamboo is a highly anisotropic material with significantly different mechanical properties along different directions. Its transverse strength is considerably lower than its longitudinal strength, making it prone to transverse shear or splitting failure. In addition, raw bamboo is combustible, susceptible to decay, and exhibits poor weather resistance. The round, hollow geometry of bamboo culms also poses challenges for structural connections, making joint strength difficult to ensure. These limitations have constrained the widespread use and promotion of raw bamboo structures in modern construction.

1.2.2 Glued Laminated Bamboo Structures

Since the 1970s, the industrial application of bamboo materials in China has gradually developed. Researchers have employed modern gluing techniques to process raw bamboo by splitting or recombining it, effectively addressing issues such as irregular geometry and large fluctuations in mechanical properties. These efforts have resulted in the production of engineered bamboo materials with more stable and superior performance. In the field of structural engineering, both domestic and international scholars have conducted exploratory studies on the application of glued laminated bamboo (glubam) as a construction material. In recent years, international research on glubam and other bio-based engineered materials has steadily increased, with a focus on material properties, joint design, and structural applications. Dutch researcher Gonzalez-Beltran[4] conducted experimental research on timber frame composite walls with bamboo plywood as facing panels. Sharma et al.[5] demonstrated through mechanical testing that glubam exhibits tensile and compressive strengths comparable to or even exceeding those of high-grade timber, with significant advantages in material uniformity and dimensional stability. Correal et al.[6] studied the dynamic behavior of bamboo and found that its damping ratio is comparable to that of timber, highlighting the potential of engineered bamboo in high-vibration environments. Okubo et al.[7] examined the durability of glubam under hot and humid conditions and reported that modified glubam retained performance better than untreated bamboo. Baharuddin et al.[8] investigated the truss connection performance of bamboo based on dowel-type joints, showing that improved joint design significantly enhances structural ductility and energy dissipation capacity. Pradhan et al.[9] focused on the mechanical behavior of hybrid bamboo-steel joints and found that the mixed joints exhibit superior bearing capacity and ductility, making them suitable for seismic applications. These international research outcomes clearly demonstrate the broad prospects for glubam and its hybrid structures in joint design and overall structural performance optimization.

As one of the countries richest in bamboo resources, China has made remarkable progress in the research and application of engineered bamboo materials, particularly in material optimization, joint design, and engineering applications. Wang et al.[10] found that after delignification, bamboo becomes softened and can be plastically formed, which improves bending toughness and forming quality, albeit often at the expense of load-bearing capacity. This study proposes an innovative approach using deep eutectic solvents (DES) to pretreat green bamboo strips, establishing a better balance between strength and toughness and significantly improving the elastic modulus. Zhang et al.[11] investigated the compressive behavior of glubam under different loading methods. Their experiments covered a temperature range from 20°C to 250°C and analyzed the effects of full-surface versus localized transverse loading on compressive performance. The study discussed failure modes, load-deformation curves, and compressive strength, revealing how loading method and temperature influence the mechanical performance of glubam. Kang et al.[12] developed a surface activation technique for bamboo that enhanced the bonding strength and water resistance between bamboo and a dialdehyde cellulose–polyamine adhesive, offering a novel strategy for the development of low-carbon, eco-friendly, and sustainable bamboo-based composites. Chen et al.[13] used a semi-circular embedment test system to study the embedding performance of glubam–timber composite joints, focusing on the effects of dowel diameter, loading direction, contact condition, connection method, and moisture content on embedment strength and stiffness. Liu et al.[14] investigated the bond performance of glubam–steel joints bonded with epoxy adhesives, and explored the roles of resin pre-coating and carbon nanotube surface treatment in joint strengthening and repair, providing valuable experimental insights for the design and rehabilitation of glubam–steel hybrid joints. Xiao et al.[15] constructed a canopy project based on a glubam–steel hybrid truss. Field measurements showed that the system had significant advantages in both mechanical performance and material efficiency. Li et al.[16, 17] designed a bamboo–steel composite roofing system for long-span roofs in public buildings. Engineering practice confirmed that the system not only reduced costs but also significantly enhanced structural stability. In 2004, the Chinese Academy of Forestry and the International Network for Bamboo and Rattan (INBAR) collaborated to construct a school building in Pingbian, Yunnan Province, using laminated bamboo beams and trusses, with bamboo plywood used for the roof and walls. In 2008, under the joint promotion of Academicians Zhang Qisheng and Lü Zhitao from Southeast University, the first two-story glubam residential demonstration building was completed on the campus of Nanjing Forestry University.

In 2005, Professor Xiao Yan's research team, based on the development of the bamboo industry in China and Hunan Province, began to study the application of glubam in modern structural engineering. Drawing inspiration from the concept of glued laminated timber (glulam), they proposed a secondarily cold-pressed glued laminated bamboo component (Glubam) based on plybamboo, and defined its structural system. During this research, the team innovatively proposed new structural systems such as lightweight bamboo structures, steel–bamboo hybrid structures, prefabricated housing, and bamboo structural frames, laying the groundwork for the engineering application of glubam.

In 2007, under the leadership of Professor Xiao Yan from the School of Civil Engineering at Hunan University, the Modern Bamboo and Composite Structures Research Institute successfully applied glubam in bridge structures for the first time. They constructed both a modern bamboo pedestrian bridge and the first modern bamboo vehicular bridge. The modular design allowed for standardized and industrialized component fabrication, playing a significant role in the development and practical implementation of modern bamboo structures. In the same year, the research team also built the first prefabricated modern bamboo house, which was put into production after comprehensive design and testing. After the 2008 Wenchuan Earthquake, glubam temporary shelters—designed by Hunan University's research institute, funded by Hunan University and the Blue Moon Fund (USA), and manufactured by

Kaisheng Bamboo and Wood Technology Co., Ltd.—were delivered to Guangyuan, Sichuan Province, for use as emergency clinics and safe classrooms in the disaster area. Since then, Professor Xiao’s team has conducted extensive experimental research on Glubam trusses[18], steel–bamboo hybrid space structures, and steel–bamboo composite trusses[19]. They also carried out detailed studies on the mechanical performance of various connections in bamboo–concrete composite beams and conducted bending performance tests on Glubam beams[20] fabricated from different types of bamboo laminates.

1.2 Research Background and Significance

Although scholars both in China and abroad have conducted in-depth studies on the fundamental properties of glued laminated bamboo (glubam), and have preliminarily explored the mechanical behavior of glubam beams, columns, and bolted joints to understand their load-bearing mechanisms and failure modes, as well as to establish corresponding calculation methods[21,22], the research in this field remains neither systematic nor comprehensive. Due to the limited market scale, many fundamental studies still lack solid theoretical foundations and experimental support, resulting in incomplete design codes and methodologies for glubam structures. Overall, the development of this research area remains in its early stages.

Compared with traditional construction materials such as concrete and steel, glubam exhibits a significant disparity between its tensile and compressive strengths. As a structural member, it often experiences ductility and splitting failure simultaneously, increasing the complexity of mechanical analysis. Moreover, glubam possesses typical characteristics of composite materials, leaving many key scientific issues unresolved. These include the lack of standardized constitutive models due to variations in manufacturing processes, the need to improve bearing capacity prediction methods for critical joints, and the absence of suitable hysteresis models for seismic design applications.

Joints, often the weakest link in modern bamboo structures, are crucial to the overall structural safety. Therefore, it is essential to conduct in-depth research on the theoretical background and design methodologies for critical joints. As modern bamboo structures expand toward mid- and high-rise buildings, height limitations are continuously being challenged, making the seismic performance of joints an increasingly critical and unavoidable issue. Among various joint types, bolted joints have gained popularity in bamboo (and timber) structures due to their reliability, simplicity in design and fabrication, and ease of construction. As a result, they have become the mainstream choice in current structural design and are widely applied in practical engineering.

In modern bamboo (or timber) structures, bolted joints can be categorized into steel-insert-plate and steel-clamp-plate types based on their connection configuration. These joints can effectively transfer shear and axial forces while dissipating energy, and their mechanical behavior often governs the overall seismic performance of the bamboo structure. Therefore, investigating the generalized force–deformation relationships of these joints under cyclic loading is critical for accurately simulating the complex mechanical response of structural components under seismic loads, and thus is of great importance for the seismic design of bamboo structures.

1. 2. 1 **Experimental Study on Glubam (Wood) Joints**

With the collective efforts of numerous researchers, a complementary research approach combining numerical simulations and experimental investigations has gradually taken shape to study the mechanical behavior of bamboo-timber joints. For example, Weng Xiaohong, Liu Weiqing[23], and others conducted experimental research on the load-carrying capacity of timber-steel plate bolted connections. The experiments involved four groups totaling twenty glulam members with different cross-sectional widths, tested under displacement-controlled loading using a servo-hydraulic universal testing machine. The observed yield modes were compared with the Johansen yield model (i.e., the European yield model). The results showed good agreement between the theoretical analysis and experimental data. Moreover, with the increase in the relative thickness of the glulam side members, the failure mode of the specimens evolved from pure bearing failure in the bolt holes to a mixed mode involving both bearing failure and bolt bending.

He Minjuan[24] and others from Tongji University studied the lateral resistance behavior of beam-column joints with bracing structures. Based on the "pinching" material model in OpenSees, they proposed a hysteretic model to describe the lateral restoring force behavior of beam-column joints with steel inserts. The experimental results indicated that the size and angle of the bracing members significantly influenced the lateral resistance of the joints. Leng Yubing[25] and colleagues conducted seismic performance tests on three types of glubam beam-column joints. The results showed that connections with embedded steel inserts exhibited significant slip deformation, and their stiffness and load-carrying capacity were both lower than those of T-type and L-type connections.

1. 2. 2 **Numerical Simulation Studies on Glubam (Wood) Joints**

The key to the numerical simulation of glubam (wood) joints lies in the development of accurate and stable hysteresis models. Such models are crucial for reliably predicting the generalized force-deformation relationships of joints under cyclic loading, and for simulating the complex mechanical responses of structures under seismic loads. Existing hysteresis models for bolted bamboo-timber joints can be broadly classified into three categories: high-fidelity 3D finite element models, low-fidelity simplified physical models, and phenomenological models.

High-fidelity 3D finite element models typically employ three-dimensional modeling approaches to capture complex mechanisms such as bolt deformation, embedding effects of the surrounding bamboo, and compressive-friction interactions at the interface. Researchers have used such models to study the mechanical behavior of bolted[26] and nailed[27] connections. Simplified physical models, on the other hand, reduce computational complexity by simplifying the mechanical mechanisms and using physical parameters to derive overall load-deformation relationships. One common approach is the beam-on-foundation model[28], which treats fasteners (e.g., bolts or nails) as beam elements with distributed plasticity, and the surrounding bamboo as distributed nonlinear springs. While both finite element and physical models can reasonably predict the hysteretic behavior of bolted bamboo-timber joints, their high computational cost limits efficiency when modeling structures with numerous joints.

Phenomenological models describe envelope curves and hysteretic characteristics using mathematical equations governed by a set of parameters[29], which are usually calibrated against experimental data to match specific material properties and joint configurations. Some model parameters require iterative numerical solutions, and heuristic optimization algorithms such as genetic algorithms[16] can be used to enhance calibration accuracy. Compared to the first two types of models, phenomenological models are less computationally intensive, adaptable to various connection types, and capable of effectively simulating structural systems at different scales.

In summary, to promote the development of modern bamboo structures and advance their application in mid- and high-rise buildings, it is imperative to address key scientific challenges in the seismic design of joints. This includes standardizing the constitutive behavior of glubam material and developing hysteresis models for glubam joints. This study begins with a fundamental investigation into the mechanical performance of glubam joints. Building on experimental findings, the research delves into the development of an orthotropic fracture-based constitutive model for glubam joints with bolted steel inserts through numerical simulations. Given the current limitations in the depth and accuracy of quasi-static analysis for glubam joints, and the significant discrepancies between finite element simulation results and actual mechanical responses reported in the literature, there remains a lack of constitutive models that can accurately capture complex hysteretic characteristics such as strength degradation, stiffness degradation, pinching effects, tension-compression asymmetry, and damage evolution. This research aims to establish a restoring force model (hysteresis model) for glubam joints based on quasi-static test data, capable of representing these complex behaviors. Such a model holds both significant academic value and promising engineering applicability.

1. 2. 3 Current Research on Parameter Identification of Numerical Hysteresis Models

Commonly used hysteresis models for simulating the behavior of bamboo-timber joints include the SAWS model, Bouc-Wen model, Pinching4 model, and DowelType model. These models typically involve a large number of parameters, making manual tuning impractical. Moreover, traditional parameter tuning methods such as least squares and finite difference often yield unstable results. Therefore, to improve the accuracy of quasi-static analysis and enhance the practical applicability of hysteresis models in engineering, researchers have conducted a series of studies on intelligent parameter identification based on artificial intelligence (AI) optimization algorithms.

Cao[30] proposed an analytical framework based on the Unscented Kalman Filter (UKF) for intelligent identification of the hysteretic behavior of cross-laminated timber (CLT) structural joints. UKF employs the Unscented Transformation (UT), which estimates the mean and covariance of model parameters using a set of deterministically selected sigma points. This framework identifies the unknown parameters of CLT connectors using experimental data, where the cyclic behavior of the CLT joints is modeled with spring elements governed by the SAWS hysteresis model. A comparison between the model prediction and the experimental hysteresis curves demonstrates high accuracy in parameter identification using the UKF, validating the effectiveness of the approach.

Giorgia[31] and colleagues conducted an in-depth numerical study on the seismic performance of light-frame timber shear walls, with a particular focus on the energy dissipation characteristics of panel-to-frame joints. In this study, zero-length elements were used to simulate the mechanical behavior of the joints, employing the SAWS model as the hysteresis rule. To enhance the predictive accuracy of the quasi-static analysis, a genetic algorithm was applied to identify the parameters of the SAWS model. By setting objective functions and defining upper and lower bounds for the search space, a reasonable parameter set was accurately identified. Incorporating these parameters into the shear wall model led to a strong agreement between the simulation and experimental results.

Cao[32] also employed a simplified numerical modeling method to study the seismic performance of timber frame structures. The shear wall region was simulated using a configuration of truss elements along four diagonal braces connected to a central spring element. The spring element followed a uniaxial Pinching4 material model to characterize hysteretic behavior and stiffness degradation. To update the simplified model, the Cubature Kalman Filter (CKF) was introduced, which effectively captured model uncertainties and accounted for modeling errors. The updated results showed that the experimental responses were well enveloped by the predicted curves generated from all cubature sigma points. Further evaluation of the mechanical performance showed that the model's peak load, yield load, and maximum load closely matched experimental values. The calibrated model demonstrated high accuracy and efficiency, making it suitable for mechanical analysis under varying loading conditions. As an effective model updating technique, the CKF approach significantly enhances the reliability of numerical models.

In the hysteresis analysis of bamboo-timber structures, accurate parameter identification is crucial for constructing reliable mechanical models. However, due to the natural heterogeneity and anisotropy of bamboo-timber materials, as well as the complexity of their hysteretic behavior, traditional empirical tuning or gradient-based optimization methods often fail to meet the requirements of both efficiency and precision. Advanced AI algorithms—such as genetic algorithms, Bayesian inference, neural networks, particle swarm optimization, and unscented Kalman filters—offer efficient tools for exploring optimal parameters in complex nonlinear systems. These algorithms enable intelligent calibration using experimental data, thereby improving the accuracy and robustness of hysteresis models while reducing computational cost and enhancing the practical utility of numerical simulations.

Optimizing hysteresis model parameter identification using AI techniques provides a solid theoretical and technical foundation for seismic analysis, structural optimization, and engineering applications of bamboo-timber structures.

Therefore, this study focuses on the parameter identification of hysteresis models for glubam joints. Based on quasi-static test data of glubam connectors, three AI-based algorithms—genetic algorithms, Bayesian inference, and neural networks—are employed for in-depth calibration and identification of key hysteresis model parameters. The performance and accuracy of each algorithm are compared and analyzed. The objective is to develop a hysteresis model for glubam joints that is both robust and broadly applicable, and to propose a comprehensive parameter prediction method to improve the accuracy of quasi-static analysis. This effort aims to support the implementation of performance-based seismic design approaches in glubam structures.

1. 2. 4 **Research Progress on Glubam Trusses and Roof Structures**

A planar truss is a lattice structure composed of bar elements, in which members mainly bear axial tension or compression under external loads. This leads to efficient and uniform force distribution, thereby reducing material consumption. Timber, with its excellent tensile and compressive properties, is well-suited for such structural systems. Additionally, its high strength contributes to the out-of-plane stability of trusses.

The roof of the Hamar Sports Hall[33] in Norway (built in 1994) is a notable example of a planar timber truss structure. The arena surrounds a 400-meter speed skating track and consists of 19 parallel glulam arches arranged in the short-span direction. The arch height and span gradually reduce at both ends. At the highest point, a long-span longitudinal arch connects all arches into an integrated system, enhancing the overall stability. From an architectural perspective, the arched roof design lowers the height of the sidewalls and draws visual attention to the roof, creating multiple transverse textures through skylight placement and the main arch. This enhances the spatial hierarchy of the structure, giving the roof the visual appearance of thick wooden planks forming a ship hull while improving natural lighting and the overall spatial experience.

The Oguni Town Community Gymnasium[34] in Japan features a large-span timber grid structure with a span of 56 meters and a longitudinal length of 46 meters. The curved timber grid is composed of 1,455 spherical joints and 5,602 timber truss members. The joints use metal spheres, each connecting eight square sugi (Japanese cedar) members with cross-sectional dimensions ranging from 90 mm to 170 mm, forming a stable three-dimensional space frame. To prevent local compressive deformation at the connections, the joints incorporate an epoxy resin injection technique, where epoxy-grouted bolts and a central insert plate enhance the overall reliability of the large-span timber grid structure.

Xie[35] and colleagues designed a long-span glubam roof truss system for the Yanling warehouse project in Zhuzhou. Two 20-meter-span full-bamboo trusses were tested under static loading: a pure glubam truss and an A-shaped hybrid truss combining steel and glubam. The study analyzed their load-bearing capacities, failure modes, and load–midspan displacement relationships. In addition, the SAP2000 finite element software was used to perform simplified numerical analysis of the trusses, and the simulation results of strain–load curves in key members were compared with experimental data.

Li[36] and colleagues designed a 12-meter-span asymmetric steel–glubam hybrid truss for roofing applications using Building Information Modeling (BIM) software. The upper chord and web members were made of glubam, while the lower chord was constructed from steel pipes. The study included detailed analysis of fabrication, transportation, prefabrication, and installation procedures, and summarized the practical benefits of the hybrid design. Experimental research on the glubam chord members and their connections provided load–displacement and load–strain data. Full-scale tests confirmed that the truss met both deflection limits and load-carrying requirements. The study also examined the mechanical performance of the truss under varying end-connection conditions and asymmetric loading scenarios.

Quaranta et al.[15] introduced a new type of bamboo-steel hybrid space truss structure, with glubam used for the upper chords and diagonal web members, and hollow-section steel for the lower chords. This innovative system is designed for roofing and medium-span pedestrian bridges. The researchers conducted dynamic experiments to investigate the truss's performance under environmental vibrations and free decay responses, focusing on its modal characteristics. Based on the test results, a recommended value for the viscous damping ratio of bolted glubam truss joints was proposed. Numerical analyses also assessed the serviceability performance of the structure under human-induced vibrations in pedestrian bridge applications.

Research on glubam roof trusses and space trusses holds both academic and engineering significance. As primary load-bearing systems, trusses and roof structures are widely used in roofing systems, bridges, pedestrian walkways, and large-span space structures, directly influencing structural performance and long-term safety. Investigating the mechanical behavior, hysteresis characteristics, and failure modes of glubam trusses contributes to a deeper understanding of their structural mechanisms and supports rational design optimization.

Moreover, the integration of modern numerical simulation techniques with AI-based optimization methods enhances the precision of seismic design, facilitating the application of glubam trusses in buildings, bridges, and post-disaster reconstruction—thereby promoting the advancement of sustainable construction technologies.

Therefore, based on the experimental study of glubam joints and a solid understanding of their fundamental mechanical behavior, this study independently designs and constructs two steel–glubam hybrid truss systems. A combined experimental and numerical simulation approach is then employed to systematically investigate the hysteretic behavior of both truss structures.

1. 2. 5 **Research Status of Hybrid Simulation Based on Model Updating**

Hybrid simulation is a method that physically tests the key components of a structure exhibiting strong nonlinear behavior, while modeling the rest of the structure—which remains in the elastic stage or exhibits weak nonlinearity and is easier to simulate computationally—as numerical substructures. In practical applications, however, nonlinear regions are often not limited to a single component. If all critical components are physically tested, it would impose high demands on loading equipment and laboratory space and significantly increase experimental costs. Typically, some critical components share similar mechanical characteristics, allowing representative elements to be selected for physical testing while modeling the remaining parts numerically to reduce resource consumption.

However, numerical models often fail to fully reflect the mechanical behavior of real components, particularly under strong nonlinear conditions where substantial discrepancies may arise. To enhance simulation accuracy, some researchers have introduced model updating techniques in hybrid simulations. These techniques adjust the numerical model of the full structure based on test results from physical substructures or the entire system, using parameter identification or optimization algorithms to bring computational predictions closer to the actual physical behavior.

The accuracy of the numerical model is critical to the reliability of hybrid simulation outcomes. Reducing the gap between the numerical model and the real specimen remains a key research challenge. Model uncertainties primarily stem from two sources: (1) constitutive model errors, i.e., the mathematical expressions used in simulations cannot fully characterize the true mechanical response of structural elements; and (2) parameter uncertainty, i.e., deviations in assigned model parameter values. Both types of errors become significant under strong nonlinear conditions and can substantially affect simulation accuracy. Therefore, optimizing and updating numerical models to better reflect real behavior is vital for improving the reliability and engineering applicability of hybrid simulations under seismic or other external loads.

Yang et al.[37] proposed a method in which hysteretic data of the physical substructure were obtained through preliminary tests to train a neural network. The pretrained neural network was then online-updated using data collected during hybrid simulations. This approach effectively yielded a more accurate representation of the true constitutive behavior of the physical specimen. The method was validated through both numerical simulations and experiments on a two-story shear structure.

Hashemi et al.[38] investigated the effectiveness of model updating under conditions where the physical and numerical substructures exhibit different degrees of nonlinearity. In their hybrid simulation of a single-span steel frame, the column experiencing larger displacement was selected as the physical substructure, while the other was modeled numerically. The method minimized the difference in restoring forces between physical and numerical substructures and employed the Unscented Kalman Filter (UKF) to identify parameters of a Bouc-Wen-based numerical model. Both numerical and experimental results confirmed that the accuracy of hysteretic modeling significantly improved only when the most nonlinear elements were physically tested.

Elanwar et al.[39] proposed a model updating method based on minimizing the stress difference between numerical and physical substructures to identify material constitutive parameters. Their numerical simulation results demonstrated that this approach significantly enhanced the accuracy of hybrid simulations.

In 2021, Guo et al.[40] introduced an offline parameter correction approach for hybrid simulations. This method updated the Bouc-Wen model parameters using experimental data from physical substructures, effectively improving simulation precision and efficiency. The method was experimentally validated in steel frame structures.

Zhong et al.[41] applied the uniform design method to identify material parameters for steel and reinforced concrete structures. The principle of uniform design ensures parameter combination uniformity while minimizing the number of required tests. This significantly reduced sample size and improved identification efficiency. The method was validated through numerical simulations of a two-story frame structure.

The core of hybrid simulation based on model updating lies in minimizing numerical errors. However, relevant studies on bamboo-timber structures remain scarce, and a complete methodological framework has yet to be established. Therefore, this study proposes to use the joints of a glubam truss structure as the physical substructure in hybrid simulation. Elastic behavior of the truss chords is modeled using beam or bar elements, while numerical hysteresis models are introduced at the joint locations to construct an integrated truss model for hybrid simulation.

Initially, the numerical hysteresis model is calibrated using uniaxial quasi-static experimental data from glubam connectors. The calibrated model is then embedded into the full truss model for quasi-static numerical simulation. Restoring force–displacement relationships are extracted at the loading points, and the discrepancy between simulated restoring forces and those measured by actuators in physical tests is used to construct an objective function. Finally, artificial intelligence algorithms are applied to further refine the hysteresis model parameters in the integrated truss system.

This hybrid simulation approach based on joint-level model updating can significantly improve the accuracy and efficiency of numerical models for glubam trusses. By bringing simulation results closer to the actual mechanical behavior of physical specimens, the method provides a reliable foundation for the engineering application and optimization design of glubam truss structures.

1.3 Main Research Content of This Study

This dissertation presents a systematic investigation into the seismic performance of glubam joints and truss structures. By integrating experimental studies, numerical simulations, artificial intelligence (AI)-based optimization, and hybrid simulation techniques, a comprehensive methodology combining testing and numerical modeling is proposed. The main research content is organized into the following five areas:

1. Mechanical and Hysteretic Behavior of Glubam Joints under Axial Loading

The study begins with experimental investigations on the mechanical performance of two types of glubam bolted joints: steel-inserted plate joints and steel-clamped plate joints. Through quasi-static cyclic loading tests, the load–displacement curves of the joints are obtained. The focus is on analyzing their load-bearing capacity, failure modes, and hysteretic characteristics.

2. Development of a Fundamental Constitutive Model for Glubam Joints

Given the difficulty of accurately capturing the complex mechanical behavior of glubam—

such as orthotropy and shear-induced cracking—with existing constitutive models, this study develops a new constitutive model based on the Hill yield criterion, augmented by an element deletion rule. The model is capable of representing both orthotropic behavior and cracking mechanisms. It is implemented in the ABAQUS finite element software via user-defined material subroutines written in Fortran.

3. Development of a Hysteresis Model for Glubam Joints

Recognizing the limitations of existing hysteresis models in simulating the complex cyclic behavior of glubam joints, this study develops a new numerical hysteresis model. The model is formulated based on experimental observations of the joint hysteresis curves and is designed to accurately represent key nonlinear features of glubam joints under cyclic loading.

4. Parameter Identification of the Hysteresis Model for Glubam Joints

To enhance the predictive accuracy of the hysteresis model, this study calibrates its key parameters using experimental data. Considering the inefficiency of manual tuning and the limitations of traditional gradient-based or empirical methods in high-dimensional nonlinear systems, advanced AI optimization algorithms—including genetic algorithms, Bayesian inference, and neural networks—are explored. These algorithms are applied for deep calibration of the model parameters, and their accuracy and performance are compared. The results of this research not only improve the precision of quasi-static analysis for glubam joints but also provide theoretical support for implementing performance-based seismic design in glubam structures.

5. Study of Steel–Glubam Hybrid Truss Structures

Building on the experimental findings on glubam joints, two types of steel–glubam hybrid truss systems are designed and constructed based on different joint configurations. A combined experimental and numerical approach is adopted to systematically analyze their mechanical behavior, failure mechanisms, and hysteretic performance. The key areas of focus include:

5.1） Experimental Study on Truss Structures

Quasi-static cyclic loading tests are conducted to evaluate the global hysteretic behavior, deformation capacity, energy dissipation, and failure modes of the trusses. The influence of different joint configurations—such as steel-inserted plate joints and steel-clamped plate joints—on the overall seismic performance of the trusses is discussed.

5.2） Hybrid Simulation Based on Model Updating

Hybrid simulation studies on bamboo-timber structures are still in an exploratory stage, and a systematic framework has not yet been established. In particular, improving the accuracy of numerical substructures in hybrid simulations remains a critical challenge. To address this, a model updating-based hybrid simulation method is proposed in this study to enhance both the accuracy and computational efficiency of numerical models for glubam trusses. The method involves the following steps:

1. **Initial Numerical Model Calibration**

Using uniaxial quasi-static experimental data of the joint connectors, the numerical hysteresis model is calibrated. The effectiveness of the initial model is verified through numerical simulations.

2. **Construction of an Integrated Truss Structure Model**

In the truss system, part of the chord members is modeled using beam or bar elements to represent elastic behavior, while the developed numerical hysteresis models are embedded at the joint locations. Quasi-static numerical simulations are performed, and the restoring force–displacement relationships at loading points are extracted and compared against those from physical truss tests.

3. **Model Updating and Optimization**

AI algorithms are employed to minimize the difference between the simulated restoring forces and those measured in physical tests. The hysteresis model parameters are iteratively updated based on this objective function. This process improves the accuracy of hybrid simulation results, bringing numerical predictions closer to the actual mechanical behavior observed in tests.

This model updating-based hybrid simulation method can significantly improve the accuracy and efficiency of numerical models for glubam trusses, offering reliable support for their practical application and design optimization.

1.4 Research Framework

This dissertation is composed of eight chapters, with the content arranged as follows:

Chapter 1: Introduction

This chapter provides an overview of the background and significance of the research, clarifies the main research objectives, and identifies the key scientific questions to be addressed.

Chapter 2: Literature Review

This chapter presents a systematic introduction to the fundamental properties of bamboo, reviews its development as a construction material, and elaborates on the manufacturing processes and widely used types of engineered bamboo. Additionally, based on existing studies, the application prospects and future development directions of bamboo in structural engineering are discussed.

Chapter 3: Materials and Testing Methods

This chapter introduces the raw materials used in this study and describes the testing methods for evaluating their properties. The corresponding test results are provided to support the subsequent experimental and numerical research.

Chapter 4: Experimental Study on Glubam Joints

This chapter outlines the design and construction of two types of glubam joints and presents the results of axial quasi-static tests. The hysteretic behavior of the joints is analyzed in detail to reveal their mechanical characteristics and failure modes.

Chapter 5: Experimental Study on Glubam Trusses and Roof Structures

Based on the design of the two joint types, two glubam truss or roof structures are independently designed and constructed. Through quasi-static testing, this chapter investigates the global hysteretic performance of the trusses and examines key factors influencing their mechanical behavior.

Chapter 6: Numerical Simulation of Glubam Joints

This chapter conducts numerical analysis of glubam joints, developing both high-fidelity 3D finite element models and low-fidelity simplified numerical models. Based on experimental data, two hysteresis models suitable for different levels of accuracy are proposed to improve the precision of joint behavior simulations.

Chapter 7: Parameter Identification and Optimization of Hysteresis Models

This chapter focuses on methods for identifying the parameters of hysteresis models for joints. It introduces AI-based optimization techniques—including genetic algorithms, Bayesian inference, and neural networks—for parameter calibration. The performance of each algorithm is evaluated by comparing simulation results with experimental data, and their advantages and limitations are systematically summarized.

Chapter 8: Model Updating for Glubam Trusses and Roof Structures

This chapter establishes numerical models for glubam truss and roof structures and conducts model updating based on quasi-static test results, aiming to enhance the accuracy and engineering applicability of the computational models.

Chapter 9: Conclusions and Outlook

This final chapter summarizes the main conclusions of the study and, considering its limitations, discusses potential directions for future research.

Based on the above research content, the technical route of this study is illustrated in Figure 1.1.

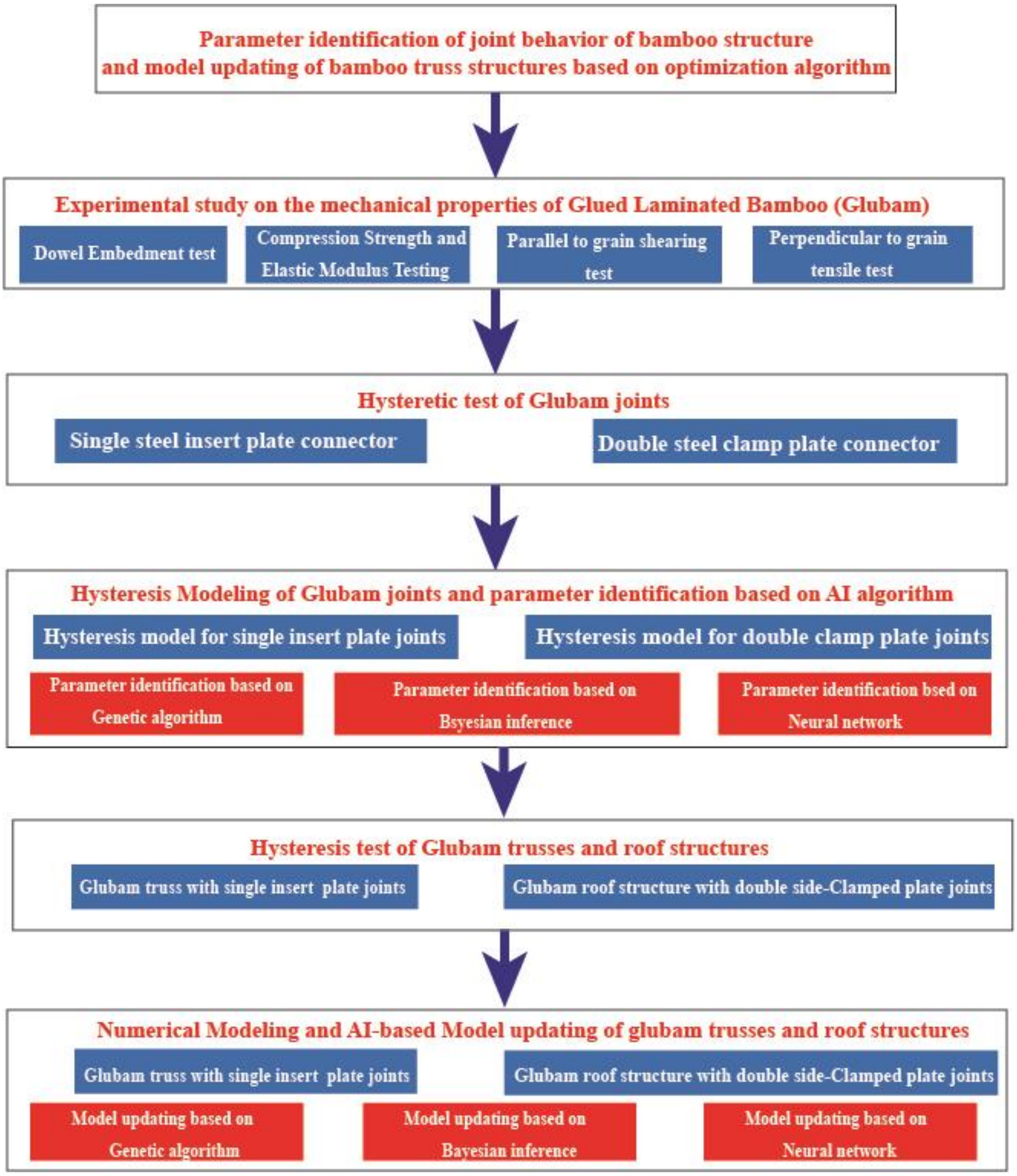

Figure 1-1 Research Workflow and Technical Scheme

`

2 Literature Review

2.1 Bamboo and Its Characteristics

2. 1. 1 Classification of Bamboo

Bamboo refers to a group of large, woody grasses belonging to the subfamily Bambusoideae of the family Poaceae. Globally, there are approximately 116 genera and 1,439 species of bamboo, predominantly distributed across tropical and subtropical regions, though they also occur naturally in temperate zones, excluding Europe and Antarctica[42]. Within the grass family, bamboo represents the only major lineage that has evolved significant diversity in forested environments.

The subfamily Bambusoideae is composed of three major phylogenetic tribes:

- Arundinarieae (temperate woody bamboos, with 533 species),
- Bambuseae (tropical woody bamboos, with 784 species), and
- Olyreae (herbaceous bamboos, with 122 species) [43].

Woody bamboos exhibit the following typical characteristics: they possess culm sheaths (specialized leaves that protect and support young shoots), complex vegetative branching systems, and external auricles on the leaf blades (usually in opposite pairs). Most woody bamboos are monocarpic, with flowering cycles that range from a few years up to 120 years, and they generally produce bisexual flowers[44,45]. In contrast, herbaceous bamboos often lack well-differentiated culm sheaths and external auricles, have limited branching, and tend to flower continuously or seasonally. Their spikelets are usually unisexual[45]. The representative morphological characteristics of woody and herbaceous bamboos are shown in Figure 2-1(a) and Figure 2-1(b), respectively.

(a) Woody Bamboo (b) Herbaceous Bamboo

Figure 2-1 Typical Morphological Characteristics of Bamboo

2. 1. 2 Growth and Structure of Bamboo

Bamboo shoots and culms develop from a dense rhizome system, which can be generally classified into two major types: monopodial and sympodial. Monopodial rhizomes possess strong horizontal growth capacity and rapid expansion rates. The buds on the rhizomes may grow vertically to form new culms or extend horizontally to expand the underground rhizome network. Bamboos with monopodial rhizomes typically exhibit a scattered clumping structure, where culms are spaced relatively far apart. These species are considered invasive, due to their aggressive spread. Monopodial bamboos are mainly found in temperate regions, with representative genera including *Phyllostachys* and *Pleioblastus*. In contrast, sympodial rhizomes are short and thick, producing densely packed culms that form a tight clumping structure. The bamboo culms grow closely together, and the clumps expand radially around a central core. These species are predominantly distributed in tropical regions, are non-invasive, and are typified by the genus *Bambusa*[46].

As illustrated in Figure 2-2, the basic anatomical components of bamboo include the culm, root system, rhizome structure, shoots, branches, and leaves.Some bamboo species exhibit sporadic flowering, such as *Phyllostachys aurea* (Golden Bamboo) in the United States and *Phyllostachys edulis* (Moso Bamboo) in China. Sporadic flowering is primarily influenced by environmental factors rather than genetic programming.

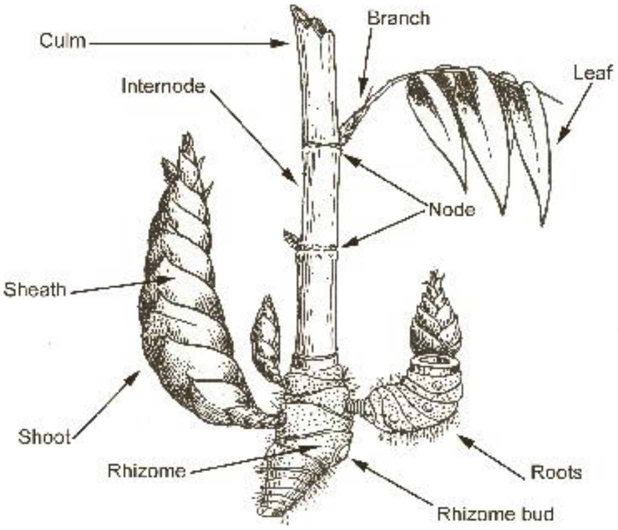

Figure 2-2 Anatomical Structure of Bamboo[47]

Zhang et al.[48] pointed out that the morphological structure of bamboo can be divided into two main components: the rhizome system and the culm system. Additionally, the bamboo plant can be further categorized into two parts based on its spatial distribution: the underground part, consisting of rhizomes, roots, and buds; and the above-ground part, consisting of culms, branches, and leaves.

Table 2-1 summarizes the functions of each structural component of bamboo. These components are functionally interrelated, working together to ensure the stable growth and development of the bamboo plant.

Table 2-1 Structure of Bamboo

Structure	Description
Rhizome	A rhizome is a horizontally growing, segmented underground stem that extends from the parent plant beneath the soil surface, enabling expansion and colonization of new habitats. The rhizome is covered with protective sheath leaves, which primarily serve to provide mechanical protection when the developing bamboo shoot breaks through the soil to form a culm.The main functions of the rhizome include the absorption, storage, and transport of water and nutrients, supporting the physiological activities of both parenchyma and vascular tissues. In addition, rhizomes possess vegetative reproduction capacity, allowing new bamboo shoots or culms to sprout from nodes. This facilitates the sustained expansion and regeneration of the bamboo population.
Culm	The bamboo culm is a cylindrical, lignified stem composed of nodes and internodes. Most bamboo culms are hollow, although some species develop solid culms. The culm structure includes sheath leaves, leaf blades, inflorescences, and a branching system. A bamboo culm typically reaches full maturity after 3 to 4 years of growth. As it matures, the material properties of the culm improve, leading to increased hardness and strength, which enhance its durability and structural performance.

Root	The root system primarily functions to support the bamboo culm, enabling it to withstand harsh weather conditions and other environmental stresses. In addition, the roots enhance the load-bearing capacity of the culm, allowing it to sustain more leaves and expand over a broader area. Another important role of the root system is the storage of nutrients, which are essential for the growth and development of the bamboo plant. Bamboo roots typically develop from the nodes of the rhizome and usually do not penetrate more than one foot below the soil surface. Morphologically, bamboo roots tend to exhibit a high degree of symmetry in both size and shape.
Branch	Nearly all bamboo species are capable of producing multiple branches from a single bud located at each node. However, certain genera have the ability to generate multiple buds at each node, which may further develop into multiple branches, resulting in a more complex branching system.
Leaf	All major structural components of bamboo—including the rhizome, culm, and branches—bear leaves. The anatomical structure of a bamboo leaf consists of three main parts: the leaf blade, leaf sheath, and ligule. At the rhizome stage, the leaves primarily exist in the form of sheath leaves, which almost entirely envelop the rhizome, providing mechanical protection during its underground expansion. As the rhizome emerges above the soil surface, the leaves gradually develop, with the leaf blade becoming the dominant structure. At this stage, the leaf takes on the essential function of photosynthesis, converting solar energy into the chemical energy required for plant growth. There is significant morphological variation in leaf forms among different bamboo species, and the external characteristics of the leaves play an important role in species classification and identification.

References：[49]

2.1.3 Cellular Structure of Bamboo

Compared to wood, bamboo exhibits a more pronounced degree of heterogeneity in its structural composition[50]. At the mesoscopic scale, bamboo is considered a multicellular biological composite material with a hierarchical structure and functionally graded architecture[51-53]. A three-dimensional reconstruction of the bamboo wall is shown in Figure 2-3[54]. The primary structural component of bamboo tissue is the vascular bundle, which is embedded within a matrix of parenchyma tissue[55]. Each vascular bundle consists of hollow vessels surrounded by sclerenchyma fibers, forming a hardened fibrous sheath. The volume fraction of vascular bundles increases radially from the inner to the outer regions of the culm wall[50,55]. A similar trend is also observed along the vertical (height) direction of the culm, although the variation is more gradual[50,55]. Moreover, the solid volume fraction within the vascular bundles also increases toward the outer culm wall. This is mainly attributed to the gradual reduction in vessel diameter along the radial direction[55]. The increasing vascular bundle volume fraction and the rising internal solid content of the bundles collectively result in a distinct radial density gradient within the bamboo culm—i.e., the outer culm tissue exhibits a higher density than the inner regions. Bamboo's epidermal layer is relatively hard and coated with a waxy surface[56], which contributes to its protective functions. As a consequence of this structural gradient, both the static bending strength and elastic modulus of bamboo increase radially from the inner to the outer wall[57].

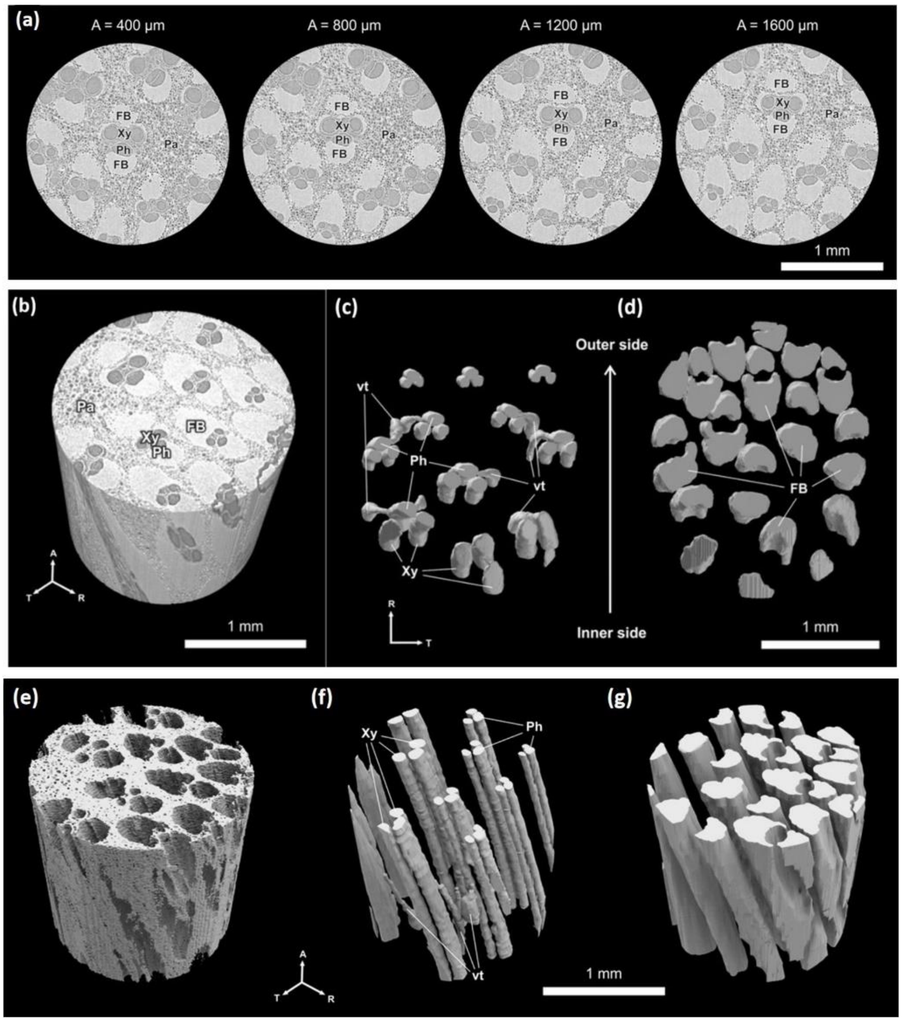

Figure 2-3 3D reconstruction stages of bamboo: (a) Cross-sections ranging from 400 mm in axial directions and anatomy `details; (b) 3D mCT reconstruction; (c) axial view of 3D segmented rendering of phloem, vascular traces and xylem, (d) fiber bundles (sclerenchyma); (e) 3D perspective rendering of the segmented tissues parenchyma, (f) conducting elements, and (g)sclerenchyma (Ph = phloem, Xy = xylem, FB = fiber bundles, Pa = parenchyma, vt = vascular traces; A = axial, T =tangential, R = radial)

References：[58]

2.2 Molecular Structure and Mechanical Properties

As described in Section 2.1, bamboo contains a large number of vascular bundles, which are primarily composed of xylem, phloem, and a surrounding fiber sheath (also referred to as a fiber cap). These vascular bundles are embedded in a parenchyma tissue matrix. The xylem and phloem are responsible for transporting water and nutrients, while the thick-walled fiber sheath serves as the main reinforcement component of the bamboo culm, providing essential mechanical support. Bamboo is capable of growing to the height of a fully mature culm within 40 to 160 days, a process mainly driven by the rapid elongation of intercalary meristems located in the internodes[56]. The continuous elongation of internodes contributes significantly to the remarkable growth rate of bamboo. However, as a monocotyledonous plant, bamboo lacks a vascular cambium, which prevents it from adding new cells through secondary growth. This means that the final diameter of the culm is determined during the initial growth stage, resulting in the characteristic slender and hollow structure of bamboo[59].

The mechanical properties of bamboo are primarily derived from the structure of its cell walls and the composition of its constituent polymers. This section explores how bamboo’s performance is determined by its microscopic cell structure, and further analyzes how these properties can be optimized and modified through material treatments and structural enhancement techniques.

2. 2. 1 Molecular Structure

The primary chemical components of bamboo include cellulose, hemicellulose, lignin, ash, and extractives. These constituents are tightly integrated within the bamboo tissue, forming a complex chemical structure[60,61]. Table 2-2 summarizes the chemical composition of *Phyllostachys edulis* (Moso bamboo) in the middle region of the culm wall. Various studies have shown that the chemical composition of the bamboo culm wall varies between the inner and outer layers, indicating that the physical and chemical properties of bamboo may differ depending on location within the culm. This suggests a degree of structural and compositional heterogeneity, which may influence the material's mechanical and functional behavior[62-65].

Table 2-2 Chemical Composition of Moso Bamboo (Culm Wall, Middle Region)

Chemical Composition	Outer layer	Middle layer	Inner layer
Cellulose	67.67	68.38	63.02
Hemicellulose	22.40	27.15	24.01
Lignin	27.90	24.01	23.68

Reference：[66]

Ether and ester linkages exist between hemicellulose and lignin. In addition, lignin and/or hemicellulose are also connected to hydroxycinnamic acids—such as ferulic acid and p-coumaric acid—via ester bonds[67]. Cellulose is a long, linear polymer composed of D-glucose units linked by β-1,4-glycosidic bonds. Cellulose chains are organized into microfibrils through intermolecular hydrogen bonding, which provides the rigidity and mechanical strength of plant cell walls[68]. Hemicellulose is a structurally diverse group of polysaccharides made up of β-1,4-linked sugar chains, often decorated with various side groups (see Figure 2-4(c)). It plays a vital role in cell wall assembly, maturation, and degradation, particularly in the secondary cell walls of woody and grass species. Unlike cellulose, hemicellulose is a heteropolysaccharide and can be categorized into four major types based on structural differences: Xylans, Glucuronoxylans ,Mixed-linkage β−(1,3;1,4)-glucans and Mannans

The structural diversity and complexity of hemicellulose present a challenge for detailed analysis of cell wall components. Notably, β−(1,3;1,4)-glucans are primarily found in Poaceae (grasses) and are uncommon in other terrestrial plants[69]. Meanwhile, β−(1,4)-mannans are widely distributed in charophyte algae[70], serving as their primary form of hemicellulose. In the primary cell walls of eudicots, glucuronoxylans are the most abundant hemicelluloses. However, in grasses such as bamboo, the hemicellulose composition differs significantly. In bamboo cell walls, both the chemical structure and content of hemicellulose vary with plant age. A study by Yue[71] reported that the main sugar components of bamboo hemicellulose include: Arabinose (6.5–25.5%), Xylose (56.1–89.6%) and Glucuronic acid (1.4–14.6%)

Among these, xylose is the dominant monosaccharide in bamboo hemicellulose. In addition, small amounts of glucose (except in 2-month-old bamboo) and galactose were also detected. Although the precise role of different hemicellulose types in determining cell wall mechanical performance remains unclear, it is hypothesized that hemicellulose interacts with cellulose via hydrogen bonds, affecting the slippage of microfibrils under load[72]. The cell walls of bamboo tissues—including fibers and tracheids—may be impregnated with lignin, making them impermeable to water. Lignin is generally regarded as a cementing agent in the cell wall, contributing to the rigidity and compressive strength of the bamboo structure. Extractives are a group of organic compounds present in bamboo in relatively small quantities, yet they have a significant impact on material performance. Extractives include pigments, phenolic compounds, turpentine, fatty acids, resins, and metabolic intermediates. These compounds not only give bamboo its distinctive color, but also enhance its natural durability. Many extractives are toxic to fungi and insects, thereby improving bamboo's resistance to biological degradation[73].

The layered structure of the bamboo cell wall is a key factor that determines its strength and mechanical performance. As shown in Figure 2-4, the multilayered structure of bamboo parenchyma and fiber cell walls is more complex than that of wood fibers. The outermost layer of a bamboo fiber is the primary wall, where microfibrils are arranged in a net-like and disordered pattern. Beneath the primary wall lies the secondary wall, which consists of up to nine (or occasionally more) alternating thick micro-scale layers and thin nano-scale layers.

In the thick layers, the microfibrils are primarily oriented along the fiber axis, with the microfibril angle gradually increasing from the middle lamella toward the lumen[74]. In contrast, in the thin layers, the microfibrils are oriented approximately perpendicular to the fiber axis. Moreover, the thin layers contain a significantly higher lignin content than the thick layers[75-77], indicating a greater degree of lignification. Between adjacent cells lies a highly lignified region known as the middle lamella, composed of a lignin–pectin complex, which functions primarily to bind the cell walls of adjacent cells, forming an integrated structure. The primary wall itself is a relatively thin layer with randomly deposited microfibrils. In some cases, the middle lamella and adjacent primary wall are collectively referred to as the primary layer[78].

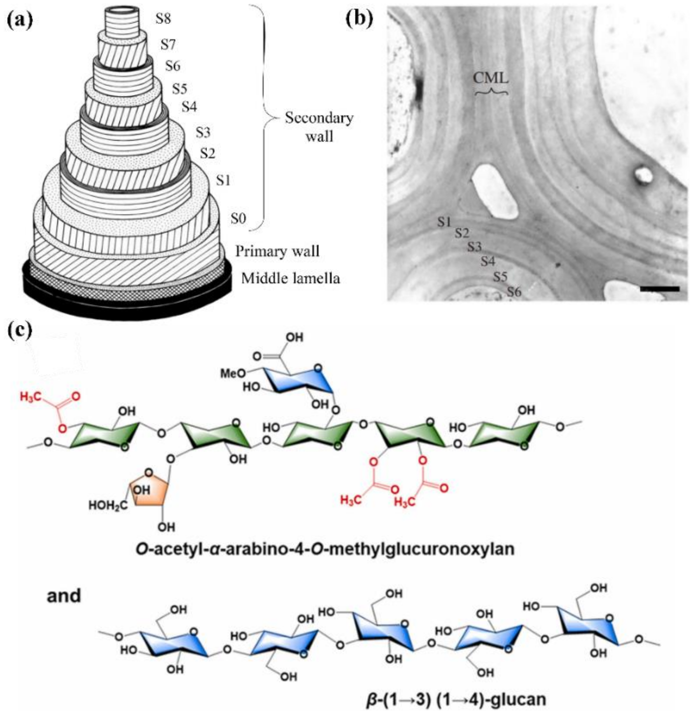

Figure 2-4 Ultrastructure of bamboo cell wall: (a) schematic model of the polylamellate structure of the bamboo fibre wall, (b) TEM cross-section of Moso bamboo fiber cell walls, (c) Structural formulas of hemicelluloses from bamboo fibres and parenchyma cells (O-acetyl-α-arabino-4-O-methylglucurono-β-(1→4)-D-xylan and β-(1→3)(1→4)-glucan)

Reference：[66, 79]

2. 2. 2 Defects and Bamboo Nodes

Due to its high moisture content during storage, bamboo is highly susceptible to fungal and insect attack[80,81]. Compared to wood, bamboo exhibits weaker resistance to decay, primarily because of its thinner cell walls, higher starch content, and the absence of naturally occurring antifungal compounds found in certain hardwoods such as teak and purpleheart[82,83]. In a study by Nandiyanto et al. [84], a soil burial test was used to evaluate microbial degradation of bamboo fiber-reinforced composites. The results revealed that bamboo-based materials were more readily decomposed and assimilated by bacteria. Therefore, strict quality inspection is necessary before bamboo is used as a structural component, to ensure protection against insect and fungal damage. Sun et al.[85] investigated the use of chitosan–copper complexes, difenoconazole, and tebuconazole to improve the antibacterial and antifungal performance of *Phyllostachys edulis* (Moso bamboo). The results showed that tebuconazole-treated bamboo fibers exhibited the best antifungal resistance. Hanim et al.[86] evaluated the effectiveness of various chemical treatments—including boiling, tributyltin oxide, tributylnaphthenate, permethrin, disodium octaborate tetrahydrate, benzalkonium chloride, and boric acid—on bamboo strips and bamboo plywood. Their findings indicated that boiling bamboo for 30 minutes improved resistance to white-rot fungi, but tributyltin oxide was found to be the most effective preservative for both bamboo and bamboo strips.

The nodes of bamboo culms have a significant impact on both physical and mechanical properties. According to Qi et al.[87], laminates made from node-free bamboo veneers exhibited superior mechanical performance compared to those containing nodes. Within bamboo strips, the node is the weakest point under tensile loading, especially when located at the tension face of bending members, such as the bottom of a beam. However, the presence of nodes had minimal influence on the overall tensile behavior. Wang et al.[88] found a correlation between the area fraction of node tissue and the tensile strength of bamboo. For instance, the strength of laminated bamboo lumber (LBL) was reduced by 29.2%, slightly lower than that of glubam (glued-laminated bamboo). In addition, bending strength was higher in node-free bamboo laminates compared to those with nodes. While the presence of nodes reduced ultimate load-bearing capacity and flexural strength, it had little effect on the bending modulus of elasticity[89].

Using serial sectioning and microscopy, Liu et al.[90] conducted a detailed investigation of the microstructure of bamboo nodes and their influence on crack propagation. The 3D distribution of vascular bundles within the node is illustrated in Figure 2-5. Two primary types of vascular bundles are present in the node region: longitudinal bundles and radial bundles[91]. The longitudinal vascular bundles within the node become thicker and their volume fraction increases. In terms of radial bundles, those in the central region are longer and thicker, while those near the lateral region are shorter and thinner. When a crack propagates into the node, it first encounters short radial bundles. The crack path is deflected at the interface between these bundles and surrounding matrix tissue, leading to the formation of interfacial cracks and the pull-out of short radial bundles, as shown in Figure 2-6. Due to this deflection, the crack deviates from its original trajectory and propagates along the fiber pull-out zone. The crack then extends into the region of long, thick radial bundles, where similar interfacial failure mechanisms occur. Because these bundles span the entire node, the crack continues to propagate radially through the node, eventually resulting in failure at the node. Due to the presence of two distinct types of radial bundles, the mode I fracture at the node evolves into a mixed-mode fracture. Compared to fracture in internodal regions, the node region exhibits greater energy dissipation mechanisms, suggesting that bamboo nodes contribute to enhanced mode I fracture resistance in the radial–longitudinal (RL) direction of laminated bamboo materials.

2. 2. 3 **Property change during modification**

Due to the strong activity of free hydroxyl groups and a variety of functional groups in the cell walls, bamboo has a strong moisture absorption capacity[85,92]. Furthermore, when the moisture content is above certain value (20%), bamboo is susceptible to attack by fungi and bacteria, which can release cellulase or hemicellulase to degrade the cell wall polysaccharides. Such biodegradation results in an unacceptable loss of mechanical properties and makes it prone to cracking and deformation, which affect the dimensional stability of bamboo materials.

During the bamboo processing, several modification methods are available to increase bamboo stability and durability.

- Thermal modification: Thermal modification can efficiently decrease the hygroscopicity of bamboo while improving its dimensional stability, anti-weathering, and corrosion resistance[93]. Existing studies indicate that high-temperature thermal modification increases the stiffness of cell walls, thereby improving the dimensional stability, hygroscopicity, and strength of bamboo sheets.
- Ultrasonic treatment: Ultrasonic treatment is an efficient and environmentally-friendly

physical treatment method. Existing studies found that hemicellulose was removed and lignin's structure was disrupted after ultrasonic treatment of Eucalyptus[94]. Futhermore, ultrasonic pretreatment improved the accessibility of pretreatment chemical impregnation agents and accelerated the loss of nutrients of bamboo[95].

- Chemical Modification: Externally applied chemical reagents react with the hydroxyl and phenyl groups of the cell wall polymers. The chemical reaction can block these hydroxyl groups, which will reduce the hygroscopicity.
- Impregnation Treatment: This method involves filling the voids within the bamboo cell wall using volume-expanding chemical agents such as monomers, polymers, resins, or waxes. These substances do not chemically react with the bamboo polymers directly, but possess a certain level of permeability, allowing them to form a thin surface film while penetrating deeply into the vessel pores of the bamboo. Although this method does not alter the molecular structure of the cell wall polymers, it can effectively increase the density of bamboo and block moisture pathways, thereby enhancing the material's dimensional stability and moisture resistance[96,97].

In contrast, during chemical and thermal modification processes, the chemical composition and structure of the bamboo cell wall are altered, enabling the tuning of its stability, durability, and mechanical performance.

2.2.4 **Research questions**

The molecular and cellular structure of bamboo forms the foundation for its application as a building material. However, at this scale, many aspects of the structure–property relationship remain unresolved, potentially affecting the processes of cultivation, harvesting, grading, and treatment of bamboo materials.

- How do molecular and cellular bamboo architecture influence its properties? In particular, what are the specific roles of the components of the cell wall?
- Can biophysical characteristics of bamboo be predicted by studying biochemical properties of the plant cell wall?
- Is it possible to modify growing bamboo to produce bamboo with desired properties, either by choosing favorable conditions, or by altering the biosynthesis of bamboo molecules?

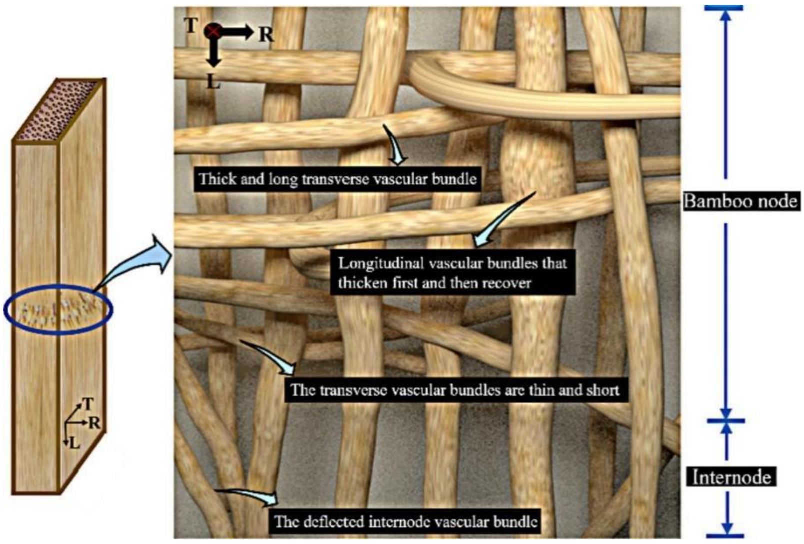

Figure 2-5 Schematic Diagram of the 3D Distribution of Vascular Bundles in a Bamboo Node

Reference：[90]

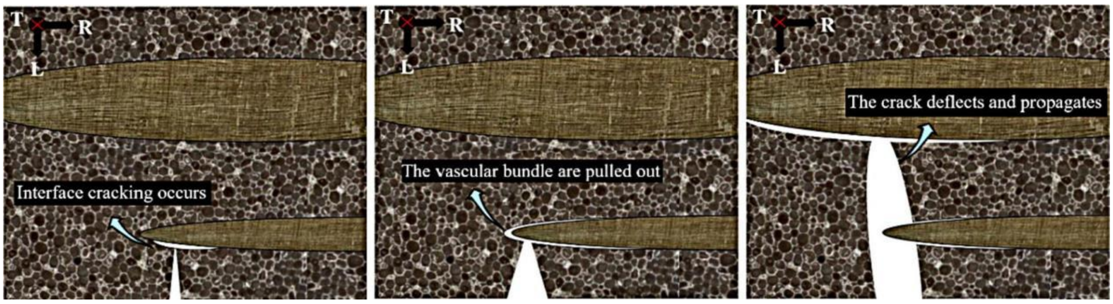

Figure 2-6 The crack deviates from its original propagation path and extends into the fiber pull-out region.

Reference：[90]

2.3 Processing of Bamboo Products

Although bamboo is generally less uniform in geometry and dimensions compared to timber, it offers significant advantages in terms of low cost, abundant availability, and widespread accessibility. Through engineered processing, bamboo can be structurally optimized to produce various engineered bamboo products. Modified and enhanced bamboo materials exhibit excellent mechanical performance, particularly a high strength-to-weight ratio, enabling bamboo to compete with more energy-intensive or high-carbon-emission construction materials. These characteristics make bamboo a promising sustainable structural material in modern construction.

2. 3. 1 **Harvesting of Bamboo**

During the growth of bamboo, mature culm leaves fix carbon dioxide（CO_2）through photosynthesis, contributing to carbon sequestration**.** To increase bamboo biomass yield, chemical fertilizers are often applied. The theoretical carbon storage (CO_2 sequestration potential) in above-ground bamboo biomass can be estimated by multiplying the mass of above-ground bamboo, its corresponding carbon content, and the molecular weight ratio of CO_2 to carbon**,** as shown in Equation 2-1**.** Life Cycle Assessment (LCA) has been widely adopted to evaluate the environmental performance of bamboo-based products. In LCA modeling, the amount of bamboo available for processing is typically estimated by applying loss coefficients derived from harvesting and manufacturing processes. Studies have shown that harvest losses—such as removed leaves and branches—account for approximately 20% to 37% of the total above-ground biomass, with an average loss rate of 29.7%[98-102] reported across multiple studies. During bamboo forest management, three types of chemical fertilizers are commonly applied: nitrogen (N), phosphorus (P), and potassium (K)[103-106]. Most studies report fertilizer usage in kilograms per hectare (kg/ha). However, in LCA calculations, it is often necessary to relate input materials such as fertilizers to intermediate products (e.g., above-ground bamboo) or functional units (e.g., specific bamboo products). Therefore, fertilizer inputs are typically converted to kilograms per ton of above-ground biomass (kg/t) for data consistency.

Studies have shown that the consumption ranges of fertilizers per ton of above-ground bamboo biomass are as follows:

- Nitrogen (N): 0.05 – 10 kg/t
- Phosphorus (P): 0.01 – 6 kg/t
- Potassium (K): 0.13 – 4 kg/t

In a bamboo management study in India, Panda[104] reported an outlier where the fertilizer input per ton of above-ground bamboo reached as high as 1,100 kg of nitrogen (N), 250 kg of phosphorus (P), and 475 kg of potassium (K). This may be attributed to the relatively low bamboo yield in the region. According to Tewari et al.[107], the bamboo yield per unit area in India is only one-fourth to one-fifth of that in China, which could explain the higher fertilizer demand per ton of bamboo produced. In addition, studies have estimated below-ground biomass using the root-to-shoot ratio, which ranges from 0.6 to 2.1[100, 108-110]. During the bamboo harvesting process, direct greenhouse gas (GHG) emissions primarily result from the use of mechanical equipment, such as chainsaws and power saws. The corresponding diesel consumption ranges from 0.2 to 7.3 liters per ton of harvested above-ground bamboo.

$$m_{CO_2} = m_{bamboo} \times C \times \frac{mw_{CO_2}}{mw_C} \tag{2-1}$$

Where：m_{CO_2} —— the mass of CO_2 sequestrated, kg.；m_{bamboo} —— the dry mass of bamboo, kg；C —— carbon content of dry bamboo, %；mw_{CO_2} —— molecular weight of CO_2；mw_C ——molecular weight of carbon。

2. 3. 2 **Drying of Bamboo**

As a natural material, bamboo is highly susceptible to fungal degradation. Unlike many wood species, bamboo lacks intrinsic protective compounds[111] and does not possess an effective sealing mechanism similar to wood. After mechanical processing, most of bamboo’s natural barriers against biodegradation are compromised, making it more vulnerable to wood-decaying fungi, which in turn can significantly impair its mechanical performance.

To ensure structural safety, the ISO 19624 standard[112] for structural bamboo specifies that “dry-graded” bamboo must have a moisture content (MC) of no more than 19%, as a prerequisite for strength grading. Additionally, dried bamboo offers several advantages:

- Improved adhesion, making it more suitable for lamination processes and enhancing the bonding quality of composite bamboo products[113, 114];
- Reduced transportation weight, leading to improved cost-effectiveness and logistical efficiency.

Bamboo’s durability and environmental adaptability can be further improved through thermal and chemical treatments. Like wood, the moisture content of bamboo significantly influences its mechanical properties, both in laboratory testing and real-world applications. Therefore, proper control of moisture content is essential.

Being a hygroscopic material, bamboo’s moisture content fluctuates with changes in ambient temperature and humidity. As such, it is critical to dry bamboo before use to match the target moisture content of the intended building environment. This helps avoid excessive deformation during natural equilibration. Moisture content is typically expressed as a percentage relative to the oven-dry mass, and the equilibrium moisture content (EMC) refers to the stable MC bamboo reaches under specific environmental conditions.

Freshly harvested bamboo may have an MC exceeding 45%, including both free water and bound water. Once all free water in the cell cavities has evaporated, the bamboo reaches its fiber saturation point (FSP)[115]. Similar to wood, bamboo's mechanical properties remain relatively stable above the FSP—a state referred to as "green bamboo". Below the FSP, bamboo's strength and stiffness increase significantly as moisture content decreases.

Wang et al.[116] found that, except for tensile strength, most mechanical properties of bamboo improve as moisture content drops below the FSP. Specifically:

- Tensile strength tends to decrease with lower MC;
- Tensile modulus of elasticity is insensitive to MC changes;
- Other strength indicators (e.g., bending, compression) increase as MC decreases.

Figure 2-7 illustrates the detailed variation in bamboo's mechanical performance across different moisture contents. Studies have shown that oven-dried bamboo (MC ≈ 0%) exhibits approximately twice the strength and stiffness of green bamboo[117, 118]. Bamboo walls contain a large number of thin-walled, highly hygroscopic cells, which begin to shrink even when MC is still above the FSP (typically 17–25%)[119]. Given that the EMC in building environments is usually around 8–12%, drying bamboo below the FSP to reduce bound water is essential to minimize dimensional deformation during service.

To improve both mechanical performance and dimensional stability, the natural moisture content of bamboo must be reduced through air drying or accelerated drying techniques. Various dehydration and drying methods are available for bamboo, including: Hot-air drying; Vacuum drying; Freeze-drying; Spray drying and Vacuum-assisted microwave drying[120, 121]. However, in the bamboo processing industry, convective drying and kiln drying remain the most commonly used industrial drying methods. While convective drying is energy-intensive and requires higher equipment standards, it remains the fastest and most efficient method for large-scale commercial bamboo drying. Kiln drying refers to the use of enclosed drying chambers—typically with volumes ranging from 30 to 100 m³—that provide controlled heating, air circulation, humidification, and ventilation. Kiln systems may use:

- Indirect heating: via steam, hot water, thermal oil, or electric elements
- Direct heating: via gas or fuel combustion

In convective kiln drying, fans installed at the top or sides circulate hot or dehumidified air through and around stacked bamboo to improve drying uniformity. Key factors influencing bamboo drying efficiency include both equipment-related and material-related variables. On the equipment side, the thermal insulation performance of the kiln and the ability to control and optimize fan speed during different stages of the drying process play significant roles. On the material side, the size and volume of the bamboo elements, their porosity and initial moisture content, as well as species-specific differences in moisture content—all substantially affect the drying rate and uniformity.

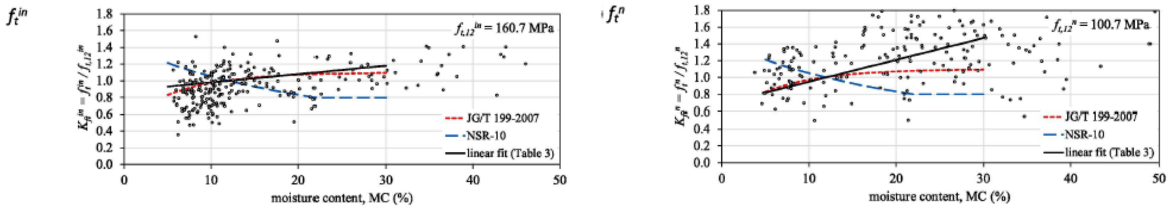

(a) Internode tension strength (b) Tension strength including nodes

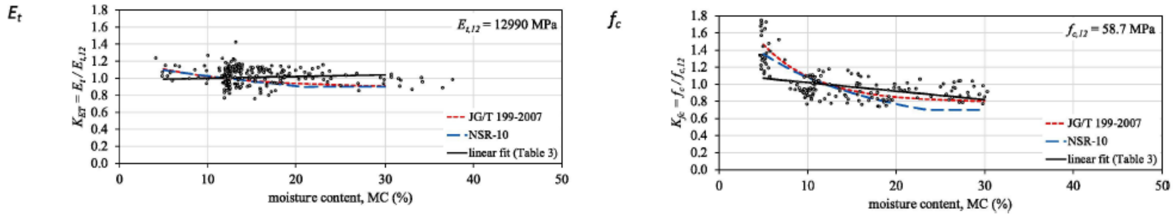

(c) Elastic modulus (d) Compressive strength

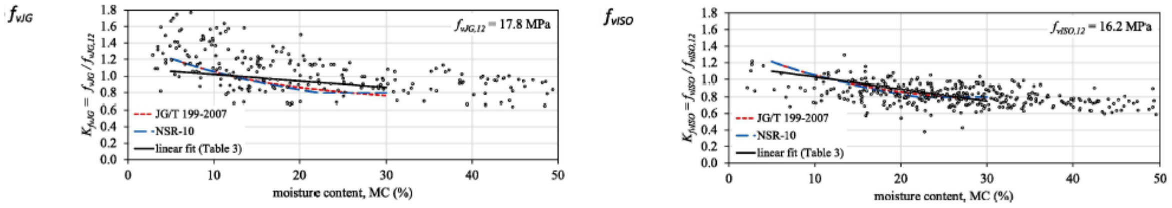

(e) Shear strength in accordance with JG/T 199–2007[122] (f) Shear strength in accordance with ISO 22157[123]

Figure 2-7 Bamboo material property results normalised by values at MC = 12%.

Engineered bamboo products are typically used in dry building envelopes, but during the construction phase, they may be exposed to excessive moisture, leading to an increase in moisture content (MC). Therefore, to ensure that bamboo can reach a stable equilibrium moisture content in service conditions, it must be dried to an MC range of 12%–20% during the manufacturing process. On construction sites, unprotected engineered bamboo may absorb moisture from high-humidity environments, causing its MC to rise above 20%. However, once the building envelope is sealed, the MC of bamboo will gradually decrease to around 12%, aligning with the indoor equilibrium humidity. The service environment classification is critical for engineered bamboo, as excessive moisture loss in indoor settings can result in dimensional shrinkage, warping, and cracking, which in turn may degrade its mechanical performance and compromise structural safety. Accordingly, proper humidity control measures must be implemented during storage, transportation, and construction to ensure the dimensional stability and long-term durability of bamboo products.

2. 3. 3 **Bamboo Processing**

After harvesting, bamboo is typically transported from plantations to sawmills for further processing, where nodes and surface defects are removed. As illustrated in Figure 2-8, approximately 50% of the raw bamboo material can be recovered and used to produce usable boards and bamboo strips, while the remaining bamboo chips, shavings, and fiber by-products are commonly utilized as biomass fuel[124] or as reinforcement in fiber-based bamboo composite panels, with certain market value.

Natural bamboo culms are often processed into structurally optimized building materials, known as engineered bamboo products (see Figure 2-8). These products are typically composed of bamboo strips, adhesives, and reinforcing agents, offering improved dimensional stability, mechanical uniformity, and enhanced durability. Major types of engineered bamboo products include:

Bamboo Sliver Board, BSB: BSB is made from bamboo slivers or woven mats/screens composed of bamboo slivers. Studies have shown that BSB can be used as load-bearing construction components, offering advantages such as low cost**,** low technical requirements**,** and high mechanical strength[125,126]. Currently, BSB is primarily used in concrete formwork and structural elements.

Bamboo Particleboard, BPB: BPB is manufactured from bamboo shavings, strips, or fibers, and is comparable in function to wood-based particleboard or medium-density fiberboard (MDF).

Bamboo Oriented Strand Board, BOSB: Developed from BPB, BOSB is produced by increasing the size of bamboo strands and aligning them in specific orientations during processing. The production technologies of BPB and BOSB are relatively mature, and the manufacturing equipment can be adapted directly from wood-based OSB production lines. However, these products are currently used mostly in packaging, furniture, and construction formwork, and have yet to achieve large-scale commercialization.

Laminated Bamboo Sheet, LBS： LBS is composed of bamboo strips, and the typical production process includes: raw bamboo slitting, coarse planing and strip selection, carbonization and drying, fine planing and adhesive application, pressing of single-layer sheets, sanding and multi-layer pressing, followed by sawing, final sanding, and dust removal[127].

Bamboo Scrimber Board, BSB： This product is made from loosely arranged bamboo fiber bundles. From a microstructural perspective, the longitudinal alignment of bamboo fibers—which possess higher strength than wood fibers—allows bamboo fiber-based products to maximize the inherent mechanical advantages of bamboo.

Flattened Bamboo Panel, FBP： In response to bamboo's thin-walled structure, FBP is produced through a process of softening, flattening, and shaping. As no adhesives are used during forming, FBP is considered environmentally friendly. It can be used in tableware, cutting boards, and similar products, and can be further enhanced with nonwoven fabric reinforcement, or joined and bonded to form structural panels for architectural applications.

Laminated Veneer Bamboo, LVB: LVB is made from thick-walled bamboo culms, although its processing is technically more complex and limited to specific bamboo species. LVB is considered a derivative of laminated bamboo lumber or bamboo scrimber and is typically manufactured using slicing or rotary cutting. Bamboo veneers are usually very thin (0.3–0.4 mm), and are mainly used in high-end applications such as furniture, decorative surfaces, handicrafts, molded panels, fans, bookmarks, and partitions.

As a natural material, bamboo exhibits inherent variability in mechanical properties[128], even among samples of the same species. This variability arises from the interaction between molecular-scale characteristics and macroscopic structure. To ensure that processed bamboo products can safely sustain their design loads in structural applications, ISO 19624 requires strength grading for each bamboo culm[112]. This standard allows structural engineers to specify a required strength grade and use its characteristic strength values in structural design calculations. Such standardized grading approaches improve the reliability and predictability of bamboo as a structural material, thereby supporting its broader application in architecture and engineering[129].

According to the ISO 19624 international standard[112], bamboo strength grading primarily includes two approaches: visual strength grading (VSG) and machine strength grading (MSG).

1. Visual strength grading (VSG)

   VSG is a grading method based on the visual assessment of bamboo’s external characteristics. It relies on manual inspection to evaluate key features that may affect the mechanical or structural performance of bamboo. These features include, for example, nodes or nodal scars on the culm surface, cracks generated during the drying process, and other visible defects that may compromise load-bearing capacity.

2. Machine strength grading (MSG)

   MSG involves the use of mechanical equipment to measure one or more indicative physical properties that are strongly correlated with the mechanical strength of bamboo. Based on these measurements, bamboo elements are classified into different strength grades.

After mechanical grading, a visual re-inspection is typically required to identify structural defects that may not be detectable through machine-based testing. This additional step helps ensure that the bamboo meets the load-bearing requirements necessary for structural applications.

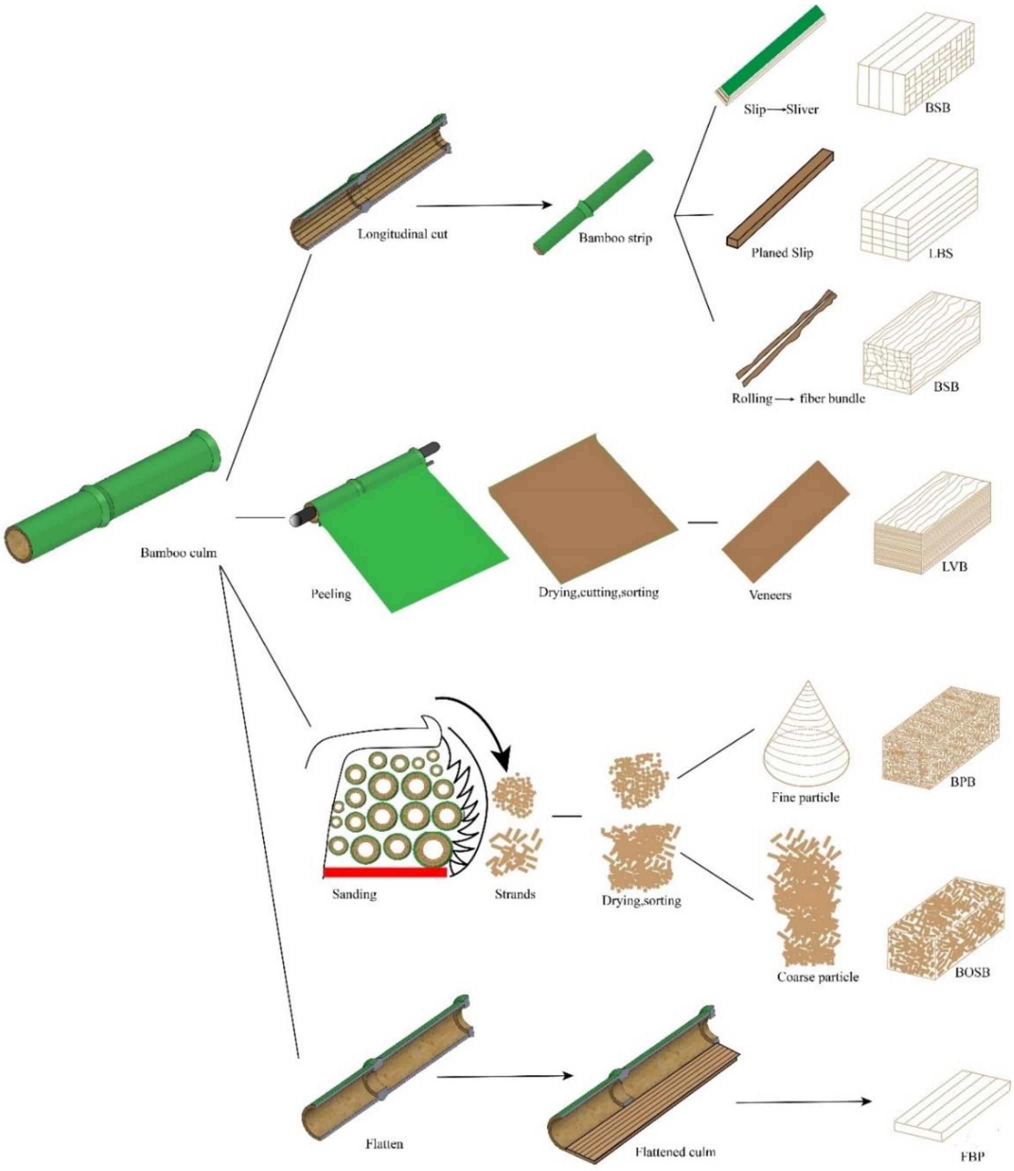

Figure 2-8 Processing Chain of Engineered Bamboo Products

By combining visual strength grading (VSG) and machine strength grading (MSG), the accuracy and reliability of bamboo classification can be improved, thereby optimizing its application in structural engineering.

After the mechanical strength grading process is completed, bamboo elements are assigned to different strength grades. The classification criteria for bamboo can generally be divided into strength-based grading and load-bearing capacity-based grading[130]. Compared to the grading standards for wood products, the classification approach for bamboo differs slightly. Wood is typically graded based on strength, particularly bending strength. For example, under the European standard BS EN 338 [131], timber strength classes range from C14 (weakest) to C50 (strongest), where the numerical value represents the bending strength in N/mm².

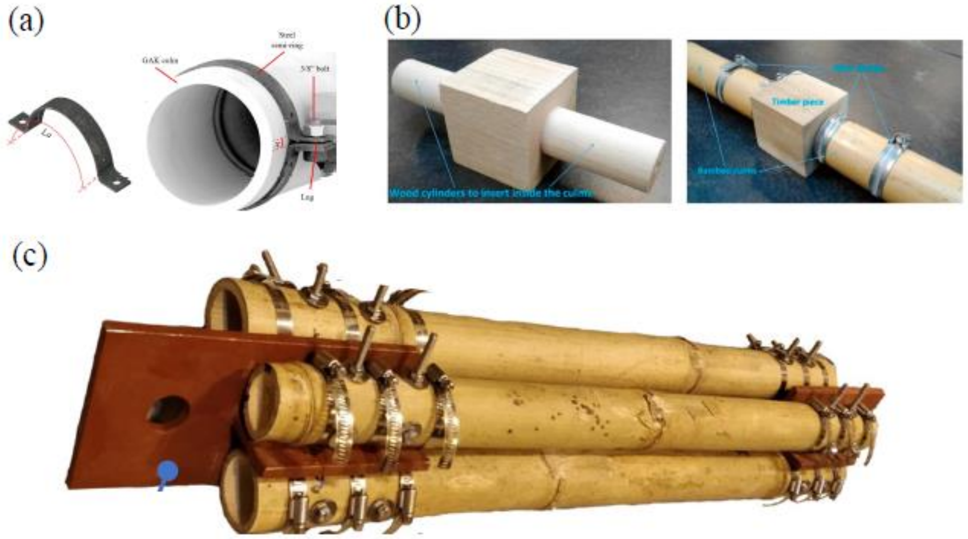

Figure 2-9 Typical Forms of Bamboo Structural Joints Reported in the Literature

Reference：[77,132,133]

Although bamboo can also be graded using strength-based approaches, extensive studies[134-136] on its bending performance have shown that load-carrying capacity-based grading methods are generally more accurate and reliable. Stress-based grading is typically based on the fundamental mechanical properties of bamboo, including modulus of elasticity (E), bending strength (σ_b), tensile strength (σ_t), and compressive strength (σ_c). In contrast, load-based grading focuses on structural performance indicators such as flexural stiffness (EI), maximum bending moment ($M_{\max}$), axial stiffness (EA), and maximum axial load capacity ($P_{\max}$).

Research by Trujillo et al.[136] demonstrated that load-based grading is more suitable for bamboo structural design, as it enables more accurate prediction of EI and $M_{\max}$, rather than simply relying on E and bending strength. Similarly, Nugroho et al.[134] also recommended the use of EI and $M_{\max}$ as key parameters for structural grading of bamboo. In a structural grading study on *Dendrocalamus asper* (giant bamboo), Nurmadina et al.[135] found that the combination of linear mass (q) and diameter squared (D²) provided the best prediction of EI, while qD was identified as the optimal predictor for $M_{\max}$.

In addition to dimensioned or machined bamboo, natural bamboo culms can also be used directly as structural components in buildings[133,137-139]. Compared to engineered bamboo products, natural bamboo is considered more environmentally friendly, as engineered products require the use of adhesives, which contribute to higher embodied energy and potential environmental impacts. However, due to the inherent variability in geometry and material properties of natural culms, the connection detailing and design complexity for structural use are significantly higher (see Figure 2-9). As a result, the use of natural bamboo culms in structural applications remains more limited compared to engineered bamboo products.

Nevertheless, many engineered bamboo products are also used in combination with natural culms in construction to improve support stiffness and shear resistance of structural components. This hybrid application strategy not only enhances structural performance, but also broadens the practical applicability of bamboo in the built environment[139].

2. 3. 3 **Future Trends and Innovations in Bamboo Structural Architecture**

Recent studies[36,139,140] have shown that novel prefabricated bamboo structural systems are gaining increasing attention and are being widely applied. Compared to traditional construction methods and materials, such prefabricated bamboo systems offer significant reductions in embodied carbon emissions and embodied energy during production and transportation. Prefabricated bamboo structures help minimize material waste, reduce construction costs, and shorten installation time.

To achieve standardization of bamboo components, researchers have developed a variety of simple and reliable connectors for the efficient joining of bamboo culms[139]. Among these, a prefabricated shear wall panel was designed, which uses bamboo culms as vertical studs and glued-laminated bamboo as the boundary framing components, as shown in Figure 2-10(a). Additionally, based on a building information modeling (BIM) platform, researchers designed a 12-meter-span asymmetrical hybrid steel–glued-laminated bamboo truss for roof systems[36]. In this hybrid structure, glued-laminated bamboo serves as the top chord and web members, while steel pipes are used for the bottom chord, as illustrated in Figure 2-10(b).

These studies and practical applications indicate that prefabrication, modularization, and material hybridization are likely to become key development directions in future bamboo architecture, enhancing the potential of bamboo as a viable material in modern construction.

In recent years, increasing attention has also been given to bamboo–timber composite bio-based materials. For example, cross-laminated bamboo and timber (CLBT) is an emerging engineered composite[141] that optimally combines engineered bamboo layers with wood layers, improving resource efficiency and providing superior basic mechanical performance compared to traditional large-scale timber products.

As an innovative engineered bio-based material, CLBT has been the focus of various studies investigating its bonding quality, durability, and mechanical performance in small-scale specimens, laying the groundwork for the future promotion of full-scale CLBT components[141–144]. Research has shown that CLBT panels with engineered bamboo as the outer layers and wood as the inner core demonstrate superior out-of-plane mechanical performance compared to traditional cross-laminated timber (CLT) made with softwood. This characteristic suggests a broader potential for CLBT in structural engineering and architectural applications.

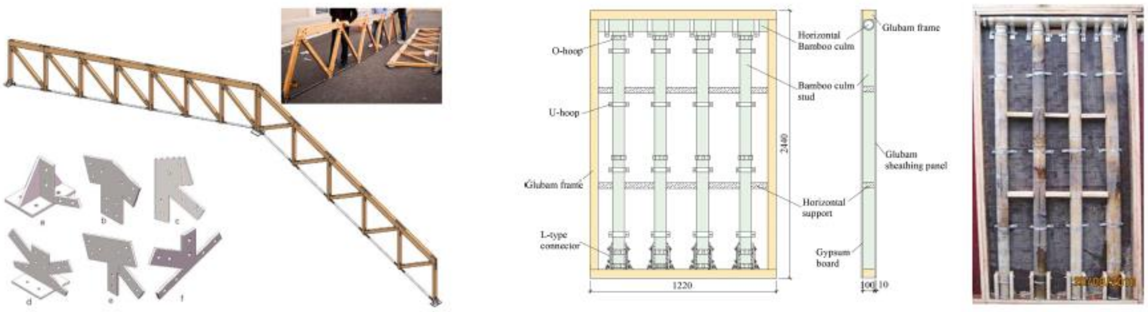

(a) Roof truss (b) Shear wall

Figure 2-10 Prefabricated Bamboo Structure

2.4 Treatment of Bamboo

In addition to drying and dimensional processing, bamboo requires durability treatment before entering the construction industry to extend its service life. Composed primarily of cellulose, hemicellulose, and lignin, bamboo is highly susceptible to biological degradation by fungi and bacteria in high-humidity environments. Its service life in structural applications is directly influenced by such degradation, making protective treatments essential. Currently, methods to improve the durability of bamboo fall into two main categories: physical treatments and chemical treatments. These methods can effectively enhance bamboo's resistance to decay, mold, and biodegradation, ensuring its long-term and stable use in the built environment.

2. 4. 1 **Overview of Bamboo Treatment Technologies**

Bamboo treatment refers to a set of processing techniques aimed at enhancing the material performance of bamboo. The primary goal is to improve its mechanical properties and durability while ensuring that the end-of-life environmental impact of treated bamboo does not exceed that of untreated material.

Key material properties targeted for improvement include dimensional stability, resistance to biological degradation, thermal stability or fire resistance, UV resistance[145], and overall mechanical strength. Currently applied physical and chemical treatments typically achieve their effects through the following mechanisms:

- Reducing moisture penetration to limit dimensional changes and inhibit microbial growth, which can be achieved through hydrophobic treatments or filler-based barriers;
- Deactivating chemically reactive groups (e.g., hydroxyl groups) to prevent microbial and insect attack, while also improving fire resistance to some extent;
- Penetrative preservative treatments that actively kill fungi, bacteria, or insects, or that incorporate fire-retardant agents to enhance thermal stability;
- Surface coatings that improve moisture resistance, biological durability, fire resistance, and UV stability.

Bamboo treatment is generally carried out using one of three strategies: cell wall modification, penetrative treatment, or surface coating. Among these, cell wall modification can be further categorized into thermal modification and chemical modification. Both approaches are considered active modification strategies, as they alter the chemical composition and properties of bamboo at the molecular level, thereby improving its overall performance.

2. 4. 2 **Thermal Modification**

Due to its practical feasibility, thermal modification is widely used in the industrial sector and is considered an effective method for improving the dimensional stability and resistance to biological degradation of both bamboo and wood[97,146-148]. During thermal treatment, the chemical composition and anatomical structure of bamboo undergo significant changes (as shown in Figure 2-11), which result in substantial improvements in durability and physico-mechanical performance.

There are two classical thermal treatment methods commonly applied to bamboo:

1. Thermal treatment in a saturated steam drying chamber:
   In this method, bamboo is treated using saturated steam at temperatures ranging from 140–160 °C.
2. Thermal treatment in a sealed kiln:
   This method involves direct heating within a sealed drying kiln, with treatment temperatures between 180–200 °C[149].

In both processes, not only is the moisture content of bamboo significantly reduced, but a series of chemical reactions are also triggered, resulting in changes to the chemical composition of the material.

Table 2-3 summarizes the compositional changes in bamboo during thermal treatment[150], including variations in holocellulose, α-cellulose, hemicellulose, lignin, and extractives. These changes have a direct influence on the mechanical properties, dimensional stability, and long-term durability of bamboo.

Table 2-3 Chemical composition of bamboo after thermal treatment

Specimen	Mass Loss （%）	Holocellulose （%）	α −Cellulose （%）	Hemicellulose （%）	Lignin （%）	Extractives （%）
Untreated	0	67.05	41.54	25.51	22.06	6.27
Heat(180 °C)	3.22	59.43	32.42	27.01	25.67	8.25
Heat(200 °C)	7.83	53.54	26.61	26.93	31.67	9.07

During thermal treatment, acetyl esters in xylan undergo hydrolysis, resulting in the formation of acetic acid. In the resulting acidic environment, hemicellulose degrades through depolymerization into oligomers and monomers, which further dehydrate to form aldehydes. This process reduces the number of hydroxyl groups in bamboo, thereby decreasing its hygroscopicity. In contrast, cellulose is less affected by thermal degradation; however, its crystallinity tends to slightly increase[150-152]. Lignin, due to its relatively high chemical stability, only undergoes significant cleavage at elevated temperatures, forming phenolic groups. These reactive lignin-derived compounds can enhance cross-linking within the cell wall, which reduces cell wall elasticity and decreases the moisture affinity and swelling tendency of cellulose microfibrils. As a result, the dimensional stability and resistance to biological degradation of bamboo are significantly improved[153-155]. Figure 2-12 presents the Fourier-transform infrared (FTIR) spectra of bamboo before and after thermal treatment. The absorption peak at 3420 cm^{-1}, which corresponds to the O–H stretching vibration of hydroxyl groups, shows a marked reduction in intensity after thermal treatment, indicating a significant improvement in bamboo’s hydrophobic properties.

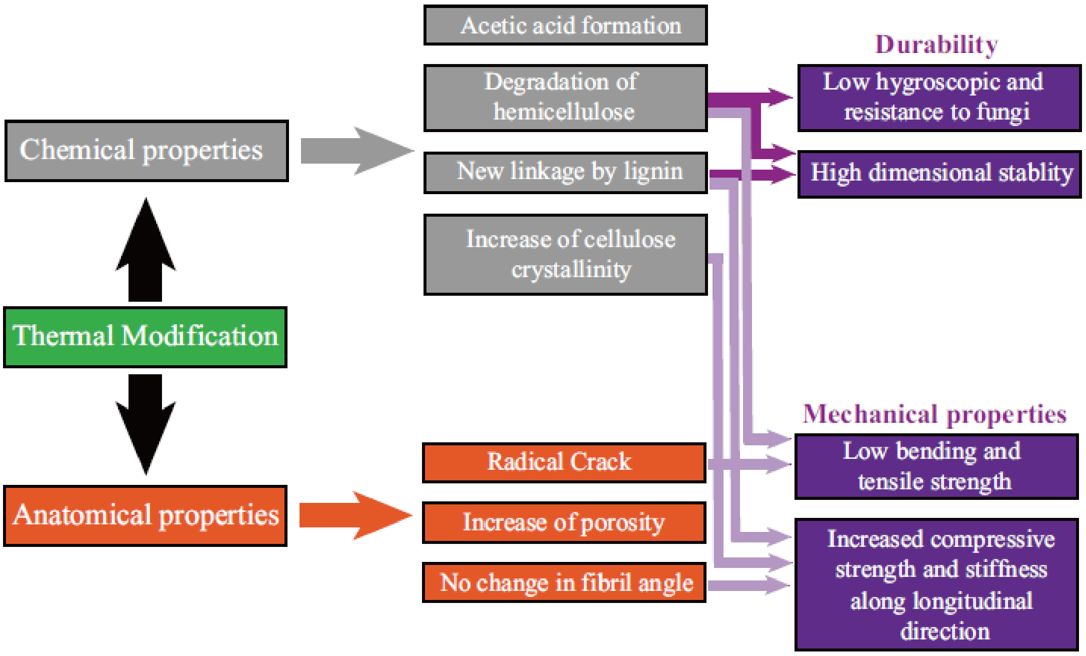

Figure 2-11 Property changes during the thermal modification process

Thermal modification not only alters the chemical composition of bamboo, but also induces significant changes in its anatomical structure. After heat treatment, cracks appear between vascular fiber cells, and parenchyma cells exhibit deformation and distortion. These changes are primarily attributed to moisture loss within the bamboo during thermal processing, which causes differential shrinkage between adjacent cells[156].

As the treatment temperature increases—particularly beyond 170 °C—the cell walls of parenchyma cells begin to delaminate and peel off. This phenomenon is mainly due to the extensive degradation of hemicellulose, which compromises the structural integrity of the cell walls. Additionally, some pits on the cell walls become smaller due to cell shrinkage, and others are blocked by recondensed lignin, further altering the bamboo’s microstructure.

After thermal treatment, the surface wettability of bamboo is significantly reduced. Compared to untreated bamboo, the contact angle of the heat-treated surface increases by 148%, indicating a substantial improvement in hydrophobicity[156].

In terms of mechanical properties, untreated bamboo shows a slightly higher average tensile modulus of elasticity than heat-treated bamboo. Its tensile strength is also marginally higher, but the difference is considered structurally insignificant[157]. For compressive properties, the compression modulus of elasticity of heat-treated bamboo is slightly higher than that of untreated bamboo, while the compressive strength remains nearly unchanged. Moreover, flexural performance is largely unaffected by thermal treatment.

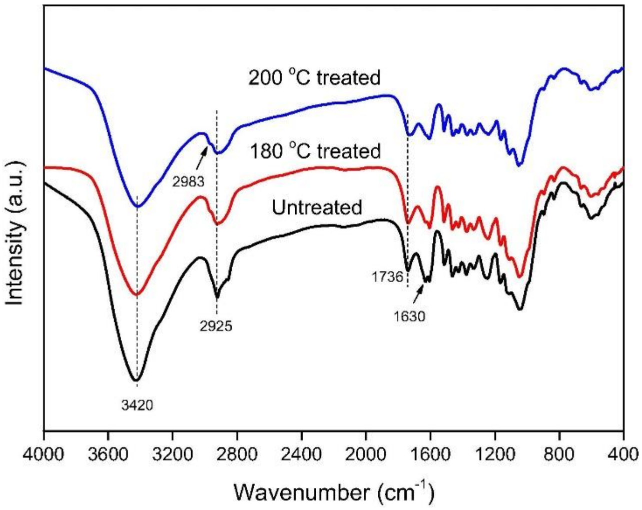

Figure 2-12 FTIR analysis of bamboo before and after thermal treatment[146]

2. 4. 3 Chemical Modification

Although traditional non-chemical treatments have been applied for bamboo protection, chemical treatment methods are generally more suitable for large-scale construction projects[158,159]. A wide range of chemical agents have been developed for the protection of both wood and bamboo to improve water resistance, insect resistance, fungal resistance, and to enhance fire retardancy. However, the use of certain chemical preservatives remains controversial. For instance, traditional wood protection solutions—while highly effective—often contain heavy metals and toxic compounds, such as chromated copper arsenate (CCA) and pentachlorophenol, which may have adverse effects on ecosystems and living organisms. Among the numerous bamboo and wood treatment methods proposed, researched, and commercialized, the use of low-cost water-soluble salts, such as borate-based compounds, is one of the most attractive alternatives. These include disodium octaborate tetrahydrate (DOT), boric acid, and borax[160-162]. Boron compounds are considered among the most effective and widely used preservatives for bamboo and wood due to their broad-spectrum biocidal properties, low mammalian toxicity, colorless and odorless nature, and strong fire-retardant characteristics[163-165]. In addition, boric acid treatment has been found to alter the surface morphology of bamboo fibers, reduce cellulose crystallinity, and form B–O–C chemical bonds within the bamboo structure, thereby enhancing its resistance to decay.

Studies have shown that boron-treated bamboo exhibits improved protective performance and may even demonstrate enhanced tensile strength, outperforming untreated bamboo in mechanical properties[80,166]. Moreover, Gauss et al.[159] explored the potential of citric acid as a treatment agent for bamboo. Citric acid acts as a crosslinking agent for cellulose, reacting with the cell wall polymers of bamboo while meeting health and safety requirements. In the wood industry, citric acid has been shown to improve product quality and reduce the environmental footprint of building materials, supporting sustainable development goals.

Due to the absence of ray cells in bamboo, it lacks a radial transport system, making chemical penetration more difficult than in wood. To address this challenge, researchers have developed a range of efficient and safe bamboo protection methods, with common chemicals including boric acid, borax, and borates.

At present, widely adopted methods for preventing bamboo biodegradation include:

- Cold soaking: A simple technique suitable for treating whole culms. Bamboo is immersed in a water-soluble preservative solution for several days, allowing the chemical to slowly diffuse into the tissue. To improve penetration, holes are drilled into each internode, enabling access to the internal culm cavity.
- Modified Boucherie method: A pressure-assisted method that forces preservatives axially through the bamboo culm from one end to the other, reducing treatment time from several days to a few hours. The system allows recirculation of the chemical solution, with filtration and replenishment maintaining concentration and enhancing resource efficiency.
- Pressure treatment: High-pressure techniques are used to force preservatives uniformly into the cell walls and vascular structures of bamboo, significantly enhancing durability.

In summary, chemical protection of bamboo focuses on improving penetration effectiveness, optimizing treatment time, and minimizing environmental impact. For further technical details on bamboo preservation methods, readers are referred to relevant studies[167,168].

2. 4. 4 **Penetrative Treatment**

Penetrative treatment refers to the diffusion of chemical agents into the cell walls or lumens of bamboo tissues, aiming to improve the material’s water resistance and fungal resistance.

Following such treatment, bamboo typically exhibits reduced permeability, increased density, and, in some cases, enhanced mechanical properties. Chen et al.[169] reported that the combination of 2,3-epoxypropyltrimethylammonium chloride (EPTAC) modification and rosin impregnation significantly improved the dimensional stability and anti-mold performance of bamboo. Their experiments showed that EPTAC can chemically react with hydroxyl groups in bamboo when applied in a NaOH/urea solvent system, thereby enhancing the material's reactivity for further modification. The rosin impregnation not only forms a hydrophobic layer on the bamboo surface, but also fills the cell wall structure[170,171], improving both physical and mechanical performance (see Figure 2-13). Moreover, due to the carboxyl groups present in rosin, ion exchange reactions can occur with quaternary ammonium hydroxides. The resulting compound, rosin choline, is water-insoluble and exhibits biological activity[172]. This suggests that the combined EPTAC–rosin treatment has strong potential to simultaneously enhance bamboo's dimensional stability and resistance to mold growth.

Penetrative modifiers may also consist of monomeric compounds that undergo polymerization and curing inside the bamboo structure to enhance its performance[173]. A representative example is furfurylation, in which furfuryl alcohol, derived from agricultural residues such as bagasse, corncobs, sunflower stalks, and birchwood chips, is used as the treatment agent. During processing, a solution composed of furfuryl alcohol, ethanol, citric acid (as catalyst), and water is introduced into the bamboo cell lumens. Upon exposure to high temperature, in situ polymerization occurs, resulting in furfuryl-modified bamboo. After surface furfurylation, bamboo exhibits significant improvements in dimensional stability, hydrophobicity, and durability, without compromising its mechanical properties. This indicates strong application potential for furfurylated bamboo in structural and environmental contexts[174].

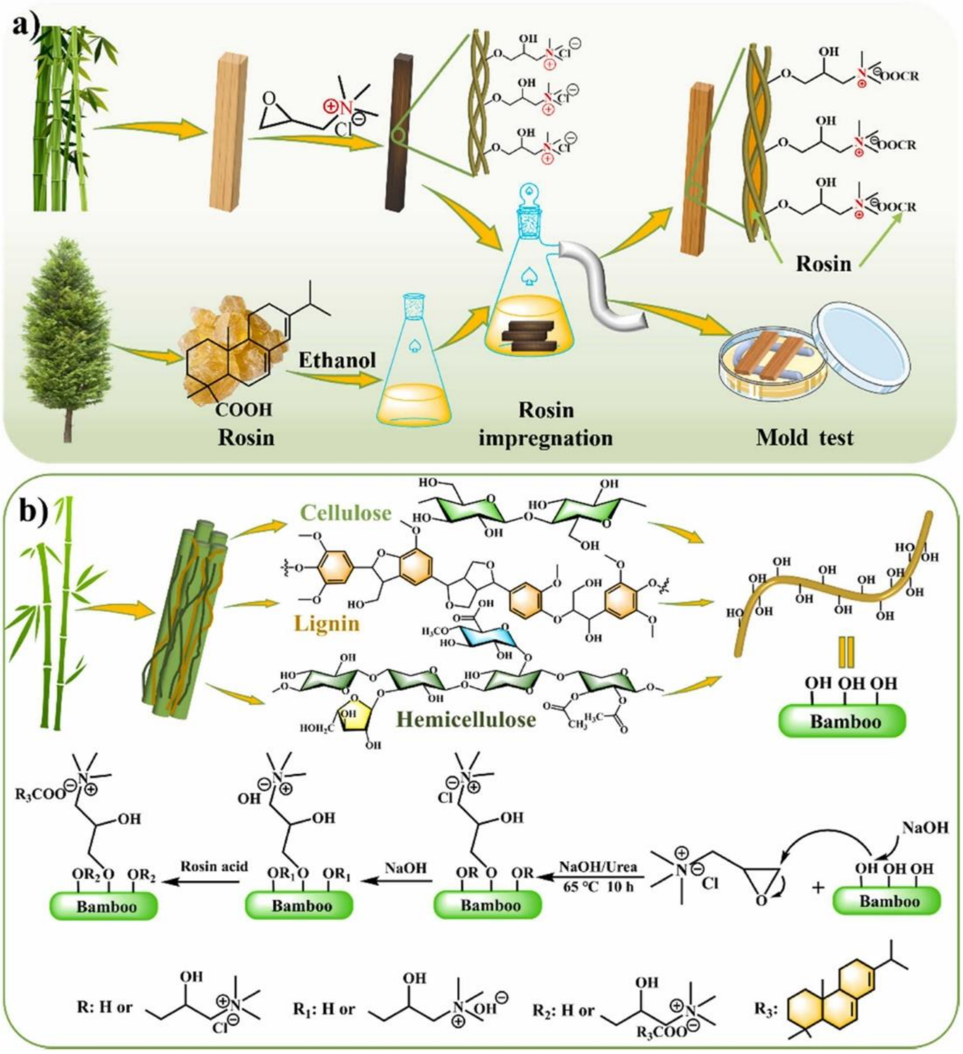

Figure 2-13 Penetrative treatment process (a) and reaction mechanism (b) for cationization-assisted rosin acid modification of bamboo

2. 4. 5 **Surface Coating Treatment**

Applying a coating or sacrificial layer to the surface of bamboo products can form a physical barrier that effectively resists weathering and degradation, while also enhancing the aesthetic appearance of the product[175, 176]. This method is particularly suitable for high value-added external bamboo applications, such as window frame joints and cladding panels. As a surface-level intervention rather than a bulk modification, coating treatment is typically performed as the final step in bamboo processing, ensuring improved weather resistance and durability during service life.

2. 4. 6 **Research Challenges**

Bamboo treatment not only extends the service life of structural bamboo, but also broadens its application scope, enabling it to meet performance requirements that untreated bamboo cannot fulfill. However, current bamboo treatment technologies still face several significant challenges. The following key issues require further investigation:

1. Development of High-Strength and Durable Bamboo

To enable the application of bamboo in high-rise buildings, it must be treated to achieve high strength and long-term durability. This remains a major challenge. Currently, the mechanical properties of bamboo-based products are largely influenced by the type and quality of adhesives used, and most existing treatment techniques offer limited improvements in this regard. Therefore, developing adhesive formulations that enhance both mechanical performance and fungal resistance presents a promising direction for future research.

2. Development of Green and Environmentally Friendly Bamboo Preservatives

Many effective bamboo preservatives currently in use are based on heavy metals or toxic compounds, such as chromated copper arsenate (CCA) and pentachlorophenol, which pose risks to both ecological systems and human health. As a result, developing eco-friendly preservatives derived from natural sources (e.g., plant resins) to replace conventional chemical agents is of great importance. Such alternatives not only help reduce the environmental impact at the end of the product’s life cycle but also contribute to lowering treatment costs. This represents a critical area for ongoing research and future implementation.

2.5 Structural Applications of Bamboo

In the 20th century, the structural use of bamboo was significantly limited by public perception and the absence of standardized codes and regulations. Nevertheless, as a traditional building material, bamboo has continued to be widely used in scaffolding, low-rise housing, and pedestrian bridges, particularly in tropical and subtropical regions such as China, India, and Malaysia, where considerable practical experience has been accumulated.

With the advent of engineered bamboo materials such as glued-laminated bamboo (glubam), laminated bamboo, and bamboo fiber-reinforced composites, long-standing challenges associated with natural bamboo—such as dimensional instability, lack of standardization, and poor durability—have been effectively addressed. These technological advancements have significantly improved the dimensional consistency, industrial processability, and environmental stability of bamboo materials, enabling them to be used in more complex structural applications such as vehicular bridges and lightweight multi-story buildings.

In recent years, the advancement of performance-based design philosophies and the gradual establishment of bamboo construction standards have facilitated the normalization and institutionalization of bamboo structures in large-scale and high-rise building projects. This section introduces the current state of advanced engineered bamboo structural systems, with a focus on their typical product forms and key technological pathways in high-performance construction applications.

2. 5. 1 **Prospects and Development Directions for Structural Bamboo Applications**

Bamboo is widely regarded as one of the most sustainable structural materials, and its outstanding mechanical properties make it highly promising for modern architectural applications. In the fiber (longitudinal) direction, bamboo exhibits compressive strengths ranging from 29.55 to 72.60 MPa, comparable to conventional reinforced concrete and, in some species, even approaching the strength levels of modern high-performance concrete. Moreover, bamboo’s tensile strength can reach 90–124 MPa, indicating its potential as a lightweight and highly efficient tensile material. These characteristics give bamboo strong prospects for axial load-bearing and tensile structural applications[177].

Bamboo’s tensile elastic modulus averages around 10,700 MPa, while its compressive elastic modulus ranges from 8,320 to 10,912 MPa, slightly higher than that of typical timber but lower than that of concrete[178]. Similar to wood, bamboo has a significantly lower density than both steel and concrete, which is particularly advantageous in applications involving long-span structures or high-rise buildings, where self-weight plays a major role in total structural load. In such scenarios, the strength-to-weight ratio and modulus-to-weight ratio become critical indicators of structural performance and material efficiency. In axial load-dominated systems, these ratios directly determine the minimum material quantity required to achieve a given structural height, span, or area. Figure 2-14 compares the performance of steel, bamboo, timber, and reinforced concrete in terms of their strength-to-weight and modulus-to-weight ratios. The results indicate that bamboo’s strength-to-weight ratio is significantly higher than that of steel, and its modulus-to-weight ratio surpasses that of reinforced concrete, highlighting its excellent mechanical efficiency in lightweight structural systems.

Therefore, in the context of lightweight construction, low-carbon design, and efficient material utilization, bamboo shows great potential as a sustainable alternative to conventional heavy construction materials. Due to its unique aesthetic form and natural material properties, raw (round) bamboo structures have recently gained widespread attention and become an important topic in both theoretical research and engineering practice. Notably, significant progress has been made in the design of joints for round bamboo members, which has broadened their application in low-rise buildings, pedestrian bridges, and other structural forms. However, raw bamboo structures still face numerous challenges in modern engineering applications. First, natural bamboo is relatively low in durability, being susceptible to mold, insect attack, UV radiation, and humidity fluctuations, all of which limit its service life. Second, the inherent variability and irregular geometry of raw bamboo members hinder standardized industrial production and modular design, restricting large-scale application in contemporary building systems. In addition, raw bamboo structures heavily rely on manual fabrication and on-site assembly, which results in low construction efficiency and difficulties in quality control. Furthermore, bamboo's limited capacity for thermal and moisture regulation may compromise indoor environmental comfort, making it difficult to meet the comprehensive performance requirements of modern architecture.

As a result of these limitations, raw bamboo structures are mainly used in regions where bamboo resources are abundant but economic development and technical capacity are limited, and are typically applied in low-cost, temporary, or landscape-oriented buildings. Given the still limited adoption of engineered bamboo products, the potential advantages of raw bamboo have yet to be fully realized, and its integration into the mainstream construction market remains constrained.

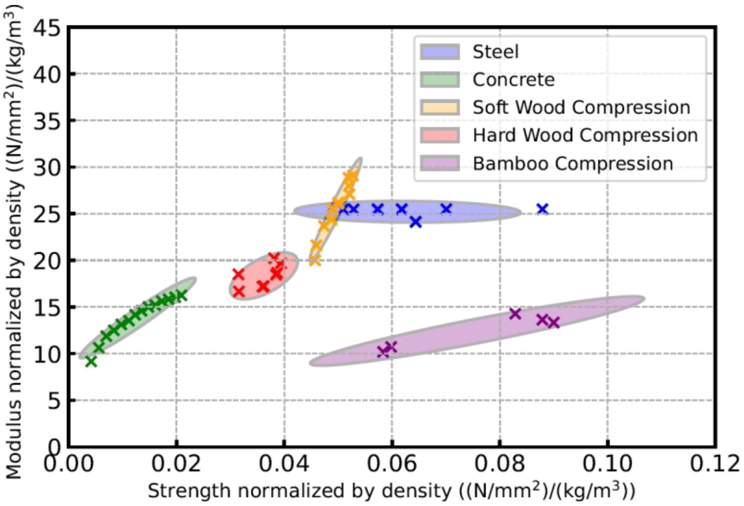

Figure 2-14 Strength-to-Weight ratio and modulus-to-weight ratio of various construction materials

The rapid development of glued-laminated bamboo (glubam) and laminated bamboo–timber composite beams has significantly overcome the traditional limitations of raw bamboo structures, such as geometric constraints and insufficient load-bearing capacity. This technological breakthrough offers new opportunities for the engineering and large-scale application of modern bamboo architecture. These engineered bamboo materials exhibit excellent dimensional stability, mechanical performance, connection compatibility, and construction adaptability, greatly enhancing both the safety and applicability of bamboo structural systems.

Driven by ongoing efforts from research institutions and universities, the engineering practice of modern bamboo structures continues to expand and is gradually penetrating fields such as multi-story buildings, bridges, and prefabricated systems. Currently, the light-frame structural system remains the most commonly used form in low- to mid-rise bamboo buildings. This system typically employs large-section engineered bamboo members (e.g., columns, beams, and trusses) as primary load-bearing components. When combined with efficient connection details and enclosure assemblies, it offers benefits such as flexible spatial configurations, ease of construction, and enhanced structural stability.

Xiao et al.[179,180] conducted systematic research on light-frame glubam structures, which consist of primary structural components and enclosure systems, with an overall design strategy that balances structural performance and assembly efficiency. In this system, the floor system is composed of secondary beams and a sub-floor layer, serving both as a load-bearing platform and a stable working surface that facilitates the accurate positioning and installation of exterior and interior wall panels. To enhance lateral load resistance, shear walls are connected to the floor diaphragm and the foundation or lower shear wall using anchoring components, ensuring effective load transfer and improving stability and ductile response under horizontal forces. The roof system typically adopts prefabricated glubam trusses, which are firmly connected to the top beams of the shear walls via metal connectors, ensuring overall roof stability and wind resistance under external loading.

With continued optimization in design methodology, connection detailing, and construction techniques, the load-bearing capacity, durability, and construction efficiency of glubam have been significantly improved. These advancements lay a solid foundation for its engineering application in low- and mid-rise buildings and provide strong support for the broader adoption of bamboo in the construction industry.

Bamboo, with its exceptional strength-to-weight ratio, is recognized as a highly efficient structural material, particularly suitable for applications where self-weight dominates the structural loading. In such cases, the material's own weight has a decisive influence on the overall structural performance. Bamboo's lightweight nature enables a reduction in structural loads and simplifies foundation design, thereby improving both cost-efficiency and construction speed.

Specifically, bamboo exhibits distinct advantages in the following structural systems:

- Roof systems: The high strength-to-weight ratio of bamboo helps reduce roof dead loads, lowering the forces transferred to the primary structure.
- Pedestrian and lightweight bridges: Bamboo enables lightweight decking with enhanced spanning capability and efficient assembly, particularly well-suited for small to medium-span bridges.
- Lateral-load resisting systems in tall buildings: Bamboo-based frames or shear walls can provide wind and seismic resistance while minimizing structural mass.

However, when external loads—such as wind or seismic forces—dominate and are not closely related to the structure's self-weight, materials like steel or reinforced concrete, with their higher absolute strength and stiffness, are often more efficient in resisting extreme loads. Consequently, bamboo alone may face limitations in load-bearing capacity and safety margins in such applications.

In modern building design, it is crucial to fully understand the mechanical characteristics and application boundaries of bamboo. By considering a structure's functional purpose and loading regime, bamboo can be appropriately selected or strategically combined with conventional materials such as steel and concrete to form hybrid systems. This complementary material approach, along with structural optimization, can ensure safety, durability, and economic performance while advancing goals of sustainable construction.

Under seismic loading, the seismic forces acting on a structure are directly proportional to its mass, in accordance with Newton's second law of motion. Hence, lighter structures experience lower inertial forces during earthquakes. Bamboo structures, due to their lightweight and inherently flexible nature, possess natural seismic advantages, including enhanced ductility and deformation capacity. These features enable bamboo structures to absorb and dissipate energy efficiently during seismic events, reducing damage and minimizing the risk of failure. With the rise of sustainable construction principles, research into bamboo applications in earthquake-prone regions has gained increasing attention. Among various factors, the seismic performance of joints is considered critical to the overall structural safety. In response, researchers have developed numerous novel joint configurations and seismic reinforcement strategies, including improvements in joint design, ductile detailing, and localized strengthening methods, all of which have significantly enhanced the ductility and energy dissipation capacity of bamboo structural systems. Through continuous optimization of connection technology, member layout, and system-level design, both the theoretical understanding and practical application of bamboo structures under seismic conditions have advanced. These studies have enriched the mechanical behavior database of bamboo structures under extreme loading and provide a robust scientific and engineering foundation for their broader use in seismic regions[181,182].

Shell structures, which primarily resist loads through in-plane compression and shear, are regarded as highly efficient systems for long-span roofs. Bamboo's hollow tubular geometry and excellent axial load-bearing capacity make it an ideal material for grid shell structures, combining structural performance with architectural aesthetics. Bamboo grid shells have been widely used in elegant long-span roofing systems. A notable example is the hyperbolic paraboloid roof in Cali, Colombia[183], designed by architect Greta Tresserra and her team. The construction methods for bamboo grid shells are highly flexible, involving either short culms or split bamboo strips. These components can be connected end-to-end using standardized joint systems, enabling the formation of continuous members of arbitrary length[184]. Such techniques expand the applicability of bamboo in complex geometrical shell structures, offering new possibilities in both structural and architectural design.

2. 5. 2 Application of Bamboo in High-Rise Buildings

Despite ongoing advancements in the performance research of engineered bamboo and continuous improvements in manufacturing techniques and connection technologies, the practical application of bamboo remains primarily concentrated in low-rise residential buildings, ornamental structures, and lightweight bridges with relatively modest load-bearing demands. It is important to note, however, that engineered bamboo materials—such as glued-laminated bamboo (glubam) and laminated bamboo—exhibit mechanical behavior and physical characteristics highly comparable to those of engineered wood, thus providing a solid material foundation for their potential application in more complex structural systems. Over the past decade, the field of high-rise timber buildings—typically defined as structures with seven or more stories—has experienced rapid development, with corresponding engineering practices and design methodologies becoming increasingly mature. This trend has inspired the exploration of high-performance bio-based materials in taller buildings and has prompted researchers and engineers to assess the feasibility and potential of using bamboo in mid- and high-rise construction. It is worth emphasizing that as building height increases, the design challenges faced by structural systems also grow substantially. In low-rise buildings, the effects of self-weight, wind, and seismic loads are relatively small. Under such conditions, shear walls often serve as the primary lateral load-resisting vertical elements, with floor slabs and roof diaphragms forming the horizontal transfer system, effectively distributing lateral loads (e.g., from wind and earthquakes) to the shear walls, and subsequently to the foundation to complete the structural load path. In contrast, high-rise buildings experience significantly increased structural self-weight and lateral load areas as height increases, placing greater demands on the lateral stiffness, ductility, and stability of the structural system. Similar to high-rise timber structures, the feasibility of high-rise bamboo construction is largely dependent on the design and optimization of a high-performance lateral load-resisting system. The configuration, material layout, and connection strategy of such a system not only determine the structure's response to wind and seismic forces, but also influence the overall safety, service life, and adoption potential of bamboo as a structural material in tall buildings. Therefore, the development of a performance-based lateral load-resisting system, specifically tailored to the unique characteristics of bamboo, is considered a critical pathway toward the engineering application of bamboo in high-rise construction.

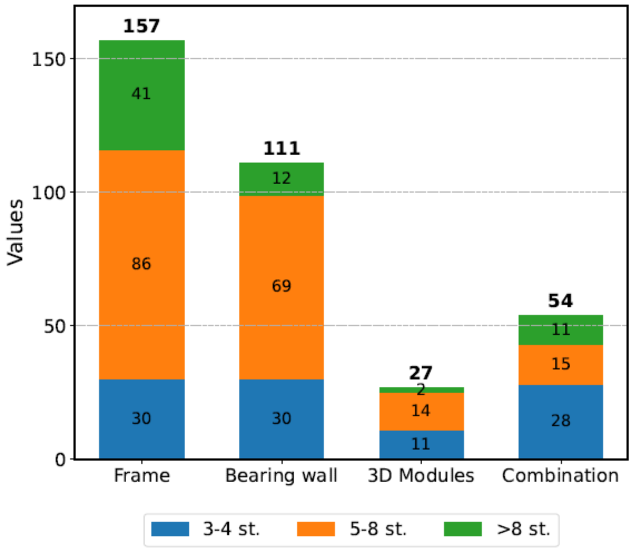

Figure 2-15 Distribution of structural system types in multi-story timber buildings

The development and promotion of high-rise bamboo structures must draw extensively from the construction experience of high-rise timber buildings. Svatoš-Ražnjević et al.[185] conducted a comprehensive study of 350 modern multi-story timber building projects constructed between 2000 and 2021, including 300 completed buildings, 12 under construction, and 38 in the design phase. As shown in Figure 2-15, frame structures accounted for the largest proportion at approximately 52%, followed by load-bearing wall systems at 31.7%. Hybrid structural systems made up 13%, and modular structures represented around 7.3%. Among high-rise timber buildings (defined as seven stories or more), 62.1% used frame systems, 18.2% used load-bearing walls, and 16.7% adopted hybrid systems. These data highlight the dominance of frame structures in tall timber buildings, reflecting their clear advantages in load-bearing capacity, lateral resistance, and constructability. Such insights offer valuable guidance for the system selection and engineering application of future high-rise bamboo buildings.

Like timber, bamboo is a brittle material with limited energy dissipation capacity. In engineered bamboo frame systems, steel plate–bolt connections are the most common joint type; however, these typically exhibit low initial stiffness and limited lateral strength. Therefore, in seismic design, engineered bamboo frames alone are not recommended as the sole lateral load-resisting system and should be supplemented by bracing systems to improve overall seismic performance. A representative example is the Tamedia Office Building in Zurich, Switzerland—a seven-story timber building with a footprint of 8,905 m², completed in 2013. The structure utilizes a beam-column frame system, with mortise-and-tenon joints for connections, showcasing the craftsmanship of timber construction. To enhance lateral resistance, single diagonal braces were added in selected spans. Wang et al.[186] studied the application of double-tube self-centering buckling-restrained braces (DT-SCBRBs) in glulam frame systems. They designed a series of six-, nine-, and twelve-story buildings with braced frames, and evaluated their seismic performance using nonlinear time-history analysis and incremental dynamic analysis. The results demonstrated the effectiveness of the system in improving the seismic resilience of bamboo–timber structures. Blomgren et al.[187] proposed a novel lateral force-resisting concept for mid- to high-rise timber buildings, called the Heavy Timber Buckling-Restrained Braced Frame (HT-BRBF). This system integrates buckling-restrained braces (BRBs) within a timber shell to enhance lateral stiffness and energy dissipation. Numerical simulations of a 12-story HT-BRBF timber building showed that this system possesses high load-bearing capacity, stiffness, and energy dissipation capability, making it a promising solution for all-timber multi-story commercial buildings. These studies indicate that by optimizing joint design and incorporating advanced lateral-force-resisting systems, the seismic performance of high-rise bamboo structures can be significantly improved, thereby providing a scientific foundation for their broader application in tall buildings.

Load-bearing wall systems primarily rely on walls to resist both vertical and lateral loads. Cross-laminated timber (CLT) is a large-format engineered wood product manufactured by orthogonally laminating timber layers, providing excellent strength in both principal directions. The rapid advancement of CLT technology has accelerated the adoption of load-bearing wall systems in timber construction. One prominent example is the Murray Grove Stadthaus in Hackney, London—a nine-story residential building recognized as the world's first all-CLT high-rise urban housing project. Its load-bearing walls, floors, stairs, and elevator cores were all constructed from CLT components. A new structural innovation is Cross-Laminated Bamboo and Timber (CLBT)[188], which integrates engineered bamboo and timber layers for enhanced performance. CLBT has been used in 3–4 story buildings and shows potential for taller structures. Due to its high in-plane shear stiffness, energy dissipation in CLBT systems is mainly achieved through anchored connections between the panels and foundations (or floors), and inter-panel connectors[189]. The development of CLBT systems opens new possibilities for load-bearing wall applications in bamboo–timber buildings, with broad prospects for improving seismic performance and sustainability.

Hybrid structural systems typically consist of frames combined with shear walls, where shear walls resist lateral loads and frames provide vertical load-bearing capacity and some degree of lateral deformation. In tall timber buildings, CLT shear walls are often centrally arranged as core walls, forming what is known as a "timber frame–core" system. This configuration provides lateral stiffness and ductility, while also integrating vertical circulation elements (e.g., elevators and stairwells) into the structural design. A notable example is the Wood Innovation and Design Centre at the University of Northern British Columbia (UNBC), completed in 2014. The six-story building stands at 29.5 meters (excluding rooftop equipment) and features glulam frames and a CLT core, demonstrating the feasibility of engineered timber in mid-rise commercial construction. Analogously, engineered bamboo products such as glubam and Cross-Laminated Bamboo (CLB) also exhibit promising potential for use in lateral-force-resisting elements. Bamboo-based shear walls offer good stiffness and strength, and by optimizing connection details, can be effectively integrated with frame systems. Research on the overall performance of engineered bamboo shear walls and their connections with frames is increasingly recognized as a key scientific issue in the design of high-rise bamboo structures, with strong implications for real-world applications. Studies[190] have shown that lightweight glubam shear walls connected by nails can offer higher strength than comparable timber shear walls, although their ductility is lower. Han et al.[191] proposed a self-centering CLB shear wall system, incorporating prestressed tendons for restoring force and friction dampers for energy dissipation. Experimental and numerical analyses confirmed its promising seismic performance, offering a viable solution for lateral resistance in tall bamboo buildings. To further balance ductility and repairability, some researchers have suggested replaceable energy-dissipating connectors at wall intersections or corners[192–194], allowing for improved post-earthquake reparability and extended service life.

Modular construction is a modern building approach that divides the structure into standardized module units, which are prefabricated in factories and assembled on-site. Among modular methods, volumetric construction—also known as three-dimensional modular construction—is the most efficient form. In this approach, 70–95%[195] of the structure is completed off-site and rapidly assembled on location. Prefabricated engineered bamboo panels, such as CLB, or wood panels, like CLT, are well-suited to modular systems[196]. For example, the Treet Tower utilizes glulam trusses for façade support and incorporates 3D prefabricated modules, grouped in sets of four stacked modules, supported by glulam frames or mechanical floors, with concrete slabs added to enhance global stability[197]. Modular construction improves on-site efficiency, reduces material waste, and enhances the industrialization of bamboo buildings. This approach offers a promising direction for scaling up the application of bamboo structures in modern construction.

2. 5. 3 Design of Ductile Connections

Ductility is a critical parameter in seismic design[198]. Since bamboo itself is not a ductile material and is prone to brittle failure under tension, bending, and shear forces, metal connectors become the primary source of ductility in bamboo structural systems and play a key role in enhancing the overall mechanical performance and ensuring structural safety. In engineered bamboo structures, the configuration of beam-to-column joints is similar to that found in glulam structures. Mechanical fastening methods such as bolting, doweling, and screwing—often combined with metal plates—are the most widely used connection techniques in light-frame bamboo structures due to their ease of installation, high construction efficiency, and relatively high strength and stiffness. However, due to bamboo's inherent brittleness and anisotropy, the risk of early splitting failure remains significant in connection zones.

Leng et al.[199] investigated three typical beam-column connection types: slotted embedded steel plate bolted connections (I-type), T-shaped extended end plate connections, and L-shaped end bracket connections. Their results showed that the main failure mode was brittle splitting along the grain in the bolted region. However, when Cross-Laminated Bamboo (CLB) was applied in the connection zone, splitting was effectively suppressed, and the failure mode shifted to delamination between laminated layers. Compared to the I-type connection, the T- and L-type connections showed significant improvements in performance: elastic stiffness increased by 215% and 169%, plastic stiffness by 153% and 53%, ultimate load capacity by 58% and 50%, and ductility by 15% and 13%, respectively.

In addition, Sarkisian et al.[200] proposed an advanced friction-damped connection system for large-scale timber buildings to replace traditional energy dissipation mechanisms based on material yielding. They developed three different types of Pin-Fuse systems tailored to various lateral-force-resisting configurations: the Pin-Fuse connection for frame joints, the Pin-Fuse frame for coupling beams and shear walls or frames, and the Link-Fuse connection for enhancing beam-to-beam or wall-to-wall coupling. All of these systems adopt a similar design approach, using pre-tensioned bolts to clamp steel plates with interleaved friction pads. When the structure is subjected to seismic loads beyond a defined threshold, the connector components undergo controlled sliding, effectively dissipating seismic energy. This strategy holds great potential for seismic design in long-span and tall bamboo structures.

In bamboo shear wall systems, typical connection methods include nailed or screwed joints—commonly used for wall-to-frame, wall-to-wall, and frame-to-frame connections[31, 158]—as well as metal plate connectors such as hold-downs and angle brackets, which are usually combined with dowel-type fasteners for wall-to-floor and wall-to-foundation anchorage. Wang et al.[201] conducted experimental studies on nailed joints and hold-down systems in lightweight glubam shear walls, and found that walls fastened with high-strength nails exhibited superior lateral performance compared to those using conventional ST nails. Lu et al.[202] investigated a Cross-Laminated Bamboo (CLB) rocking shear wall equipped with bending-friction coupled dampers (BFCDs) as hold-down connections. Experimental results indicated enhanced energy dissipation and ideal flag-shaped hysteresis curves under quasi-static loading, suggesting strong seismic resilience.

Li and Tsavdaridis[203] introduced a series of novel seismic connections for Cross-Laminated Timber (CLT) structures. Their research demonstrated that most of the newly proposed connections significantly improved ductility and resulted in more predictable deformation modes while preventing damage to the wood itself. A new prefabricated connection system was also proposed for use in modular CLT buildings, which featured interlocking joints that allow for rapid assembly. Within this system, a specially designed three-dimensional steel connector functions as the designated weak link, ensuring that under seismic excitation, it yields first while other structural elements remain elastic. To support the implementation of safe design principles in future codes and connection testing protocols, Ottenhau et al.[204] proposed a performance-based design guideline for ductile joints in timber and bamboo structures, aimed at improving the seismic reliability of these biobased systems.

2. 5. 4 Research Challenges

To advance the application of bamboo structures in larger-scale and higher-performance engineering contexts, several critical scientific issues and research demands have become increasingly prominent. Due to bamboo's excellent strength-to-weight and stiffness-to-weight ratios, it is particularly well-suited for the construction of ultra-lightweight structural systems. However, such lightweight systems tend to exhibit high sensitivity in dynamic responses and are more susceptible to external disturbances such as acoustic transmission, wind-induced vibrations, and seismic actions. Therefore, in-depth studies are urgently needed to optimize the dynamic performance of bamboo structures and enhance their service safety and comfort under complex environmental conditions.

In recent years, timber buildings have achieved significant breakthroughs in height, with many research advances and engineering practices in mid- to high-rise applications laying a solid foundation for the industrialization of timber construction. By contrast, although engineered bamboo is regarded as a promising alternative to timber due to its favorable mechanical properties and sustainability attributes, its current application remains largely confined to low-rise buildings and lightweight structures, and its full potential has yet to be realized. Given the similarities between engineered bamboo and engineered timber in terms of material properties—as well as bamboo's unique advantages such as high strength-to-weight ratio and renewability—it is necessary to draw upon the developmental pathways and practical experience of timber construction in taller buildings. This entails developing appropriate design and construction strategies tailored to bamboo's distinct characteristics. Simultaneously, comprehensive research is required at multiple levels, including material behavior, component performance, and overall structural systems, to establish robust design theories and analytical models that can ensure the safety, reliability, and applicability of bamboo structures in mid- to high-rise applications. Continued progress in these research areas will provide a solid theoretical and technical foundation for the broader adoption of bamboo structures in taller and larger-scale buildings, thereby supporting the global shift toward green, low-carbon, and sustainable architecture.

An efficient and highly ductile connection system is central to the design of lateral-force-resisting bamboo structures. Connections are the key transmission points for internal forces within a structure, and their performance directly affects the overall strength, stiffness, and energy dissipation capacity of the bamboo structural system. This, in turn, governs the structure's safety and resilience under wind and seismic loads. It is therefore imperative to systematically investigate the influence of different connection types on the performance of bamboo lateral-force-resisting systems, and to develop reliable design methodologies and evaluation frameworks to enhance structural seismic capacity and operational safety. Looking ahead, sustainability, reliability, and resilience will be the defining goals of bamboo structural development. To ensure the widespread and long-term integration of bamboo in modern construction systems, future research must focus on key areas such as material performance enhancement, optimization of connection design, rationalization of joint configurations, and the standardization and industrialization of bamboo components. By systematically improving bamboo's adaptability, durability, and engineering feasibility in complex built environments, this research will lay the groundwork for the expanded use of bamboo structures in mid- to high-rise buildings, seismic-resistant architecture, and green, sustainable construction.

3 Material Testing of Glubam

3.1 Overview

Due to variations in application conditions, species, and growth environments, bamboo exhibits significant dispersion and uncertainty in its mechanical properties. Even bamboo from the same species and geographical origin may present considerable differences in anatomical structure and physical behavior between springwood and summerwood, earlywood and latewood, and internodal and nodal regions. Therefore, even within the same batch of bamboo material, it is necessary to conduct systematic material property tests using randomly sampled specimens prior to mechanical modeling and numerical simulations. This approach ensures that the parameters used in subsequent theoretical analyses and finite element modeling are both accurate and representative.

In this study, all critical mechanical parameters used in theoretical calculations and finite element models were derived from experimental material tests. The corresponding experimental results provide a reliable data foundation and technical basis for the structural performance evaluation and parameter selection in later bamboo structure analyses.

This chapter first presents a comprehensive mechanical characterization of the glued-laminated bamboo (glubam) used in the study. For comparative purposes, a typical engineered wood composite—Laminated Veneer Lumber (LVL)—was selected as a benchmark. LVL is composed of wood veneers approximately 2–4 mm thick, bonded and laminated in the same grain direction, typically using poplar as the base material. In contrast, the glubam used in this study is fabricated from flattened moso bamboo strips (with thicknesses ranging from 5 to 40 mm), which are bonded and laminated under pressure to achieve superior strength and dimensional stability.

Figure 3-1 illustrates the coordinate reference system adopted in the testing and modeling of these two types of orthotropic materials (LVL and glubam), providing a foundation for later comparisons of mechanical performance and anisotropic behavior. As shown, the x-axis corresponds to the longitudinal (grain) direction, the y-axis to the transverse direction, and the z-axis to the thickness or lamination direction.

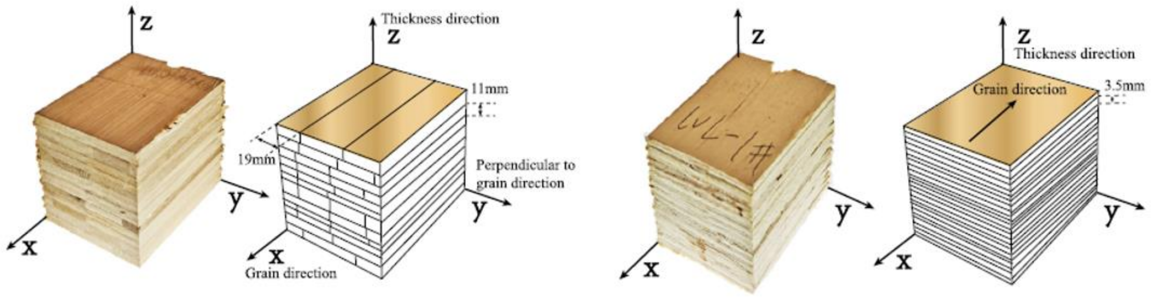

(a) glubam (b) LVL

Figure 3-1 Material Orientation and Coordinate System

3.2 Testing Methods

To support subsequent theoretical analysis and numerical modeling, and to accurately obtain the key mechanical properties of the materials used, a comprehensive series of mechanical tests was conducted on the glued-laminated bamboo (glubam) material. The test program primarily included: parallel to grain compressive strength ($f_{c,0}$), elastic modulus (E_0), parallel to grain shear strength ($f_{v,0}$), perpendicular to grain tensile strength ($f_{t,90}$), dowel embedment strength ($f_{h,0}$) and its corresponding stiffness ($k_{h,0}$), as well as density (ρ). In this notation, the subscript "0" denotes the longitudinal (grain) direction, which corresponds to the x-axis in the coordinate system shown in Figure 3-1, while "90" denotes the transverse direction, corresponding to the y-axis.

These mechanical properties form the essential experimental basis and parameter support for subsequent studies on connection performance, member-level force analysis, and full-structure mechanical modeling. Figure 3-2 summarizes the specimen geometries and associated test setups used to characterize the aforementioned material properties. To improve the representativeness and statistical reliability of the data, no fewer than 10 specimens were tested for each parameter, ensuring the results exhibit good repeatability and accuracy.

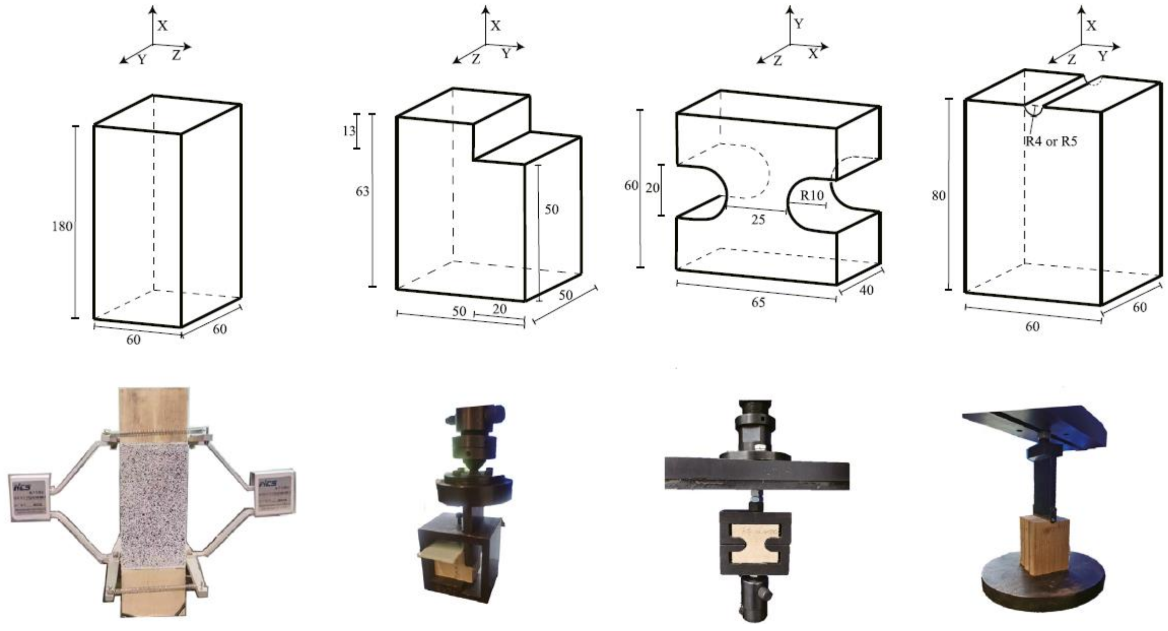

(a) $f_{c,0}$ and E_0 (b) $f_{v,0}$ (c) $f_{t,90}$ (d) $f_{h,0}$ and $k_{h,0}$

Figure 3-2 Specimen Geometry and Testing Apparatus for Material Property Evaluation

According to GB/T 50329-2002[205], the compressive strength $f_{c,0}$ and E_0 of the glued-laminated bamboo were determined. The arrangement of sensors and specimens is shown in Figure 3-2a, where one extensometer was fixed at each end of the specimen to record the deformation during the compression process. The compressive elastic modulus in the longitudinal direction (parallel to the grain), denoted as（E_0）, was calculated using the following equation[205]:

$$E_0 = \frac{L}{A} \cdot \frac{\Delta F}{\Delta u} \tag{3-1}$$

Where：L —— Gauge length of the extensometer； A —— Cross-sectional area of the specimen； ΔF —— Load increment within the proportional range； Δu —— Compressive deformation corresponding to the load increment ΔF .

$f_{v,0}$ was determined according to the methods specified in ASTM D143[206]. The geometric dimensions of the specimens are shown in Figure 3-2b.

Following ASTM D143[206]， $f_{t,90}$ was tested using specimens with the geometric dimensions shown in Figure 3-2c, and the property was calculated using the following formula:

$$f_{t,90} = \frac{P_{\max}}{b_0 t_0} \tag{3-2}$$

Where：$P_{\max}$ —— Peak load measured during the experiment； $b_0 = 25mm$ —— Minimum width of the specimen； t_0 —— Minimum thickness of the specimen； as illustrated in Figure 3-2c.

$f_{h,0}$ was tested according to the method specified in ASTM D5764-97a [207]. Four specimens were prepared for each material type. The geometric dimensions of the specimens are shown in Figure 3-2d. In the test, smooth tungsten steel dowels with diameters of 8 mm and 10 mm were used to compress the slotted specimens.

The embedment stiffness $k_{h,0}$, obtained from the dowel-embedment test, is calculated within the 10% to 40% range of the peak load. It is defined as the ratio of bearing stress to the corresponding displacement within this interval.

The density was determined according to the procedure specified in GB/T 50329-2002[205]. Specimens were cut to dimensions as prescribed by the standard. The oven-dry weight was obtained by drying the specimens in a ventilated oven until a constant weight was achieved (typically between 48 to 72 hours).

Additionally, the mechanical properties of the bolts used in the node connectors were tested, specifically the bending yield moment（M_y）and nominal yield strength（f_{yb}）. All bolts used in the connection joints in this study were Grade 8.8 high-strength bolts. The tests were conducted in accordance with ASTM F1575-2003[208].

The nominal yield strength f_{yb} was calculated using the following formula:

$$f_{yb} = \frac{3 \cdot P \cdot s_{bp}}{2 \cdot d^2} \tag{3-3}$$

Where： P —— Bending yield moment corresponding to the load at 5% offset (N·mm)； s_{bp} —— Span between the supports of the test fixture (mm)； d —— Diameter of the bolt (mm).

In the experiment, a three-point bending test was performed on six bolts — three with a diameter of 8 mm and three with 10 mm, each with a length of 180 mm — to determine the bending yield moment M_y and subsequently compute the nominal yield strength.

$$M_y = \frac{1}{6} d^3 f_{yb} \quad （3\text{-}4）$$

3.3 Test Results

Table 3-1 summarizes the average values and coefficients of variation (CV) for various mechanical properties of LVL and Glubam. The results indicate that LVL exhibits a relatively higher elastic modulus E_0, whereas Glubam demonstrates superior compressive strength $f_{c,0}$, highlighting a distinct difference in stiffness and strength emphasis between the two materials. Similar value ranges have been reported in previous studies on LVL[205,209-211] and Glubam[212-214], corroborating the validity and reference value of the current test results. Glubam also shows slightly higher shear strength parallel to grain $f_{v,0}$ and tensile strength perpendicular to grain $f_{t,90}$ compared to LVL. The embedment strength $f_{h,0}$ and embedment stiffness $k_{h,0}$ in the parallel-to-grain direction were determined from the stress–displacement curves obtained in the dowel bearing strength test (as illustrated in Figure 3-3). These curves clearly show that Glubam possesses higher dowel bearing strength and stiffness (see Figure 3-4), consistent with similar findings in the literature[199,215]. It is worth noting that the parallel-to-grain dowel embedment stiffness $k_{h,0}$ is typically expressed as a ratio of stress to displacement. In analytical models based on the Winkler foundation approach[216], this value is often multiplied by the dowel diameter to convert it into a stiffness per unit length, making it suitable for use in continuous media models. Finally, the results show that the density (ρ) of LVL and Glubam is relatively similar, indicating a certain degree of comparability in their physical characteristics.

Table 3-1 Test Results of Mechanical Properties for Glubam and LVL Materials (Values in Parentheses Indicate Coefficients of Variation)

Material	E_0 [GPa]	$f_{c,0}$ [MPa]	$f_{v,0}$ [MPa]	$f_{t,90}$ [MPa]	$f_{h,0}$ [MPa]	$f_{h,0}$ [MPa]	$k_{h,0}$ [MPa/mm]	$k_{h,0}$ [MPa/mm]	ρ [kg/m$^{3]}$
LVL	11（13%）	38（6%）	6.9（7%）	1.8（5%）	40（3%）	37（8%）	42（4%）	45（10%）	614（7%）
glubam	8.6（8%）	62（13%）	8（11%）	2.6（14%）	86（4%）	81（7%）	79（4%）	61（6%）	749（5%）

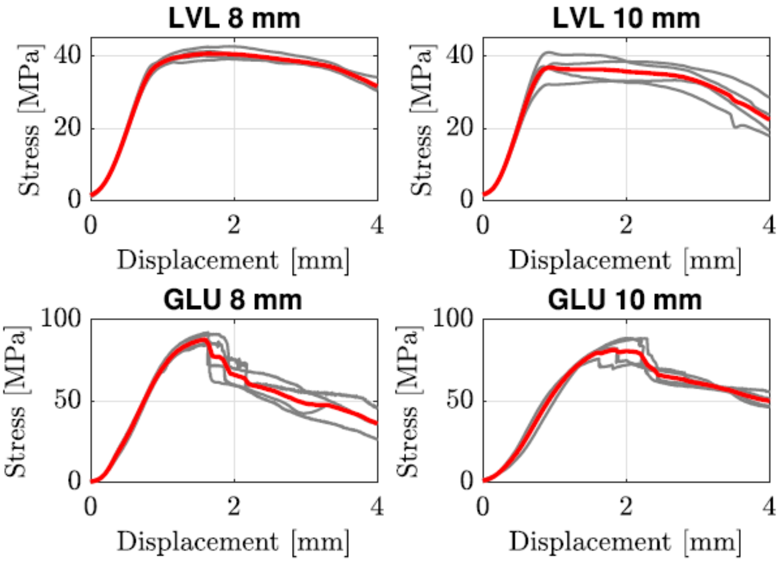

Figure 3-3 The stress–displacement relationship curve in the embedment test.

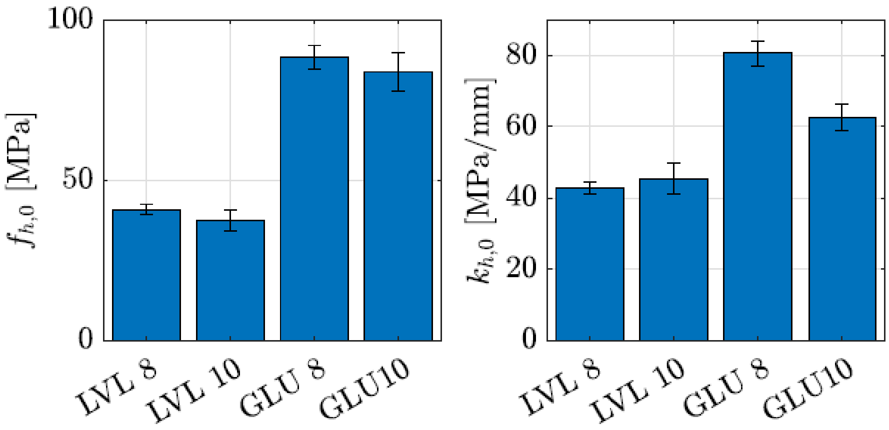

Figure 3-4 Embedment Strength and Stiffness

Table 3-2 presents the average values and corresponding coefficients of variation (CV) for the bending yield moment M_y and nominal yield strength f_{yb} obtained from mechanical tests on 8.8-grade bolts. As expected, the bending yield moment increases significantly with the bolt diameter, which is primarily attributed to the enhancement of second-order effects resulting from the quadratic growth of the moment of inertia (since $M_y \propto d^4$).

In addition, the results also reveal a slight upward trend in nominal yield strength with increasing diameter. This trend can be attributed to the idealized assumption adopted in the calculation model (Equation 3-3), which presumes a fully plastic stress distribution across the bolt cross-section at yield. This assumption leads to variations in stress response under different bolt diameters.

Table 3-2 Mechanical Properties of Grade 8.8 Bolt

d[mm]	$M_y\,[N \cdot m]$	$f_{yb}\,[MPa]$
8	62 (3%)	721 (3%)
10	137 (5%)	824 (5%)

This chapter presents a systematic investigation of the material properties of glubam, one of the primary engineered bamboo materials used in this study, through comprehensive mechanical testing. Laminated Veneer Lumber (LVL), a commonly used engineered wood product, was selected as a benchmark for comparative analysis. The objective is to provide a robust material foundation and experimental data support for subsequent research on joint performance, component modeling, and truss system analysis, while also evaluating the applicability and advantages of glubam in modern structural engineering.

The comparative analysis reveals that glubam exhibits superior performance over LVL in several key mechanical properties. For instance, glubam demonstrates significantly higher average compressive strength in the longitudinal direction, indicating enhanced load-bearing capacity. In terms of embedment strength, glubam shows greater resistance to localized compressive stresses in joints, suggesting greater potential for applications in connection design and detailing. Additionally, the elastic modulus values of both materials are comparable, indicating that glubam has a similar deformation control capacity and offers adequate stiffness for use in flexural members.

It is worth noting that although the densities of glubam and LVL are similar, their internal structures and fiber orientations differ, leading to variations in shear strength and tensile strength perpendicular to the grain. LVL exhibits more consistent performance in the transverse direction, whereas glubam shows greater variability in transverse tensile strength, which may be attributed to factors such as interlayer bonding quality, fiber compaction, and manufacturing process control.

To further support the connection analysis, this study also included supplementary testing of 8.8-grade steel bolts to determine their bending yield moment and nominal yield strength under three-point bending. The results indicate that the yield moment increases significantly with bolt diameter, which aligns with the theoretical prediction that the moment of inertia scales with the fourth power of diameter. Similarly, nominal yield strength shows a slight increasing trend with diameter, likely due to the idealized assumption of fully plastic cross-sections in the calculation model. These findings provide essential stiffness and strength parameters for subsequent modeling of connection hysteresis behavior.

In summary, this chapter demonstrates, through systematic testing and comparative evaluation, the feasibility of using glubam as a high-performance engineered bamboo material in structural applications. Compared to LVL, glubam exhibits superior strength and comparable stiffness, highlighting its promising potential in structural engineering. The results not only supply key material parameters for the following chapters on joint behavior, connection modeling, and truss system analysis but also offer theoretical and empirical support for the broader adoption of engineered bamboo in modern green construction.

4 Experimental Study on Glubam Joint

4.1 Overview

In lightweight truss and roof systems, metal connectors are widely used, and their mechanical performance largely determines the overall structural behavior and load-bearing capacity of the members. As a result, the design of such structural components often boils down to the design of the joints themselves. This characteristic marks a significant difference between bamboo-wood structures and traditional reinforced concrete or steel structures, and it highlights the critical role of joint design in bamboo and timber structural systems.

Post-earthquake investigations of light-frame timber housing in North America[217] have shown that insufficient seismic performance is primarily attributed to discontinuous load paths. Common reasons include: (1) Inadequate connections between structural components, such as poor anchorage to the foundation or insufficient wall-to-wall and wall-to-roof connections; (2) Lack of bracing, for instance due to excessive wall openings; (3) Separation of components, such as detached porch roofs or other cantilevered structures; (4) Irregular or uneven stiffness distribution across the structure.

Under extreme wind loads such as hurricanes, failures in light roof trusses often originate from weak roof system connections, especially poor anchorage between the roof and wall systems, detachment of roofing panels, or failure of the roof covering materials. In some cases, foundation failure or the absence of proper anchorage between the structure and the foundation can also lead to severe structural damage.

Similar to seismic loading scenarios, the continuity of the load transfer path and integrity of the structural system are key to improving wind resistance. Case studies and related research on past hurricane events consistently indicate that the reliability of joint connections is a decisive factor in ensuring continuous and efficient load transfer among truss and roof components. Weak joints are often the “weakest link” leading to system-level failure.

Therefore, to improve the wind resistance and ductility of the structural system, it is essential to conduct systematic investigations into the performance of joint connections.

4.2 Glubam Joint Connector Design and Fabrication

Steel side-plate and steel insert-plate connectors are among the most commonly used joint types in lightweight timber trusses and roof structures, and they are well-established in wood construction engineering. However, despite their extensive application in timber structures, research into their performance in bamboo structures remains relatively limited—especially in terms of systematic experimental studies and parametric analyses.

To address this research gap, this study designed two types of glubam structural connectors based on the relevant principles from the timber design code GB 50005[218]: steel insert-plate connectors and steel side-plate connectors, as illustrated in Figures 4-1 and 4-2.

To systematically investigate how joint configuration parameters affect mechanical performance, four different configurations were developed for each connection type. These variations include changes in connection dimensions, number of bolts, and bolt arrangement patterns, aiming to provide a comprehensive dataset for comparative analysis in the following sections.

4. 2. 1 **Steel Insert-Plate Glubam Connectors**

For the design of the steel insert-plate connectors, this study considers two key parameter variables: the number of bolts and bolt diameter. Specifically, two connection configurations were designed: single-bolt and double-bolt connections. Within each configuration, two bolt diameters (8 mm and 10 mm) were further considered, resulting in a total of four connector configurations, as summarized in Table 4-1.

In terms of specimen construction, the steel insert plates used in all connector types had a uniform thickness of 8 mm, and the connected glubam timber elements had cross-sectional dimensions of 60 mm × 60 mm. All steel plates and associated steel components were made of Q235 steel, and the bolts used were standard Grade 8.8 high-strength bolts, ensuring sufficient connection strength and experimental repeatability.

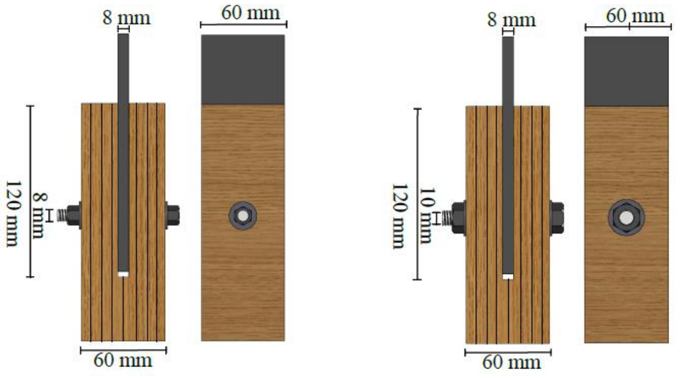

(a) G-S-8 (b) G-S-10

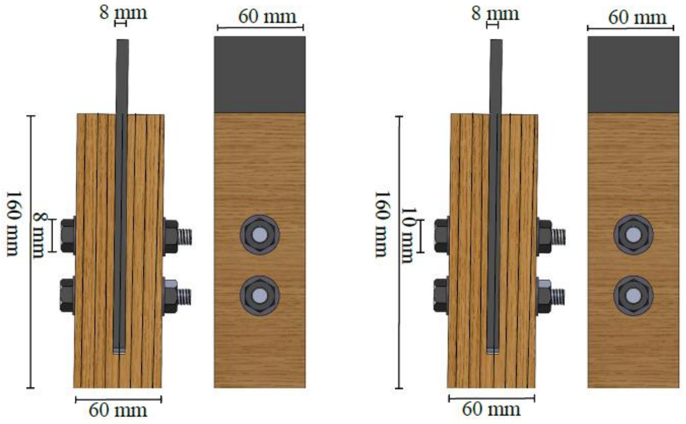

(c) G-D-8 (d) G-D-10

Figure 4-1 Steel Insert-Plate Glubam Connectors

Table 4-1 Specimen Configurations of Steel Insert-Plate Glubam Connectors

Specimen	Bolt Diameter	Bolt Number
G-S-8	8	1
G-S-10	10	2
G-D-8	8	1
G-D-10	10	2

4. 2. 2 **Steel Side-Clamped-plate Glubam Connectors**

For the steel side-clamped-plate connectors, this study focused on varying the bolt diameter as the primary design parameter. Four bolt diameter configurations were established—10 mm, 12 mm, 14 mm, and 16 mm—resulting in four types of test specimens. Detailed configurations are presented in Table 4-2.

In terms of specimen geometry, the thickness of the steel side plates was uniformly set to 10 mm. The glubam timber elements used in the connections had cross-sectional dimensions of 140 mm in width and 52 mm in thickness.

All steel components used in the connection assembly were made from Q235 mild structural steel, and standard 8.8-grade high-strength bolts were used to ensure adequate connection strength and stiffness. This also helped guarantee good comparability and representativeness among all test specimens under the experimental conditions.

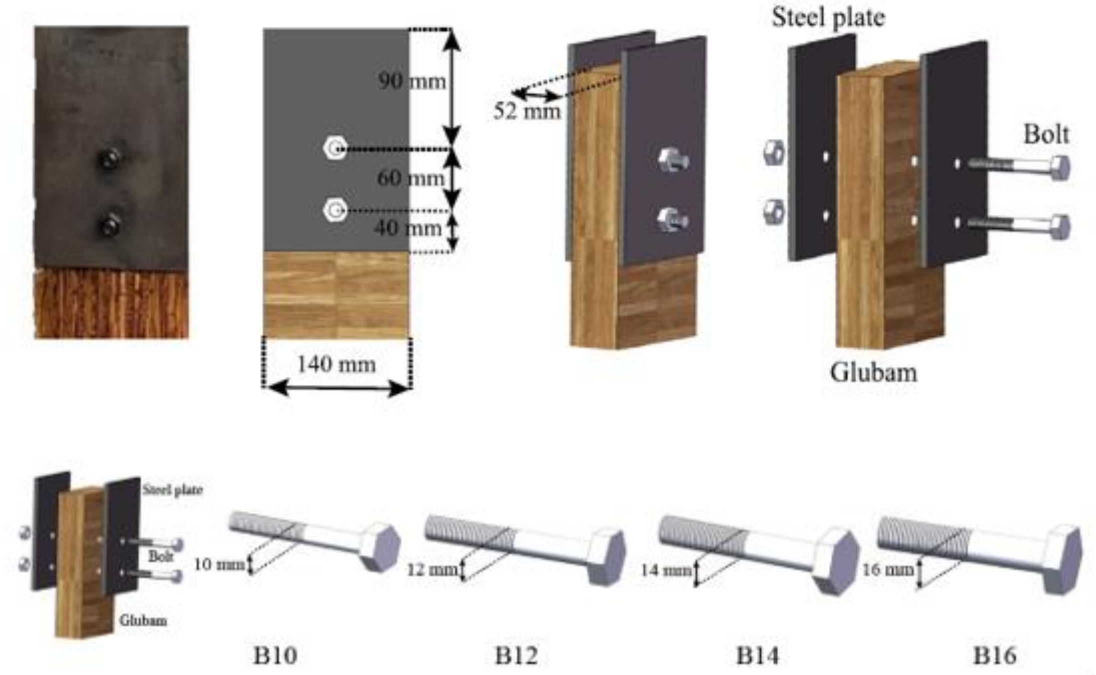

Figure 4-2 Steel Side-Clamped-plate Glubam Connectors

Table 4-2 Specimen Configuration Details of Steel Side-Clamped-plate Glubam Connectors

Specimen	Bolt Diameter	Bolt Number
B-10	10	2
B-12	12	2
B-14	14	2
B-16	16	2

4.3 Experimental Study on Steel Insert-Plate Glubam Connectors

This section presents a comprehensive experimental study on the axial mechanical performance of Steel insert-plate Glubam Connectors. The primary testing methods include monotonic tensile tests and low-cycle reversed loading tests to evaluate their mechanical response under both static and simulated seismic loads. To better understand the failure mechanisms and failure modes during loading, this study employs Digital Image Correlation (DIC) technology to observe and analyze the localized strain field at critical regions of the specimens with high precision. This enables the quantitative identification and mechanistic interpretation of deformation behaviors in vulnerable areas.

4. 3. 1 **Specimen Design and Fabrication**

To conduct axial performance tests of Steel insert-plate Glubam Connectors, the specimens were designed with full consideration of compatibility with testing equipment and the reliability of force transmission during loading. Each specimen was specifically designed to connect to the upper and lower grips of the testing machine, ensuring accurate axial load transfer without introducing additional bending moments or eccentricities. To prevent local crushing failure or significant deformation at the connection region due to stress concentration, steel transition plates were used at both ends of the specimens to enhance the rigidity of load transfer between the specimen and the grips.

Specifically, embedded steel plates with different functions were designed for both ends of the specimen (see Fig. 4-3): one end serves as the test end, where the connector is expected to deform and fail; the other end is a fixed anchorage, designed to have sufficient strength to prevent premature failure, and thus adopts a four-bolt symmetrical layout to ensure stability. Considering the constraints of limited loading space and the need to maintain sufficient stiffness of the specimen, the total length of the specimen was set to 550 mm. This configuration minimizes the interaction between the test end and fixed end, while meeting the stroke and space requirements of the testing setup.

The Glubam components used in the specimens had a cross-section of 60 mm × 60 mm, fabricated based on the connector design scheme shown in Fig. 4-1. All timber elements were sourced from the same batch to ensure material consistency and experimental repeatability. At both ends of each timber member, a rectangular slot with a width of 8 mm was cut to embed the steel insert plate. The steel insert plates were fabricated from Q235 steel using laser cutting, with precise holes drilled at designated locations. The plates were rectangular, with a width matching the timber cross-section (60 mm), and a length equal to the embedded slot length plus an additional 100 mm to accommodate the testing machine grips (see Fig. 4-3).

To facilitate the measurement of displacement during loading, a rectangular 90° protrusion was added to the steel plate at the test end to mount displacement sensors (see Fig. 4-4(c)). For ease of assembly and to accommodate construction tolerances, the pre-drilled holes in the Glubam components were made 0.5 mm larger than the bolt diameter. Standard 8.8-grade high-strength bolts were used for all connections, and torque was precisely controlled using a calibrated torque wrench to ensure consistency and repeatability among specimens. Pre-test trials indicated that the recommended tightening torques were 0.7 N·m and 1.0 N·m for 8 mm and 10 mm bolts, respectively. Proper torque control not only enhances the interface friction between steel and Glubam but also prevents bolt or washer embedment into the Glubam surface, thereby avoiding unintended failure modes caused by local crushing.

In summary, the specimen design in this study balances mechanical rationality, geometric compatibility, and connection reliability, while fully considering the practical engineering applicability and experimental operability of the connection configuration. This provides a solid physical foundation and structural assurance for obtaining reliable mechanical response data in subsequent loading tests.

To obtain full-field strain and deformation information in the connection zone during testing, the opposite side of the test end (i.e., the side with bolt heads and nuts) was pretreated for DIC measurement. Specifically, at a region 230 mm from the specimen end, a white matte base coat was uniformly applied, followed by randomly distributed black speckles to form a high-contrast texture pattern suitable for DIC image recognition and displacement tracking. The DIC measurement area is illustrated in Fig. 4-4(d).

All Glubam timber elements used in this study were precisely processed using a CNC drilling machine (Uli-CNC, Model K1) at the CNC fabrication center of the Haining International Campus, Zhejiang University. This ensured consistency in hole positions and dimensional accuracy, significantly improving the assembly quality and repeatability of the specimens. Meanwhile, all steel components were fabricated via laser cutting to ensure that the outlines, hole positions, and geometric dimensions of critical connection parts met the intended design specifications, thus ensuring reliable performance analysis in subsequent experimental loading.

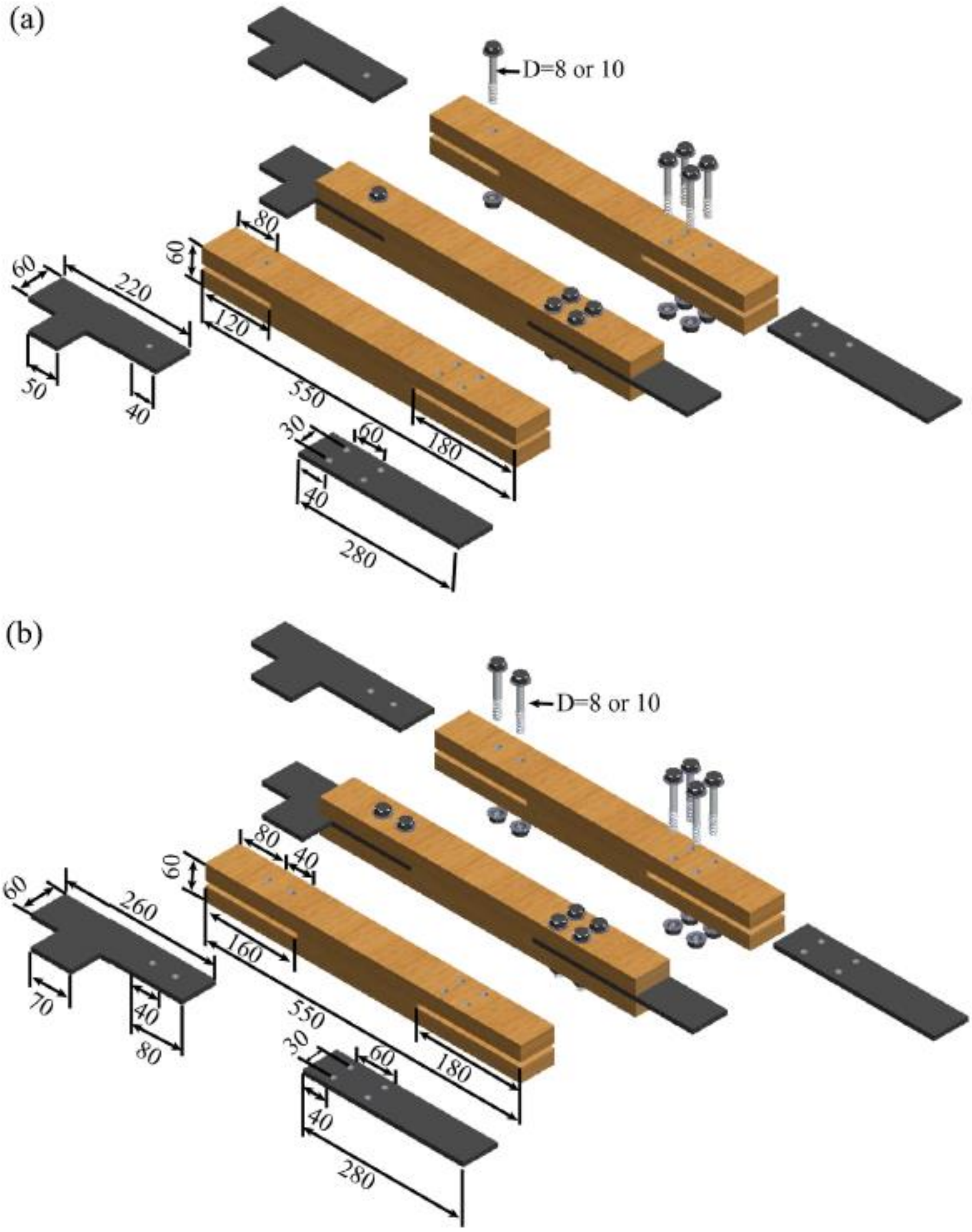

Figure 4-3 Mechanical Test Specimens for Steel Insert-Plate Glubam Connectors:(a) Single bolt specimen;(b)Double bolt specimen

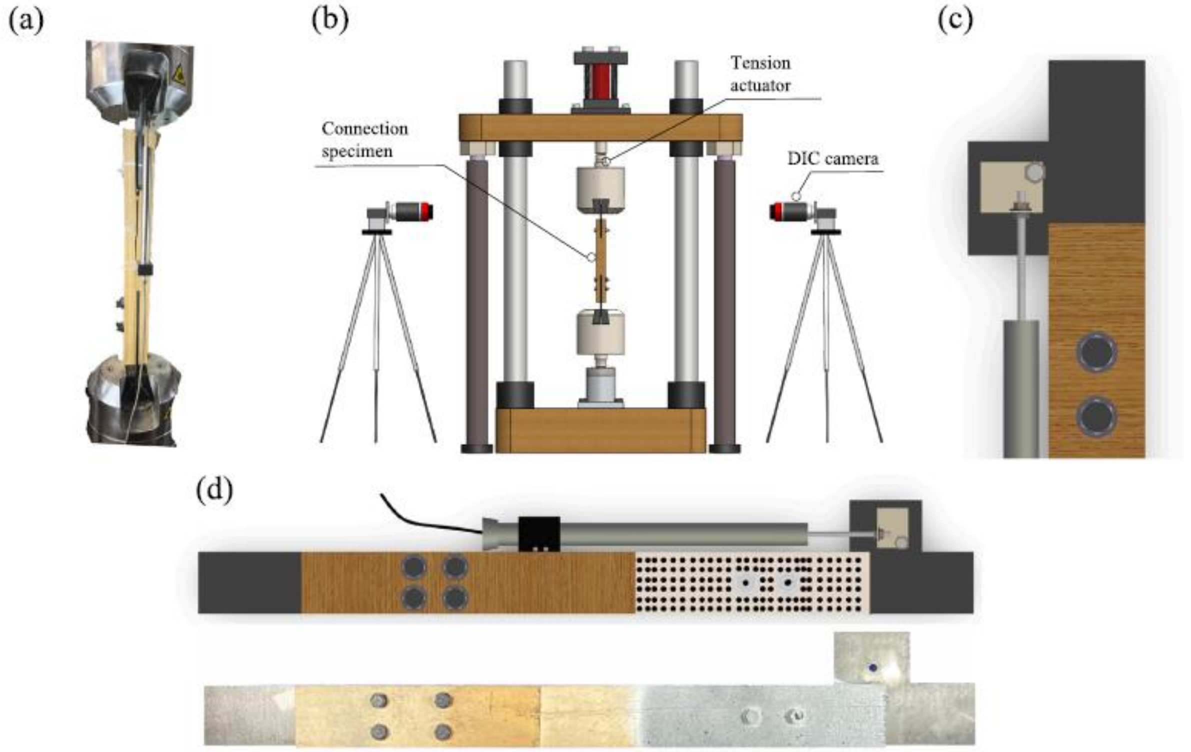

Figure 4-4 Test setup and instrumentation: (a) photograph of the test setup; (b) schematic diagram of the loading configuration; (c) detail of displacement sensor installation; (d) speckle pattern region used for DIC analysis.

4. 3. 2 Test Setup and Methodology

Figure 4-4 illustrates the experimental setup and measurement system arrangement for axial loading tests on the Steel insert-plate Glubam Connectors. A 100 kN servo-hydraulic actuator (Model: 186E, WANCE Ltd.) was used to apply axial loads under controlled conditions, capable of both monotonic tensile loading and low-cycle reverse loading modes. Load data were recorded in real-time via the actuator's internal sensor, ensuring loading accuracy and data synchronization. Axial displacement in the connector region was measured using a high-precision linear variable differential transformer (LVDT). The sensor’s upper end was fixed to the upper loading steel plate and its lower end was anchored at the mid-height of the glubam specimen, minimizing interference from fixture slippage or local deformation and accurately capturing the deformation response of the connector.

Prior to testing, to meet the image texture recognition requirements of the Digital Image Correlation (DIC) system, the specimen surface was first uniformly coated with matte white primer, followed by application of randomly distributed black speckles. This created a high-contrast texture region suitable for strain field measurement (see Figure 4-4(d)). The DIC measurement system was arranged in a stereo configuration using two synchronized cameras (each equipped with a 25 mm lens) operating at 2 frames per second. Cameras were symmetrically positioned on both sides of the specimen with lenses perpendicular to the speckle area to minimize image distortion and improve the accuracy of displacement field reconstruction. The monitored area of interest measured 60 mm × 230 mm, covering the primary load-bearing region of the connection. To ensure consistent illumination and image quality, two constant-intensity LED light sources provided symmetrical lighting, minimizing interference from ambient light and improving strain measurement stability and data reliability. DIC data analysis was conducted using GOM Correlate software. This software tracks square sub-regions (facets) in the initial image and performs grayscale matching across subsequent image sequences to reconstruct displacement and strain fields under different loading steps. Facet layout was based on the high-contrast random speckle pattern, ensuring adequate grayscale variation for stable correlation. To balance resolution and computational efficiency, a facet size of 19 pixels and a point distance of 16 pixels were adopted—parameters shown to be effective for large deformation analysis in bamboo components. All data processing followed the standardized procedures within GOM Correlate, including image preprocessing, correlation calculation, displacement vector reconstruction, and strain derivation, ensuring repeatability and credibility of results.

Both the monotonic and cyclic tests in this study were designed and conducted in accordance with European Standard EN 12512[219]. The monotonic test included two stages: preloading and formal loading. During preloading, the specimen was loaded up to 10% of the estimated ultimate load (based on preliminary trials), held for 120 seconds, then unloaded and held at zero load for 30 seconds to eliminate non-structural deformation from initial contact adjustment[220]. The formal loading phase followed using displacement control at a rate of 1.5 mm/min until the displacement reached 40 mm, at which point the test was terminated. The purpose of preloading was to reduce initial interface friction and contact-related deformations between glubam and the steel insert-plate, thereby improving test stability and repeatability.

Two low-cycle reverse loading protocols were adopted in accordance with EN 12512[219] to evaluate the hysteretic behavior and energy dissipation capacity of the connectors under varying loading paths. The first was a non-reversed modified version of the EN 12512[219] standard, in which displacement cycles were applied only between zero and the positive (tensile) direction, without reverse loading[221]. This mode simulates tensile-dominated cyclic responses and is illustrated in Figure 4-5. The yield displacement Δy was determined based on the specific connector configuration, using curve fitting at the yield inflection point in monotonic load-displacement results as defined in EN 26891:1991. Displacement control was used with a loading rate of 0.2 mm/s, and the test was terminated at a maximum slip of 30 mm. The second protocol involved bidirectional cyclic loading (Figure 4-6), incorporating both tensile and compressive displacements to evaluate the full hysteretic performance of the connector. Displacement control was again used, with a loading rate of 0.6 mm/min. The amplitude of each loading cycle increased incrementally as a multiple of the yield displacement Δy. Termination criteria included a maximum displacement of 30 mm or the occurrence of visible failure or fracture in the connector.

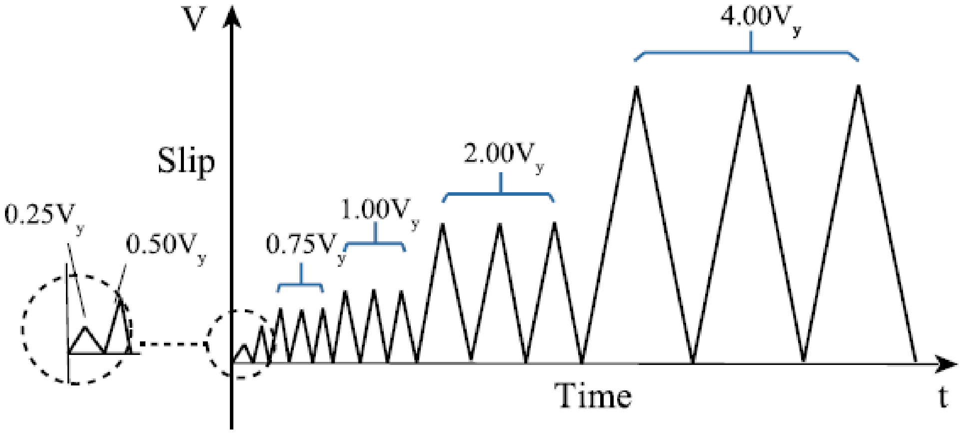

Figure 4-5 Tensile-Side Cyclic Loading Protocol

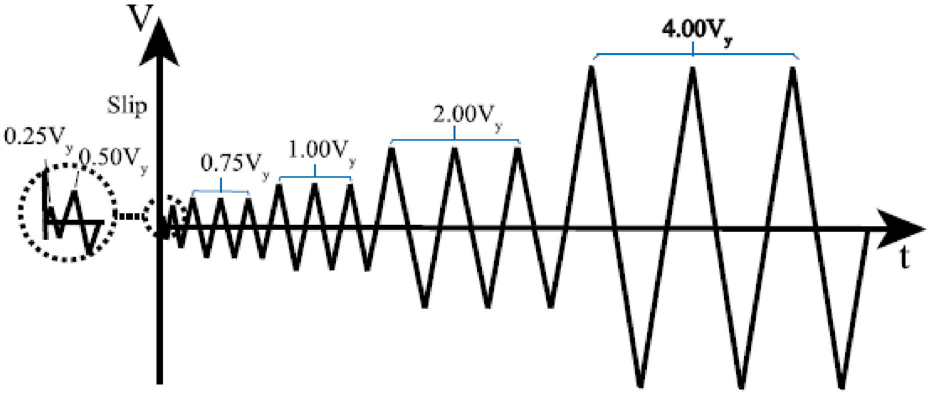

Figure 4-6 Tension–Compression Cyclic Loading Protocol

4. 3. 3 **Testing Results**

4. 3. 3. 1 **Monotonic Test**

The load–displacement curves obtained from the monotonic tensile tests of the Steel insert-plate Glubam Connectors are shown in Figure 4-7. The figure includes the raw data curves from three repeated tests (gray lines), as well as the averaged displacement response curve derived from the three datasets (red solid line). As illustrated, the results exhibit good consistency, validating the repeatability of the testing method and the stability of the measured data. The mechanical response of the connector observed in Figure 4-7 can be generally divided into four typical stages: initial linear-elastic stage, nonlinear growth stage, load-bearing plateau stage, and final failure stage. At the failure stage, the specimens presented two distinct failure modes—typical shear failure and splitting failure—depending on the connector geometry and material characteristics. Similar load–displacement evolution features were reported in the study by Liu et al.[222], which also confirmed that light-frame timber connections experience a multi-stage evolution process under monotonic loading, thus further supporting the reasonableness and representativeness of the observations in this study.

The first stage is the initial slip phase, typically occurring at displacements less than 1 mm during the early loading. In this phase, the mechanical response is primarily governed by interface friction between the steel insert plate and the internal slot surface of the glubam, as well as engagement adjustments resulting from the clearance and geometric tolerances between the bolt and the bolt hole[223,224]. Since this stage mainly reflects contact adjustment rather than material deformation, its contribution to the overall structural behavior is minimal and can be reasonably simplified or ignored in analysis.

The second stage is the elastic working phase, in which the load–displacement response exhibits a near-linear trend, representing the overall stiffness of the connector within the elastic range. The equivalent stiffness in this phase is closely related to the structural parameters of the specimen and is primarily determined by the bending stiffness of the bolt and the embedment stiffness of the surrounding material[225,226] (see Tables 3-1 and 3-2 for material parameters). Studies have shown that increasing bolt diameter significantly enhances the bolt's bending stiffness, thus improving the overall stiffness of the connection system. Specifically, since the bolt's bending stiffness is proportional to the fourth power of its diameter, an increase from 8 mm to 10 mm would theoretically result in a stiffness improvement of approximately 45%. Moreover, increasing the number of bolts effectively improves the overall stiffness by providing multiple load paths, thereby reducing the deformation of any single connection point and enhancing the deformation resistance of the entire joint.

The third stage marks the transition into nonlinear deformation of the connector. Two typical mechanisms may occur in this stage: (1) embedment deformation of the bolt into the glubam block, and (2) bending of the bolt near the steel plate interface, forming plastic hinges. The embedment deformation typically shows an ideal plastic load–displacement response[227]—after reaching a certain load level, the specimen maintains a relatively stable load-bearing capacity. In contrast, when the bolt undergoes bending and plastic hinge formation, strain hardening is observed, with the load continuing to increase as displacement grows[228,229]. In this study, for instance, the load–displacement response of the G-S-10 specimen exhibited an ideal plastic characteristic, with no significant bolt bending observed, indicating that embedment failure between the bolt and glubam surface dominated. In comparison, the G-D-8 specimen showed a gradually increasing load during the large displacement phase, suggesting post-embedment bolt bending and strain hardening, indicative of a typical plastic hinge behavior.

The fourth stage represents the final failure stage, typically characterized by shear failure or fiber-splitting failure in the glubam block[230], accompanied by a significant drop in load, indicating a complete loss of load-bearing capacity[231] and irreversible structural failure. Generally, increasing the number of bolts enhances load distribution capacity, while larger bolt diameters improve bending stiffness and embedment strength. As such, increases in these two parameters usually result in higher ultimate load capacity, which helps delay the onset of final failure and improves the overall strength and stability of the connection system.

To quantitatively evaluate the mechanical performance of the connector, the load–displacement curves were processed according to the ASTM D5764-97a[207] standard. A set of representative performance indicators was extracted to characterize the overall behavior of the connection under monotonic loading. These indicators include the initial stiffness (k_e), yield load (F_y), maximum load (F_u), and ductility (D). As illustrated in Figure 4-8, the initial stiffness is calculated as the slope of the secant line between the $0.1F_u$ and $0.4F_u$ points on the load–displacement curve, which effectively captures the stiffness characteristics of the connection in its elastic stage. It can be expressed as:

$$k_e = \frac{0.3F_u}{V_{0.4} - V_{0.1}} \qquad \text{(4-1)}$$

Where： $V_{0.4}$ —— the displacement corresponding to 0.4 F_u ; $V_{0.1}$ —— the displacement corresponding to 0.1 F_u . The ductility can be expressed as:

$$D = \frac{V_u}{V_y} \tag{4-2}$$

Where： V_u —— represents the ultimate displacement, corresponding to the point where the load drops to 80% F_u ; F_y and V_y are determined using an offset method, where a secant line with an offset of 0.05d (as shown by the red dashed line in Figure 4-8) is constructed-here, d denotes the bolt diameter. The intersection of this offset line with the load-displacement curve is defined as the yield point[206].

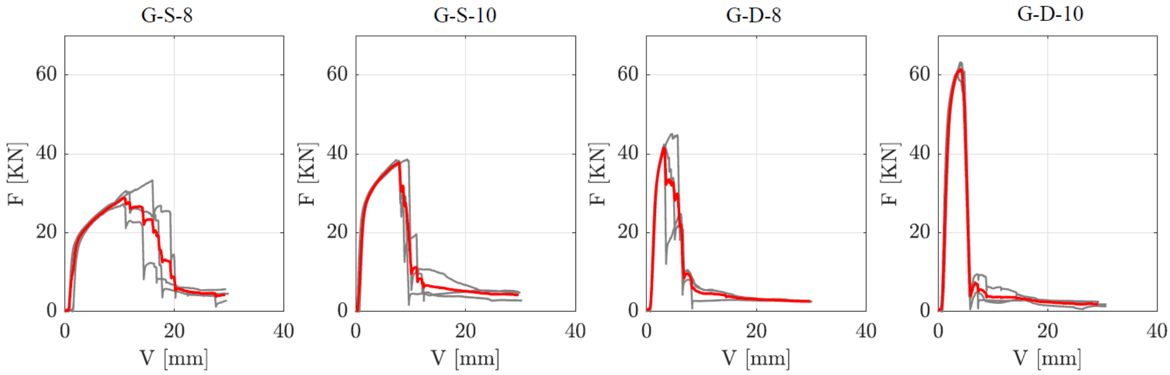

Figure 4-7 Monotonic Tensile Test Results of Steel Insert-Plate Glubam Connectors

Table 4-3 summarizes the key mechanical performance indicators obtained from the monotonic tensile tests for each type of specimen, including initial stiffness k_e, yield load F_y, maximum load F_u, and ductility coefficient D. A statistical analysis of the results was also conducted.

From the observed statistical trends, it is evident that increases in bolt diameter and the number of bolts lead to significant improvements in initial stiffness, yield load, and maximum load. This indicates that the load-bearing capacity and stiffness of the connectors are highly sensitive to geometric parameters. Conversely, the ductility coefficient D tends to decrease with these parameter increases, suggesting that improvements in connection stiffness may come at the cost of reduced ductility.

A more detailed comparison between the S10 group (single bolt, 10 mm diameter) and the D8 group (double bolts, 8 mm diameter) shows that although the D8 group uses smaller diameter bolts, it exhibits superior performance in terms of initial stiffness, yield load, and maximum load. However, its ductility is relatively lower. This outcome suggests that bolt quantity has a greater influence on connection performance than bolt diameter. Increasing the number of load paths proves more effective in enhancing the overall load-bearing capacity and stiffness of the structural joint than simply increasing the stiffness of a single load path.

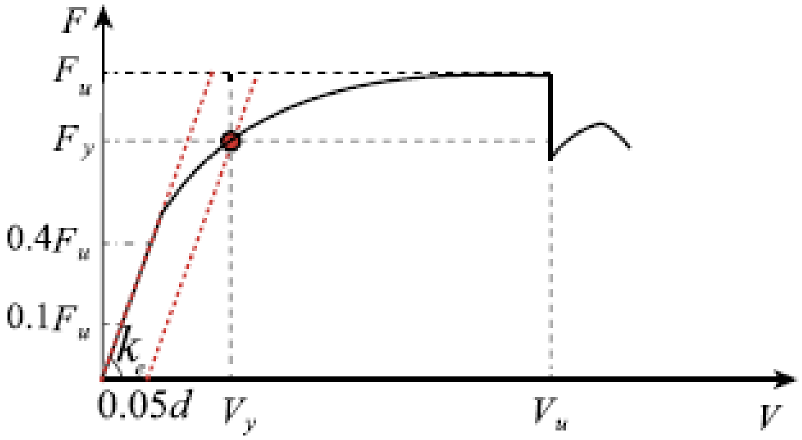

Figure 4-8 Definitions of Mechanical Performance Indicators

Table 4-3 Summary Of Mechanical Properties Of Steel Insert-Plate Glubam connectors

Specimen	k_e	$\overline{k_e}$	F_y	$\overline{F_y}$	F_u	$\overline{F_u}$	D	$\overline{D}$
	$[kN/mm]$		$[kN]$		$[kN]$			
G-S-8-1	28.77		17.06		27.30		6.58	
G-S-8-2	23.95	24.48	17.01	17.25	30.60	30.40	6.35	7.22
G-S-8-3	20.73		17.68		33.30		8.74	
G-S-10-1	34.99		27.20		38.59		4.80	
G-S-10-2	44.54	37.48	26.50	26.97	38.46	38.27	6.14	5.19
G-S-10-3	32.92		27.20		37.76		4.64	
G-D-8-1	31.71		36.19		45.07		2.10	
G-D-8-2	39.34	33.33	34.52	36.47	42.12	43.21	2.39	1.93
G-D-8-3	28.92		38.70		42.43		1.31	
G-D-10-1	58.86		53.30		60.25		3.04	
G-D-10-2	43.92	49.70	53.97	54.03	62.98	62.15	2.22	1.98
G-D-10-3	46.33		54.83		63.21		2.34	

Table 4-4 presents the surface damage patterns of the Glubam block on the side with the bolt heads and nuts, as captured by the Digital Image Correlation (DIC) system. These images were recorded at the critical moment when cracks first appeared in the specimens, typically corresponding to the initial significant drop in load, and thus reflecting the onset of failure in the connection system. Test results indicate that the failure modes of the connectors varied significantly with changes in bolt number and diameter and can be broadly categorized into two types: shear failure and splitting failure. In some specimens, a combination of both failure modes was observed[232-234], or the formation of plastic hinges near the steel plate side of the bolts, which highlights the energy dissipation capability of the connectors in the plastic stage. For example, the G-S-8 specimen demonstrated relatively high ductility, with noticeable localized deformation zones observed during the test. Due to the strong embedment constraint effect near the steel plate end of the bolts, combined with a certain degree of “rope effect” [235], this type of connection tends to form localized plastic hinges, which helps delay the onset of global failure.

Overall, the high embedment strength of Glubam material (see Table 3-1) effectively suppressed the development of bolt embedment deformation along the hole walls. Thus, no typical bolt embedment failure was observed within the load range covered in this study. In terms of connection configuration, although double-bolt connections exhibited superior load-bearing capacity compared to single-bolt connections, their ductility performance was slightly inferior. Similar to the single-bolt specimens, the double-bolt specimens also showed a coexistence of shear and splitting failure modes. Additionally, some double-bolt specimens clearly exhibited shear failure regions between the two bolts, further revealing the synergistic force transfer mechanism between the multiple load paths within the connector.

Table 4-4 Failure Modes of Steel Insert-Plate Glubam Connectors under Monotonic Tensile Loading (Single-Bolt Specimens)

Specimen	G-S-8-1	G-S-8-2	G-S-8-3	G-S-10-1	G-S-10-2	G-S-10-3
Bolt head						
Bolt Nut						

In this study, two-dimensional Digital Image Correlation (2D-DIC) was employed to conduct detailed observation and quantitative analysis of the deformation evolution behavior of the connectors near the critical stage preceding failure (i.e., Stage IV). This technique enables high-resolution acquisition of full-field displacement and strain distributions on the surface of the joints, thereby revealing the local mechanical response characteristics prior to failure. The predominant failure modes observed during the experiments were shear failure and splitting along the fiber direction (see Figure 13). To further investigate the strain evolution mechanisms associated with these failure modes, this study focused on the pre-crack zone near the initial crack emergence side (i.e., Stage IV), and extracted the primary strain fields and shear angle distributions in this area using 2D-DIC. The strain definitions and calculation methods followed the approach proposed by Mai et al.[236] Table 4-6 summarizes representative DIC results for selected specimens at this stage. Considering the high consistency in loading paths and failure mechanisms among different specimens, only representative images and data are presented herein for brevity; the remaining specimens exhibited similar deformation patterns and strain characteristics and are not discussed individually.

Table 4-5 Failure Modes of Steel Insert-Plate Glubam Connectors under Monotonic Tensile Loading (Double-Bolt Specimens)

Surface	G-D-8-1	G-D-8-2	G-D-8-3	G-D-10-1	G-D-10-2	G-D-10-3
Bolt head	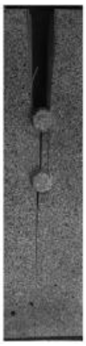					
Bolt Nut				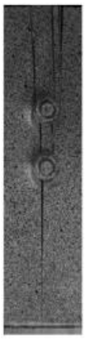		

The DIC analysis results reveal that while the spatial distribution of principal strain fields and shear angle fields varies across specimens, they exhibit certain consistent patterns overall. For all single-bolt Steel insert-plate Glubam Connectors, the high-strain zones typically originate at the end of the bolt hole and extend longitudinally along the glubam member. The extent of this strain distribution is closely related to the specific configuration of the specimen. These high-strain zones often manifest as one or more localized shear strain bands (shear planes), forming potential failure paths. For instance, specimens G-S-8-2 and G-S-10-1 represent two typical failure modes. In the pre-failure stage of G-S-8-2, three distinct high principal tensile strain zones emerged above the bolt, indicating a mixed failure mode combining shear and splitting. In contrast, specimen G-S-10-1 exhibited a single concentrated principal strain zone above the bolt, suggesting a splitting-dominated failure mechanism. These differences further demonstrate that Steel insert-plate Glubam Connectors may undergo shear failure, splitting failure, or a combination of both, depending on the connection configuration and material response.

For all double-bolt connections, the principal strain distributions exhibited more complex patterns: two prominent strain concentration zones typically appeared in the region between the bolts, indicating a dominant shear failure mechanism. Additionally, a concentrated strain region similar to that observed in single-bolt specimens was found near the first bolt. The distribution of shear angles was highly correlated with the principal strain field. High shear angle zones were typically found surrounding the areas of principal strain concentration and exhibited a characteristic antisymmetric pattern, suggesting significant localized shear deformation. These patterns provide critical evidence for identifying failure mechanisms and predicting crack propagation paths.

Table 4-6 Strain Fields at Failure (Principal Strain and Shear Angle)

Specimen	G-S-8-3	G-S-10-1	G-D-8-2	G-D-10-1
Principal Strain	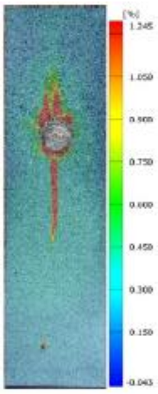	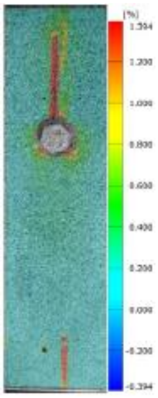	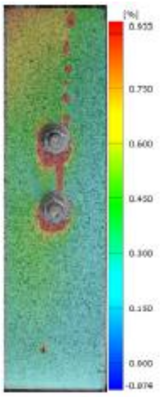	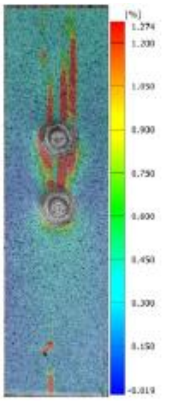
Shear angle	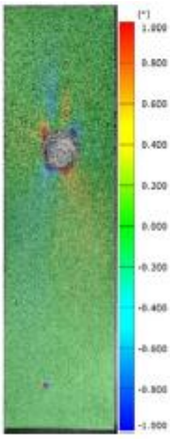	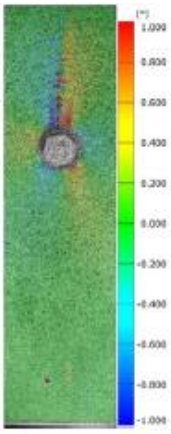	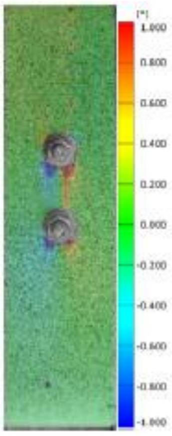	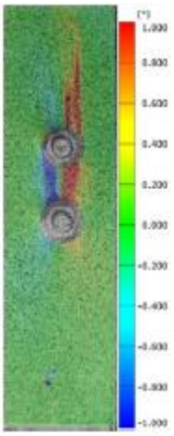

4. 3. 3. 2 Tensile-Side Cyclic Loading Test

Figure 4-9 presents the hysteresis curves obtained from forward tensile cyclic loading tests on three groups of Steel insert-plate Glubam Connectors with identical configurations. As shown in the figure, the three repeated tests for each specimen group exhibit consistent overall response characteristics and good repeatability. The shape of the hysteresis loops and the trends in energy dissipation capacity remain generally consistent across specimens, indicating that the connection type exhibits stable hysteretic performance under the given experimental conditions.

Figure 4-10(a) shows the equivalent viscous damping ratio V_{eq} calculated for each loading cycle based on the experimental data. The analysis reveals that increasing the bolt diameter enhances the energy dissipation capacity of the joint, as evidenced by the higher damping values. Moreover, increasing the number of bolts significantly improves the system's damping performance, with a noticeable increase in the overall energy dissipation level when the number of bolts is doubled.

Overall, the equivalent damping ratio tends to increase gradually with the number of loading cycles. However, in the early stages of loading, the damping ratio is relatively high due to initial local damage and stress redistribution within the specimen during the first few cycles. This phenomenon leads to a non-linear growth in the damping ratio over time. As shown in Figure 4-10(a), the equivalent viscous damping ratios for the connection specimens fall within the range of 0.03 to 0.30, which aligns with the typical damping range observed in light-frame timber structures and engineered bamboo structures. For most specimens, the damping capacity peaks around the 12th to 15th cycle. After that, due to damage accumulation, the hysteresis loops begin to narrow, and the energy dissipation capacity reaches saturation or shows a slight decline.

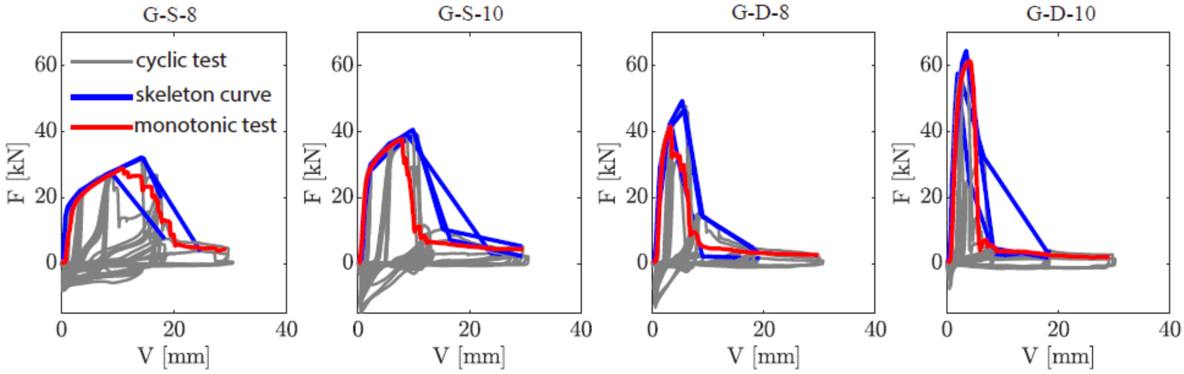

Figure 4-9 Load–Displacement Curves from Tensile-Side Cyclic Tests

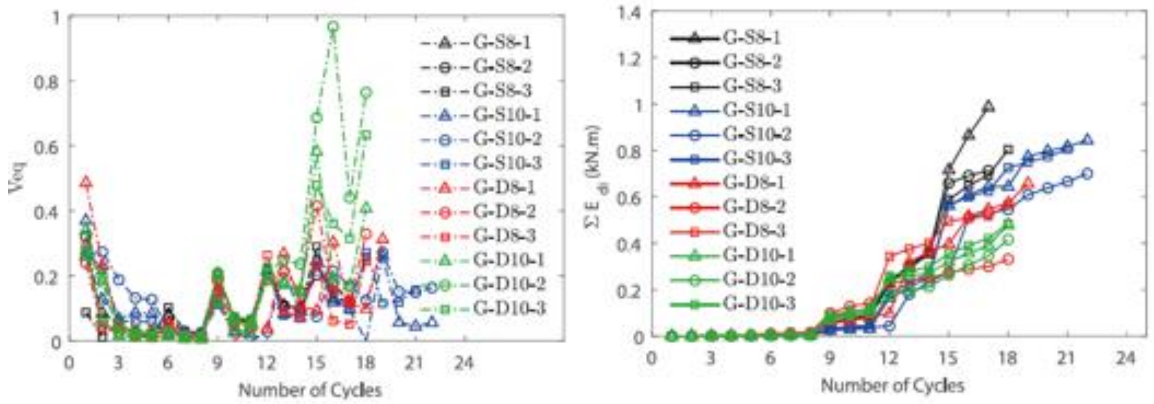

(a) equivalent viscous damping ratio V_{eq} (b) Cumulative energy dissipation $\sum E_{di}$

Figure 4-10 Variation of Equivalent Viscous Damping and Cumulative Energy Dissipation with Loading Cycles

Figure 4-10(b) illustrates the variation in total energy dissipation $\sum E_{di}$ of different connection specimens throughout the cyclic loading process. The results show that during the initial few loading cycles, the energy dissipation level of the components remains relatively stable, with a slow rate of increase. At this stage, energy dissipation is primarily attributed to contact adjustment, initial frictional slip, and localized micro-damage, reflecting the adaptive deformation behavior of the connections in early loading. As the number of cycles increases, the connectors enter a pronounced nonlinear response phase, where cumulative damage effects intensify, leading to a significant enhancement in per-cycle energy dissipation. This results in an accelerated growth of the total dissipated energy. In the later stages of loading, the energy dissipation curve becomes markedly steeper, indicating the connectors' excellent sustained energy-dissipating capacity and hysteretic stability.

Overall, the total energy dissipation exhibits an approximately exponential relationship with the number of loading cycles, suggesting that the energy dissipation capacity of the connection system does not degrade rapidly under repeated loading and maintains a certain level of cyclic ductility. Moreover, the results demonstrate that Glubam connection specimens consistently show excellent energy dissipation performance at all stages of loading. Compared with similar timber-based structural systems, Glubam connectors exhibit stronger hysteretic energy dissipation capabilities, highlighting their high engineering application potential—especially in structural systems where seismic energy dissipation capacity is critically required.

4. 3. 3. 3 **Tension-Compression Cyclic Loading Test**

Figure 4-11 summarizes the hysteresis curves and skeleton curves obtained from the Steel insert-plate Glubam Connectors under tension-compression cyclic loading conditions. Overall, the load–displacement responses of Glubam joints under reversed loading exhibit a relatively short load plateau stage followed by a prolonged stable crack propagation phase. This behavior indicates that the connection configuration retains a certain degree of ductility and energy dissipation potential even after reaching its ultimate load-carrying capacity.

Comparative analysis of different connection configurations shows that double-bolt connections generally exhibit higher load-bearing capacity than single-bolt ones. However, this comes at the cost of slightly reduced ductility. The reduced ductility can be attributed to the constrained development of localized large-deformation zones in multi-bolt configurations, which results in higher stiffness but limits plastic deformation capacity. Under tensile loading, failure typically occurs due to fiber-parallel splitting or shear failure—two common bolt connection failure mechanisms. In some specimens, such as the G-S-8 series, only localized crushing or compression deformation was observed during the tensile test (see Figure 4-12(a)), without developing into full failure, indicating a certain reserve of safety during the initial loading stage.

Under compressive loading, the mechanical response in the displacement range of 0 to -4 mm closely mirrors that of the tensile side, showing symmetric stiffness and deformation characteristics. However, once the displacement exceeds -4 mm, a sharp load increase is observed, with no apparent yielding plateau. This nonlinear response is primarily attributed to a 4 mm structural gap intentionally left at the bottom of the mortise during specimen fabrication. When the compressive displacement surpasses this gap, the steel insert plate comes into contact with the bottom of the mortise, introducing a new load transfer path. This structural detail effectively creates a reactive support point during compression, significantly enhancing the connection's compressive load-carrying capacity. This explains why some specimens exhibit higher compressive than tensile capacity.

Ultimately, under continued loading, the specimens generally fail through full-depth splitting. Cracks initiate at the contact region between the steel plate and the bottom of the mortise and propagate upward along the fiber direction through the Glubam block, forming a complete failure crack (see Figure 4-12(d)).

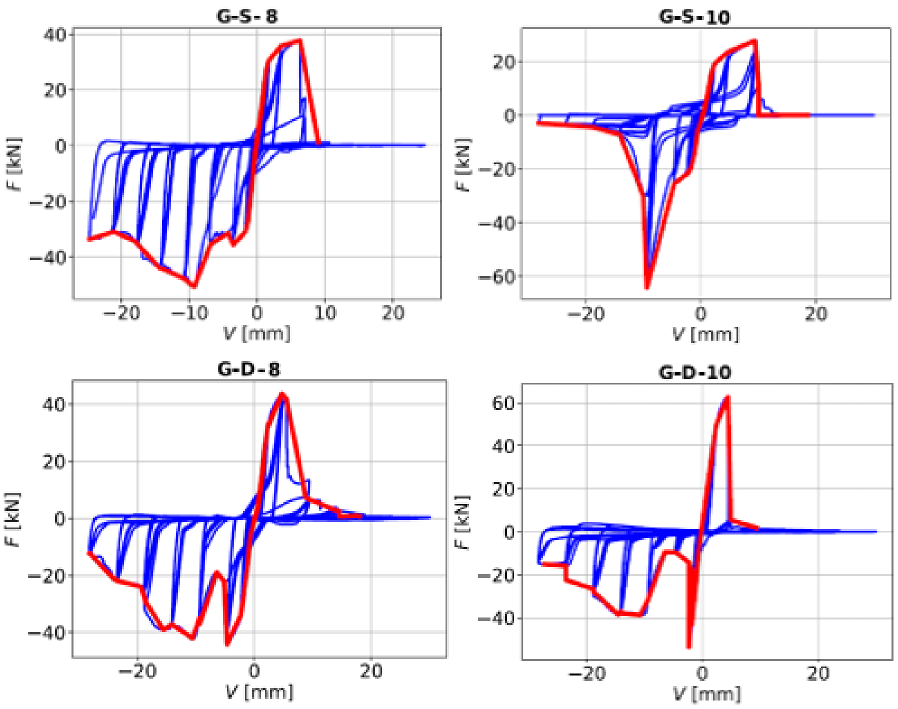

Figure 4-11 Hysteresis Curves and Skeleton Curves under Tension–Compression Cyclic Loading.

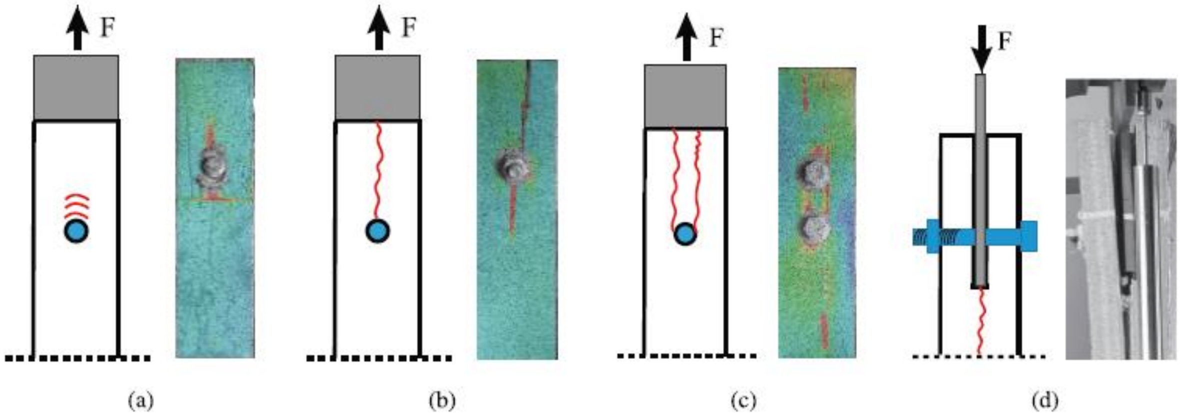

(a) (b) (c) (d)

Figure 4-12 Failure Pattern under Tension-Compression Cyclic Loading

4.4 Experimental Study On Steel Side-Clamped-Plate Glubam Connectors

This section focuses on the axial performance of Glubam connectors using steel side-clamped plates, with particular emphasis on their hysteretic behavior under cyclic loading. Given that the core objective of this study is to investigate the hysteresis characteristics of Glubam joints and to develop a suitable hysteresis constitutive model along with parameter identification, this section does not detail the monotonic loading test results. Instead, the emphasis is placed on the quantitative characterization of hysteretic performance and the identification of failure mechanisms, in order to provide experimental evidence and parameter support for subsequent modeling and numerical simulation.

4. 4. 1 **Specimen Design and Fabrication**

The test specimens used in this section were specifically designed and fabricated to ensure reliable integration with the loading system and to enable stable load application. To prevent local damage or large deformations of the Glubam blocks during testing, different connection schemes were employed at the upper and lower ends of the loading setup. At the upper loading end, a high-strength steel pin with a diameter of 40 mm was used to connect the specimen to the actuator, secured with a custom-fabricated steel clamping fixture to provide a stable loading path and proper alignment. At the lower fixed end, the specimen was bolted to the test setup base using two high-strength bolts of 30 mm diameter, again with custom clamps to ensure connection stiffness and installation accuracy.

To accommodate the above connection methods, different types of steel side-clamped-plate connector configurations were installed at both ends of each specimen (see Figure 4-13). The upper end was designated as the active loading end, where the failure was expected to occur, while the lower end was designed as the fixed end, with enhanced structural stiffness and load-carrying capacity to ensure that it would remain intact and undeformed throughout the test. The fixed end used two large-diameter bolts to meet the requirements of rigid restraint and anti-slip performance.

The total length of the specimen was determined by balancing experimental feasibility with structural response fidelity. On one hand, the specimen needed to be long enough to minimize interference between the tested and fixed ends; on the other hand, it had to comply with spatial and stroke constraints of the testing machine. Consequently, all specimens were uniformly fabricated with a length of 900 mm. Based on the connection configuration shown in Figure 4-2, the cross-section of each specimen was 52 mm × 140 mm, and all Glubam blocks were cut and processed from the same batch to ensure consistency.

Bolt holes were predrilled on both the Glubam and steel plate components. The steel side-clamped plates were made of Q235 hot-rolled steel and cut to shape using precision laser cutting, with bolt holes drilled at designated positions to ensure accuracy and consistency in assembly. The steel side plates had a rectangular cross-section with a base width of 140 mm. The total length was determined by the combined requirements of embedding depth and an additional 300 mm extension, which allowed for the connection to the actuator pin and installation of displacement sensors (see Figure 4-13).

To ensure precise installation and accommodate construction tolerances during assembly, the bolt holes in the Glubam blocks were 0.5 mm larger in diameter than the bolts. Bolt torque control was a critical factor for ensuring experimental accuracy. High-strength bolts were pre-tightened using a calibrated torque wrench to prevent the washers from being embedded into the Glubam surface due to excessive tightening, which could otherwise cause localized damage. Based on preliminary tests, the optimal pre-tightening torques for bolts with diameters of 8 mm and 10 mm were determined to be 0.7 N·m and 1.0 N·m, respectively—sufficient to guarantee reliable friction transfer without inducing premature failure.

All Glubam components used in this study were processed using an automatic CNC drilling machine (Uli-CNC, Model K1) at the Haining International Campus of Zhejiang University, ensuring precise and consistent hole positions. All steel plate components were fabricated and drilled using laser cutting machines to achieve high processing precision. These efforts ensured excellent repeatability and geometric consistency of the test specimens, thereby providing a solid basis for the subsequent hysteresis performance evaluation.

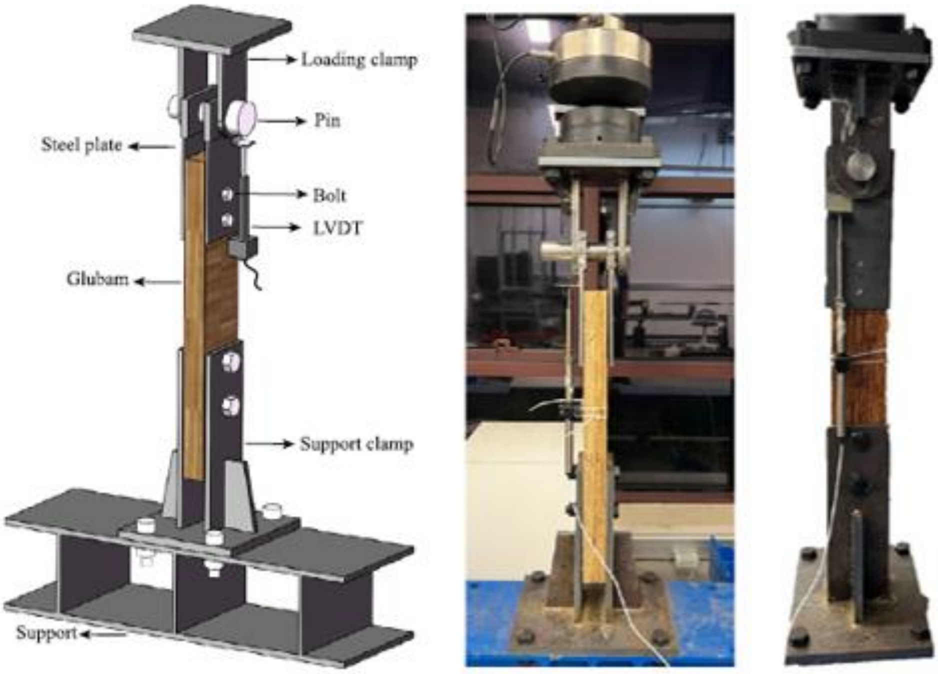

Figure 4-13 Experimental Setup and Equipment for Steel Side-Clamped-plate Glubam Connectors

4. 4. 2 **Test Setup and Procedure**

Figure 4-13 illustrates the test setup and loading system for the steel side-clamped-plate Glubam connectors. To systematically evaluate the influence of different connector configurations on the hysteretic behavior of joints, a series of axial cyclic loading tests was conducted based on the four connector types described in Figure 4-2. The axial loading was applied using a 500 kN servo-hydraulic actuator (Model: 186E, WANCE Ltd.) mounted vertically on a rigid steel frame. The actuator operated under displacement control, with the input displacement commands preprogrammed via a computer interface to ensure precise loading paths.

However, due to inherent feedback delays and equipment-related discrepancies, the actual displacement delivered by the actuator might deviate slightly from the programmed target values. To address this, an external measurement system was employed to calibrate the real-time displacement. Specifically, linear variable differential transformers (LVDTs) were mounted on the specimen surface to measure the relative slip between the upper steel clamp plate and the Glubam body. During testing, the actuator control system continuously adjusted its motion based on real-time feedback from the LVDTs to achieve accurate displacement control.

The cyclic loading protocol followed the European Standard EN 12512 [219], employing a constant-amplitude displacement-controlled approach. The loading rate was uniformly set at 0.2 mm/s. The loading was continued until the specimen exhibited visible failure and could no longer sustain axial force, with specific failure modes to be discussed in subsequent sections. The naming convention and configuration parameters of each test specimen are detailed in Table 4-2, where key factors such as connector type, bolt diameter, and bolt number were considered to facilitate comparative analysis and data interpretation.

4. 4. 3 **Test Results**

Figure 4-14 presents representative hysteresis curves obtained from cyclic loading tests on four types of Steel Side-Clamped-plate Glubam Connectors. During testing, the mechanical response of the joints could be clearly divided into five distinct phases: initial slip stage, elastic stage, yielding stage, loading plateau, and failure stage. These stages were well reflected in the shape and evolution of the hysteresis loops. The initial slip stage was primarily attributed to geometric clearance between the bolt diameter and the predrilled holes in the Glubam members, which caused minor relative slip at the beginning of loading due to incomplete contact. As loading continued into the elastic phase, the connectors exhibited a nearly linear load–displacement relationship. This was followed by yielding and plastic development, during which the hysteresis loops gradually opened, indicating increasing energy dissipation. Overall, the designed connection configurations exhibited excellent ductility and significant energy dissipation throughout the cyclic loading process. The wide and stable hysteresis loops, without signs of brittle fracture, confirmed the good seismic resilience and cyclic stability of these connectors. As shown in Figure 4-15, the failure modes observed during cyclic loading primarily fell into three typical categories: (1) bolt fracture at the mid-length; (2) shear failure at the bolt head; and (3) shear failure of the Glubam block between two bolts. Bolt fracture and shear failures often occurred at zones of localized stress concentration, especially under higher loading levels or after a larger number of cycles. For example, specimen B-10 mainly exhibited bolt rupture and head shear failure, whereas specimens B-12, B-14, and B-16 were more prone to shear failure within the Glubam material between bolts.

Bolt diameter had a notable influence on both the failure modes and hysteretic performance of the joints. Bolts with smaller diameters typically resulted in more uniform stress distribution across their cross-sections, leading to more coordinated deformation and enhanced energy dissipation. These bolts tended to fail through more ductile mechanisms, such as plastic yielding or local buckling, demonstrating better hysteretic toughness and greater energy dissipation capacity. In contrast, bolts with larger diameters were more susceptible to localized stress concentrations, which could trigger brittle failure mechanisms, such as material cracking or local crushing. These failure modes were usually accompanied by rapid energy release and lower dissipation, resulting in reduced envelope areas of the hysteresis loops and diminished joint ductility and stability. These findings indicate that the mechanical performance of the Glubam joints is not only influenced by bolt configuration but also significantly affected by bolt diameter. Therefore, joint design should carefully balance strength and ductility to optimize seismic performance.

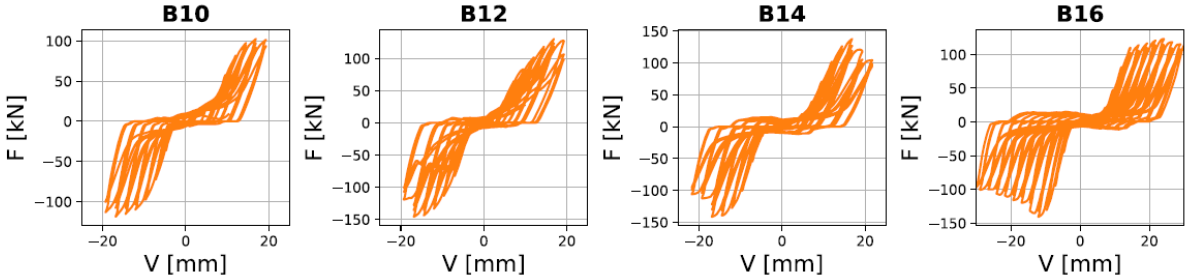

Figure 4-14 Hysteretic Test Results Of Steel Side-Clamped-Plate Glubam Connectors

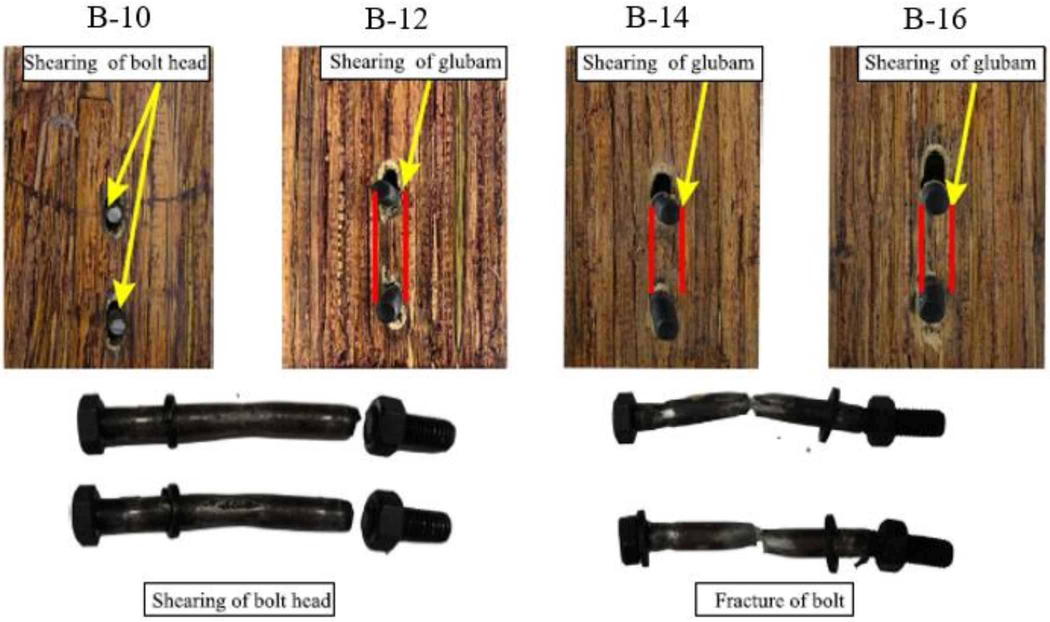

Figure 4-15 Failure Pattern of Steel Side-Clamped-Plate Glubam Connectors

5 Experimental Study on Glubam Trusses and Roof Systems

5.1 Overview

This chapter presents a systematic experimental investigation into the mechanical performance of roof truss systems constructed from glubam (glue-laminated bamboo). The primary objective is to comprehensively assess the load-bearing capacity, deformation characteristics, and failure mechanisms of glubam trusses under cyclic loading conditions, thereby evaluating the safety and applicability of such systems in modern structural engineering. With the growing promotion of engineered bamboo in sustainable construction, roof truss systems based on glubam components have demonstrated promising potential for development. However, research on their global structural performance remains relatively limited, particularly in terms of hysteretic behavior, joint coordination mechanisms, and failure modes under repeated loading scenarios.

To address these gaps, this chapter adopts quasi-static cyclic loading tests as the principal method of investigation. Through an integration of experimental data and hysteresis performance analysis, the study aims to elucidate the mechanical response of glubam roof trusses under extreme conditions such as seismic loading. The scope of the research includes: a detailed introduction to the design parameters of the roof truss specimens, their structural detailing, joint configurations, boundary conditions, and experimental setup; observation and analysis of mechanical responses and damage evolution during the hysteresis testing process; and quantitative assessment of structural performance through key indices extracted from hysteresis curves (e.g., stiffness degradation, energy dissipation capacity, and ductility factors). This chapter focuses on three core aspects: hysteretic behavior, energy dissipation mechanisms, and failure evolution. It systematically reveals the force-resisting characteristics of glubam roof truss structures under varying construction parameters. The results highlight the influence of joint types and structural detailing on truss performance and identify the dominant failure modes along with their underlying mechanisms. The findings not only provide essential experimental support for the numerical modeling and parameter identification in subsequent chapters but also establish a theoretical and technical foundation for the structural design, seismic optimization, and practical application of glubam roof truss systems.

In summary, this chapter fills a critical gap in the experimental study of engineered bamboo truss systems from a structural mechanics perspective, and lays the groundwork for advancing the standardization and systematization of glubam structural systems in theory and practice.

5.2 Configuration and Fabrication of Glubam Trusses and Roof Systems

Steel insert-plate and steel side-clamped-plate connectors are among the most commonly used connection types in lightweight timber roof and truss structures, having been widely applied and well developed within conventional timber engineering. However, systematic studies on the application of these connection forms in engineered bamboo systems—such as glubam trusses and roof structures—remain limited, particularly concerning global structural performance, hysteretic behavior, and failure mechanisms.

To address this gap, and based on the previously completed hysteresis performance studies of engineered bamboo joints using steel insert-plate and steel side-clamped-plate connectors, this research further expands the scope by designing and constructing two types of engineered bamboo truss and roof systems, as shown in Figures 5-1 and 5-2. Corresponding to the four configurations of steel insert-plate joints and four configurations of steel side-clamped-plate joints investigated earlier, a total of four glubam truss specimens with steel insert-plate connections and four roof truss specimens with steel side-clamped-plate connections were fabricated and tested.

By systematically comparing the mechanical responses of different connector types within complete structural assemblies, this study aims to clarify the influence of joint configuration parameters on the global structural behavior. The findings provide essential experimental evidence and theoretical insights to support the seismic design and performance optimization of engineered bamboo truss systems in future engineering applications.

5. 2. **Steel Insert-Plate Glubam Planar Truss**

The steel insert-plate glubam planar truss designed in this study adopts the Warren truss configuration, a structural form composed of a series of triangular units known for its excellent mechanical performance and geometric stability. The defining feature of the Warren truss is the use of alternating diagonal web members between the upper and lower chords, enabling a more uniform distribution of internal forces during loading and thereby enhancing the overall stiffness and stability of the structure. This type of truss is widely used in structural design, especially under combined tension and compression loading conditions, making it particularly suitable for lightweight roof systems. Within the glubam roof truss system, the Warren truss is considered an ideal solution for engineered lightweight structures due to its simplicity, clearly defined force paths, and reduced number of joints. Given the high tensile and compressive strength and favorable ductility of glubam, its integration with the efficient load-transferring mechanism of the Warren truss is expected to significantly improve both the load-bearing and seismic performance of the structural system.

Each Warren truss specimen in this study consists of nine members, with an overall span of approximately 2.7 meters and a height of about 0.6 meters. The geometric layout of the truss is illustrated in Figure 5-1. All truss members were fabricated using CNC precision machining techniques at the Haining International Campus of Zhejiang University, utilizing a Uli-CNC automatic drilling machine (Model K1). The fabrication process included cutting the glubam members to the specified lengths, milling slot openings at the center of each end, and drilling bolt holes at designated positions to ensure accurate alignment and geometric consistency during joint assembly. All joints in the truss were constructed using steel insert-plate connectors, with each member fixed in place by embedded steel plates and bolts. The geometry and dimensions of the insert plates were customized according to the number of branch connections required at each node, as illustrated in Figure 5-1. In addition, the steel plates located at the truss ends and top loading points were fabricated with through-holes of 36 mm in diameter to allow connection with the loading actuators and boundary support system.

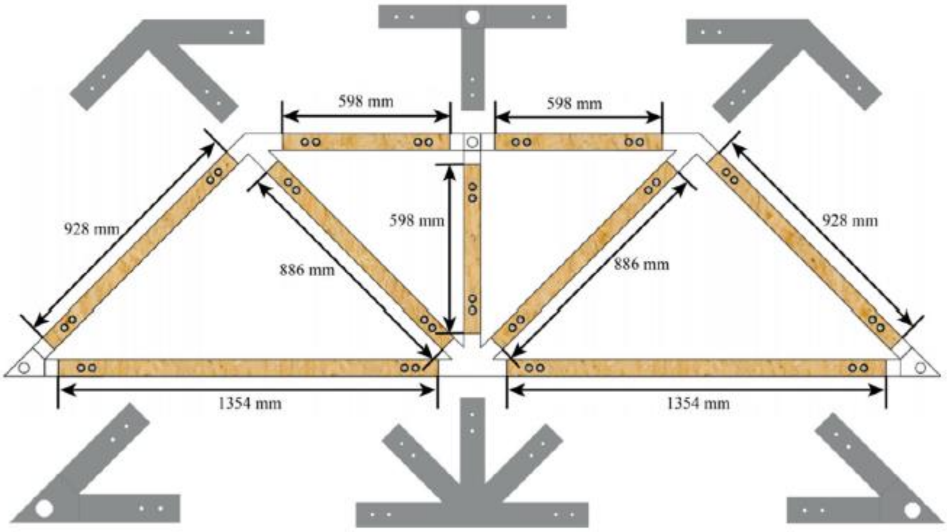

Figure 5-1 Geometric Diagram of the Steel Insert-Plate Glubam Warren Truss

To systematically investigate the influence of connection configuration on truss performance, this study designed four different configurations of hybrid planar Warren trusses based on the four types of steel insert-plate glubam joint configurations analyzed in the previous section (with bolt diameters of 8 mm and 10 mm, and using either single-bolt or double-bolt connections). These truss specimens aim to reveal the effects of varying joint parameters on the overall hysteretic behavior, stiffness degradation, and failure modes of the glubam truss system.

5. 2. 2 **Steel Side-Clamped-plate Glubam Roof Truss**

In this study, four steel side-clamped-plate glubam roof trusses were designed and assembled, corresponding to the four connection configurations of Steel Side-Clamped-plate Glubam Connectors proposed in the previous research. Each truss consists of nine members, forming a single-span symmetrical triangular roof truss with an overall span of approximately 4 meters. The geometric dimensions and construction details are illustrated in Figure 5-2.

All members of the roof trusses are connected to glubam components using bolted steel side-clamped plates. The geometry of each steel plate was custom-designed according to the number of members converging at the joint to meet the structural requirements of multi-branch connections. Specific shapes and hole arrangements of the joint plates are also shown in Figure 5-2.

To ensure high assembly precision and fabrication consistency, all truss members were machined using computer numerical control (CNC) drilling equipment. During fabrication, each glubam member was first cut to its designated length as per design requirements. Then, positioning holes were drilled at both ends to guarantee coaxial alignment for bolt installation and to match the steel joint plates with high dimensional accuracy. Once drilling and end preparation were completed, the members were assembled using high-strength bolts to ensure reliable connection stiffness and continuous load transfer throughout the structure.

Additionally, to meet the boundary connection requirements of the hysteresis loading tests, 50 mm diameter holes were drilled into the steel joint plates located at both ends of the bottom chord and at the center of the top chord. These holes were used to install pin connections, allowing hinged articulation between the truss and the two end supports, as well as mechanical coupling between the actuator and the truss's top loading point. This setup ensured a clear load path, appropriate boundary constraints, and realistic, controllable loading conditions during the experimental process.

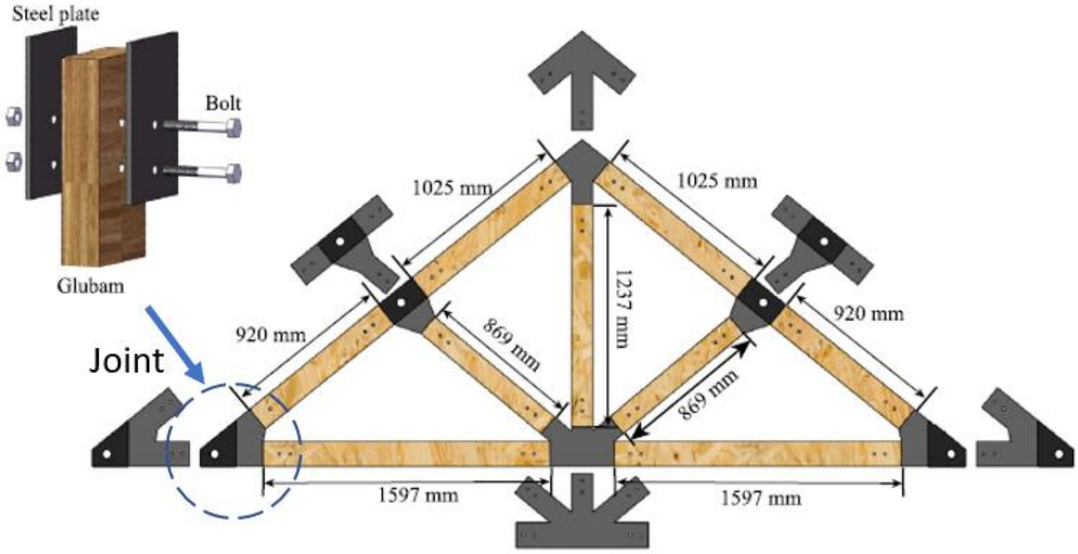

Figure 5-2 Geometrical Dimensions of the Steel Side-Clamped-plate Glubam Roof Truss

5.3 Experimental Study on the Steel Insert-Plate Glubam Warren Truss

This section presents an experimental study on the hysteretic performance of the steel insert-plate Glubam planar Warren truss. A quasi-static cyclic loading protocol was employed to evaluate the mechanical response of the structure under repeated loading. To enable a more systematic and comprehensive analysis of the failure modes and localized damage evolution during the loading process, Digital Image Correlation (DIC) technology was introduced. This non-contact, high-resolution measurement method was applied to critical regions around the connection joints and vulnerable components. Through DIC, full-field strain distributions and crack propagation characteristics on the surface of the specimens were accurately captured, significantly enhancing the understanding of the structural failure mechanisms.

5. 3. 1 **Test Methods**

Consistent with the node-level testing protocols, two cyclic loading schemes were employed in the truss experiments, both based on the EN 12512 [219] standard. The first scheme is a non-reversed, modified version of the EN 12512 [219] procedure, in which cyclic displacements are applied between zero and a predefined positive (tensile) displacement value without entering the compression range[221]. The loading cycle mechanism is illustrated in Figure 4-5. The yield displacement V_y used in the test was determined based on monotonic loading results for each joint configuration, following the yield point identification procedure outlined in EN 26891. This test was displacement-controlled with a constant loading rate of 0.2 mm/s.

The second loading scheme, illustrated in Figure 4-6, involved fully reversed cyclic loading with displacement control in both tensile and compressive directions, aiming to simulate the realistic hysteretic response under bidirectional loading. The displacement amplitude was incrementally increased based on the respective yield displacement of each truss specimen, and the loading rate was set to 0.6 mm/min. The loading process continued until significant structural failure occurred or the target displacement limit was reached. In this study, all trusses with single-bolt joints were tested under the first loading scheme, while trusses with double-bolt joints were subjected to the second loading scheme, ensuring a comprehensive evaluation of the influence of different joint configurations on the structural hysteresis behavior.

Figure 5-3 shows the experimental setup for the planar truss tests. The truss ends were connected to steel supports via hinge pins, and these supports were firmly anchored to a strong floor (reaction base), forming a statically indeterminate symmetrical structural system. This arrangement minimized the effects of boundary condition variability on the test results and enhanced overall stability during testing. The symmetrical configuration also simplified the monitoring of nonlinear hysteretic responses and facilitated subsequent numerical modeling, reducing analysis complexity.

Vertical loads were applied through a hydraulic actuator mounted on a reaction frame. The actuator was flexibly connected to the steel node plate at the midspan of the top chord using a hinge pin, ensuring consistent axial load application. To prevent out-of-plane deformation of the truss during loading, lateral restraint devices were installed to confine the top and bottom chords, maintaining axial force dominance in the members and improving the accuracy and control of the experimental results.

To capture strain responses in critical truss members, strain gauges were installed on selected top and bottom chord members, as illustrated in Figure 5-3. Given the geometric and loading symmetry of the structure, strain gauges were installed on only one side of each truss specimen. Each specimen was instrumented with two sets of strain gauges on representative members to analyze internal force distributions and provide essential data for subsequent structural analysis and model calibration.

A unified naming convention was adopted for specimen identification. The format is G-D(S)-X-PT, where G indicates the use of Glubam as the material, D(S) refers to the number of bolts per branch in the joint—D for Double Bolt and S for Single Bolt, X denotes the bolt diameter (in mm), and PT stands for Planar Truss. Detailed specimen IDs and configurations are summarized in Table 5-1.

Table 5-1 Summary Of Steel Insert-Plate Glubam Truss Specimens

Specimen	Joint Configuration	
	Bolt Diameter	Bolt Number
G-S8-PT	8	1
G-S10-PT	10	2
G-D8-PT	8	1
G-D10-PT	10	2

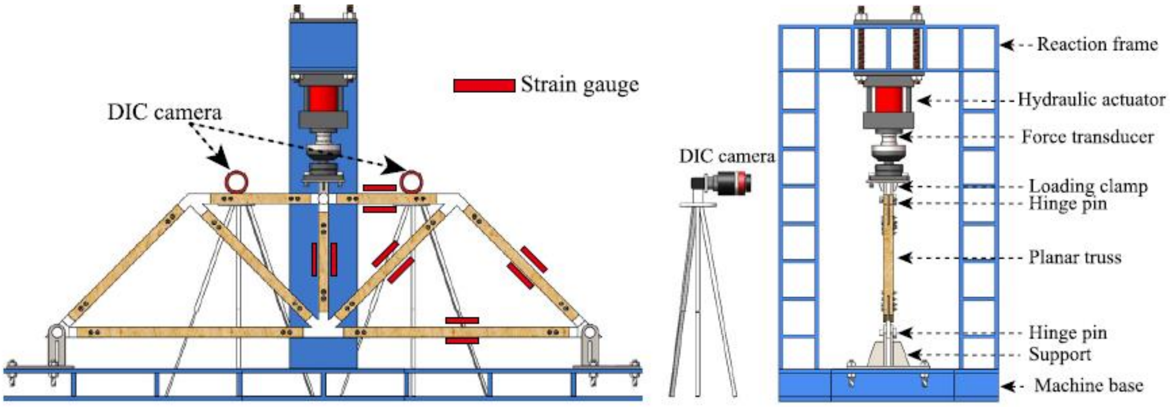

Figure 5-3 Front and Side Views of the Loading Setup for the Steel Insert-Plate Glubam Warren Truss

5. 3. 2 Test Results

Figure 5-4 presents the hysteresis curves and corresponding failure modes of the four planar trusses. The displacement V indicated in Figure 5-4 refers to the vertical displacement at the midspan node of the top chord (as illustrated in Figure 5-3).

The mechanical response of the planar truss structures under cyclic loading exhibited strong similarities to the hysteretic behavior observed in their corresponding Steel insert-plate Glubam Connectors (see Figure 4-1). However, at the structural level, more complex characteristics emerged. Notably, in the initial loading stage, the hysteresis curves of the planar trusses displayed more pronounced initial slippage, especially during the negative loading phase. This behavior is primarily attributed to the assembly tolerance between the steel supports and the hinge pins, which resulted in relative sliding, as well as out-of-plane deformation effects caused by asymmetric constraints during negative displacement.

Overall, the truss structures demonstrated consistent performance in terms of initial stiffness, peak load capacity, and ductility when compared to their respective Steel insert-plate Glubam Connector tests, further validating the rationality of translating and amplifying connector-level mechanical performance to the structural scale (see Figure 4-1). In most of the tested trusses, failure initiated at the ends of the top chord or vertical members in the form of splitting cracks, indicating that tensile stress concentration was the dominant failure mechanism. It is worth noting that the specimen labeled G-D10-PT exhibited a different crack initiation pattern, with the first visible crack emerging in the midsection of a diagonal brace on the right side. This observation aligns with the measured strain distribution patterns during testing and suggests that the force distribution among different members under cyclic loading significantly influences the failure mode. The underlying mechanisms will be further discussed in the numerical modeling and calibration chapters.

To provide a clearer and more comprehensive understanding of the localized failure evolution in Steel insert-plate Glubam Warren trusses under cyclic loading, two-dimensional Digital Image Correlation (2D-DIC) was employed to measure and analyze the full-field strain and displacement fields in critical connection zones. As shown in Figure 5-5, pronounced strain concentration regions were observed around the bolt and nut areas, represented by red hot zones, indicating strong embedment effects and indentation deformation in the glubam members due to bolt interaction. Additionally, red band-like regions developing along the fiber direction were observed in some tension members, typically signifying the onset of splitting failure and revealing a tendency for fiber separation under cyclic loading.

This section highlights the specimen G-D8-PT as a representative case to demonstrate the typical outcomes of DIC analysis. The results not only reveal the local deformation characteristics of the connection areas and critical members in spatial detail but also confirm the consistency and validity of translating node-level hysteresis behavior to the full structural response. These findings provide empirical support for the refinement of joint modeling and structural performance prediction in subsequent chapters.

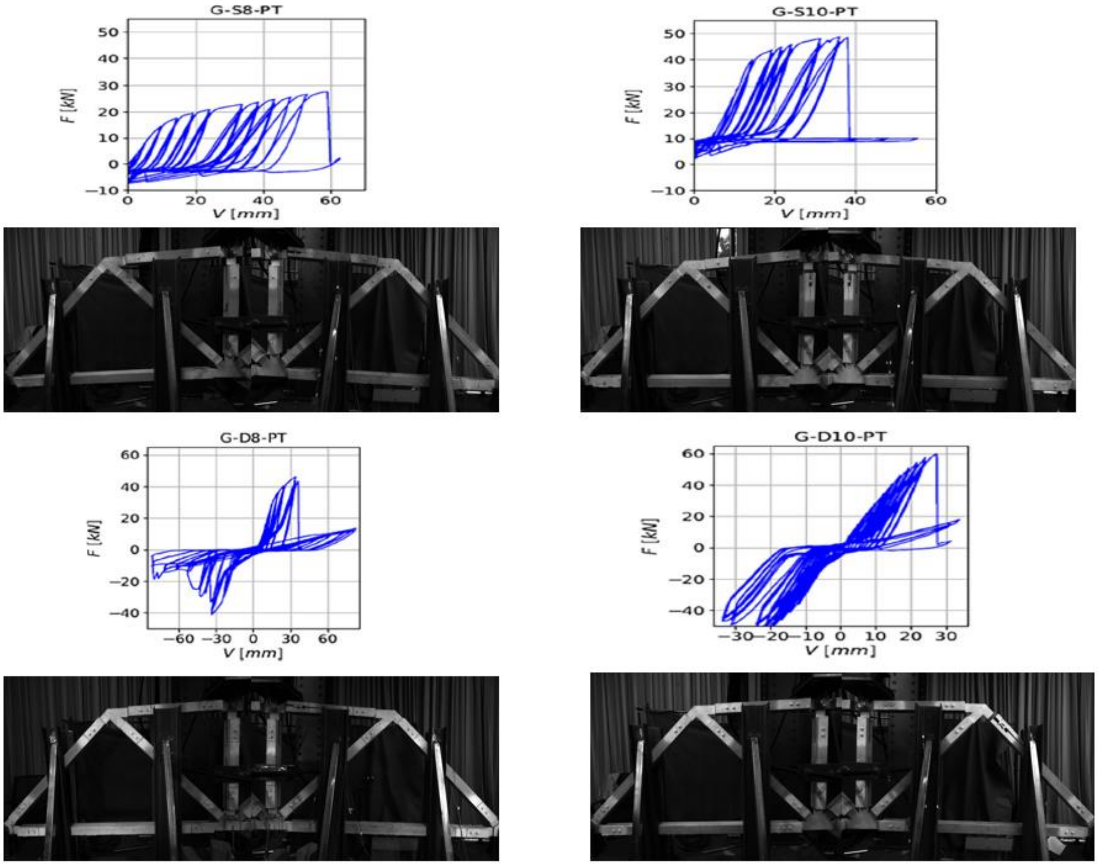

Figure 5-4 Load–Displacement Curves and Experimental Setup Photos of Steel Insert-Plate Glubam Warren Trusses under Hysteretic Loading

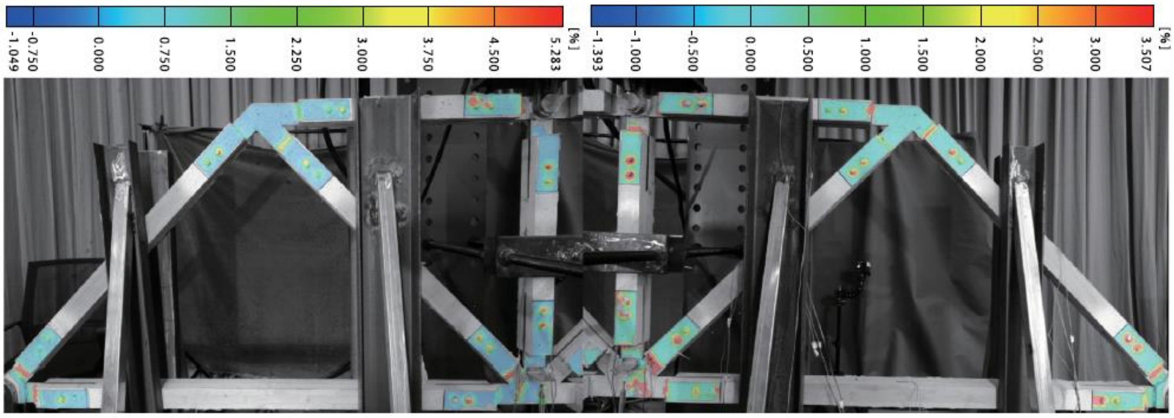

Figure 5-5 Stress Field of Steel Insert-Plate Glubam Warren Truss under Hysteretic Loading

5.4 Experimental Study on Steel Side-Clamped-Plate Glubam Roof Trusses

This section presents a hysteretic performance testing program focused on the Steel Side-Clamped-Plate Glubam Connector system used in roof truss structures. Cyclic loading tests were conducted to systematically evaluate the mechanical response of these connections under repeated loading conditions. The objective is to provide experimental evidence for understanding their hysteretic behavior and energy dissipation capacity.

5. 4. 1 Test Methods

The experimental loading system for the Steel Side-Clamped-Plate Glubam roof truss is illustrated in Figure 5-6. In this setup, the truss ends are connected via pinned joints to two steel support bases, which are themselves rigidly fixed to the foundation through hinge pins, thereby forming a simply supported boundary condition (see Figure 5-6). A steel connector is installed at the mid-span of the top chord, where a hinge pin links it to a vertically oriented hydraulic actuator mounted on the reaction frame to apply vertical loads. The loading protocol adopts displacement control and follows a predefined displacement history curve.

Since the primary goal of this study is to investigate the axial mechanical performance of the roof truss and its connections under uniaxial loading, it is critical to ensure that the truss members are subjected solely to axial tension and compression during testing. To suppress out-of-plane deformation, a specially designed lateral restraint system was installed. This system consists of multiple steel limit plates and bracing rods that provide near-rigid lateral constraints (as shown in Figure 5-9), ensuring that the member deformation develops predominantly along their axial direction.

To accurately capture the deformation response during loading, strain gauges were affixed to key members of the truss. Their layout is shown in Figure 5-6. Considering the geometric and loading symmetry of the truss, strain gauges were only placed on one half of the structure to minimize redundancy and enhance measurement efficiency. For each selected member, strain gauges were installed symmetrically on both sides to detect any potential bending effects, thus verifying whether the axial force assumption holds.

The cyclic loading tests were displacement-controlled with a loading rate of 0.2 mm/s, conducted in accordance with the EN 12512 standard. The naming convention for the tested Steel Side-Clamped-Plate Glubam roof trusses follows the format A-RT, where A indicates the bolt diameter, and RT stands for roof truss, as summarized in Table 5-2.

Table 5-2 Summary Of Steel Side-Clamped-Plate Glubam Roof Truss Specimens

Specimen	Joint Configuration	
	Bolt diameter	Bolt number
10-RT	10	2
12-RT	12	2
14-RT	14	2
16-RT	16	2

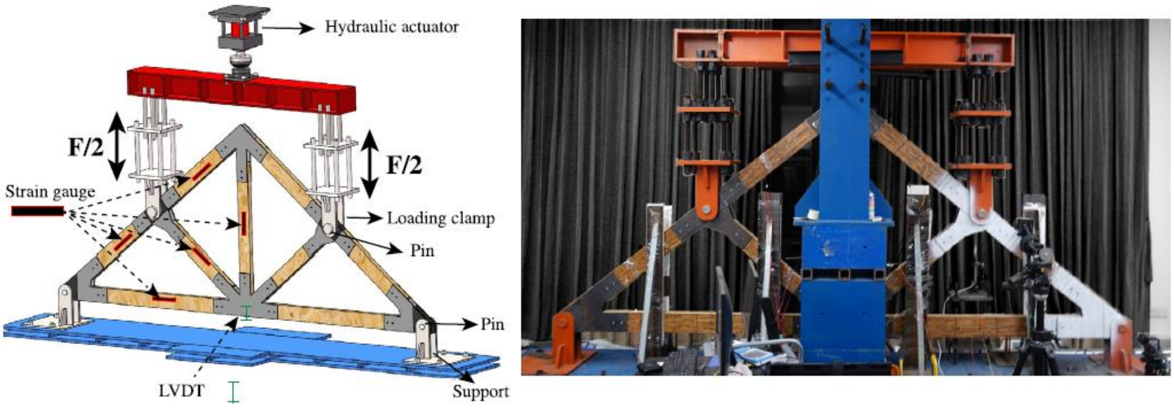

Figure 5-6 Schematic and On-site View of the Loading Setup for the Steel Side-Clamped-Plate Glubam Roof Truss

5. 4. 2 **Test Results**

Figure 5-7 presents the hysteresis curves obtained from cyclic loading tests on four groups of Steel Side-Clamped-Plate Glubam roof trusses. In terms of global response, the hysteretic characteristics of the glubam roof trusses show a high degree of consistency with the connection-level performance discussed in Section 4.3. All specimens demonstrate clear ductile behavior and notable energy dissipation capacity.

However, compared to the connection-level tests, the truss structures exhibit a more pronounced initial slip stage in their hysteresis curves, especially under compressive loading paths. This phenomenon is likely attributable to two primary factors: (1) minor assembly tolerances between the steel support and the pin connections may result in looseness at the beginning of loading, leading to observable structural slip; and (2) during compressive loading, certain components may experience slight out-of-plane displacement, which could further influence the apparent stiffness and exacerbate the initial slip behavior.

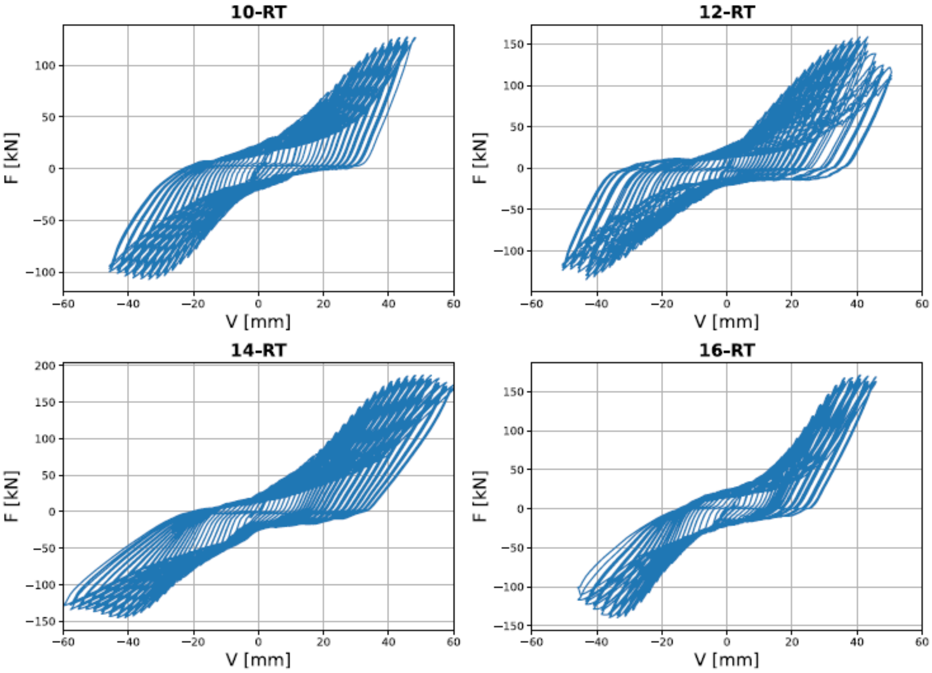

Figure 5-7 Load–Displacement Curves of Steel Side-Clamped-Plate Glubam Roof Trusses under Cyclic Loading

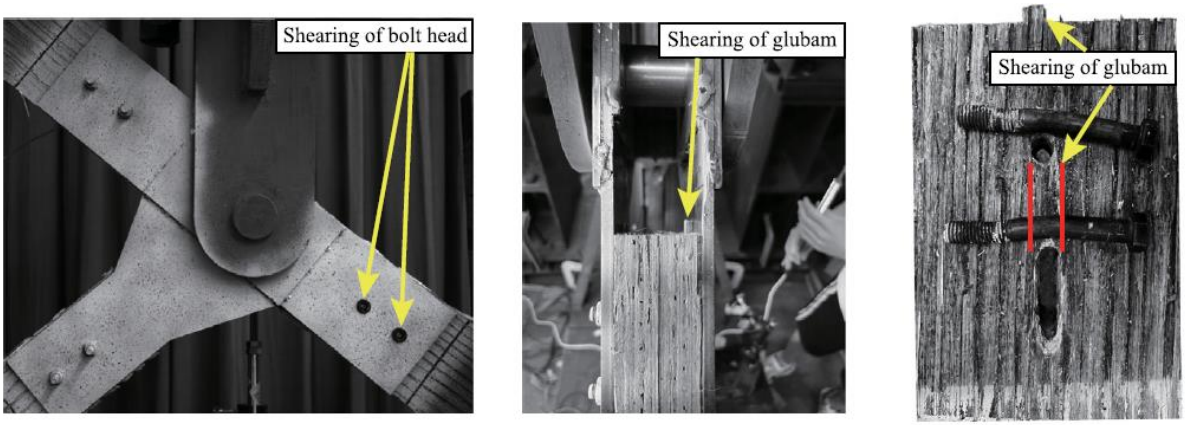

Figure 5-8 Typical Failure Modes of Steel Side-Clamped-Plate Glubam Roof Trusses under Hysteretic Loading

Figure 5-8 illustrates the failure modes observed in typical steel side-clamped-plate Glubam roof trusses during the hysteresis loading process. In nearly all test specimens, failure initiated at the upper chord region connected to the steel support. The dominant failure patterns were bolt shaft fractures and shear failure at the bolt heads. This failure location is consistent with force analysis: as primary tension and compression members, the upper chord end joints are subjected to repeated axial stress reversals during cyclic loading, leading to fatigue accumulation and localized stress concentrations that eventually trigger failure.

Overall, the failure modes observed in the full-scale roof trusses under cyclic loading align closely with those identified in the component-level tests of the steel side-clamped-plate Glubam connectors (as discussed in Chapter 4). The failures were predominantly brittle in nature, occurring in the steel bolts through fracture or shear. Throughout the tests, no significant structural degradation or instability was observed in the Glubam members themselves, indicating that failure was confined primarily to the connection zones. This result further confirms the critical role of the connector design in governing the seismic performance of Glubam truss systems; the geometry and detailing of the joints directly influence the global hysteresis behavior and overall structural reliability.

More specifically, the 10-RT specimen demonstrated the lowest load-bearing capacity, primarily due to early-stage bolt fracture. In contrast, the 12-RT, 14-RT, and 16-RT specimens exhibited different failure mechanisms, with shear failure occurring between Glubam components rather than premature bolt failure. This indicates a transition in the governing failure mode from connector-dominated to member-dominated as bolt diameter increases. Notably, the ultimate load capacities of the 12-RT, 14-RT, and 16-RT trusses were relatively close, suggesting that once the bolt diameter reaches a certain threshold, further increases have diminishing returns on structural capacity. At this point, the shear strength of the Glubam material becomes the limiting factor.

This analysis highlights the decisive influence of joint configuration on the hysteretic performance of Glubam roof trusses. Properly designing connector parameters—such as bolt number and diameter—can significantly enhance initial stiffness and load-bearing capacity while also controlling the ductility and failure mode under extreme loading scenarios such as earthquakes. Therefore, future engineering designs should prioritize optimization and performance alignment of connection joints to improve the overall seismic resilience and safety margin of engineered bamboo structural systems. Figure 5-9 presents photographs of the four Glubam truss specimens with steel side-clamped-plate connectors, visually capturing their loading states and failure patterns under different connector configurations.

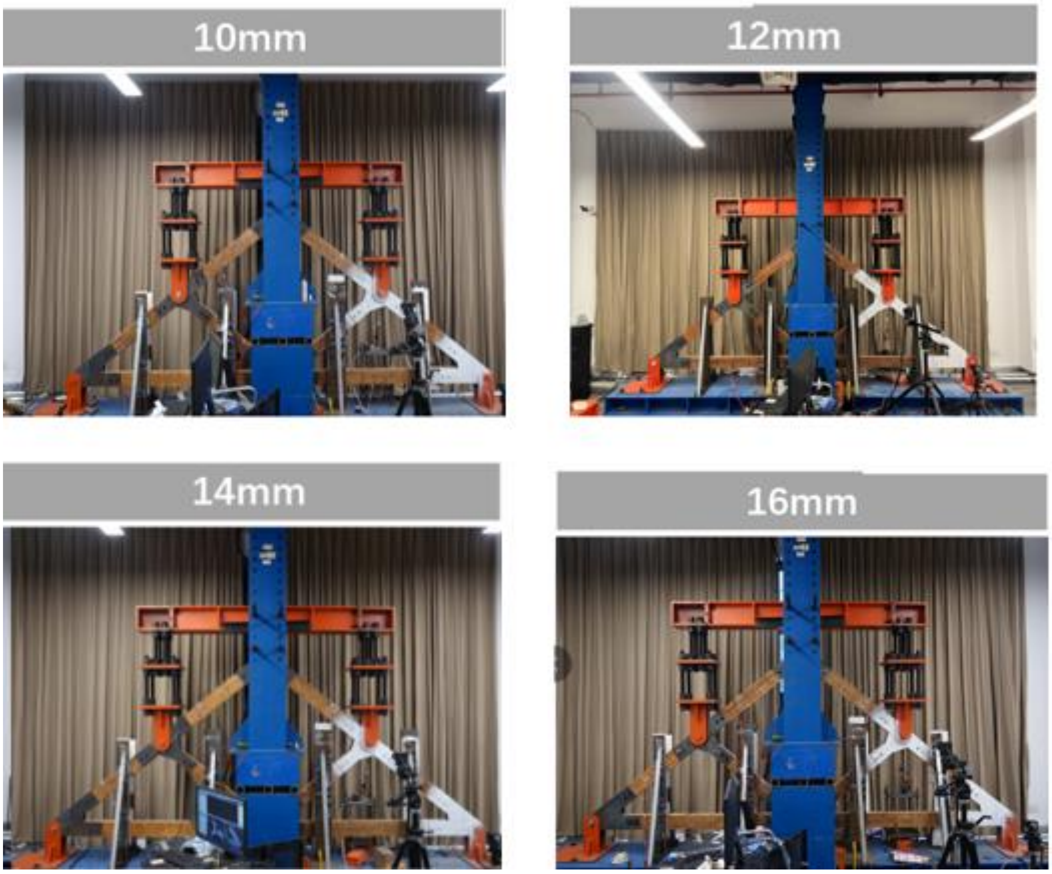

Figure 5-9 Test Setup Photographs of Steel Side-Clamped-Plate Glubam Roof Trusses

6 Numerical Simulation Study of Glubam Joints

This chapter presents a comprehensive numerical investigation into the mechanical behavior of Glubam (glue-laminated bamboo) joints. Through a multi-level modeling strategy, the study aims to reveal the load transfer mechanisms, failure modes, and key influencing factors associated with various joint configurations. Given the structural complexity of Glubam connections and the diverse loading conditions encountered in practical engineering applications, both high-fidelity and low-fidelity numerical models are developed to balance accuracy and computational efficiency, thereby supporting multiscale performance analysis of the joints.

The contents of this chapter include the development of numerical models, selection of constitutive material models, definition of boundary conditions and loading protocols, meshing strategies, and discussion of model validation and simulation results. The high-fidelity finite element (FE) models incorporate realistic joint geometries and detailed material properties to capture the nonlinear behaviors such as contact interaction between bolts and bamboo, embedment deformation of steel plates, and localized splitting of bamboo. These models are suited for detailed joint analysis and local failure mechanism studies. In contrast, the low-fidelity phenomenological models simplify mechanical assumptions to represent the joint behavior through hysteresis modeling and parameterized response expressions, providing an efficient approach for system-level analysis and design optimization.

To ensure the reliability and applicability of the models, their predictions are systematically validated against the experimental data presented in the previous chapters. The comparison confirms that the high-fidelity models effectively simulate bolt-bamboo interface slip, bolt bending, and local damage phenomena, while the low-fidelity models demonstrate good accuracy and high efficiency across multiple parametric scenarios.

In summary, the numerical simulation results presented in this chapter provide both theoretical support for seismic performance assessment and structural optimization of Glubam joints, and a solid foundation for the subsequent simulation and hybrid experimental research of Glubam truss and roof systems. Furthermore, the proposed high- and low-fidelity modeling framework and validation approach offer a generalized methodological reference for the design, analysis, and standardization of engineered bamboo structures in practice.

6.1 Numerical Simulation Study of Steel Insert-Plate Glubam Connectors

6. 1. 1 **High-Fidelity 3D Finite Element Modeling**

Bio-based construction materials such as laminated bamboo (e.g., Glubam) often exhibit pronounced delamination and crack propagation behavior due to their naturally porous and layered microstructure. When subjected to external loads, their structural connections tend to experience complex failure modes, typically dominated by crack-induced brittle fractures accompanied by localized plastic deformation. However, most existing modeling approaches for bio-based material joints either focus on the elastic stage or use simplified hysteretic models to approximate plastic behavior. These methods fail to adequately capture the coupled crack-plastic response that occurs in real connections under complex loading conditions, thus limiting their ability to predict the true mechanical performance of joint components.

To improve the accuracy and reliability of performance assessment for laminated bamboo joints, it is essential to establish a high-fidelity finite element model capable of simultaneously characterizing the nonlinear plastic behavior and crack evolution of orthotropic materials like Glubam. Integrating plastic yielding and crack propagation into a unified constitutive framework remains a key challenge in the modeling of bio-based joints and is fundamental to the development of numerical models for connection design optimization and seismic performance analysis.

This section focuses on the development of a high-fidelity finite element (FE) model for Steel Insert-Plate Glubam Connectors, aiming to provide an in-depth understanding of their nonlinear mechanical behavior and failure mechanisms through numerical simulation. The model is constructed and validated based on the experimental results presented in previous chapters to ensure its physical realism and engineering applicability.

The modeling procedure includes a detailed description of the material constitutive relationships used in the FE simulations, covering the following aspects:

1. Elastic response of Glubam: Modeled as an orthotropic material to account for directional stiffness differences.
2. Nonlinear plastic behavior: Introduced to simulate localized yielding and hysteretic effects under cyclic loading.
3. Bolt–bamboo embedment interaction: Modeled using an effective beam-on-foundation (BOF) approach to capture contact stiffness and local crushing mechanisms at the bolt interface.

4. Crack evolution: Represented through element deletion criteria to describe splitting and shear failure in the bamboo matrix.

Furthermore, the implementation of these constitutive behaviors is facilitated using ABAQUS user-defined subroutines (UMAT), where the custom material models are coded and validated through benchmark tests. The modeling workflow and simulation setup within the ABAQUS environment are also described in detail.

Before applying this model to broader studies and engineering design applications, its predictive capability must be rigorously validated. To this end, the final part of this section presents a model validation study based on comparisons between the 3D finite element model (3D FEM) predictions and experimental results, including load–displacement curves and measured strain fields.

6. 1. 1.1 Modeling of Orthotropic Elastic Behavior

As a structural engineering material, Glubam exhibits pronounced orthotropic elastic properties. The orthotropic elastic behavior primarily refers to the directional differences in the stress–strain relationships—specifically along the fiber direction, transverse direction, and through the laminated thickness. These differences arise from the anisotropic internal structure and fiber orientation inherent to the material.

Before yielding (under compression) or failure (under tension and shear), the stress–strain response of Glubam can be accurately described using a linear elastic orthotropic compliance tensor. This relationship is defined as follows:

$$\varepsilon = C^e \sigma \qquad \text{(6-1)}$$

The tensor C^e mentioned above is the fourth-order linear elastic compliance tensor for orthotropic materials. In the matrix form, C^e and its inverse D^e represent the compliance and stiffness tensors, respectively, and are commonly used for structural analysis of laminated wood or other engineered wood-based products. These materials exhibit direction-dependent mechanical properties, making such tensor representations essential for accurately capturing their behavior under loading.

The compliance matrix C^e is typically expressed using Voigt notation, which simplifies the fourth-order tensor into a 6 × 6 matrix format. This approach facilitates practical modeling of orthotropic elastic behavior in engineering applications. The components of C^e depend on the material's elastic moduli E_1、E_2、E_3 along three orthogonal directions (typically corresponding to the longitudinal, transverse, and thickness directions), the shear moduli G_{12}, G_{13}, G_{23}, and Poisson's ratios μ_{ij}, which describe the ratio of transverse strain to axial strain under uniaxial stress. The compliance matrix is given as:

$$C^e = \begin{pmatrix} \frac{1}{E_1} & \frac{-\mu_{21}}{E_2} & \frac{-\mu_{31}}{E_3} & 0 & 0 & 0 \\ \frac{-\mu_{12}}{E_1} & \frac{1}{E_2} & \frac{-\mu_{32}}{E_3} & 0 & 0 & 0 \\ \frac{-\mu_{13}}{E_1} & \frac{-\mu_{23}}{E_2} & \frac{1}{E_3} & 0 & 0 & 0 \\ 0 & 0 & 0 & \frac{1}{G_{12}} & 0 & 0 \\ 0 & 0 & 0 & 0 & \frac{1}{G_{13}} & 0 \\ 0 & 0 & 0 & 0 & 0 & \frac{1}{G_{23}} \end{pmatrix} \tag{6-2}$$

The inverse of the compliance matrix C^e is the stiffness matrix D^e, which characterizes the material's resistance to deformation under applied loads. Like the compliance matrix, the stiffness matrix is also expressed using Voigt notation as a 6×6 matrix. The derivation of the stiffness matrix from the compliance matrix involves the inversion of a system Δ defined by the interdependence between Poisson's ratios and elastic moduli, and requires calculation of the determinant of the system:

$$\Delta = 1 - \mu_{12}\mu_{21} - \mu_{23}\mu_{32} - \mu_{13}\mu_{31} - 2\mu_{21}\mu_{32}\mu_{13} \tag{6-3}$$

The fourth-order orthotropic linear elastic stiffness tensor D^e is expressed as:

$$D^e = \begin{pmatrix} \frac{E_1(1-\mu_{23}\mu_{32})}{\Delta} & \frac{E_1(\mu_{21}+\mu_{31}\mu_{23})}{\Delta} & \frac{E_1(\mu_{31}+\mu_{21}\mu_{32})}{\Delta} & 0 & 0 & 0 \\ \frac{E_2(\mu_{12}+\mu_{32}\mu_{13})}{\Delta} & \frac{E_2(1-\mu_{13}\mu_{311})}{\Delta} & \frac{E_2(\mu_{32}+\mu_{12}\mu_{31})}{\Delta} & 0 & 0 & 0 \\ \frac{E_3(\mu_{13}+\mu_{23}\mu_{12})}{\Delta} & \frac{E_3(\mu_{23}+\mu_{13}\mu_{21})}{\Delta} & \frac{E_3(1-\mu_{12}\mu_{21})}{\Delta} & 0 & 0 & 0 \\ 0 & 0 & 0 & G_{12} & 0 & 0 \\ 0 & 0 & 0 & 0 & G_{23} & 0 \\ 0 & 0 & 0 & 0 & 0 & G_{31} \end{pmatrix} \tag*{（6-3）}$$

In this constitutive model, the orthotropic axes are denoted as 1, 2, and 3, corresponding to the grain direction (X-axis), the direction perpendicular to the grain (Y-axis), and the lamination direction (Z-axis), respectively, as shown in Figure 3-1. Due to the orthotropic nature of glubam, the elastic moduli, shear moduli, and Poisson’s ratios differ along these three orthogonal directions. However, based on the symmetry of the compliance matrix C^e and D^e, the following relationships hold:

$$\frac{\mu_{12}}{E_1}=\frac{\mu_{21}}{E_2};\frac{\mu_{23}}{E_2}=\frac{\mu_{32}}{E_3};\frac{\mu_{13}}{E_1}=\frac{\mu_{31}}{E_3} \qquad (6\text{-}4)$$

Therefore, to fully characterize the linear elastic orthotropic behavior of such materials, a total of nine mechanical parameters must be determined: three elastic moduli（E_1, E_2, E_3）、three shear moduli（G_{12}, G_{13}, G_{23}）and three Poisson’s ratios（$\mu_{12}, \mu_{13}, \mu_{23}$）.

6. 1. 1.2 Orthotropic Plasticity Modeling

Glubam exhibits pronounced orthotropic plastic characteristics, with its plastic behavior varying along different material directions. Orthotropic plasticity primarily describes the differences in stress–strain response beyond the yield point along the three principal axes—typically the grain direction, the direction perpendicular to the grain, and the lamination direction.

The Hill yield criterion is widely used to characterize the plastic behavior of orthotropic materials[238,239], as it takes into account both the material anisotropy and the anisotropic nature of yielding[240]. The Hill yield criterion has been successfully applied in various research contexts, such as dowel-type connections in cross-laminated timber (CLT) [241], embedded steel rod connections[233] in timber structures, and traditional mortise-and-tenon joints in wood construction[242].

In this study, the elastic-plastic stiffness for orthotropic materials is derived based on the Hill yield criterion. The derivation is first presented in tensor form and subsequently expressed in the corresponding elastic-plastic stiffness matrix form. This systematic approach enables a comprehensive analysis of the mechanical behavior under various loading conditions, facilitating a deeper understanding of glubam’s mechanical response and enhancing the predictive capability of the numerical model.

- **Tensor Form of the Constitutive Relationship for Orthotropic Materials Based on the**

Hill Yield Criterion

For orthotropic materials, the Hill yield criterion is expressed as follows:

$$f(\sigma_{ii})=\bar{\sigma}=\sqrt{\frac{1}{2}\left[\alpha_{12}(\sigma_{11}-\sigma_{22})^2+\alpha_{23}(\sigma_{22}-\sigma_{33})^2+\alpha_{31}(\sigma_{33}-\sigma_{11})^2\right]+3\alpha_{44}\sigma_{12}^2+3\alpha_{55}\sigma_{23}^2+3\alpha_{66}\sigma_{31}^2} \qquad (6\text{-}5)$$

Where， f is the yield function； $\bar{\sigma}$ is the equivalent stress； σ_{11}， σ_{22} and σ_{33} denote the normal stresses； σ_{12} 、 σ_{23} and σ_{31} are the shear stress； α_{ii} represents an anisotropic parameter.

In practical applications, changes in strain (deformation) are typically tracked in incremental form. The total strain increment, denoted as $d\varepsilon_{ij}$, is considered to be the sum of the elastic (recoverable) strain increment, $d\varepsilon_{ij}^{e}$, and the plastic (permanent) strain increment, $d\varepsilon_{ij}^{p}$, that is:

$$d\varepsilon_{ij}=d\varepsilon_{ij}^{e}+d\varepsilon_{ij}^{p} \qquad (6\text{-}6)$$

The plastic strain components are determined by the flow rule, which relates them to the yield function as:

$$\text{follows: } d\varepsilon_{ij}^{p}=\lambda\frac{\partial f}{\partial\sigma_{ij}} \qquad (6\text{-}7)$$

Where， λ is a coefficient，can be assumed as $\lambda=hdf$ ， and is the hardening modulus. thus：

$$d\varepsilon_{ij}=d\varepsilon_{ij}^{e}+hdf\frac{\partial f}{\partial\sigma_{ij}} \qquad (6\text{-}8)$$

Stress-Strain relationship during elastic stage can be assumed as：

$$\sigma_{kl}=a_{klij}^{e}\varepsilon_{ij}^{e} \qquad (6\text{-}9)$$

Where a_{klij}^{e} is the elastic stiffness tensor.

According to Equation (6-8), it follows that:

$$a_{klij}^{e}d\varepsilon_{ij}=d\sigma_{kl}+hdfa_{klij}^{e}\frac{\partial f}{\partial\sigma_{ij}} \qquad (6\text{-}10)$$

$$\frac{\partial f}{\partial \sigma_{kl}} a_{klij}^{e} d\varepsilon_{ij} = \frac{\partial f}{\partial \sigma_{kl}} d\sigma_{kl} + hdf \frac{\partial f}{\partial \sigma_{kl}} a_{klij}^{e} \frac{\partial f}{\partial \sigma_{ij}} \tag{6-11}$$

Where：

$$df = \frac{\partial f}{\partial \sigma_{kl}} d\sigma_{kl} \tag{6-12}$$

By substituting Equation (6-12) into Equation (6-11), we obtain:

$$hdf = \frac{\frac{\partial f}{\partial \sigma_{kl}} a_{klij}^{e} d\varepsilon_{ij}}{\frac{1}{h} + \frac{\partial f}{\partial \sigma_{pq}} a_{pqrs}^{e} \frac{\partial f}{\partial \sigma_{rs}}} \tag{6-13}$$

By substituting Equation (6-13) into Equation (6-10), we obtain:

$$d\sigma_{kl} = \left(a_{klij}^{e} - \frac{a_{klfg}^{e} \frac{\partial f}{\partial \sigma_{fg}} \frac{\partial f}{\partial \sigma_{mn}} a_{mnij}^{e}}{\frac{1}{h} + \frac{\partial f}{\partial \sigma_{pq}} a_{pqrs}^{e} \frac{\partial f}{\partial \sigma_{rs}}} \right) d\varepsilon_{ij} \tag{6-14}$$

The above equation represents the constitutive relation of orthotropic materials in tensor form, where the terms within the brackets denote:

$$a_{klij} = a_{klij}^{e} - \frac{a_{klfg}^{e} \frac{\partial f}{\partial \sigma_{fg}} \frac{\partial f}{\partial \sigma_{mn}} a_{mnij}^{e}}{\frac{1}{h} + \frac{\partial f}{\partial \sigma_{pq}} a_{pqrs}^{e} \frac{\partial f}{\partial \sigma_{rs}}} \tag{6-15}$$

For hardening materials, the plastic work is defined as:

$$dW_p = \sigma_{ij} d\varepsilon_{ij}^{p} \tag{6-16}$$

By substituting Equation (6-17) and (6-5) into Equation (6-16), we obtain:

$$dW_p = \lambda \overline{\sigma} \tag{6-17}$$

On the other hand, the plastic work can also be expressed in terms of the equivalent stress and the equivalent plastic strain as:

$$dW_p = \overline{\sigma} d\overline{\varepsilon}_p \tag{6-18}$$

By combining Equations (6-17) and (6-18):

$$\lambda = d\overline{\varepsilon}_p = \frac{d\overline{\sigma}}{\overline{H}} \tag{6-19}$$

In the above equation, $\overline{H}$ represents the slope of the $\overline{\sigma} - \overline{\varepsilon}_p$ curve, which can be obtained from experimental results. It is worth noting that:

$$\lambda = hdf = hd\overline{\sigma} = \frac{d\overline{\sigma}}{\overline{H}} \tag{6-20}$$

Thus：

$$h = \frac{1}{\overline{H}} \tag{6-21}$$

In practical computations, the relationship between the equivalent stress $\overline{\sigma}$ and the equivalent strain $\overline{\varepsilon}$ is typically derived based on experimental results obtained along the principal material direction. The variations in material properties along other directions are systematically adjusted using anisotropic parameters α_{ij}. The method for determining the anisotropic parameters α_{ij} is discussed in detail in the following sections.

- **Matrix Form of the Constitutive Relationship for Orthotropic Materials Based on the Hill Yield Criterion**

In the engineering analysis of orthotropic materials, the stress vector and strain vector are expressed using Voigt notation, which is essential for defining the material response under various loading conditions. The stress vector $\{\sigma\}$ and strain vector $\{\varepsilon\}$ are given as follows:

$$\{\sigma\} = \{\sigma_{11} \quad \sigma_{22} \quad \sigma_{33} \quad \sigma_{12} \quad \sigma_{23} \quad \sigma_{31}\} \tag{6-22}$$

$$\{\varepsilon\} = \{\varepsilon_{11} \quad \varepsilon_{22} \quad \varepsilon_{33} \quad r_{12} \quad r_{23} \quad r_{31}\} \tag{6-23}$$

These equations are intended to capture the dynamic relationship between stress and strain, encompassing both the elastic and plastic behavior of the material:

$$\{d\sigma\}=\left([D]^e-\frac{[D]^e\left\{\frac{\partial f}{\partial\sigma}\right\}\left\{\frac{\partial f}{\partial\sigma}\right\}^T[D]^e}{\frac{1}{h}+\left\{\frac{\partial f}{\partial\sigma}\right\}^T D^e\left\{\frac{\partial f}{\partial\sigma}\right\}}\right)(d\varepsilon) \tag{6-24}$$

The terms D^e in the equation have already been presented in Equation (6-3). The elasto-plastic stiffness matrix $[D]$ is expressed as follows:

$$[D]=[D]^e-\frac{[D]^e\left\{\frac{\partial f}{\partial\sigma}\right\}\left\{\frac{\partial f}{\partial\sigma}\right\}^T[D]^e}{\frac{1}{h}+\left\{\frac{\partial f}{\partial\sigma}\right\}^T D^e\left\{\frac{\partial f}{\partial\sigma}\right\}} \tag{6-25}$$

The yield function is modified to account for anisotropic behavior, which is characterized by α_{ij}:

$$\left\{\frac{\partial f}{\partial\sigma}\right\}=\frac{1}{2\overline{\sigma}}\begin{bmatrix}\alpha_{11}\sigma_{11}-\alpha_{12}\sigma_{22}-\alpha_{31}\sigma_{33}\\-\alpha_{12}\sigma_{11}+\alpha_{22}\sigma_{22}-\alpha_{23}\sigma_{33}\\-\alpha_{31}\sigma_{11}-\alpha_{23}\sigma_{22}+\alpha_{33}\sigma_{33}\\6\alpha_{44}\sigma_{12}\\6\alpha_{55}\sigma_{23}\\6\alpha_{66}\sigma_{31}\end{bmatrix}=\frac{1}{2\overline{\sigma}}\{B\} \tag{6-26}$$

In the equation, B denotes the vector of partial derivatives, and $\{\phi\}$ represents the product of $[D]^e$ and $\{B\}$, given explicitly as follows:

$$[D]^e\left\{\frac{\partial f}{\partial\sigma}\right\}=[D]^e\frac{1}{2\overline{\sigma}}\{B\}=\frac{1}{2\overline{\sigma}}\{\phi\} \tag{6-27}$$

In the equation, $\overline{\sigma}$ is the effective stress at initial yielding.

In the yield function, we assume：

$$\alpha_{11}=\alpha_{12}+\alpha_{31},\alpha_{22}=\alpha_{12}+\alpha_{23},\alpha_{33}=\alpha_{23}+\alpha_{31} \tag{6-28}$$

By applying Equation (6-28) and substituting it into the elasto-plastic stiffness matrix equation, we obtain:

$$[D]^e\left\{\frac{\partial f}{\partial\sigma}\right\}=[D]^e\frac{1}{2\overline{\sigma}}\{B\}=\frac{1}{2\overline{\sigma}}\{\phi\} \tag{6-29}$$

Substituting it into the elasto-plastic stiffness matrix equation yields:

$$[D]=[D]^e-\frac{\{\phi\}\{\phi\}^T}{\{B\}^T\{\phi\}+4\overline{\sigma}^2\overline{H}} \tag{6-30}$$

Where, $\overline{H}$ represents the hardening modulus. The term $\overline{\sigma}^2\overline{H}$ contributes to adjusting the influence of material hardening behavior on the overall stiffness matrix computation.

This improved model is capable of more accurately capturing the complex interactions between stress and strain in orthotropic materials. The method for determining the anisotropic parameters α_{ij} is discussed in detail in the following sections.

- **Determination of Anisotropic Parameter**

The Hill yield criterion provides a systematic approach for determining anisotropic parameters based on the yield stresses obtained from uniaxial tension and shear tests along the principal material directions. This criterion is suitable for orthotropic materials and effectively captures their strength variations and mechanical behavior under different loading directions.

Given the effective stress at initial yielding $\overline{\sigma}_0$, which is typically selected based on the yield stress in a reference direction (e.g., when direction 1 is chosen as the reference, $\overline{\sigma}_0=\sigma_{011}$), the anisotropic parameters α_{ij} can be calculated using the experimentally measured yield stresses（σ_{0ij}）. These experimental tests measure the initial yield stress of the material under compression or shear conditions along different principal directions:

$$\begin{gathered}\alpha_{13}+\alpha_{31}=2\left(\frac{\overline{\sigma}_0}{\sigma_{011}}\right)^2,\quad \alpha_{13}+\alpha_{23}=2\left(\frac{\overline{\sigma}_0}{\sigma_{022}}\right)^2,\quad \alpha_{23}+\alpha_{31}=2\left(\frac{\overline{\sigma}_0}{\sigma_{033}}\right)^2\\ \alpha_{44}=\frac{1}{3}\left(\frac{\overline{\sigma}_0}{\sigma_{012}}\right)^2,\quad \alpha_{55}=\frac{1}{3}\left(\frac{\overline{\sigma}_0}{\sigma_{023}}\right)^2,\quad \alpha_{66}=\frac{1}{3}\left(\frac{\overline{\sigma}_0}{\sigma_{031}}\right)^2\end{gathered} \tag{6-31}$$

To derive the individual values of each α_{ij}, the corresponding equations can be solved simultaneously. This involves algebraic manipulation to isolate each term while accounting for the interactions between different directions resulting from the orthotropic nature of the material.

$$\begin{aligned}
\alpha_{12} &= \left(\frac{\overline{\sigma_0}}{\sigma_{011}}\right)^2 + \left(\frac{\overline{\sigma_0}}{\sigma_{022}}\right)^2 - \left(\frac{\overline{\sigma_0}}{\sigma_{033}}\right)^2 \quad ; \quad \alpha_{44} = \frac{1}{3}\left(\frac{\overline{\sigma_0}}{\sigma_{012}}\right)^2 \\
\alpha_{12} &= -\left(\frac{\overline{\sigma_0}}{\sigma_{011}}\right)^2 + \left(\frac{\overline{\sigma_0}}{\sigma_{022}}\right)^2 + \left(\frac{\overline{\sigma_0}}{\sigma_{033}}\right)^2 \quad ; \quad \alpha_{55} = \frac{1}{3}\left(\frac{\overline{\sigma_0}}{\sigma_{023}}\right)^2 \\
\alpha_{12} &= \left(\frac{\overline{\sigma_0}}{\sigma_{011}}\right)^2 - \left(\frac{\overline{\sigma_0}}{\sigma_{022}}\right)^2 + \left(\frac{\overline{\sigma_0}}{\sigma_{033}}\right)^2 \quad ; \quad \alpha_{66} = \frac{1}{3}\left(\frac{\overline{\sigma_0}}{\sigma_{031}}\right)^2
\end{aligned} \qquad （6\text{-}32）$$

This method provides a robust framework for calibrating the material model based on empirical data, allowing it to reflect the actual behavior of the material.

6. 1. 1.3 Fracture Behavior Modeling

Although the Hill yield criterion partially captures the softening behavior of glubam, it does not account for cracking. To address this, the present study attempts to simulate fracture behavior by removing damaged elements along potential crack paths, as illustrated in Figure 6-1[243-245]. The fracture of glubam primarily manifests as shear failure, which is a critical factor leading to connection failure[246,247]. To simulate this behavior, a user-defined material subroutine (UMAT) was implemented in ABAQUS to incorporate a damage function[246,248] defined as follows:

$$D = \left(\frac{\overline{\sigma}}{f_{t,90}}\right)^2 + \left(\frac{\overline{\tau}}{f_{v,0}}\right)^2 \qquad （6\text{-}33）$$

Where, $\overline{\sigma}$ and $\overline{\tau}$ represent the tensile stress perpendicular to the grain direction（σ_{22}） and the shear stress parallel to the grain direction （σ_{12}）, respectively. $f_{t,90}$ and $f_{v,0}$ denote the tensile strength perpendicular to the grain and the shear strength parallel to the grain, respectively. Their values can be referenced from the experimental results presented in Section 3.3 of this study.

In this study, the damage variable D from Equation (6-33) was implemented in the user subroutine. When D reaches a value of 1, the subroutine assigns a zero-stress state to the corresponding element and removes it from the mesh. The width of each removed element is approximately 0.1 mm to ensure computational convergence. The total length of the element removal zone extends from the wall of the bolt hole to the top end of the component, and the total removed area corresponds to the combined area of two shear failure planes, as shown in red in Figure 6-1. The computation terminates when the block between the two shear planes is fully sheared off.

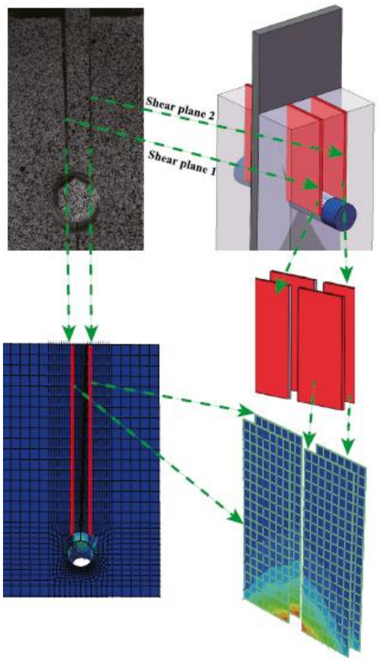

Figure 6-1 Potential Shear Fracture Zone

The element removal process is as follows:

1. Retrieve the tensile stress perpendicular to the grain direction σ_{22} and the shear stress parallel to the grain direction σ_{12} from the state variables in the ABAQUS user subroutine, and check the damage variable D.

$$D_e = \left(\frac{\sigma_{22,e}}{f_{t,90}}\right)^2 + \left(\frac{\sigma_{12,e}}{f_{v,0}}\right)^2 = 1 \qquad (6\text{-}34)$$

Where， e is the element identification number used to link the element to be checked.

2. If an element satisfies the condition defined in Equation (6-34), it is removed by setting its material properties to zero. When the ii element is removed, redundancy may occur in the Jacobian matrix, which in turn affects the tangent stiffness matrix K_T.

$$K_T = \begin{bmatrix} K_{11}^e & \cdots & K_{1i}^e & \cdots & K_{1n}^e \\ & \ddots & \vdots & & \\ K_{i1}^e & \cdots & K_{ii}^e = 0 & \cdots & K_{in}^e \\ & & \vdots & \ddots & \\ K_{n1}^e & \cdots & K_{ni}^e & \cdots & K_{nn}^e \end{bmatrix} \tag{6-35}$$

Where, n denotes the total number of elements.

3. Initiate a new step based on the updated tangent stiffness matrix of the reduced structure (i.e., by removing the rows and columns associated with the iith element), and repeat Steps 1 and 2.

- **Algorithm Design for Plasticity–Fracture Behavior**

The plasticity–fracture constitutive algorithm for glubam is outlined in Table 6-1. The process begins with inputting material parameters, including material constants, reference yield stress, anisotropic parameters, hardening function, and hardening modulus. Next, the orthotropic elastic stiffness matrix is constructed, and the total elastic stress tensor is calculated. In the following step, the equivalent stress is evaluated and substituted into the yield function to determine whether plastic deformation occurs. If plasticity is detected, the plastic strain increment is calculated based on the hardening modulus and the plastic flow rule. The stress components are then obtained to evaluate the damage function. The damage state is tracked using state variables within the ABAQUS user subroutine. If damage occurs, the state variable is set to 0, and the corresponding element is removed from the mesh. If no damage is detected, the state variable remains 1, and the stress components continue to be updated according to the standard elasto-plastic stiffness matrix. The next iteration then begins, and the computation proceeds until all elements along the target fracture planes are removed or the analysis fails to converge.

Table 6-1 Plasticity–Fracture Constitutive Model Algorithm for Glubam

```
Algorithm Workflow

Original Value: $\varepsilon_0 = 0; \varepsilon_0^p = 0; \sigma_0 = 0$
Input Material Parameters: Material Constants $\{E_1, E_2, E_3, \mu_{12}, \mu_{13}, \mu_{23}, G_{12}, G_{13}, G_{23}\}$; Reference Yielding Stress $\sigma^0$; Anisotropic Parameters $\alpha_{ij}$; Selection of a Hardening Function and Calculation of Hardening Modulus $\overline{H}$
1. Forming the Orthotropic Elastic Stiffness Matrix and Calculating the Total Elastic Stress Tensor Based on Equation (6-3). $\sigma_{j+1} = \sigma_j + [D]^e \Delta\varepsilon$
2. Calculation of Stress Components, Deviatoric Stress, and Equivalent Stress Based on Equation (6-5). $\overline{\sigma}$
3.Plasticity Verification:
    3.1 Evaluation of the Yield Function (6-5) $\rightarrow f(\sigma_{ii}) = \overline{\sigma} \le 0$?
    3.2 Yes $\rightarrow$ NO Plasticity
        $\Delta\varepsilon_0^p = 0$
    3.3 No $\rightarrow$ Plasticity Algorithm
        3.3.1 According to hardening modulus $\overline{H}$ and flow rule, calculating $d\overline{\varepsilon}_{pl}$
            $d\overline{\varepsilon}_{ij}^p = \frac{df}{\overline{\overline{H}}} \frac{\partial f}{\partial \sigma_{ij}}$
        3.3.2 Obtain Equivalent Plastic Strain $\overline{\varepsilon}_{pl}$ and store $\overline{\varepsilon}_{pl}$ in the state variables 1 → STATEV(1)
            $\overline{\varepsilon}_{pl} = \overline{\varepsilon}_{pl} + d\overline{\varepsilon}_{pl}$
4.Damage Verification
    4.1 Obtain the stress components and evaluate the damage function.
        Eq. (6-34) $\rightarrow D = \left(\frac{\overline{\sigma}}{f_{t,90}}\right)^2 + \left(\frac{\overline{\tau}}{f_{v,0}}\right)^2 \le 1$?
    4.2 Yes $\rightarrow$ No Damage
        4.2.1 According to Eq. (6-30), Calculating the elasto-plastic stiffness matrix. $[D]$。
        4.2.2 Update the stress components
            $\{\sigma_{ij}\} = \{\sigma_{ij}\} + [D]\{d\varepsilon_{ij}\}$
        4.2.3 Update the state variables 2 $\rightarrow$ STATEV(2)        STATEV(2) = 1
    4.3 No $\rightarrow$ Damage Algorithm
        4.3.1 Set the elasto-plastic stiffness matrix to zero. $[D] = 0$
        4.3.2 Update state variable 2 $\rightarrow$ STATEV(2)        STATEV(2) = 0
5. Next iteration
```

- **Experimental Validation of the Plasticity–Fracture Constitutive Law**

Figure 6-2 compares the experimental results from a typical embedment test with the finite element simulation results based on the proposed constitutive model. The constitutive behavior of the glubam material was implemented via a user-defined subroutine, with specific parameter settings detailed in Table 6-1. The model incorporates both the Hill yield criterion and an element removal scheme to simulate the anisotropic yielding behavior and brittle fracture process of the material.

The simulation results demonstrate that the model effectively reproduces the crack propagation paths observed during the experiment. The predicted fracture trajectory shows a high degree of consistency with the actual failure patterns captured in test photographs. Furthermore, the simulated load–embedment displacement response curve exhibits a distinct softening phase, reflecting the progressive reduction in stiffness caused by the sequential removal of failed elements. This behavior closely corresponds to the localized crushing and splitting failure observed experimentally, further validating the model's accuracy in capturing the embedment failure mechanisms of glubam (see Shi et al.[249] for additional details related to the model).

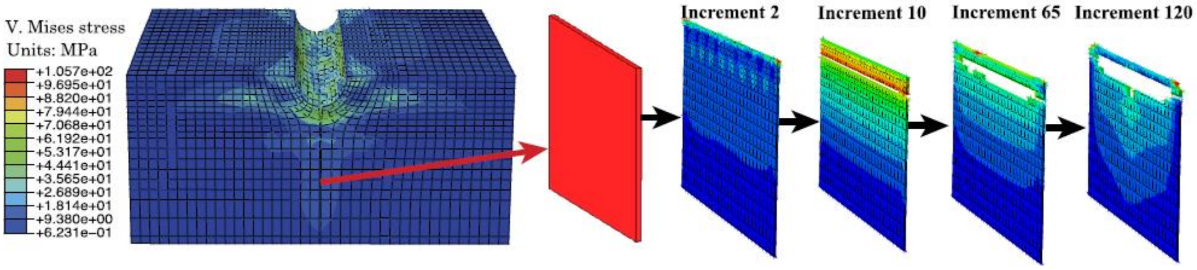

Figure 6-2 Evolution of Element States Along the Prescribed Crack Plane During Fracture Propagation in the Finite Element Model of the Bolt-Hole Embedment Test

6. 1. 1.4 Effective Foundation Model Properties for the Embedment Zone

In this study, the wood foundation model was applied to bamboo elements in the embedment zone (i.e., the region near the bolt, shown as the yellow area in Figure 6-4) to capture the localized crushing behavior caused by embedment compression. In this model, material hardening is accounted for using a bilinear fit of the performance curve obtained from bolt-hole bearing tests (as shown in previous studies[249]), illustrated in Figure 6-3.

Following the analytical approach proposed by Hong and Barrett[250], the constitutive behavior of glubam within the embedment zone is determined based on the fitted results of the bolt-

]

hole bearing tests. The foundation modulus and foundation yield point are defined from the load–embedment displacement curve of the bearing test.

From the bilinear fitted curve, the initial slope and the breakpoint between the two linear regions are identified. The nominal foundation modulus and the nominal yield point can then be calculated as follows:

$$k = \frac{P_y}{W_y} \tag{6-36}$$

Where k is the nominal foundation modulus（MPa）, P_y is the yield load per unit length（N/mm）from the bilinear load-per-length vs. embedment displacement curve, W_y is the corresponding yield displacement (mm) from the same curve.

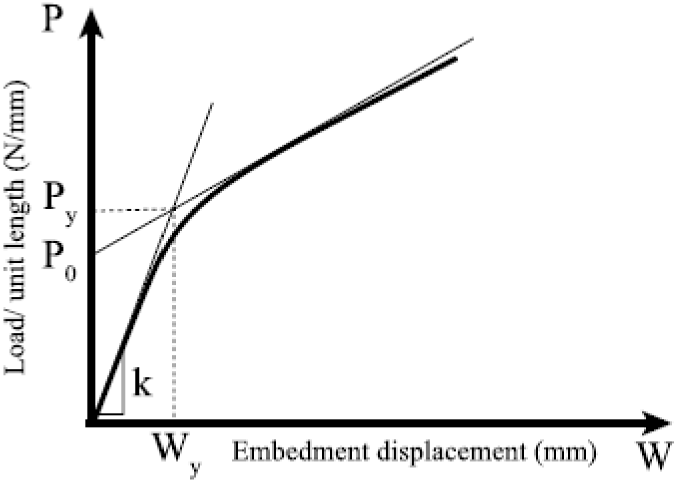

Figure 6-3 Bilinear Backbone Curve Fitted to Bolt-Hole Embedment Test Data

In the bamboo foundation model, the nominal foundation modulus （$E_{1,F}$）along the grain direction is determined based on the experimental results described above. The effective foundation moduli in other directions ($E_{2,F}$, $E_{3,f}$, etc.) are then derived through proportional transformation, based on the same ratio between the foundation modulus and the elastic modulus in the corresponding directions, as follows:

$$\frac{E_{1,F}}{E_1} = \frac{E_{2,F}}{E_2} = \frac{E_{3,F}}{E_3} \tag{6-37}$$

In the bamboo foundation model, Poisson's ratios ($\mu_{12,F}$, $\mu_{13,F}$, etc.) are assumed to be the same as those used in the standard material properties. The final parameters of the bamboo foundation model can be found in previous studies. Compared to the elastic constants obtained directly from conventional material tests, the elastic constants in the three orthogonal directions within the foundation model are significantly reduced. This is consistent with the method proposed by Hong and Barrett[250], who employed effective (i.e., reduced) foundation properties—representing the material surrounding the bolt—to better match the observed stiffness in experimental results.

6. 1. 1.5 High-Fidelity 3D Finite Element Simulation of the Axial Behavior of Steel Insert-Plate Glubam Connectors

- **Finite Element Implementation**

Figure 6-5 illustrates the three-dimensional finite element model (3D FEM) of the steel insert-plate glubam bolted connection, developed using ABAQUS. The model consists of three main components: the steel insert plates, bolts, and glubam blocks. All geometric dimensions were modeled strictly according to the actual dimensions of the physical specimens to ensure the accuracy and comparability of the simulation results.

During the modeling process, all components were discretized using eight-node linear brick elements (C3D8) in ABAQUS, allowing for high modeling precision and accurate mechanical response representation. The steel plates and bolts were modeled as isotropic elastic–perfectly plastic materials. The material parameters were assigned based on the properties of Q345 steel: a modulus of elasticity (MOE) of 210 GPa, Poisson’s ratio of 0.3, and a yield stress of 345 MPa for the steel plates.

For the bolts, mechanical properties were assigned based on their actual diameters—8 mm and 10 mm. The yield stresses were set to 721.52 MPa and 823.98 MPa, respectively, to reflect the performance differences between bolts of different specifications under load.

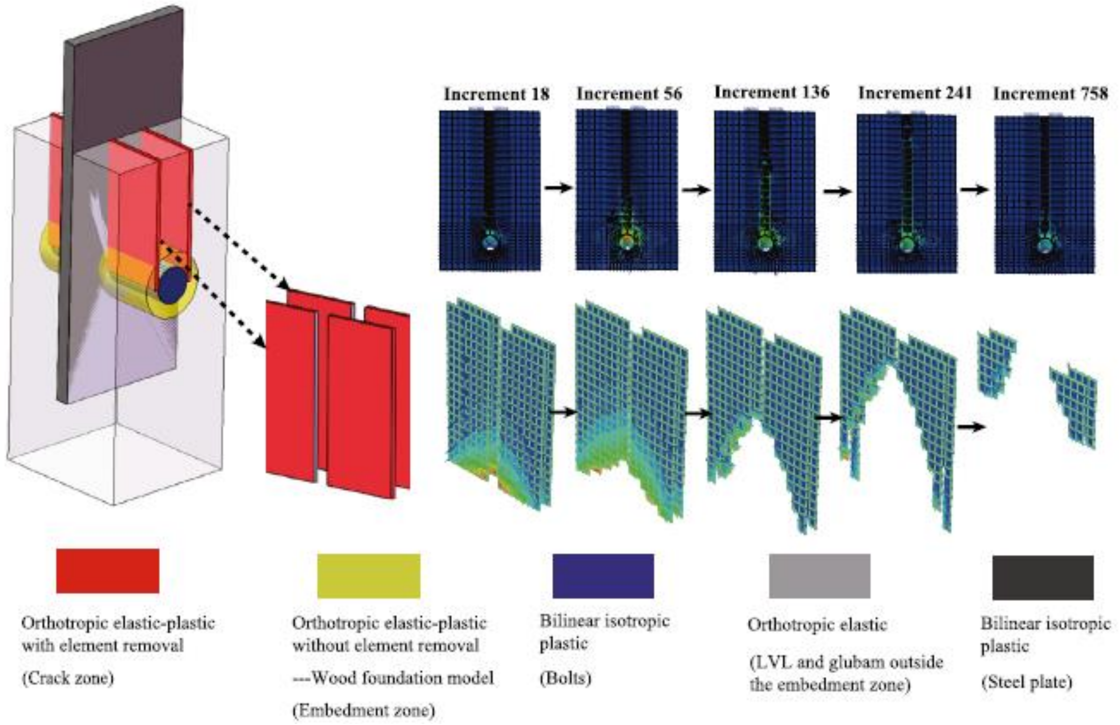

Figure 6-4 Material Constitutive Assignment and Element State Evolution Along the Prescribed Crack Plane in the G-M-S10 Finite Element Model

Previous studies have shown that the constitutive law assigned to elements outside the embedment zone (gray area in Figure 6-4) has a negligible effect on the overall response of the model, while the constitutive behavior of elements within the embedment zone (red area in Figure 6-4) plays a dominant role. As a result, different material properties were assigned to elements in the glubam block depending on their location—whether outside the embedment zone, within the embedment zone, or in the fracture region. The material partitioning of the glubam block is illustrated in Figure 6-4. Elements outside the embedment zone (gray area) were assumed to follow an orthotropic linear elastic material law. The elastic moduli used were determined from compression tests on prismatic specimens (refer to Shi et al.[249]). These regions were meshed using adaptive grid refinement, with an average mesh size of approximately 3 mm. For the embedment zone, elements were assigned an orthotropic elasto-plastic constitutive model governed by the Hill yield criterion. The Hill yield function was implemented directly through the ABAQUS user interface by inputting the corresponding anisotropic yield parameters, without the need for a user subroutine. The material properties in this region were consistent with those defined in the effective foundation model (see Section 6.1.1.4).

In the fracture region (red area in Figure 6-4), elements were modeled using the orthotropic elasto-plastic constitutive law with the Hill yield criterion, combined with an element deletion criterion. Both the Hill yield criterion and the element removal scheme in this region were implemented via a user-defined subroutine. The fracture region was assigned a thickness of 0.1 mm, with an average mesh size of about 3 mm. The material parameters for glubam were based on experimental results reported in Shi et al[249].

All contact surfaces were defined with hard contact interaction properties. The Coulomb friction coefficient for all interfaces was set to 0.5. Additionally, to simulate the initial slip stage[252] caused by bolt–wood clearance at the bolt holes, a clearance tolerance of 0.5 mm was specified between the bolt and the surrounding wood elements in the ABAQUS model.

- **High-Fidelity Numerical Simulation Results and Experimental Validation**

This subsection compares the experimental results and numerical simulation outcomes for the steel insert-plate glubam connectors under monotonic tensile loading and cyclic loading.

Figure 6-5 presents the simulated failure mode of a typical specimen obtained through finite element modeling (FEM). The results clearly show the characteristic shear-off failure pattern, consistent with the experimentally observed behavior. Figure 6-4 illustrates a comparison of element states along the predefined crack plane during fracture propagation. It can be observed that the elements gradually disappear along the crack plane, ultimately forming the complete fracture path.

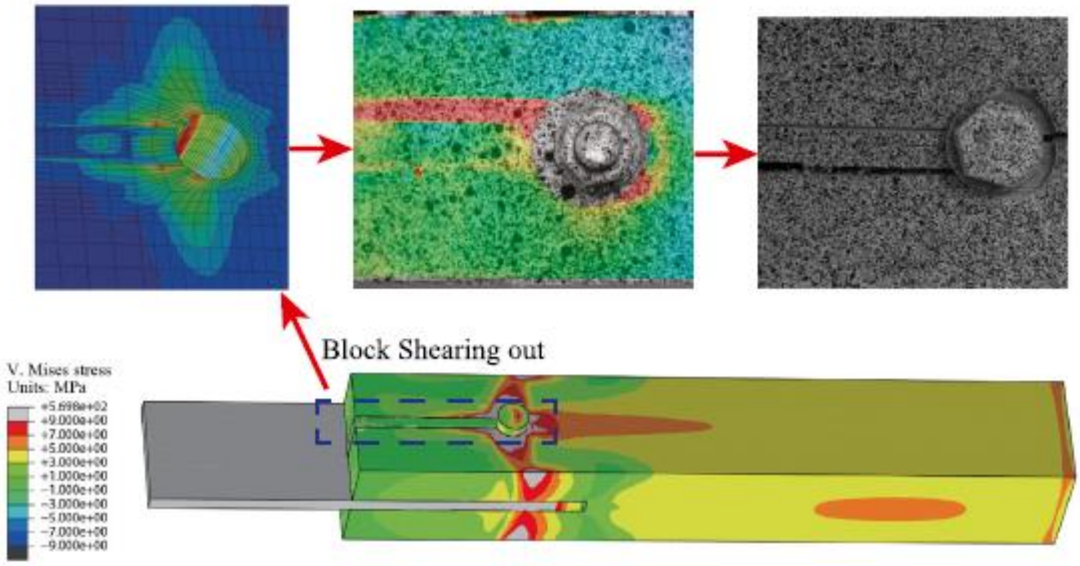

Figure 6-5 Comparison Between Experimental Failure Mode and High-Fidelity 3D Finite Element Simulated Failure Mode

As shown in Figure 6-6, the proposed plasticity–fracture coupled constitutive model is capable of accurately simulating the stiffness degradation observed in the monotonic loading tests. It successfully reproduces the full failure process of the connector following the peak load plateau. The model's predictions for both the peak load and ultimate displacement agree well with the experimental data, validating its applicability and reliability in static nonlinear analyses.

Furthermore, Figure 6-7 presents a comparison between the experimental and numerical results for various specimens under cyclic loading. It can be observed that the plasticity–fracture model realistically captures the key mechanical features of the hysteretic response, including the envelope behavior of the backbone curve, pinching effects, stiffness degradation, and strength degradation. The overall shape and detailed local response of the hysteresis loops predicted by the simulation show good agreement with the experimental results.

In summary, the finite element model developed in this study demonstrates strong simulation capability under both monotonic and cyclic loading conditions. It effectively predicts the nonlinear mechanical behavior of glubam steel insert-plate bolted connectors under different loading scenarios.

To quantitatively assess the predictive accuracy of the finite element model, the Relative Root Mean Square Error (RRMSE) is used to compare the predicted response with the experimental response. RRMSE provides a measure of error between two signals, **a** (tested values) and **b** (predicted values), and is defined as:

$$RRMSE(a,b)=\frac{\sqrt{\left[\frac{1}{N_s}\sum_{i=1}^{N_s}\left(a_i-b_i\right)^2\right]}}{\sqrt{\left[\frac{1}{N_s}\sum_{i=1}^{N_s}\left(a_i\right)^2\right]}}\times 100\left(\%\right) \qquad （6\text{-}38）$$

Where N_s represents the total number of data samples in the signal.

Table 6-2 presents the calculated Relative Root Mean Square Error (RRMSE) values between the finite element model predictions and the actual (experimental) responses, as defined by Equation (6-38). For monotonic loading responses, the RRMSE remains below 15%, while for hysteretic responses, it remains below 20%. These results confirm the effectiveness and reliability of the finite element model proposed in this study.

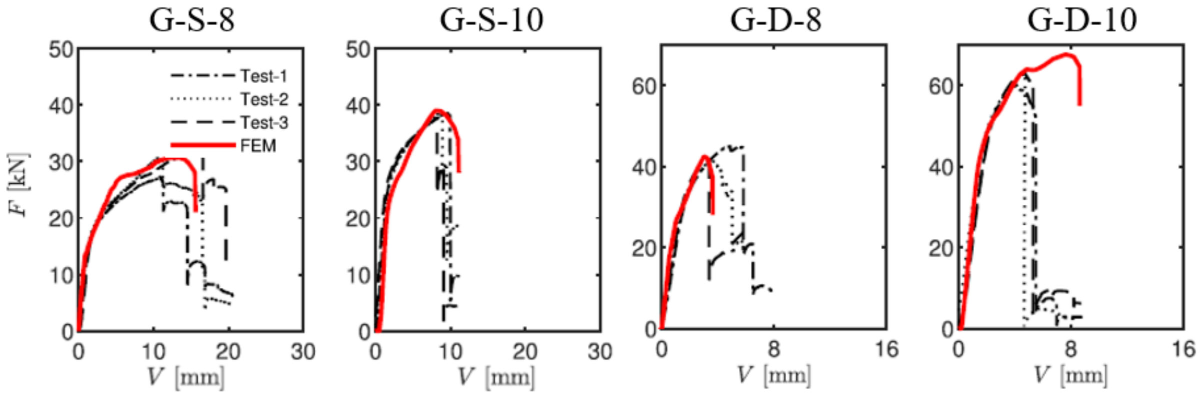

Figure 6-6 Comparison of Load (F)–Displacement (V) Results from Finite Element Analysis and Experimental Tests under Monotonic Loading

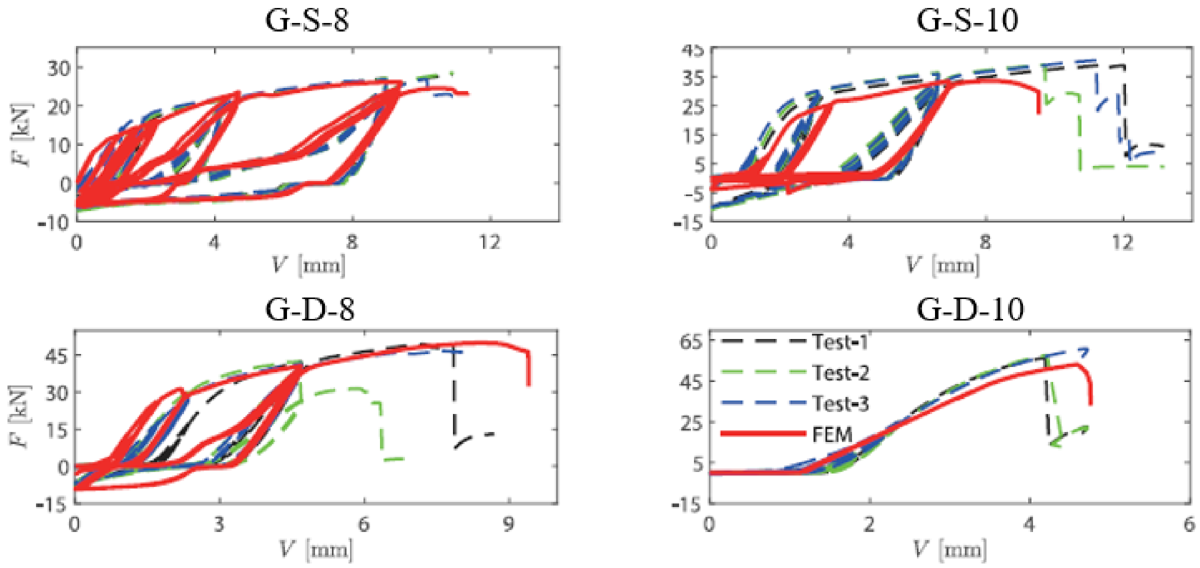

Figure 6-7 Comparison of Load–Displacement Results from Finite Element Analysis and Experimental Tests under Cyclic Loading

Table 6-2 Relative Root Mean Square Error (RRMSE) Between Test Results and Finite Element Predictions

Specimen	Monotonic Response				Hysteresis response			
	G-S-8	G-S-10	G-D-8	G-D-10	G-S-8	G-S-10	G-D-8	G-D-10
	14.68%	7.62%	14.48%	9.92%	19.41%	16.95%	11.57%	13.35%

6. 1. 2 **Low-Fidelity Simplified Numerical Simulation**

As previously mentioned, existing phenomenological hysteresis models face significant limitations in fully capturing the complex nonlinear behavior exhibited by steel insert-plate glubam connectors under cyclic loading—particularly with respect to pinching effects, stiffness degradation, strength deterioration, and diverse failure modes. These limitations hinder a deeper understanding of the mechanical mechanisms of such connectors and impede improvements in engineering design reliability.

To address this, a simplified numerical hysteresis model was developed in this study, based on experimental observations, to simulate the cyclic response of steel insert-plate glubam joints. The model was implemented using the open-source platform OpenSeesPy, which offers flexible material modeling capabilities and strong support for secondary development, making it well-suited for nonlinear structural analysis and hysteretic behavior research.

The core concept of the simplified model assumes that all nonlinear deformation and energy dissipation are concentrated at specific locations within the connection region, while the remaining parts of the connector respond approximately elastically. To implement this concept, a multi-node overlap technique was used, in which multiple coincident nodes were placed at designated positions and connected by several groups of ZeroLength elements arranged in series or parallel to construct an interface with equivalent nonlinear behavior.

As shown in Figure 6-8, the proposed model primarily consists of two types of uniaxial nonlinear material elements: Pinching4 elements and elastic–perfectly plastic gap elements. The elastic–perfectly plastic gap elements are used to simulate the initial slip behavior of the connector, reflecting the “zero-stiffness” response caused by clearance and looseness in the early loading stage. The Pinching4 elements simulate the overall nonlinear hysteretic response of the connection, effectively reproducing key features such as pinching, strength degradation, stiffness degradation, and asymmetry in the hysteresis loops.

The Pinching4 material model is constructed using a piecewise linear backbone curve and includes rules[32,220,253] for simulating pinching effects as well as degradation in stiffness and strength. The model is defined by 38 parameters, as listed in Table 6-3, and its hysteresis rules during cyclic loading are illustrated in Figure 6-8(b). It is worth noting that although the Pinching4 model can represent most hysteretic characteristics, the initial slip behavior arising from construction gaps also plays a significant role in the overall mechanical performance of the steel insert-plate glubam connectors.

To simulate this slip behavior, this study adopts the modeling method proposed by He et al.[24], incorporating an idealized elastic–perfectly plastic gap-type uniaxial element (Gap Element) as the constitutive element in the numerical model. Key features of this element include an initial gap value, elastic stiffness, and a yield stress threshold. Specifically, before the deformation reaches the set gap value (in either tension or compression), the element remains in a zero-stiffness state and generates no axial force. Once the deformation exceeds the gap, the element enters a linear elastic phase up to the yield stress, after which it exhibits ideal perfectly plastic behavior. This gap model effectively captures the initial sliding phase observed during cyclic loading of the connectors, which is caused by manufacturing tolerances, looseness, and early contact surface deformation.

Subsequent sections will detail the modeling process, parameter definitions, and numerical implementation for both tensile and compressive loading paths. Through the development and validation of this simplified numerical model, the study achieves a relatively accurate simulation of the mechanical response of steel insert-plate glubam connectors under cyclic loading, particularly in capturing critical features such as initial slip, yielding transitions, and energy dissipation.

Table 6-3 Parameters of the Pinching4 Material Model in OpenSeesPy

Parameter	Description
$ePf_1, ePf_2, ePf_3, ePf_4$	denotes the force points on the positive response envelope
$ePd_1, ePd_2, ePd_3, ePd_4$	denotes the displacement points on the positive response envelope
$eNf_1, eNf_2, eNf_3, eNf_4$	denotes the force points on the negative response envelope
$eNd_1, eNd_2, eNd_3, eNd_4$	denotes the displacement points on the negative response envelope
$gK_1, gK_2, gK_3, gK_4, gK_{\lim}$	controls cyclic degradation model for unloading stiffness degradation
$gD_1, gD_2, gD_3, gD_4, gD_{\lim}$	controls cyclic degradation model for reloading stiffness degradation
$gF_1, gF_2, gF_3, gF_4, gF_{\lim}$	controls cyclic degradation model for strength degradation
$rDispP, rDispN$	denotes the ratio of the deformation at which reloading occurs to the max/min historic deformation demand
$fForceP, fForceN$	denotes the ratio of the deformation at which reloading occurs to the max/min historic deformation demand
$\mu ForceP, \mu ForceN$	denotes the ratio of strength developed upon unloading from negative load to the max/min strength developed under monotonic loading
gE	denotes maximum energy dissipation

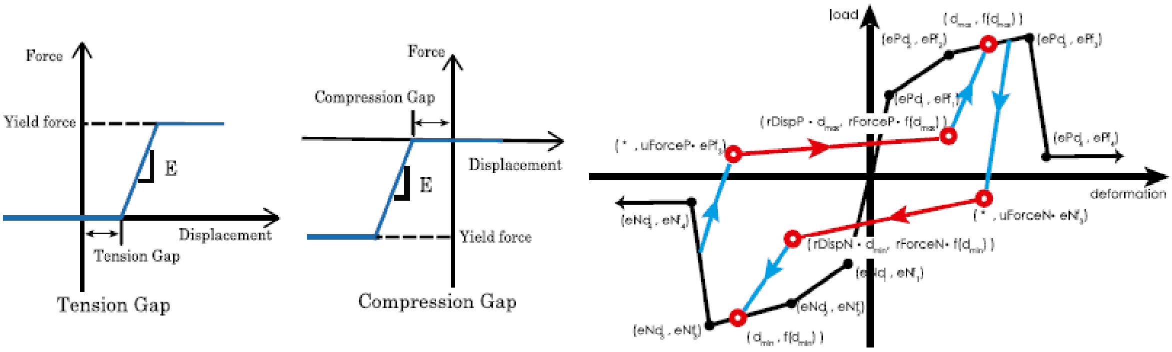

(a) (b)

Figure 6-8 Constitutive Laws of the Elastic–Perfectly Plastic Gap Element (a) and Pinching4 Element (b)

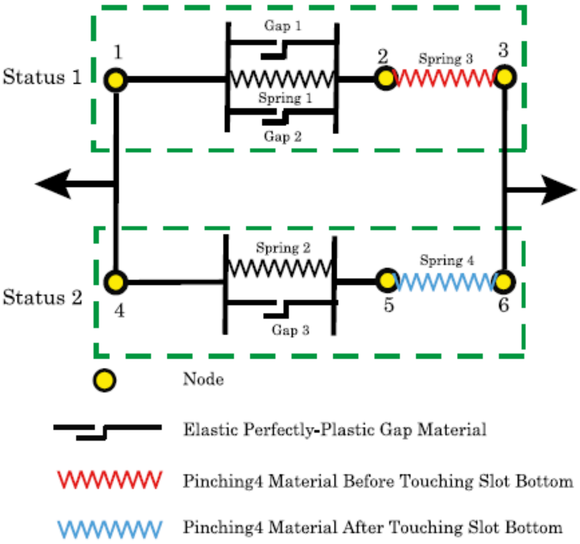

Figure 6-9 Simplified Numerical Model of Steel Insert-Plate Glubam Connectors under Bidirectional Tension–Compression Loading

Under tension–compression cyclic loading, the steel insert-plate glubam bolted connection exhibits pronounced nonlinear hysteretic characteristics. As shown in Figure 6-9, its mechanical response can be divided into two typical stages. The first stage is the initial loading stage, during which the axial displacement of the steel insert-plate under compressive load is relatively small and does not yet make contact with the bottom of the glubam groove. At this point, the bolt bears the majority of the load, and the connection exhibits an initial sliding behavior and a nonlinear response prior to contact. The second stage is the contact stage. As the displacement continues to increase, the steel insert-plate begins to contact the bottom of the groove, and the glubam material in the contact region starts to bear additional compressive stress, forming a multi-path load transfer mechanism. This leads to a pronounced contact-induced stiffness hardening effect. The mechanical response during this stage becomes significantly more complex and is accompanied by strongly nonlinear behavior, such as strength degradation, stiffness degradation, and hysteretic pinching.

To comprehensively simulate the characteristic mechanical behavior of the connector in these two stages, this study proposes two hysteresis models corresponding to the load transfer mechanisms in the initial and contact stages, respectively. These two sub-models are coupled in parallel to construct a unified composite model capable of capturing the complex hysteretic behavior of the steel insert-plate glubam bolted connection. Each sub-model consists of a combination of Pinching4 hysteretic material elements and ideal elastic–perfectly plastic gap elements, arranged through appropriate series–parallel configurations.

The constitutive model used for Gap1, Gap2, and Gap3 is the ideal elastic–perfectly plastic gap material model (as illustrated in Figure 6-9). Specifically, Gap1 is assigned to the tension direction, while Gap2 and Gap3 are assigned to the compression direction. Gap1 and Gap2 are configured to simulate the initial slip behavior, which may result from manufacturing tolerances or built-in slack in the design and can occur in both forward and reverse directions. Gap3 simulates the zero-stiffness behavior observed in Stage II (see Figure 6-10), which corresponds to the phase before the steel plate contacts the groove bottom. To prevent significant deformation after the slip phase (i.e., to ensure quasi-rigid behavior), the elastic modulus EEE of the gap elements is set to a relatively high value.

For the hysteretic components, Spring3 and Spring4 adopt the Pinching4 material model to simulate the overall nonlinear hysteretic behavior observed in each stage. In addition, two low-stiffness elastic spring elements (Spring1 and Spring2) are placed in parallel with Gap1 and Gap2 to improve convergence during the sliding phase, without significantly influencing the nonlinear response.

To better interpret the contributions of each stage, Figure 6-10 presents the simulated cyclic response of specimen G-D-8 under bidirectional loading. Specifically, Figures 6-10(a) and 6-10(b) show the responses corresponding to Stage I and Stage II, respectively, while Figure 6-10(c) illustrates the combined response obtained by superimposing the two. As shown in Figure 6-10(c), the combined simulation results exhibit strong agreement with the experimental data. This demonstrates that the final composite hysteretic model can accurately reproduce the nonlinear cyclic behavior of the steel insert-plate glubam connection under both tension and compression. The model not only enhances our understanding of the mechanical response of such connectors but also provides a robust foundation for future modeling efforts at the structural system level.

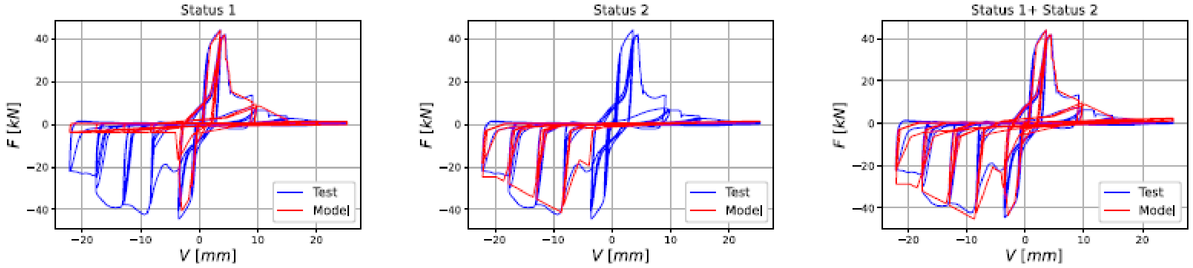

(a) (b) (c)

Figure 6-10 Simulated bidirectional load response of specimen G-D-8: Stage 1 response (a) and Stage 2 response (b); combined overall response obtained by paralleling the two stages (c).

6. 1. 2. 1 Low-Fidelity Numerical Model Simulation Results and Experimental Validation

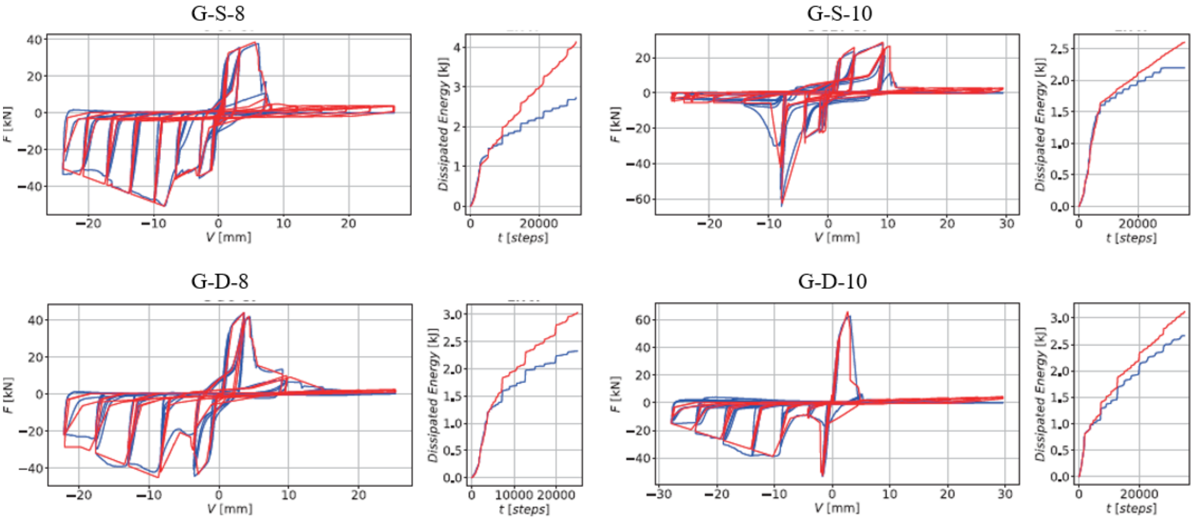

Figure 6-11 Comparison of hysteresis curves and energy dissipation between model simulation results (red lines) and experimental results (blue lines).

This section aims to briefly report the predictive results of the low-fidelity numerical model. It should be noted that the simulation results presented here are primarily based on model parameters identified and calibrated using an artificial intelligence optimization algorithm, which will be detailed in subsequent chapters. Therefore, the specific procedures for parameter identification, the principles of the optimization algorithm, and its implementation process will be systematically discussed later and are not repeated here.

As shown in Figure 6-11, a comparison between the predicted curves of the numerical model and the corresponding experimental data reveals that the proposed simplified model demonstrates good accuracy in capturing the hysteretic response of the steel insert-plate glubam connectors. In particular, it shows high consistency with the experimental results in terms of the shape of the hysteresis envelope, the trend of stiffness degradation, and the energy dissipation capacity. These results indicate that the simplified model not only achieves acceptable engineering-level accuracy but also offers significant advantages in computational efficiency, making it well-suited for rapid response analysis and performance evaluation at the structural system level.

Based on these validation results, it can be preliminarily concluded that the low-fidelity model possesses strong engineering applicability and potential for broader adoption. In future studies, this model will be further integrated into the mechanical analysis framework of macro-scale structural systems, to simulate the overall seismic response of glubam truss structures under complex loading conditions such as earthquakes. This will provide a simplified yet efficient modeling tool for engineering design and performance-based seismic analysis.

6.2 Numerical Simulation Study of Steel Side-Clamped-plate Glubam Connectors

6. 2. 1 **High-Fidelity 3D Finite Element Simulation**

This section mainly introduces the high-fidelity finite element modeling method for Steel Side-Clamped-plate Glubam Connectors and presents a validation analysis of the model based on experimental data. Since the material constitutive modeling used in this finite element model is essentially consistent with that adopted in Section 6.1.1 for the high-fidelity model of Steel Insert-plate Glubam Connectors—including elastic behavior, plastic behavior, and an effective base material model considering bolt embedding effects—related modeling details will not be repeated here.

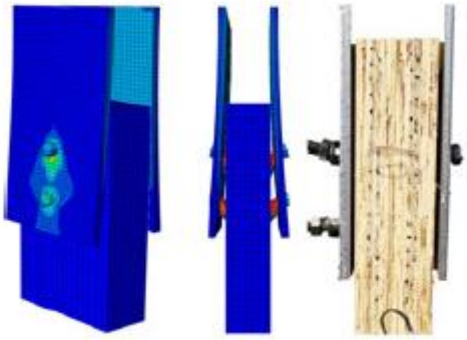

Figure 6-12 3D Finite Element Model and Test Specimen of Steel Side-Clamped-plate Glubam Connector

However, when the material property parameters obtained directly from experiments were used for model calculations, the preliminary simulation results exhibited significant response variability, resulting in a relatively poor model fit. To address this issue, and differing from the modeling approach used for the steel insert-plate connectors, this section introduces a Monte Carlo stochastic simulation method for the high-fidelity numerical analysis of the Steel Side-Clamped-plate Glubam Connectors. Specifically, instead of assigning a single deterministic value to each key material parameter, a reasonable range of distribution is defined, within which random sampling is conducted. Each set of sampled parameters is then used in the 3D finite element model for simulation analysis, thereby more realistically reflecting the influence of material property uncertainties on the connection's response behavior.

In terms of computational implementation, the finite element models are solved using a parallel multi-threading strategy. Each simulation task runs in parallel on two CPU cores, based on a 15-thread computation framework. This strategy significantly improves simulation efficiency and greatly reduces the computation time required for large-sample Monte Carlo simulations, thus enabling a systematic evaluation of the response variability of the connectors induced by fluctuations in material properties. A total of 600 parameter samples and numerical simulations were conducted in this study, ultimately yielding 600 sets of finite element simulation results.

Figure 6-12 presents the detailed 3D finite element model of the Steel Side-Clamped-plate Glubam Connector along with a photograph of the corresponding test specimen. From the perspectives of geometric configuration, connection structure, and boundary conditions, it can be seen that the finite element model provides an accurate geometric representation of the actual specimen.

Figure 6-13 compares the axial response results under monotonic tensile loading from the 600 finite element simulations with the corresponding experimental data. The results indicate that the numerical model is capable of accurately capturing the stiffness variation, ultimate load-bearing capacity, and failure trend exhibited during the loading process, thereby fully validating the model’s effectiveness and reliability in representing the true mechanical behavior of the connector.

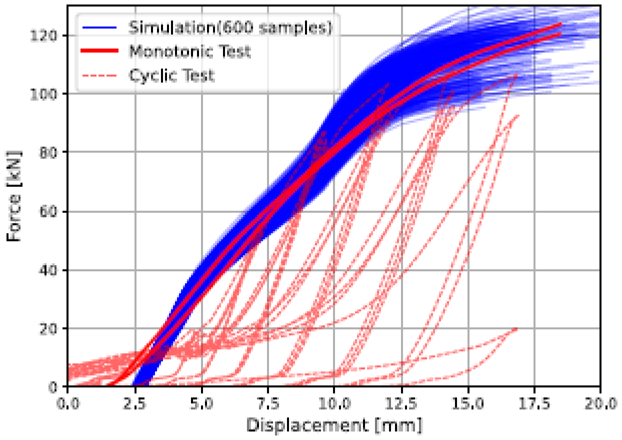

Figure 6-13 Comparison of Axial Responses between 600 Finite Element Models of Glubam Connectors under Monotonic Loading and Experimental Results

In addition, Figure 6-14 presents the stress distribution contour plots of both the glubam component and the bolt component during the loading process, extracted from three representative finite element model samples. By examining the distribution and evolution of stress concentration regions, the model's predictive capabilities regarding the bolt–bamboo contact interface embedding effects, stress redistribution in the joint region, and potential failure paths are further substantiated.

Comprehensive analysis indicates that the developed 3D finite element model of the Steel Side-Clamped-plate Glubam Connector is capable of effectively capturing the typical nonlinear mechanical behavior of this type of joint under actual loading conditions.

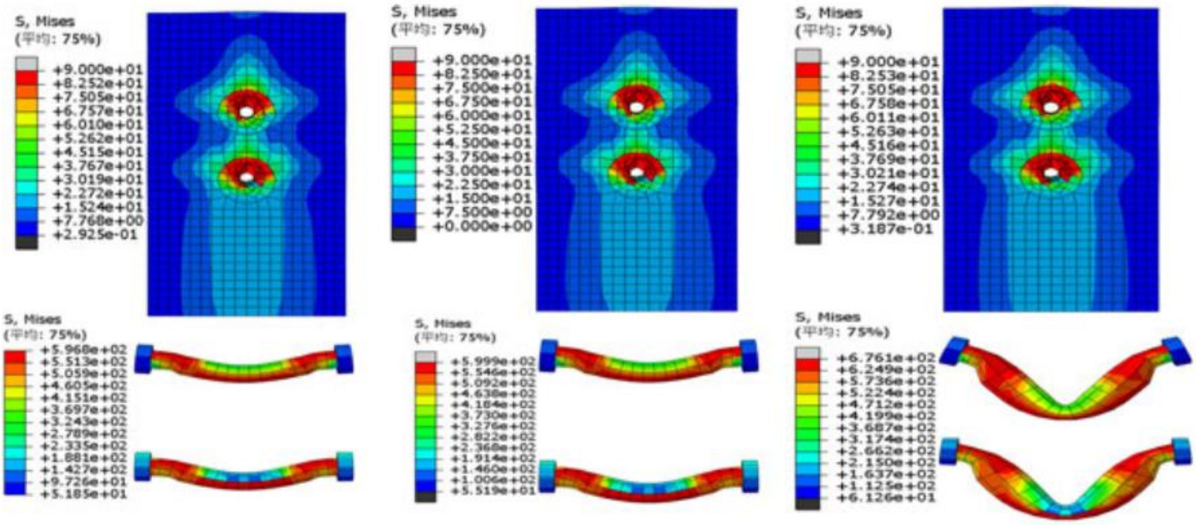

Figure 6-14 Stress Fields of Three Finite Element Models Generated Using Three Sets of Parameters Sampled via Monte Carlo Simulation

6. 2. 2 **Low-Fidelity Simplified Numerical Simulation**

To achieve a favorable balance between model prediction accuracy and computational efficiency, this study proposes a simplified yet generalizable phenomenological model for simulating the nonlinear mechanical response of Steel Side-Clamped-plate Glubam Connectors under cyclic loading. By explicitly defining the hysteresis envelope paths and associated mechanical effects, the model effectively captures the hysteretic behavior of the connection components.

The modeling strategy adopted in this study is inspired by the methodological frameworks proposed by Xu[254] and Yang[255], among others. The core idea is to decompose the hysteretic response of the connector into a parallel combination of multiple fundamental connection units, thereby constructing a controllable and scalable joint response model. Specifically, the connector is modeled using the two-dimensional axial connector element CONN2D2 available in the ABAQUS platform. Each connection unit is assigned a typical material mechanical behavior, including: elastic–plastic behavior (referred to as the EP material model), stop behavior (S material model), and locking behavior (L material model).

In this simplified model, all connector units are placed at exactly overlapping nodal positions—i.e., all mesh nodes are coincident—forming an idealized "concentrated node model." This arrangement ensures that the nonlinear mechanical behavior of the connector units acts solely along the tensile and compressive degrees of freedom, without coupling with other degrees of freedom. Such simplification reduces modeling complexity and significantly enhances computational efficiency.

Figures 6-15 to 6-17 respectively illustrate the typical response characteristics of the three types of connector units (EP, S, and L) under different loading paths, intuitively presenting their hysteresis behavior patterns.

Figure 6-18 shows the schematic construction of the simplified numerical model for the Steel Side-Clamped-plate Glubam Connector, demonstrating the logical framework for simulating composite hysteretic behavior through the parallel arrangement of different types of connector units.

This phenomenological model, through its modular and parametric design, effectively captures the major nonlinear mechanical characteristics of the Steel Side-Clamped-plate Glubam Connector under cyclic loading. It not only provides reliable accuracy and general applicability but also exhibits strong integrability and engineering potential, making it suitable for subsequent system-level hysteresis analysis and seismic performance evaluation.

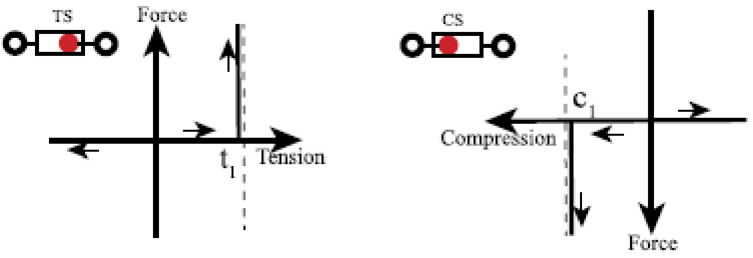

(a) Behavior of Tension-STOP (TS_i) material

(b) Behavior of Compression-STOP (CS_i) material

Figure 6-15 Material Model Behavior of STOP (S)： Tension-STOP (TS)Material Model （a） andCompression-STOP (CS) Material Model（b）

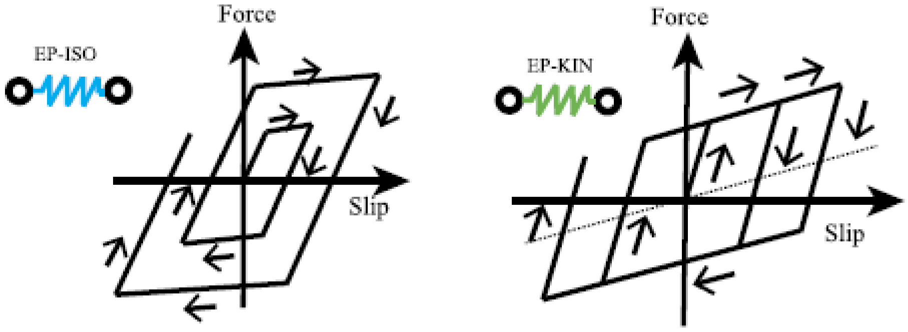

(a) Isotropical hardening of Elastic-plastic material (EP-ISO)

(b) Kinematic hardening of Elastic-plastic material (EP-KIN)

Figure 6-16 Behavior of the Elastic–Plastic (EP) Material Model: (a) Isotropic Hardening Elastic–Plastic (EP-ISO) Material Model and (b) Kinematic Hardening Elastic–Plastic (EP-KIN) Material Model

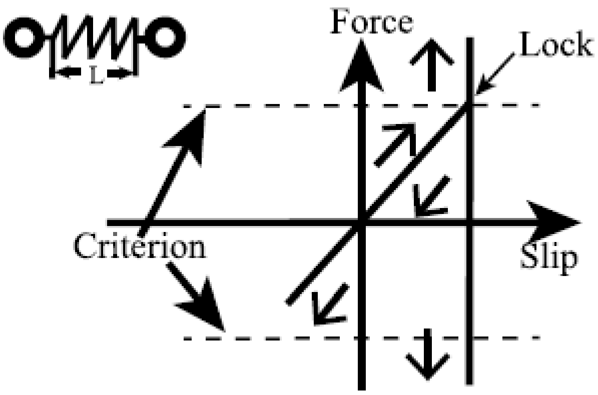

Figure 6-17 Behavior of LOCK (L) Material Model

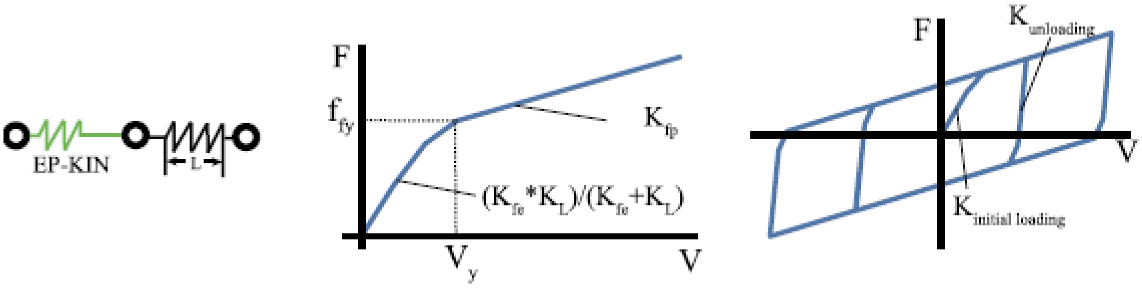

(a) Model of fastener (b) Monotonic behavior of fastener (c) Hysteresis behavior of fastener

Figure 6-18 Constitutive Rules of the Bolt Model: (a) Construction of the Simplified Bolt Behavior Model, (b) Monotonic Behavior of the Bolt, and (c) Hysteretic Behavior of the Bolt

6. 2. 2. 1 **Basic Material Model**

In the models presented in this study, elastic–plastic elements with a single degree of freedom are employed, as only uniaxial behavior is considered. Accordingly, the EP (elastic–plastic) material model requires the definition of four parameters:

(i) elastic stiffness,
(ii) yield strength,
(iii) post-yield stiffness, and
(iv) hardening rule.

The hardening rules adopted in this study include isotropic hardening and kinematic hardening, as illustrated in Figures 6-16(a) and (b), respectively. The corresponding material models are denoted as EP-ISO and EP-KIN.

In the isotropic hardening rule, the center of the yield surface remains at its original position while the yield surface expands with a positive post-yield stiffness.

In contrast, the kinematic hardening rule maintains the shape of the yield surface but allows its center to shift in response to changes in the yield stress.

The behavior of the S material can be described as that of a slider moving within a groove of finite length. This type of element consists of two nodes—one representing the slider and the other the groove—as shown in Figures 6-15(a) and (b). The minimum and maximum deformation limits are defined by the two ends of the groove, and the deformation of the element occurs within this confined range, with no friction involved.

Therefore, the STOP material is categorized into Tension-STOP (TS) and Compression-STOP (CS) types, which respectively constrain deformation in the tensile and compressive directions.

The mechanical behavior of the L material element is shown in Figure 6-17. This element model is assigned a locking threshold, which can be defined based on either deformation (displacement) or internal force. Prior to reaching this threshold, the L element behaves according to its assigned constitutive behavior—typically linear elastic. However, once the deformation or internal force exceeds the predefined threshold, the element transitions into a "locked" state, effectively behaving as a rigid link: the relative displacement between the two nodes is fixed thereafter, and the mechanical response is equivalent to an ideal rigid connection. In this study, the L element is primarily modeled using linear elasticity, and the internal force is used as the locking criterion. This setup is intended to simulate the “locking” phenomenon observed in connector components once they reach ultimate deformation or stress levels. It effectively captures the stiffness transition and mechanical behavior of the connector under specific loading conditions.

6.2.2.2 Simulation of Bolt Load-Bearing Behavior

The mechanical behavior of the bolt is modeled through a series combination of the EP-KIN material element and the L material element, as illustrated in Figure 6-18(a). In this configuration, the EP-KIN element captures the fundamental elastic–plastic response of the bolt, while the L element simulates the post-yield stiffness variation and locking effect. Within this modeling framework, the locking threshold of the L material element is set equal to the yield strength of the EP-KIN element. This setup enables the model to accurately represent the low-stiffness embedding stage of the bolt before yielding, and to trigger a stiffness transition through the locking unit after yielding, thereby more realistically reproducing the mechanical evolution of the bolt under loading.

Experimental results have shown that the initial loading stiffness $K_{initial-loading}$ of the connector is always lower than the unloading stiffness $K_{unloading}$ (see Figure 6-18(c)). To simulate this phenomenon, the locking material model is embedded into the bolt modeling system, enabling the model to effectively replicate the nonlinear characteristics of the unloading path.

In summary, the mechanical contribution of the bolt under monotonic loading can be expressed through the following formulation, which considers the superposition mechanism of the series-connected material units. This expression provides a theoretical basis for subsequent numerical analysis and parameter identification.

$$F_f\left(V\right)=K_{\mathrm{fe}}K_L/\left(K_{fe}+K_L\right)\cdot V\left(0\le V\le V_y\right) \tag{6-39}$$

$$F_f\left(V\right)=K_{fp}\left(V-V_y\right)+f_{fy}\left(V\ge V_y\right) \tag{6-40}$$

6. 2. 2. 3 Simulation of Glubam Load-Bearing Behavior

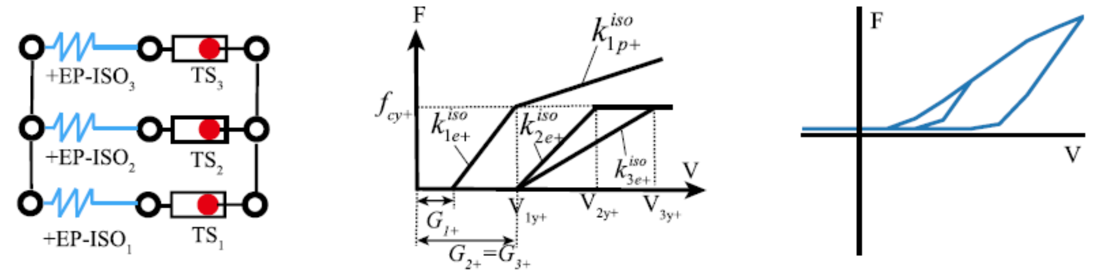

(a) Model of tension-sided glubam crushing

(c) Monotonic behavior of tension-sided glubam crushing model

(e) Hysteresis behavior of tension-sided glubam crushing model

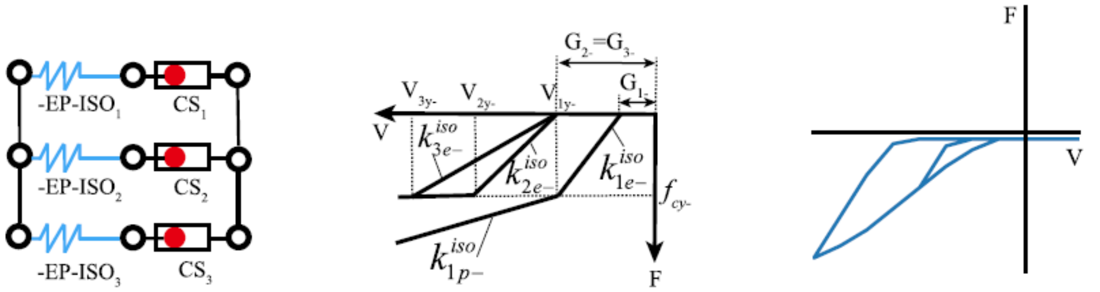

(b) Model of compression-sided glubam crushing

(d) Monotonic behavior of compression-sided glubam crushing model

(f) Hysteresis behavior of compression-sided glubam crushing model

Figure 6-19 Constitutive Rules of the Glubam Bearing Model on the Tension and Compression Sides: (a, b) Configurations of the Glubam Bearing Model, (c, d) Monotonic Behavior of the Glubam Bearing Model, and (e, f) Hysteretic Behavior of the Glubam Bearing Model

To simulate the localized bearing deformation and permanent damage around the bolt holes in the glubam material during bolted connection, this study constructs a corresponding constitutive model by using a series combination of ±EP-ISO and ±STOP material elements, as illustrated in Figure 6-19. Based on the directionality of structural loading, the mechanical responses of the glubam material on the tension side and the compression side during bolt loading are modeled separately, as shown in Figures 6-19(a) and 6-19(b), respectively.

Specifically, in the tensile loading path, the model uses a parallel combination of three +EP-ISO material elements and a TS (Tension Stop) material element to simulate the tensile-side yielding behavior caused by contact between the bolt and the glubam hole wall under tensile or reverse (i.e., re-tension after unloading) loading. This mechanism effectively captures phenomena such as yield delay, stiffness recovery, and energy dissipation under tensile loading.

Correspondingly, for the compressive loading path, the model adopts a parallel combination of three −EP-ISO material elements and a CS (Compression Stop) material element to describe the bolt–glubam contact and compressive yielding behavior during compressive or reverse (i.e., re-compression after unloading) loading. This approach realistically reproduces local crushing at the hole wall, asymmetric hysteresis, and residual plastic deformation under compression.

In this modeling framework, the ±EP-ISO elements represent ideal elastic–plastic behavior during the yielding process of glubam on the tension and compression sides, while the STOP elements (TS and CS) are responsible for controlling the loading path and switching contact states, thereby enhancing the model's ability to simulate nonlinear hysteretic responses—especially under multiple loading cycles and load reversals.

For the TS material, the maximum allowable displacement between the slider and the right end of the groove (i.e., the upper limit) is defined as the corresponding gap width G_{i+} （$i = 1, 2, 3$）, which simulates the initiation of contact between the bolt and glubam in the tensile direction. To prevent unintended contact in the opposite (left) direction, the minimum allowable distance (lower limit) is set to a large, unreachable value (e.g., 30 mm), ensuring it does not constrain the element during the loading process. Figures 6-19(c) and 6-19(e) show the monotonic and hysteretic responses simulated using the TS material under bolt-induced tensile bearing action on glubam.

For the CS material, the slider–groove left-end distance is set equal to the initial compression gap width G_{i-} （$i = 1, 2, 3$）, capturing the compressive-side gap behavior, while the right end is also assigned a value much greater than the actual deformation capacity to prevent its activation. Figures 6-19(d) and 6-19(f) present the corresponding simulation results under compressive loading conditions, illustrating the monotonic and hysteretic deformation responses due to bolt-induced compressive bearing action on glubam.

The TS and CS material elements are used to model the tensile and compressive force states and irreversible deformation behavior of the connection joint, respectively. They effectively capture the asymmetric contact behavior and stress–strain evolution between the fastener and glubam material during cyclic loading.

The development of the glubam compression model is based on the following two fundamental assumptions:

(i) the yield strengths of $\pm EP - ISO_1$、$\pm EP - ISO_2$ and $\pm EP - ISO_3$ are equal;

(ii) $\pm EP - ISO_2$ and $\pm EP - ISO_3$ can be idealized as perfectly elastic–perfectly plastic materials.

These assumptions facilitate a smoother elastic–plastic transition in the force–slip response curve and allow the loading and unloading stiffnesses to be independently defined, thereby more realistically capturing the nonlinear response characteristics of the connection under cyclic loading. Based on the above model and assumptions, the compressive resistance of glubam can be calculated using the following formalized equations. These equations explicitly reflect the mechanical response asymmetry of the connector under tension and compression, particularly highlighting the asymmetric resistance distribution caused by material boundary condition differences.

In the modeling process for the load-bearing behavior of glubam, the following key assumptions are made at both the theoretical and numerical implementation levels:

(i) the yield strengths of EP_1、EP_2 and EP_3 are identical;

(ii) EP_2 and EP_3 follow a perfectly elastic–perfectly plastic constitutive relationship;

(iii) the hardening behavior of $EP_i\left(i=1,2,3\right)$ is governed by an isotropic hardening rule.

These assumptions are introduced to simplify the modeling of the material's constitutive behavior while ensuring that the model is capable of capturing gradual elastic–plastic transitions during both loading and unloading paths.

On this basis, the force–slip curve can exhibit distinct loading and unloading stiffness, better reflecting the nonlinear mechanical behavior of actual connector components under cyclic loading.

Following this modeling logic, the compressive resistance of glubam can be computed using the mathematical expressions provided below, which describe the material's mechanical contributions at different loading stages.

$$F_{c\pm}\left(V\right)=\sum F_{i\pm}\left(V\right) \qquad \left(i=1,2,3\right) \tag{6-41}$$

$$F_{i\pm}\left(V\right)=0 \qquad \left(\left|V\right|\le G_{i\pm}\right) \tag{6-42}$$

$$F_{i\pm}\left(V\right)=k_{is\pm}^{iso}\left(V-G_{i\pm}\right) \qquad G_i\le\left|V\right|\le V_{iy\pm} \tag{6-43}$$

$$F_{i\pm}\left(V\right)=k_{ip\pm}^{iso}\left(V-V_{iy\pm}\right)+f_{cy\pm} \qquad \left|V\right|\ge V_{iy\pm} \tag{6-44}$$

Where， $F_{i\pm}$ is the force generated in the glubam model by the ±EP-ISO and ±STOP material combination of the *i*-th group, $G_{i\pm}$ is the gap of $STOP_{i\pm}$ element, $V_{iy\pm}$ is the yield displacement of the *i*-th combination of EP-ISO and STOP materials in the glubam compression model, $k_{ie\pm}^{iso}$ is the elastic stiffness of $\pm EP-ISO_i$ material, $k_{ip\pm}^{iso}$ is the post-yielding stiffness of $\pm EP-ISO_i$ element ($k_{2p\pm}^{iso}=k_{3p\pm}^{iso}=0$), $f_{cy\pm}$ is the yielding strength of $\pm EP-ISO_i$ element.

6. 2. 2. 4 **Integrated Connector Model**

The modeling of the Steel Side-Clamped-plate Glubam Connector is carried out using the two-dimensional axial connector element *CONN2D2* provided by ABAQUS. In this numerical model, each connector element is assigned a distinct material behavior to represent the key mechanical characteristics of the joint, including elastic–plastic response (EP material model), stop behavior (S material model), and locking behavior (L material model).

Within this modeling framework, all nodes are placed at the same geometric location, and the mechanical behavior acts only along the degrees of freedom in the tensile and compressive directions of the connector elements.

As described earlier, the bolt and glubam contributions to the load-bearing mechanism are modeled independently. The overall mechanical response of the connector is formed by the parallel superposition of these two components. Based on this superposition assumption, the load-bearing capacity of the connector under external loading can be calculated using the following mathematical expression:

$$F\left(V\right)=F_f\left(V\right)+F_c\left(V\right) \qquad (6\text{-}45)$$

A schematic of the complete connector model is shown in Figure 6-20. The model successfully captures three key characteristics exhibited in the hysteretic behavior of the glubam connector: pinching effect, asymmetry, and strength degradation.

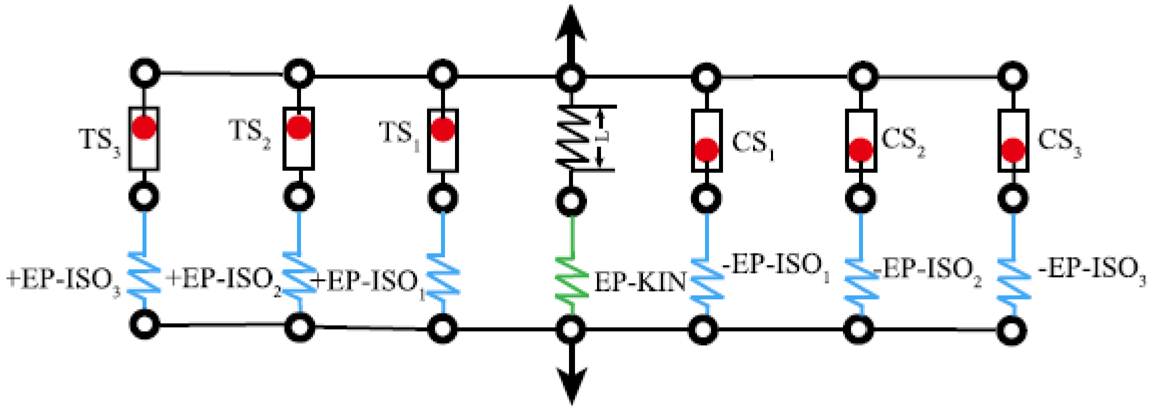

Figure 6-20 The Asymmetric Pinching and Damage (APD) Hysteresis Model Proposed for the Steel Side-Clamped-plate Glubam Connector

- **Simulation of Pinching Behavior**

As the loading continues to increase, the bolts exert localized compressive forces on the bamboo fibers, resulting in irreversible deformation. Since the compressed bamboo fibers cannot fully recover, the affected regions are unable to provide immediate load-bearing response in subsequent loading cycles, leading to a reduction in connection stiffness[256]. This phenomenon manifests as a typical pinching effect in the hysteresis behavior, which is one of the most prominent nonlinear characteristics in timber and bamboo-based structures.

To accurately simulate this phenomenon, TS and CS material elements are employed in this study to capture the irreversible deformation of glubam under compression and to effectively reproduce the pinching behavior observed in the hysteresis curves.

- **Simulation of Asymmetric Behavior**

As previously mentioned, the hysteretic behavior of glubam components in structural design may exhibit significant asymmetry[257]under different loading conditions, resulting in differentiated mechanical responses under positive and negative loading directions.

In the proposed connector model, the constitutive models for the tensile and compressive sides are coupled in parallel to simulate the hysteretic responses in both loading directions. This approach enables the independent characterization of nonlinear behavior during the tensile and compressive phases and accurately captures the asymmetry in the hysteresis loops caused by differences in material properties, connection configurations, and loading conditions.

By superimposing the contributions from both sides, the model is capable of effectively reproducing the asymmetric hysteretic response of the connector under cyclic loading, thereby enhancing the accuracy of mechanical behavior prediction.

- **Simulation of Damage Behavior**

To accurately simulate the strength degradation observed in hysteretic behavior, damage criteria are introduced into the constitutive models of $+EP-ISO_1$ and $-EP-ISO_1$. These criteria are used to describe the strength attenuation processes on each side, respectively. As illustrated in Figures 6-21(a) and 6-21(b), the damage criteria are defined by two thresholds—（F_{d+} and F_{d-}）—along with the corresponding damage indices—（I_{d+} and I_{d-}） for compression. These parameters clearly specify the initiation and termination points of damage evolution. Based on these criteria, the modified hysteretic responses incorporating damage effects are shown in Figures 6-21(c) and 6-21(d). It can be observed that the introduced damage mechanism effectively captures the strength degradation features of the hysteresis curves. When considering the damage effects, the resisting force generated by the combination of tensile and compressive material elements can be computed using the following equations:

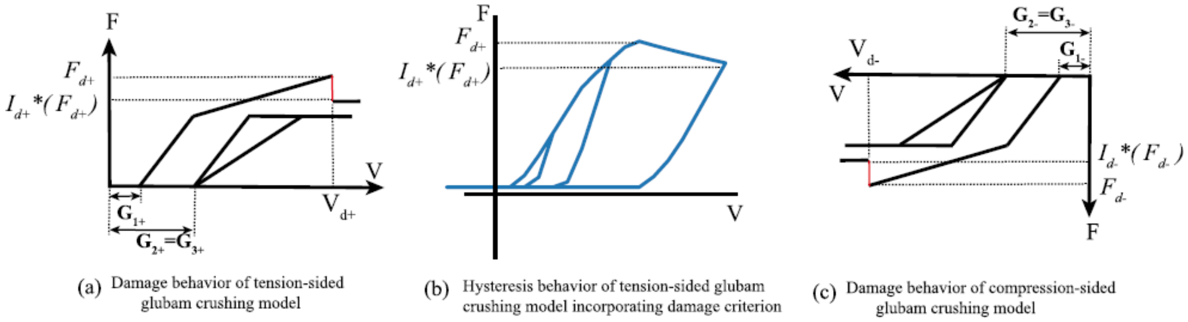

(a) Damage behavior of tension-sided glubam crushing model

(b) Hysteresis behavior of tension-sided glubam crushing model incorporating damage criterion

(c) Damage behavior of compression-sided glubam crushing model

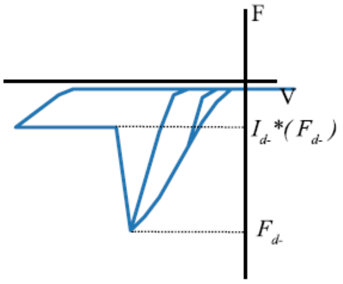

(d) Hysteresis behavior of compression-sided glubam crushing model incorporating damage criterion

Figure 6-21 Damage Behavior in the Compressive Deformation of Glubam

$$F_{1\pm}(V)=0 \qquad \left(|V|\le G_{1\pm}\right) \tag{6-46}$$

$$F_{1\pm}(V)=k_{1e\pm}^{iso}\left(V-G_{1\pm}\right) \qquad \left(G_{1\pm}\le|V|\le V_{1y\pm}\right) \tag{6-47}$$

$$F_{1\pm}(V)=k_{1p\pm}^{iso}\left(V-V_{1y\pm}\right)+f_{cy\pm} \qquad \left(V_{1y\pm}\le|V|\le V_{d\pm}\right) \tag{6-48}$$

$$F_{1\pm}(V)=k_{d\pm}\left(V-V_{d\pm}\right)+I_{d\pm}*F_{d\pm} \qquad \left(|V|\ge V_{d}\right) \tag{6-49}$$

6. 2. 2. 5 Low-Fidelity Numerical Model Simulation Results and Experimental Validation

This subsection provides a brief summary of the prediction results obtained from the low-fidelity numerical model. As these results are primarily based on parameter identification using artificial intelligence optimization algorithms—which will be introduced in detail in the following chapter—this section focuses only on the preliminary analysis of the model's predictive performance, aiming to validate its rationality and applicability.

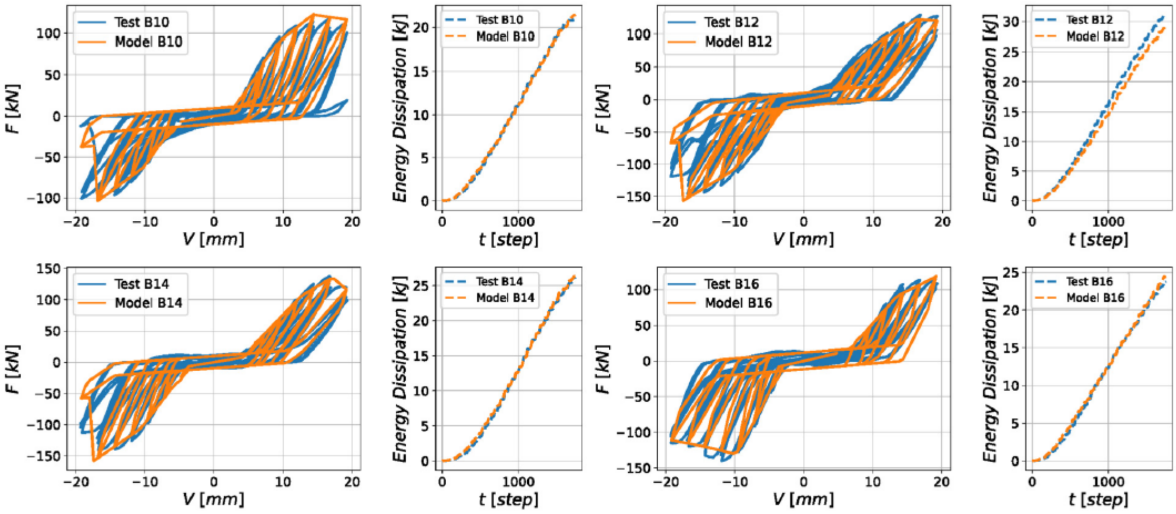

Figure 6-22 Comparison Between Experimental Hysteretic Response and Predicted Response of the Low-Fidelity Numerical Model

Figure 6-22 compares the hysteretic behavior and energy dissipation time history observed in the benchmark experiment with the predictions of the proposed simplified numerical model. The results indicate that the model can accurately reproduce the pinching effect, damage evolution, and asymmetry in the hysteretic response. In addition, the experimentally measured energy dissipation curve matches well with the numerically predicted values, demonstrating the high reliability of the simplified model in capturing the energy dissipation characteristics of the connector.

The predictive performance of the APD hysteresis model is further compared with three classical hysteresis models commonly cited in the literature. These include:

(i) the SAWS model (also known as MSTEW), originally proposed by Stewart et al.[258] and later refined by Folz & Filiatrault[259];

(ii) the Pinching4 model developed by Lowes et al.[260]; and

(iii) the DowelType model proposed by Dong et al.[253].

All three models have been integrated into the OpenSees platform. The SAWS and Pinching4 models are primarily used for simulating the hysteretic behavior of timber connectors, while the DowelType model is a recently introduced model specifically designed for wood fastener simulation.

Figure 6-23 presents a comparison of the hysteretic responses predicted by these four models against the experimental results. The model proposed in this study is referred to as the Asymmetric Pinching Damaged (APD) Hysteresis Model. To quantitatively evaluate the predictive accuracy of each model, the predicted and experimental responses are compared using the Relative Root Mean Square Error (RRMSE), as summarized in Table 6-4. In this study, the RRMSE is employed to quantify the error between two signals, and it is defined as follows:

$$RRMSE(a,b)=\frac{\sqrt{\left[\frac{1}{N_s}\sum_{i=1}^{N_s}\left(a_i-b_i\right)^2\right]}}{\sqrt{\left[\frac{1}{N_s}\sum_{i=1}^{N_s}\left(a_i\right)^2\right]}}\times 100\left(\%\right) \qquad （6\text{-}50）$$

Where，**a** represents tested values，**b** represents model predicted values，N_s represents the total number of data samples in the signal.

Table 6-4 RRMSE Between Experimental and Model-Predicted Responses

Model	Joint Configuration			
	B10	B12	B14	B16
APD	8.32%	13.38%	7.56%	9.75%
Saws	17.64%	25.31%	21.44%	32.21%
Pinching4	12.64%	16.32%	13.45%	12.58%
DowelType	7.65%	14.72%	9.53%	8.34%

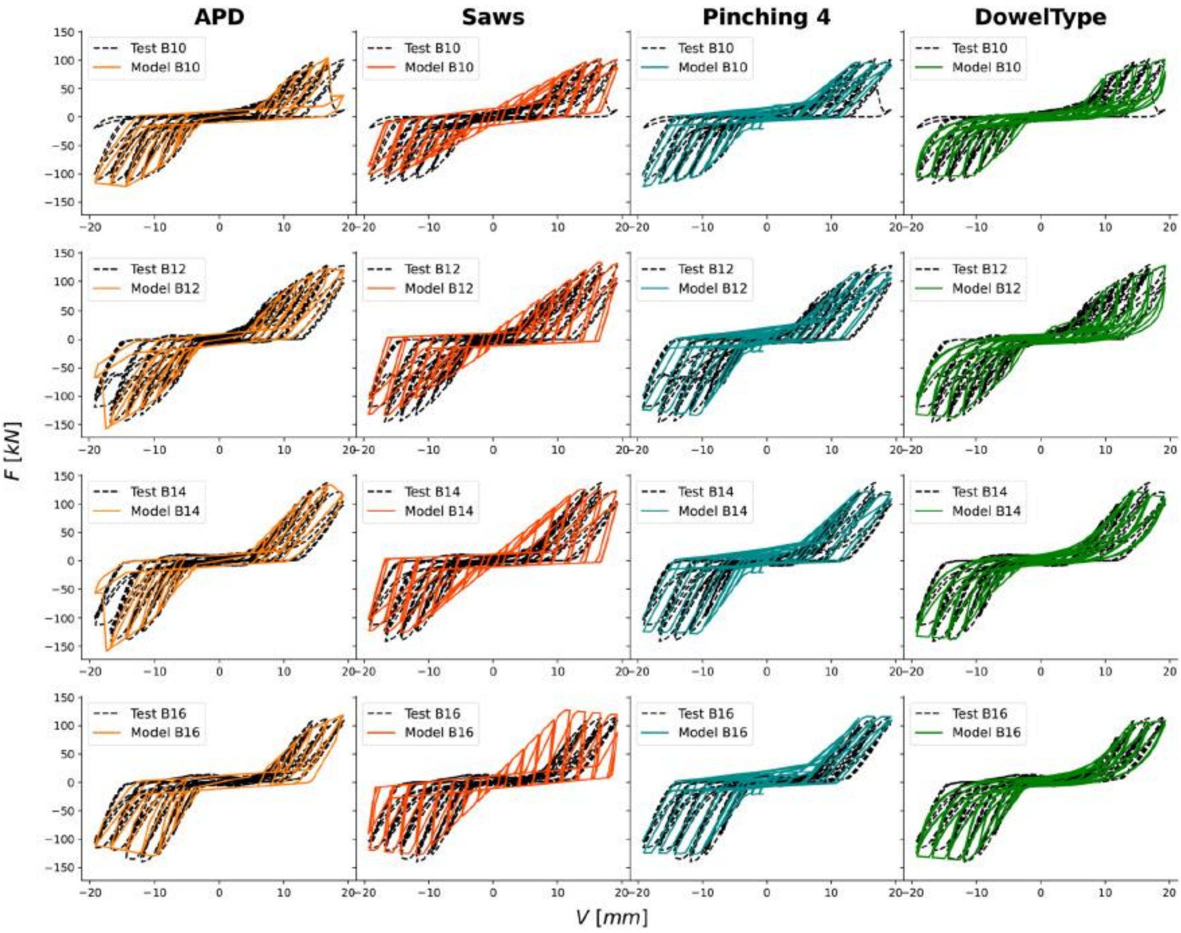

Figure 6-23 Comparison of Hysteretic Responses Predicted by Four Models with Experimental Results (APD Model is the One Proposed in This Study)

The comparison results indicate that, under all test conditions, the APD model and the DowelType model exhibit the highest fitting accuracy and are able to closely reproduce the experimental results. The Pinching4 model ranks next in terms of accuracy, while the SAWS model performs the worst and fails to capture the key hysteretic characteristics observed in the experiments.

The fitting results validate the applicability of the APD model, demonstrating its ability to comprehensively capture all major hysteretic features observed in the tests, including asymmetric response, pinching effect, and damage behavior. These capabilities make the APD model highly valuable for engineering applications involving the simulation of complex joint hysteretic responses.

7 Parameter Identification of the Hysteresis Model for Glubam Joints

In the previous section, two low-fidelity simplified numerical models were introduced for Steel Insert-plate Glubam Connectors and Steel Side-Clamped-plate Glubam Connectors. Due to the complexity of the mechanical behavior of such connectors, the developed numerical models involve multiple tunable parameters, making the parameter identification process highly nonlinear. Efficient and accurate identification of these parameters thus becomes a critical challenge.

Traditional manual tuning methods are time-consuming and labor-intensive, and they often fail to converge to the global optimum, making them impractical. Similarly, conventional optimization techniques (e.g., the Newton method and its variants, quasi-Newton methods, and least squares regression[261,262]) often perform poorly in handling highly nonlinear problems, as they are prone to being trapped in local minima, thereby compromising both the accuracy and stability of parameter identification.

To enhance the practical value of the proposed numerical models, this study explores and compares several advanced parameter identification techniques, ultimately selecting and further developing the following three optimization strategies:

(i) Genetic Algorithm (GA),
(ii) Attention-Based Neural Network[263], and
(iii) Bayesian Inference Method.

All three methods are capable of efficiently searching for optimal parameters in high-dimensional nonlinear spaces, significantly improving the predictive accuracy and computational efficiency of the numerical models.

In this section, we focus on the parameter identification and optimization of the hysteresis model for glubam joints using the three aforementioned optimization algorithms (GA, attention-based neural network, and Bayesian method). Hysteresis models are critical tools for describing the mechanical behavior of materials and structures under cyclic loading, especially for bamboo-based systems exhibiting complex nonlinear responses. Accurate identification and calibration of model parameters are essential to improving the predictive capability of such models.

To ensure that the hysteresis model for glubam connectors can accurately simulate the actual mechanical behavior, this study first identifies and optimizes key model parameters based on experimental data and numerical simulation results. Specifically, by comparing the experimentally measured load–displacement curves with the simulation outputs, model parameters are iteratively adjusted to maximize the agreement between model predictions and experimental observations, thereby enhancing model reliability and applicability.

This section will present a detailed overview of the parameter identification methodology, including the experimental dataset used, the implementation steps of each optimization algorithm, and the computational workflow. A comparative evaluation of the performance of different optimization strategies will also be conducted. The final optimized parameters will serve as a solid foundation for the subsequent updating of the glubam truss structural model.

7.1 Parameter Identification Algorithms

7. 1. 1 **Parameter Identification Based on Genetic Algorithm**

The Genetic Algorithm (GA) is an optimization technique that simulates the process of biological evolution in nature and belongs to the class of evolutionary algorithms. By mimicking mechanisms such as natural selection, crossover, and mutation, GA demonstrates significant advantages in solving complex optimization problems. The core concept of GA is to discover the global optimum through cooperation and competition among a population of individuals (i.e., candidate solutions). Compared with traditional optimization methods, GA does not rely on gradient information and can effectively avoid being trapped in local minima, making it particularly suitable for high-dimensional, nonlinear, and multi-modal optimization problems.

In the context of parameter identification, GA performs optimization through the following main steps:

1.Population Initialization:

A set of initial candidate solutions (i.e., individuals) is generated. Each individual is represented by a set of parameters, typically encoded using binary or real-valued genes.

2.Fitness Evaluation:

Each individual is evaluated using a fitness function, which quantifies how well it performs. In parameter identification problems, the fitness function is usually defined to minimize the error between the model output and experimental data. A higher fitness value indicates that the corresponding parameters are closer to the true values.

3.Selection:

Individuals with higher fitness are more likely to be selected for reproduction. Common selection methods include roulette wheel selection, tournament selection, etc., where the selection probability is proportional to the individual's fitness.

4.Crossover (Recombination):

Selected individuals undergo crossover to produce new offspring, simulating the recombination of genetic material from parent individuals. Crossover helps maintain genetic diversity and generates new candidate solutions.

5.Mutation:

Random changes are applied to the genes of individuals to simulate natural mutations. Mutation introduces new genetic diversity into the population and helps prevent premature convergence to local optima.

6.Termination Condition:

The algorithm stops when a predefined condition is met, such as reaching the maximum number of generations or achieving a target fitness threshold. The best solution found is then output.

GA offers several advantages, including strong global search capability, fast convergence, and the ability to handle complex constraints. Therefore, it has been widely applied in solving challenging parameter identification problems. Specifically, for hysteresis model calibration, GA can automatically adjust model parameters to minimize the error between simulated and experimental results, thus improving the predictive accuracy of the model.

In the parameter identification process of the hysteresis model for glubam joints, the Genetic Algorithm (GA) adaptively adjusts key model parameters to achieve high-accuracy fitting with experimental data. This method not only significantly improves the accuracy of parameter identification but also provides an efficient and robust optimization strategy for other material or structural models exhibiting complex nonlinear behavior.

The parameters optimized using GA can more realistically reflect the actual mechanical behavior of glubam under cyclic loading, thereby enhancing both the engineering applicability and predictive capability of the model.

In this study, the set of model parameters for the hysteresis model of glubam joints is organized into a parameter vector θ, and systematically calibrated using experimental data to ensure that the simulated force–displacement response closely matches the experimental observations.

Ultimately, the optimal parameter set for each specimen is determined by minimizing the following objective function:

$$OF\left(\theta\right)=\frac{\int_{v_0}^{v_f}\left|\left[F_e\left(v\right)-F_s\left(\theta,v\right)\right]\right|dv}{\int_{v_0}^{v_f}\left|F_e\left(v\right)\right|dv} \tag{7-1}$$

Where， v_0 and v_f represent the initial and final displacement records, respectively; $F_e\left(v\right)$ denotes the force obtained from experimental data; and $F_s\left(\theta,v\right)$ denotes the force simulated by the proposed model.

7. 1. 2 **Fast Deterministic Parameter Identification Based on Neural Networks**

Neural Networks (NNs) are computational models inspired by the structure and functionality of the human nervous system. They are widely used in data processing, pattern recognition, classification, regression analysis, and optimization problems. A neural network consists of multiple layers of interconnected nodes (neurons), typically including an input layer, one or more hidden layers, and an output layer. Each neuron transmits information through weighted connections, and the neuron’s output is the result of processing the weighted input via an activation function. Neural networks can adaptively learn patterns from data and optimize their internal weight parameters through training, enabling them to model and solve complex problems.

In the context of parameter identification, neural networks offer a distinct advantage in handling nonlinear and complex input–output relationships. Traditional optimization methods often struggle with nonlinear and high-dimensional problems, being prone to local minima and reliant on substantial prior knowledge. In contrast, neural networks can automatically extract complex relationships between inputs and outputs from data, and optimize weights through backpropagation algorithms, minimizing the error on the training data.

The application of neural networks in the parameter identification of hysteresis models is particularly significant. By learning the complex nonlinear mapping between multiple input and output variables, neural networks can efficiently identify key parameters in the hysteresis model. Their powerful self-learning capability enables the automatic recognition of hysteretic features from experimental data, leading to precise parameter optimization and enhanced model fitting accuracy and predictive capability.

The process of using neural networks for hysteresis model parameter identification generally involves the following steps:

1. Data Preparation:
   Collect experimental data related to hysteretic behavior, such as force–displacement or stress–strain curves. This data serves as the foundation for network training.
2. Network Architecture Design:
   Choose an appropriate neural network architecture based on the complexity of the problem and the characteristics of the data. Common structures include Feedforward Neural Networks (FNNs) and Convolutional Neural Networks (CNNs). FNNs are typically used for regression and prediction tasks, while CNNs perform well in extracting spatial features from data.
3. Training and Optimization:
   During training, the neural network adjusts its weights to minimize a defined loss function (e.g., mean squared error, cross-entropy). A large amount of experimental data is used to guide the learning process, and weight updates are iteratively performed using gradient descent or its variants (e.g., the Adam optimizer).
4. Validation and Testing:
   After training, unseen data is used to evaluate the model’s generalization ability. This step is crucial for assessing the predictive accuracy and practical performance of the model.

The advantages of neural networks in hysteresis model parameter identification go beyond accuracy. They can handle large-scale datasets, automatically learn from complex experimental data, and do not rely on traditional mathematical derivations required by conventional optimization methods. Additionally, neural networks offer high adaptability: they can be flexibly adjusted to different material types and structural behaviors by modifying the network architecture and training approach.

In summary, neural networks provide an efficient and automated tool for identifying parameters in hysteresis models. They significantly enhance both the accuracy and efficiency of parameter identification, offering a new approach for modeling complex structural behaviors and showing great potential for broad engineering applications.

7. 1. 3 **Parameter Identification Based on Bayesian Inference**

Bayesian inference is a statistical method based on Bayes' theorem, widely applied in parameter estimation, model selection, and uncertainty quantification. It updates beliefs about unknown parameters by integrating prior information with experimental data, resulting in a posterior distribution. This approach is particularly effective in handling uncertainty, making it well-suited for parameter identification problems, especially when dealing with complex models or limited data. Bayesian inference provides more robust and reliable estimations under such conditions.

The core idea of Bayesian inference is to update the known prior distribution to obtain the posterior distribution using observed data. In parameter identification, this means combining reasonable prior knowledge with experimental observations to refine the distribution of the model parameters. Compared to traditional point estimation methods, Bayesian inference offers a more comprehensive estimation by providing not only an optimal parameter value but also a quantified uncertainty range for that estimate.

Bayesian inference has significant value in the parameter identification of hysteresis models, which often involve multiple latent parameters with complex nonlinear relationships. Experimental data may also be affected by noise and various uncertainties. By systematically incorporating prior knowledge and experimental data, Bayesian inference enables efficient estimation of model parameters while also quantifying the uncertainty of those estimates.

In practical applications, Bayesian inference typically relies on numerical methods, as analytical solutions to posterior distributions are rarely tractable. Common approaches include:

- Markov Chain Monte Carlo (MCMC) methods: These approximate the posterior distribution by constructing a sample path and performing multiple samples from it.
- Variational Inference (VI) methods: These approximate the posterior by optimizing a lower bound on the likelihood, often providing faster inference than MCMC in high-dimensional problems.

In this study, Bayesian inference is applied to identify the key parameters of the glubam joint hysteresis model. By integrating experimental data with prior knowledge, the posterior distributions of the parameters are constructed, offering robust estimates that serve as a foundation for both model application and uncertainty analysis.

The advantages of Bayesian inference lie not only in its ability to improve the accuracy of parameter identification, but also in its capacity to quantify the uncertainty of the estimated results, thereby enhancing the credibility of model predictions. This makes it particularly suitable for engineering problems under high uncertainty, providing a solid scientific basis for hysteresis model optimization and application, as well as more comprehensive information for engineering design and structural safety assessment.

The process of parameter identification using Bayesian inference in this study is illustrated as follows:

Let $\mu_k \in \mathbb{R}^{n_\mu}$ and $y_k \in \mathbb{R}^{n_y}$ denote the input and output response vectors measured at time t_k (or time step k), respectively. These measurements are obtained from sensors installed on the experimental setup. Assuming that the responses are recorded over N time steps, the observed input–output dataset can be represented as $\Phi = (\mu, y)$,where $\mu = \left[\mu_1^T, \mu_2^T, \cdots, \mu_N^T\right] \in \mathbb{R}^{(n_\mu \times N)\times 1}$ and $y = \left[y_1^T, y_2^T, \cdots, y_N^T\right] \in \mathbb{R}^{(n_y \times N)\times 1}$. At time step k, let $y_k^{FE} = h_k(\mu_k; \theta) \in \mathbb{R}^{n_y}$ denote the response predicted by the model h under the influence of the measured input history $\mu_{1:k} = \left[\mu_1^T, \mu_2^T, \cdots, \mu_k^T\right] \in \mathbb{R}^{(n_\mu \times k)\times 1}$,given an unknown parameter vector $\theta \in \mathbb{R}^{n_\theta}$ (to be identified). The measurement equation used in this study is defined as follows:

$$y_k = h_k(\mu_{1:k}; \theta) + w_k \tag{7-2}$$

Where $w_{1:k} = \left[w_{1,k}, w_{2,k}, \cdots, w_{n_y,k}\right]^T$ denote the measurement error/noise at time step k. Specifically, $w_{i,k}$ represents the discrepancy between the measured value from the ith output channel and the finite element model prediction at time step k. In the measurement equation, the noise term is assumed to be additive, aggregating all sources of uncertainty and added directly to the finite element model's predicted response.

For the method described in this study, the parameter vector θ may include any unknown time-invariant parameters, such as hysteresis model parameters, loading conditions, boundary conditions, and geometric parameters of the finite element model. The prediction error can be expressed in the following form:

$$w_k = y_k - h_k(\mu_{1:k}, \theta) \tag{7-3}$$

The Bayesian approach adopts a systematic parametric model and uses data from the system to estimate the values of the uncertain parameter vector by maximizing the posterior probability density function (PDF) in

Bayes' theorem, thereby obtaining the most probable value (MPV) estimate. The posterior distribution of the model parameters θ to be identified is given by:

$$p\left(\theta|y_k\right)=\frac{p\left(y_k|\theta\right)\times p(\theta)}{p\left(y_k\right)} \qquad (7\text{-}4)$$

In practical applications, due to numerous sources of uncertainty, the measured response μ_k and the finite element model prediction y_k often do not match. These uncertainties include:

(a) Uncertainty in measured outputs caused by sensor noise;

(b) Uncertainty in unmeasured or partially measured inputs, along with sensor noise associated with the measured inputs;

(c) Uncertainty related to the model structure or form, meaning the selected model class may not be capable of representing the true system (neglecting such model form errors can introduce estimation bias and reduce the predictive capability of the model);

(d) Uncertainty in the model parameters, under the assumption that the model structure/form is known.

In simple terms, the goal of Bayesian model updating is to estimate or update the posterior distribution of the parameter vector θ while considering all relevant sources of uncertainty. In this study, particular attention is given to model uncertainty, also referred to as epistemic uncertainty, whereas aleatory uncertainty—which relates to inherent randomness and variability—is not considered. Therefore, the parameter identification process is based on the result of a single experiment, with an emphasis on improving the consistency between model predictions and observed structural behavior within the context of these epistemic uncertainties.

From a Bayesian perspective**,** parameter identification is accomplished by computing the posterior probability density function (PDF) of the parameters given the measurement data, for example, by evaluating $p\left(\theta|y_{1\to k}\right)$. If the problem is globally identifiable, the most probable value (MPV) of the parameter vector can be determined as follows:

$$\theta_{MPV}=\underset{\theta}{\arg\max}\left[p\left(\theta|y_{1\to k}\right)\right] \qquad (7\text{-}5)$$

Where $p\left(\theta|y_{1\to k}\right)$ is the posterior PDF.

Given a uniform prior distribution for θ, the most probable value (MPV) estimation problem in Equation (7-6) becomes equivalent to maximum likelihood estimation (MLE), i.e.,

$$\theta_{MPV} = \arg\max_{\theta}\left[p\left(y_{1\to k}|\theta\right)\right] \tag{7-6}$$

Where $p\left(y_{1\to k}|\theta\right)$ is the likelihood function.

When the prediction error w_k in Equation (7-3) is assumed to follow a zero-mean Gaussian process with a diagonal covariance matrix **R**, Equation (7-6) can be expressed as:

$$p\left(y_{1\to k}|\theta\right) = \prod_{i=1}^{k} p\left(w_i\right) = \prod_{i=1}^{k}\frac{1}{\left(2\pi\right)^{n_\theta/2}\left|R\right|^{1/2}}e^{-\frac{1}{2}\left(y_i-h_i(\theta)\right)^T R^{-1}\left(y_i-h_i(\theta)\right)} \tag{7-7}$$

In this equation, | **R** | denotes the determinant of the covariance matrix R\mathbf{R}R, and n_θ is the number of parameters to be identified. Obtaining θ from Equation (7-6) is equivalent to minimizing the negative log-likelihood function, expressed as:

$$\theta_{MPV} = \arg\min_{\theta}\left[-\ln\left(p\left(y_{1\to k}|\theta\right)\right)\right] = \arg\min_{\theta}\left[-J\left(\theta, y_{1\to k}\right)\right] \tag{7-8}$$

Where $J\left(\cdots\right)$ is the objective function.

$$J\left(\theta, y_{1\to k}\right) = \frac{1}{2}\sum_{i=1}^{k}\left(\left(y_i - h_i\left(\theta\right)\right)\right)^T R^{-1}\left(y_i - h_i\left(\theta\right)\right) + \frac{kn_\theta}{2}\ln\left(2\pi\right) + \frac{k}{2}\sum_{j=1}^{n_\theta}\ln\left(R\right) \tag{7-9}$$

However, it is often intractable to analytically derive the full joint posterior distribution. In this study, we address this challenge using the Sequential Monte Carlo (SMC) method, which samples from the joint posterior distribution. The SMC algorithm is a parallel extension of the Markov Chain Monte Carlo (MCMC) method and is well-suited for sampling in high-dimensional parameter spaces. Its parallel nature makes it highly efficient for updating large-scale, nonlinear finite element models using high-performance computing resources. Unlike traditional MCMC methods, SMC is capable of effectively handling complex posterior distributions with flat regions or multiple modes—distributions that are commonly encountered in non-identifiable or locally identifiable problems.

Table 7-1 Sequential Monte Carlo Algorithm

Initialize：	N_p ,j = 0, ESS_0 = N_P , $\beta_0 = 0$, Generate N_p samples $\left\{\theta^i_{j=0}; i = 1,\dots,N_p\right\}$ from the prior probability density function $p\left(\theta\right)$.
While $\beta_j \le 1$：	Stage Number $j = j+1$ Choose β_j such that $ESS_j = 0.95\times ESS_{j-1}, \beta_j = \min\left(\beta_j, 1\right)$， βj = miñ(βj , 1) Weighting： $w^i_j = p\left(y\middle|\theta^i_{j-1}\right)^{\beta_j-\beta_{j-1}}$， 对于 $i = 1,\dots,N_p$

	Resampling：$\theta_j^i = \theta_{j-1}^i$ with probability w_j^l， for $i=1,\dots,N_p$ perturbation：θ_j^i Start a MCMC chain at θ_j^i， and take N_{MCMC} steps，with target distribution $p(\theta \mid y)_{\beta_j}$， for each $i=1,\dots,N_p$. Gather last sample of each MCMC chain to obtain $\left\{\theta_j^i; i=1,\dots N_p\right\}$.
End：	Save last stage $m=j$ $\left\{\theta_m^i; i=1,\dots N_p\right\}$ are the samples of the target posterior $p(\theta \mid y)$.

Note：N_p：Particles Number，ESS：Effective Sample Size，β：Tempering parameter，j：Stage Number，θ：unknown parameter vector to be updated，θ_j^i：i th particle of θ at stage j.

In this study, instead of sampling directly from the target posterior distribution—which is often difficult to characterize precisely—we employ the Sequential Monte Carlo (SMC) method to sample from the joint posterior probability density function (PDF) defined in Equation (7-4). This method introduces a temperature parameter, denoted as β, to control the proximity between intermediate distributions and the final target posterior distribution.

The temperature parameter is initially set to a small value and is gradually increased from 0 to 1 throughout the sampling process, ensuring a smooth transition toward the target distribution. At each iteration stage of the SMC algorithm, the posterior distribution corresponding to the current temperature is used to generate samples, as described in Equation (7-10). As β increases, these samples progressively converge toward the target posterior distribution.

Ultimately, the samples output by the algorithm are regarded as representative samples of the target posterior distribution. This approach enables efficient approximation of complex probability distributions, thereby enhancing the stability and accuracy of parameter estimation.

$$P(\theta \mid y, \beta) \propto P(y \mid \theta)^{\beta} P(\theta) \tag{7-10}$$

Where β is the tempering parameter

At each stage of the SMC algorithm, the tempered posterior distribution is represented by a set of weighted samples, also referred to as particles. These particles are iteratively updated to progressively approach the target posterior distribution.

In addition, at each stage, SMC employs an independent Markov Chain Monte Carlo (MCMC) sampling method, which uses the current set of samples from the tempered posterior as the starting point to gradually converge to the posterior distribution at the next temperature level. This ensures the stability and convergence of the sampling process across iterations.

The detailed procedure of the SMC algorithm used in this study to sample from the joint posterior distribution defined in Equation (7-10) is systematically described in Table 7-1, which outlines the sampling, resampling, and weight update mechanisms applied at each temperature stage.

7.2 Parameter Identification of the Hysteresis Model for Steel Insert-plate Glubam Connectors

The hysteresis model proposed in this study for Steel Insert-plate Glubam Connectors is governed by a total of 79 parameters: 38 parameters for the first Pinching4 material element, 38 parameters for the second Pinching4 material element, and 3 parameters for the Gap material element. A summary of the parameters to be identified is provided in Table 7-2.

Table 7-2 Summary of Hysteresis Model Parameters for Steel Insert-plate Glubam Connectors

Material Model	Parameter	Parameter Number
Status 1		
Pinching4 1#	$ePf_1, ePf_2, ePf_3, ePf_4,\ ePd_1, ePd_2, ePd_3, ePd_4$	1-8
	$eNf_1, eNf_2, eNf_3, eNf_4,\ eNd_1, eNd_2, eNd_3, eNd_4$	9-16
	$rDispP,\ fForceP, uForceP, rDispN,\ fForceN, uForceN$	17-22
	$gK_1, gK_2, gK_3, gK_4, gK_{\lim}, gD_1, gD_2, gD_3, gD_4, gD_{\lim},$	23-38
	$gD_1, gD_2, gD_3, gD_4, gD_{\lim},\ gE$	
Gap 1	gap	39
Gap 2	gap	40
Status 2		
Pinching4 2#	$ePf_1, ePf_2, ePf_3, ePf_4\ ePd_1, ePd_2, ePd_3, ePd_4$	41-48
	$eNf_1, eNf_2, eNf_3, eNf_4\ eNd_1, eNd_2, eNd_3, eNd_4$	49-56
	$rDispP,\ fForceP, uForceP, rDispN,\ fForceN, uForceN$	57-62
	$gK_1, gK_2, gK_3, gK_4, gK_{\lim}\ gD_1, gD_2, gD_3, gD_4, gD_{\lim}$	63-78
	$gD_1, gD_2, gD_3, gD_4, gD_{\lim}\ gE$	
Gap 3	gap	79

7. 2. 1 **Genetic Algorithm Parameter Identification Results**

In this study, the Genetic Algorithm (GA) was implemented using the PyGAD optimization library. Prior to solving the optimization problem, the value ranges of the model parameters were first assumed in order to define a reasonable search space. To ensure the effectiveness and convergence of the optimization process, a preliminary analysis of the parameters was conducted to determine appropriate search intervals before formal optimization.

Tables 7-3 and 7-4 list the upper and lower bounds of the search space as well as the final identified optimal values for the parameters of the two Pinching4 material models under tension–compression cyclic loading.

Additionally, Table 7-5 presents the search space ranges and the optimized parameter values for the three Gap material models under the same loading condition.

The identification of these optimized parameters provides critical support for the accurate calibration of the numerical model and further enhances its capability to simulate the hysteretic behavior of the connector.

Table 7-3 Parameter Identification Results and Search Space for 1# Pinching4

Specimen	G-S-8	G-S-10	G-D-8	G-D-10	Searching Space	
Parameter	Identified	Identified	Identified	Identified	Lower	Upper
ePf_1	23.8	22.5	61.3	44.2	6.25	125
ePd_1	0.38	0.68	1.31	0.69	0.13	2.5
ePf_2	49.4	27.7	70.6	62.8	9.25	185
ePd_2	1.41	1.75	6.30	0.73	0.38	7.5
ePf_3	50.4	44.1	31.8	104	11.25	225
ePd_3	5.16	8.46	4.13	2.42	1	20
ePf_4	5.23	3.14	3.69	3.78	3.05	61
ePd_4	7.53	8.70	18.8	4.62	1.25	25
eNf_1	-41.4	-28.2	-76.1	-78.4	-125	-6.25
eNd_1	-0.93	-0.28	-2.31	-1.32	-2.5	-0.13
eNf_2	-45.6	-30.8	-59.2	-71.8	-185	-9.25
ePd_2	-2.40	-2.90	-2.95	-1.83	-7.5	-0.38
eNf_3	-45.6	-15.30	-48.9	-19.5	-225	-11.25

$eN\,d_3$	-3.30	-3.36	-3.24	-1.82	-20	-1
$eN\,f_4$	-1.35	-4.28	-5.90	-5.80	-16	-0.8
$eN\,d_4$	-3.80	-9.6	-6.11	-4.30	-24	-1.25

Table 7-3 (Continued)

Specimen	G-S-8	G-S-10	G-D-8	G-D-10	Searching Space	
Parameter	Identified	Identified	Identified	Identified	Lower	Upper
$rDispP$	0.58	0.49	0.53	0.69	0.13	2.5
$fForceP$	0.20	0.32	0.31	0.16	0.06	1.25
$uForceP$	0.18	0.08	0.18	0.078	0.013	0.25
$rDispN$	0.46	0.75	0.22	0.46	0.13	2.5
$fForceN$	0.21	0.32	0.26	0.29	0.06	1.25
$uForceN$	0.12	0.14	0.03	0.14	0.007	0.14
gK_1	0.29	0.31	0.48	0.32	0.025	0.5
gK_2	0.13	0.34	0.22	0.44	0.025	0.5
gK_3	0.37	0.42	0.23	0.05	0.025	0.5
gK_4	0.21	0.43	0.03	0.08	0.025	0.5
gK_{lim}	0.06	0.03	0.41	0.37	0.025	0.5
gD_1	0.10	0.24	0.45	0.03	0.025	0.5
gD_2	0.46	0.05	0.10	0.19	0.025	0.5
gD_3	0.13	0.32	0.27	0.35	0.025	0.5
gD_4	0.48	0.20	0.09	0.21	0.025	0.5
gD_{lim}	0.03	0.07	0.06	0.44	0.025	0.5
gF_1	0.1	0.31	0.44	0.44	0.025	0.5
gF_2	0.37	0.40	0.45	0.41	0.025	0.5
gF_3	0.05	0.26	0.10	0.31	0.025	0.5
gF_4	0.07	0.45	0.33	0.25	0.025	0.5
gF_{lim}	0.33	0.50	0.47	0.35	0.025	0.5
gE	23.5	12.64	19.99	26.6	2.5	50

Table 7-4 Parameter Identification Results and Search Space for 2# Pinching4

Specimen	G-S-8	G-S-10	G-D-8	G-D-10	Searching Space	
Parameter	Identified	Identified	Identified	Identified	Lower	Upper
ePf_1	24.6	20.5	62.3	48.4	6.25	125
ePd_1	0.48	0.69	1.52	0.83	0.13	2.5
ePf_2	47.5	26.8	72.1	63.2	9.25	185
ePd_2	1.34	1.86	6.20	0.76	0.38	7.5
ePf_3	52.5	44.2	33.6	99.8	11.25	225
ePd_3	5.43	9.45	5.10	2.45	1	20
ePf_4	4.39	2.08	4.39	1.68	1.25	25
ePd_4	7.18	9.75	18.1	4.90	1.25	25
eNf_1	-42.8	-22.8	-76.8	-78.4	-125	-6.25
eNd_1	-0.86	-0.28	-2.08	-1.32	-2.5	-0.13
eNf_2	-45.3	-31.1	-60.3	-72.08	-185	-9.25
ePd_2	-2.40	-3.76	-2.76	-1.73	-7.5	-0.38
eNf_3	-46.5	-12.58	-52.6	-19.5	-225	-11.25
eNd_3	-3.20	-3.80	-3.12	-1.62	-20	-1
eNf_4	-1.63	-1.46	-6.08	-1.88	-25	-1.25
eNd_4	-4.05	-9.8	-6.09	-4.46	-25	-1.25

Table 7-4 (Continued)

Specimen Parameter	G-S-8 Identified	G-S-10 Identified	G-D-8 Identified	G-D-10 Identified	Searching Space Lower	 Upper
rDispP	0.54	0.66	0.32	0.68	0.13	2.5
fForceP	0.32	0.32	0.31	0.16	0.06	1.25
uForceP	0.12	0.08	0.18	0.078	0.013	0.25
rDispN	0.42	0.75	0.22	0.46	0.13	2.5
fForceN	0.19	0.32	0.26	0.29	0.06	1.25
uForceN	0.08	0.14	0.03	0.14	0.007	0.14
gK_1	0.29	0.31	0.48	0.32	0.025	0.5
gK_2	0.13	0.34	0.22	0.44	0.025	0.5
gK_3	0.37	0.42	0.23	0.05	0.025	0.5
gK_4	0.21	0.43	0.03	0.08	0.025	0.5
$gK_{\lim}$	0.06	0.03	0.41	0.37	0.025	0.5
gD_1	0.10	0.24	0.45	0.03	0.025	0.5
gD_2	0.46	0.05	0.10	0.19	0.025	0.5
gD_3	0.13	0.32	0.27	0.35	0.025	0.5
gD_4	0.48	0.20	0.09	0.21	0.025	0.5
$gD_{\lim}$	0.03	0.07	0.06	0.44	0.025	0.5
gF_1	0.12	0.31	0.44	0.44	0.025	0.5
gF_2	0.37	0.40	0.45	0.41	0.025	0.5
gF_3	0.05	0.26	0.10	0.31	0.025	0.5
gF_4	0.07	0.45	0.33	0.25	0.025	0.5
$gF_{\lim}$	0.33	0.50	0.47	0.35	0.025	0.5
gE	23.5	12.64	19.99	26.6	2.5	50

Table 7-5 Parameter Identification Results and Search Space for 3 Gap Material

Specimen		G-S-8	G-S-10	G-D-8	G-D-10	Searching Space	
Material	Parameter	Identified	Identified	Identified	Identified	Lower	Upper
Gap 1	gap	-0.22	-0.3	-0.32	-0.23	-1.6	-0.08
Gap 2	gap	0.31	0.6	0.47	0.2	0.08	1.6
Gap 3	gap	-3.3	-3.9	-3	-3.4	-10	-0.5

After substituting the identified optimal parameters into the numerical hysteresis model, the predicted hysteresis curves can be obtained. To validate the accuracy of the model, the simulation results are compared with experimental data, as shown in Figure 7-1. The comparison demonstrates a high level of agreement between the simulated and experimentally measured hysteresis curves, indicating that the developed model can accurately reproduce the hysteretic behavior of the connector.

Further analysis shows that the model effectively captures the strength envelope of the force–displacement curve and reasonably reflects the hysteretic characteristics observed during the experiment. In particular, the model successfully simulates the initial slip behavior, especially in the vicinity of the origin during the early stages of loading. Moreover, the model demonstrates accurate tracking of both loading and unloading paths, offering a reliable description of the cyclic response of the joint under repeated loading.

The cumulative energy dissipation, used as an error metric, also serves to quantify the discrepancy between simulation results and experimental observations. The cumulative dissipated energy over time can be calculated using the following expression[266-268]:

$$E_d\left(t\right)=\int_0^t F\left(t\right)V\left(t\right)dt \tag{7-11}$$

Where， t is the experimental time， E_d is the cumulative energy dissipation.

The comparison based on cumulative dissipated energy is also presented in Figure 7-1. As shown, the numerical simulation closely matches the experimental results in terms of cumulative energy dissipation, especially in the pre-cracking stage of the specimens, where the model accurately predicts the structure's energy dissipation capacity. However, in certain cases, the model slightly overestimates the dissipated energy compared to the experimental data, particularly during the force degradation phase of the loading process. This discrepancy becomes more pronounced at larger displacements, suggesting that the model's description of the hysteretic energy dissipation mechanism under extreme loading conditions still involves some degree of error.

This deviation may be attributed to the model's simplified treatment of damage accumulation, material degradation, and contact nonlinearity, which leads to a somewhat conservative prediction of energy dissipation in the large-deformation phase. Nevertheless, the model is still capable of reasonably representing the energy dissipation characteristics of glubam joint connectors under cyclic loading, and thus provides a reliable numerical tool for subsequent structural analysis and engineering applications.

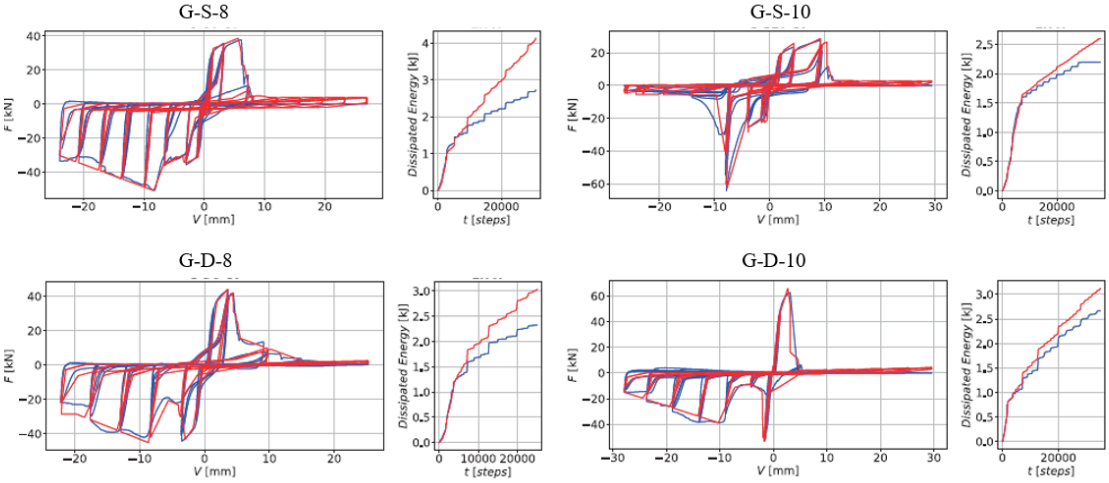

Figure 7-1 Comparison Between Model Predictions and Experimental Results After Parameter Identification (Load–Displacement Relationship and Energy Dissipation Time History)

7. 2. 2 Neural Network-Based Parameter Identification Results

While the Genetic Algorithm (GA)-based identification method offers the potential for accurate prediction, it is limited in terms of computational efficiency (as discussed in Section 7.2.1). Neural network-based parameter estimation has been applied in several previous studies[269,270]. However, the model proposed in this study exhibits significantly higher degrees of freedom—with up to 79 tunable parameters, compared to the 10 to 20 parameters typically considered in existing work—and multiple parameter combinations may lead to similar model responses. This makes direct training and prediction using neural networks suboptimal.

To address this challenge, this study proposes an innovative parameter estimation approach that integrates neural networks with sensitivity analysis. Through sensitivity analysis, the most influential parameters affecting the model response are first identified, effectively reducing the dimensionality of the parameter search space. This step significantly improves both the training efficiency and prediction accuracy of the neural network.

Subsequently, a neural network is constructed and trained based on the filtered subset of key parameters to optimize the parameter identification process. This approach not only enhances computational efficiency but also improves model robustness while maintaining a high level of predictive accuracy.

7. 2. 2. 1 **Parameter Sensitivity Analysis**

To support the identification of model parameters, a sensitivity analysis was first performed[31,269] on the parameters to be estimated. In order to evaluate the sensitivity of parameters in the Pinching4 material model, a forward finite difference method was employed, using a gradually reduced perturbation $\left|\left(\xi-1\right)\theta\right|$ for analysis.

The perturbation factor ξ was applied as a scaling coefficient, ranging from 0.6 to 1.4, relative to the baseline parameter vector θ, which was previously obtained using the Genetic Algorithm (GA). Next, the mean squared error (MSE) between the predicted and baseline force F_s responses was computed to obtain the normalized response sensitivity. To rank the model parameters according to their sensitivity, the unit response sensitivity ψ_i of the ith parameter was defined as follows:

$$\psi_i\left(\xi_i\in\left[0.6,1.4\right]\right)=\frac{1}{n}\left[F_s\left(\xi_i\theta,v\right)-F_s\left(\theta,v\right)\right]^T\left[F_s\left(\xi_i\theta,v\right)-F_s\left(\theta,v\right)\right] \qquad （7\text{-}12）$$

Where， n is the length of vector F_s and ξ_i is a row vector with a nonzero value only in the ith column ，（eg， $\xi_1=\left[\xi_1 \quad 0 \quad \dots \quad 0\right]$）.

In this section, the sensitivity analysis is conducted specifically for the experimental case G-D-8, as the results for all cases exhibit similar trends. Figure 7-2(a) presents the sensitivity ranking of the hysteresis model consisting of 79 tunable parameters under cyclic loading conditions. These parameters include:38 parameters from the Pinching4 spring model #1, 2 parameters from the Gap element in Phase 1 (initial loading stage), 38 parameters from the Pinching4 spring model #2, and 1 parameter from the Gap element in Phase 2 (contact loading stage).

The parameter indexing and ordering follow the definitions provided in Table 7-2.According to Equation (7-12), the reference parameter vector for the sensitivity analysis is set to zero, as illustrated in Figure 7-2(b).

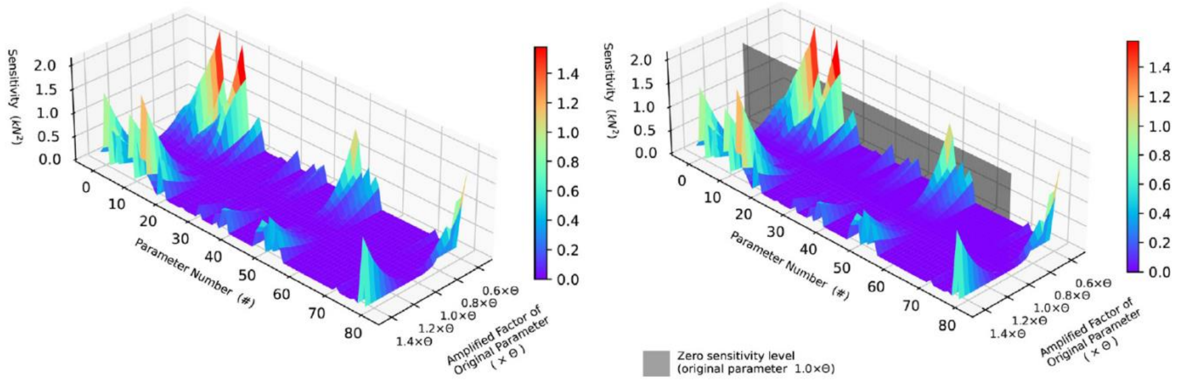

(a) (b)

Figure 7-2 Global Parameter Sensitivity of the Two Pinching4 Materials in Specimen G-D-8;Figure (b) illustrates the zero-sensitivity region when using the original parameters $(1.0\times\theta)$

7. 2. 2. 2 Method Overview

The neural network-based parameter estimation approach adopted in this study consists of the following three key steps:

(1) Database Construction Using Latin Hypercube Sampling (LHS):

The high degree of freedom in the proposed model makes it impractical to fully explore the entire parameter space. In addition, purely random sampling methods (e.g., Monte Carlo) may lack sufficient representativeness. Therefore, Latin Hypercube Sampling[271] (LHS) is used in this step to reduce the total number of required samples while maintaining coverage across the parameter space.

Specifically, the upper and lower bounds for each parameter are the same as previously defined and are uniformly divided into 10 sampling intervals. Based on the LHS method, a total of 5000 valid samples are generated after excluding combinations that fail to converge.

These samples are randomly split into a training set (3000 samples), a validation set (1000 samples), and a test set (1000 samples). The force sequence (representing the simulated structural behavior) and the corresponding parameter vectors are treated as the input and output of the neural network, respectively.

(2) Sensitivity-Guided Neural Network Training:

The Transformer[263,272], a powerful and widely recognized neural network architecture, is adopted due to its strong ability to capture patterns in sequential data (such as the force–time series used in this study) and make accurate predictions.

As revealed in the parameter sensitivity analysis in Section 7.2.2.1, the importance of different parameters varies significantly. Therefore, the sensitivity results are used to guide the training and optimization process.

Inspired by related work[273], particularly in the area of physics-informed response modeling[274,275], this guidance is incorporated into the training through modifications to the loss function:

$$Loss_{Mask} = \max\left(\sqrt{sensitivity_{norm}}, 0.1\right) \times Loss_{MSE} \tag{7-13}$$

Where, $Loss_{Mask}$ denotes the modified loss function, and $sensitivity_{norm}$ represents the array of normalized sensitivity values for all parameters, computed based on Equation (7-12), where the most important parameter is normalized to a weight of 1.0. $Loss_{MSE}$ refers to the standard mean squared error (MSE) loss. Considering the difference between global sensitivity and local sensitivity, and drawing inspiration from the well-known scaled dot-product attention mechanism, Equation (7-13) incorporates a square root operation and a minimum weight threshold. This design prevents the complete neglect of certain parameters and avoids extreme imbalance in weight values across the parameter set.

(3) Ensemble Prediction and Cross-Validation

The ensemble strategy is a widely adopted approach aimed at canceling out individual model biases through averaging[276,277]. However, the presence of divergent samples not only limits the accuracy of the model but also hinders the ensemble prediction process.

Divergent results are typically characterized by large deviations from the true values, which may introduce significant errors into the averaged prediction sequence. As a result, the mean squared error (MSE) between divergent and convergent predictions is expected to be substantially higher than the MSE within the set of convergent predictions.

This discrepancy allows for the effective filtering of divergent samples, thereby ensuring more accurate and reliable analysis without directly relying on the true force–time sequence. To this end, a cross-validation-based filtering process is proposed. In Filter 1, a variable is calculated using Equation (7-14) to eliminate predictions with large bias—typically corresponding to divergent samples. For Filter 2, if the number of remaining predictions after filtering is less than a specified threshold, the entire ensemble prediction is considered unstable. Finally, in Filter 3, if the predicted maximum force $\left(Force_{\max}\right)$ is significantly greater than the peak load capacity of the target specimen, the corresponding prediction is deemed unreasonable and discarded.

$$MSE_{Ave,i} = \frac{1}{N}\sum_{j=1}^{N} MSE_{fun}\left(\mathrm{Pr}\,ed_i, \mathrm{Pr}\,ed_j\right) \tag{7-14}$$

Where N denotes the total number of predictions (models), $\mathrm{Pr}\,ed_i$ represents the prediction result of model i， MSE_{func} is the conventional mean squared error (MSE) loss function, and $MSE_{Ave,i}$ denotes the average MSE between prediction I and all other predictions.

7. 2. 2. 3 Identification Results

Based on the statistical distribution of all prediction results, the maximum acceptable value of MSE_{Ave} was set to 2000, and $Force_{\max}$ was set to 500, which is approximately ten times the peak load observed in the experiment. A total of six independent models were trained for prediction. If the number of remaining models after filtering is less than or equal to two (i.e., if more than two-thirds of the models are rejected), the final prediction is discarded due to significant instability. The results are illustrated in Figures 7-3, 7-4, and 7-5. The model series labeled “Asse” represents the ensemble prediction results. The ensemble predictions achieved an average MSE loss of 43.6, which is 30.2% lower than that of individual model predictions. In total, 53.8% of the test samples had MSE losses below 25, and 92.5% of the samples had MSE losses below 100. Only a small portion (4.3%) of the samples exhibited MSE losses exceeding 150. As shown in Figure 7-5, predictions with MSE loss below 25 and 100 can be regarded as accurate and acceptable, respectively. The number of divergent predictions generated by the ensemble strategy was only 19 out of 1000 test samples. This represents a 71.5% reduction in divergent predictions, thereby significantly enhancing the practical applicability of the method. The cross-validation-based filtering process plays a critical role in this performance improvement. Without filtering, the average MSE loss of the ensemble predictions increases by 11.1% (rising to 48.5), and the number of divergent predictions increases to 159—which is 7.4 times higher than with filtering—substantially limiting the utility of the proposed method. In addition, the prediction time per sample is less than one second, demonstrating very high computational efficiency.

In summary, the proposed neural network-based method provides reasonably accurate and efficient predictions, making it a valuable tool for parameter estimation across various scenarios.

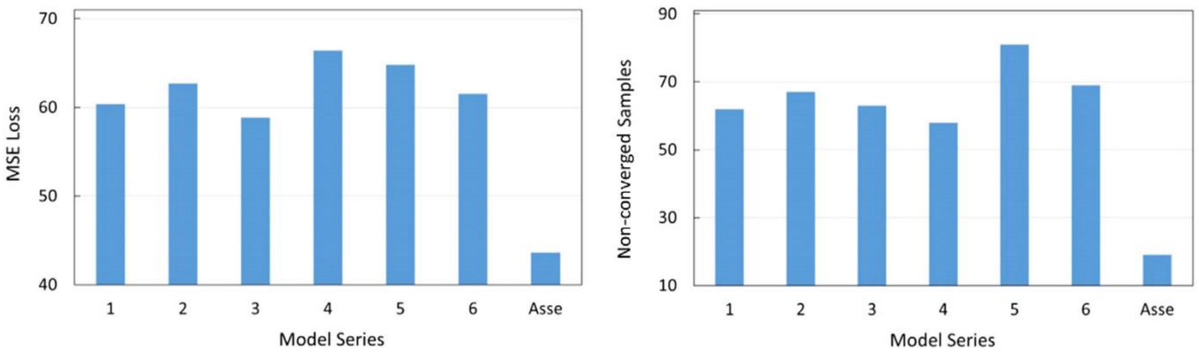

Figure 7-3 Average MSE Loss and Number of Divergent Samples in Each Prediction

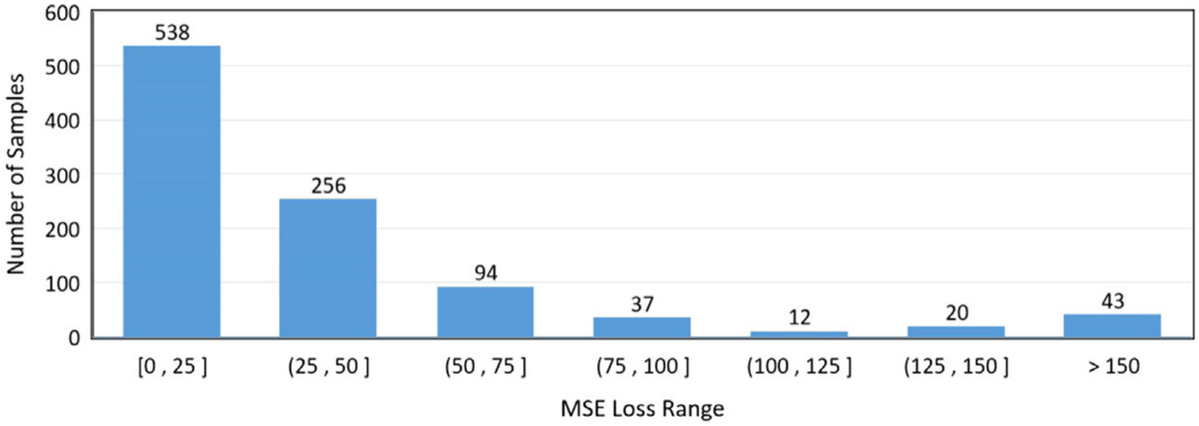

Figure 7-4 Sample Distribution Across Different MSE Loss Ranges in the Ensemble Prediction Case (Test Dataset)

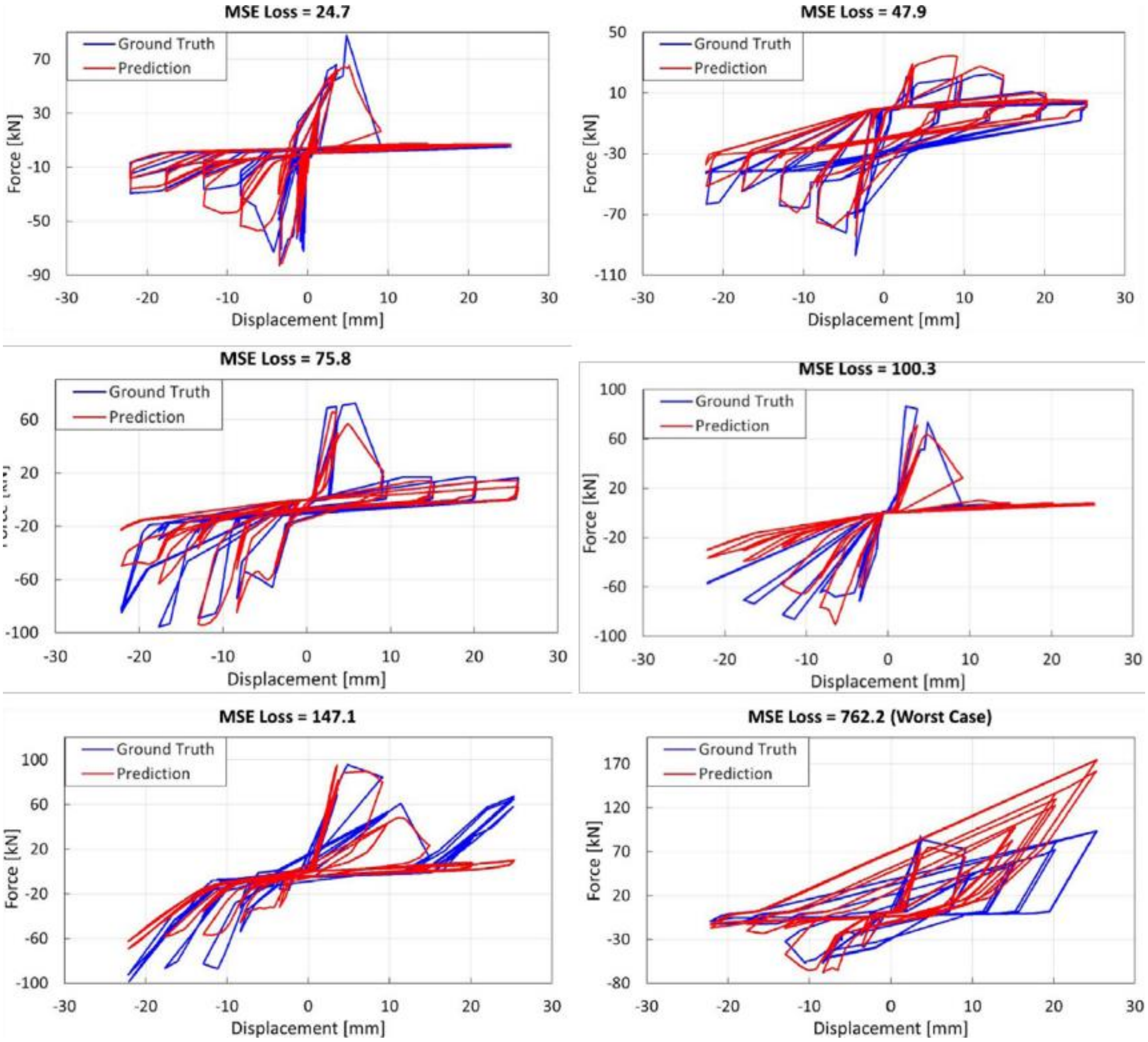

Figure 7-5 Visualization of Typical Prediction Results Under Different MSE Levels (Ensemble Prediction)

7. 2. 3 Bayesian Parameter Identification Results

7. 2. 3. 1 Reduction of the Model Parameter Set

When selecting key model parameters for identification, it is essential to strike an optimal balance among parameter sensitivity, physical significance, and computational cost. As shown in Figure 7-2, most of the highly sensitive parameters are located within the parameter range 1 to 16 of the Pinching4 material model (see parameter definitions in Table 7-2). From a physical standpoint, the first 16 parameters（ $ePf_1 - ePf_4$ ； $ePd_1 - ePd_4$ ； $eNf_1 - eNf_4$ ； $eNd_1 - eNd_4$ ）in each Pinching4 material model control the backbone curve of the hysteresis model, and are therefore crucial for capturing the mechanical behavior of the connector.

In addition, slip behavior has a significant influence on the overall performance of the joint connector, highlighting the importance of these parameters within the model.

As a result, a total of 35 parameters were selected for Bayesian identification of the hysteresis model under tension–compression cyclic loading. These include: the first 16 parameters from Pinching4 material #1; another 16 parameters from Pinching4 material #2, and 3 parameters from the Gap material model. The remaining parameters are assigned constant values, consistent with those identified using the Genetic Algorithm, in order to reduce computational complexity and enhance optimization efficiency. This strategy ensures that the model maintains a reasonable computational cost while preserving computational accuracy and respecting the physical rationality of the parameterization.

7.2.3.2 Identification Results

In this study, the prior probability density function (PDF) of the model parameters is assumed to be mutually independent and constructed based on empirical mean values. Each prior is described using a truncated normal distribution. The upper and lower bounds of the distribution are defined using a magnification factor of 5.0 and a reduction factor of 0.2, respectively, while the coefficient of variation for the prior standard deviation is set to 0.1.

Based on this configuration, a total of 160 samples were generated and divided into 2 parameter chains to ensure adequate sampling diversity and representativeness.

During the parameter identification and model validation process, the Sequential Monte Carlo (SMC) sampling method was first used to compute posterior parameter samples. These posterior values were then substituted into the hysteresis model to generate predicted responses.

The predicted results were compared with experimental measurements to assess the model's accuracy, as shown in Figure 7-6. The results indicate a high degree of consistency between the predicted and measured hysteresis curves, verifying the model's ability to effectively capture the force–displacement behavior of the connector. In particular, the model accurately reproduces the slip behavior observed near the origin. In addition, Figure 7-7 presents a statistical comparison between the experimental results and the 160-sample-based model predictions, including the force–time history, backbone curve, and cumulative energy dissipation over time. The analysis shows that the model slightly overestimates energy dissipation during the force degradation phase, and this deviation becomes more pronounced as displacement increases, especially in both the tensile and compressive regions. However, the model still provides accurate predictions of energy dissipation in the pre-cracking stage, and overall demonstrates a high level of predictive accuracy. Despite minor discrepancies in certain stages, the proposed hysteresis model accurately characterizes the strength envelope of the force–displacement curve and effectively captures the cumulative energy dissipation behavior of the connector.

Overall, the model exhibits strong accuracy and reliability in evaluating the cyclic response of glubam connectors, and offers a solid theoretical foundation for practical engineering applications and design optimization.

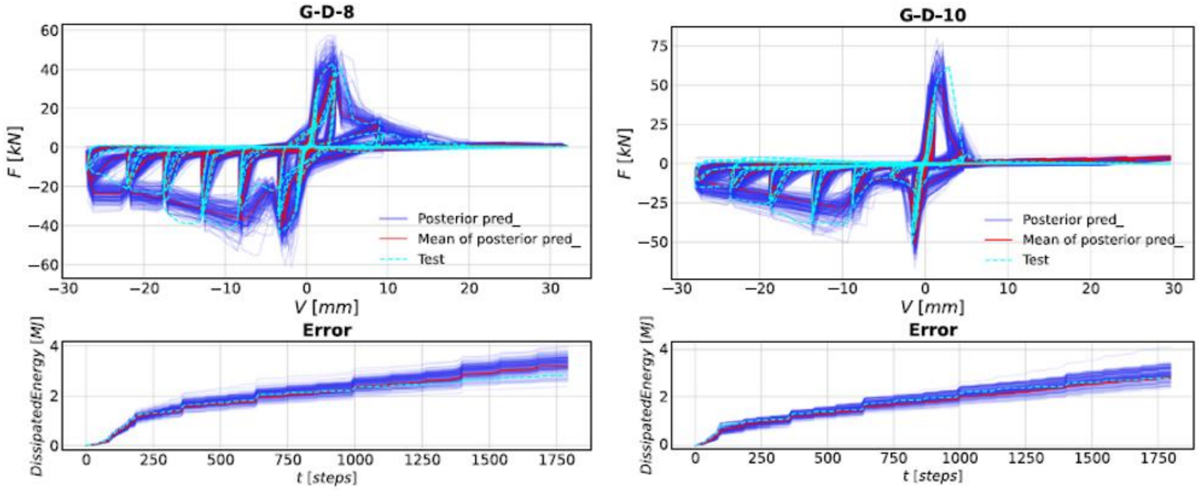

Figure 7-6 Predicted Results Obtained by Substituting Posterior Samples and Posterior Mean Parameters Identified via Bayesian Inference

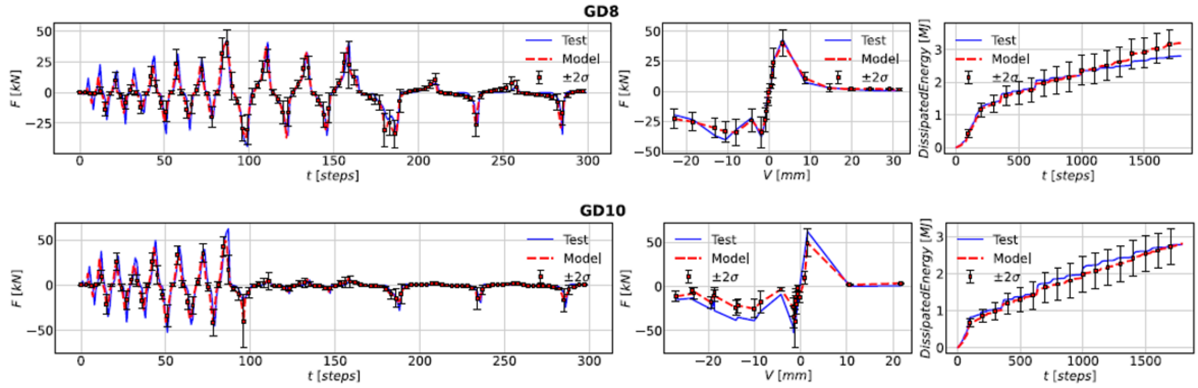

Figure 7-7 Comparison Between Test Results and Posterior Predictions Based on 160 Sample Statistics: Force–Time History (First Column), Backbone Curve (Second Column), and Cumulative Energy Dissipation–Time History (Third Column)

To gain deeper insight into the differences between the experimental results and model predictions, it is essential to perform a comprehensive analysis of the probability distribution of the predicted responses. To this end, the output response data from 160 posterior sample cases were aggregated, and basic statistical metrics including the mean and standard deviation （σ） were computed.

Figure 12 presents a full comparison between the mean of the 160 samples and the experimental data in terms of the force–time history, backbone curve, and cumulative energy dissipation–time history. The error bars in the figure represent a confidence interval of $\pm 2\sigma$. The results indicate that the model-predicted confidence bands consistently encompass the experimental observations, further validating the accuracy of the selected model parameters in representing the actual mechanical behavior of the connection.

In particular, the comparisons for the backbone curve and cumulative energy dissipation show an exceptionally high degree of consistency within the $\pm 2\sigma$ range, demonstrating that the proposed numerical model can reliably simulate the nonlinear hysteretic response of the glubam connectors under cyclic loading.

7. 2. 4 **Comparison of the Three Parameter Identification Methods**

In the previous sections, three different approaches were applied and validated for estimating the parameters of the proposed hysteresis model: the Genetic Algorithm (GA), the deterministic neural network-based method, and the probabilistic Bayesian inference method. To evaluate the performance of these methods, their prediction results were compared using representative experimental data. A typical case is visualized in Figure 7-8, and a comparative summary of the characteristics and applicability of each method is presented in Table 7-6, which serves as a basis for providing practical guidance on method selection.

As revealed by the comparative analysis in Figure 7-8 and Table 7-6, each method exhibits distinct advantages and limitations in terms of accuracy, efficiency, and stability.The Bayesian method is the only probabilistic approach, capable of quantifying parameter uncertainty. Although its prediction accuracy is moderate, its computational efficiency is relatively low, making it more suitable for scenarios where uncertainty quantification is essential. The Genetic Algorithm achieved the highest prediction accuracy among all methods, with moderate computational cost. However, its optimization performance is highly dependent on the initial parameter settings, leading to lower stability. Therefore, it is recommended to be used in combination with preliminary parameter estimation to enhance optimization robustness. The neural network-based method provides the highest computational efficiency, though its prediction accuracy is slightly lower than that of GA. This makes it more suitable for rapid estimation tasks or the early stage of large-scale parameter identification.

In summary, the choice of method should be based on specific application requirements: For scenarios emphasizing accuracy and stability, the Genetic Algorithm is preferable. For fast parameter estimation, the neural network approach offers clear advantages. For uncertainty analysis, the Bayesian method is the most appropriate choice. The findings of this study offer valuable guidance for future work on the optimization and application of hysteresis models in structural analysis and design.

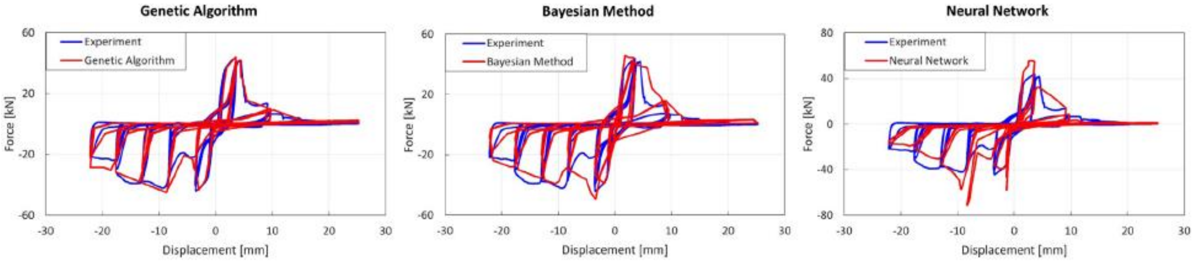

Figure 7-8 Comparison of the Three Methods in the Analysis of a Representative Experimental Case (G-D-8)

Table 7-6 Characteristics and Comparison of the Three Methods

Method	Genetic algorithm	Neural network	Bayesian Methods
Accuracy	High，MSE=8.7	Relatively low，MSE=27.6	Medium，MSE=16.1
Time spent in optimization process	Around 6h	Training：0.5h； Prediction：Less than 1s	Around 6h
Sequence length in optimization	25000	25000	1800
Overall efficiency	Medium	Low	High
Level of detail of output	Deterministic	Deterministic	Probabilistic, with uncertainty
Stability	Unstable(largely depend on the initial population）	Medium(somehow depend on the initialization and hyperparameter	Stable(with a reasonable prior distribution)

Recommended situations	Accurate parameter identification based on preliminary	Fast and preliminary parameter	Uncertainty quantification of parameters

7.3 Parameter Identification of the Hysteresis Model for Steel Side-Clamped-plate Glubam Connectors

The hysteresis model proposed in this study for Steel Side-Clamped-plate Glubam Connectors is governed by 20 parameters. To improve both the efficiency and accuracy of parameter identification, this section introduces artificial intelligence (AI) algorithms to enable intelligent and automated calibration.

Three previously discussed AI-based optimization methods—Genetic Algorithm (GA), Neural Network (NN), and Bayesian Inference—are employed to identify the model parameters of the hysteresis system.

It is important to note that the hysteresis model proposed for the steel side-clamped-plate glubam connector is not purely phenomenological; all parameters possess clear physical interpretations, and several can be derived directly from experimental observations in combination with Equations (6-39) to (6-48).

Therefore, to balance physical interpretability with identification precision, a two-stage strategy—combining coarse estimation and refined optimization—is adopted in this section:

1. Preliminary Parameter Estimation (Coarse Stage):
   Based on experimental observations and in conjunction with Equations (6-39) to (6-48), key parameters in the hysteresis model are initially estimated to provide a reliable reference for subsequent optimization.
2. Refined Parameter Identification:
   Building upon the coarse estimates, reasonable upper and lower bounds for each parameter are defined using magnification and reduction factors around the estimated values. Within this constrained search space, the Genetic Algorithm, Neural Network method, and Bayesian Inference are individually applied to further refine the parameters and ensure the model accurately fits the experimental data.

This two-stage approach—combining physics-informed coarse estimation with AI-driven fine optimization—strikes an effective balance between physical rationality and computational efficiency. It leverages prior knowledge from experimental data and analytical formulas, while also utilizing the power of machine learning algorithms for precise and efficient parameter identification, thereby ensuring the developed hysteresis model performs well in terms of both computational accuracy and physical consistency.

7. 3. 1 **Preliminary Parameter Estimation**

Predefining the values of certain parameters and constraining the search space for the remaining parameters not only significantly reduces the computational cost of the calibration process but also improves convergence and accuracy during optimization. Therefore, performing a preliminary estimation of parameters before optimization is essential. This process mainly involves extracting key feature points and relevant parameters from the experimental hysteresis curves—such as initial stiffness K and yield slip V_y—in order to establish a reasonable initial parameter range. This section provides a detailed explanation of the definition of hysteresis curve feature points and the methodology for coarsely determining model parameters. To simplify the analysis, this discussion focuses only on the model parameters governing the positive loading side of the hysteresis curve. Parameters for the negative loading side can be derived based on symmetry assumptions or similar techniques.

To solve for all unknown parameters controlling the positive side of the hysteresis curve, the following quantities need to be specified: the initial stiffness K, the yield slip V_y, and five key feature points on the positive side of the hysteresis curve: P_1、P_2、P_3、P_4 and P_5, as illustrated in Figure 7-9.

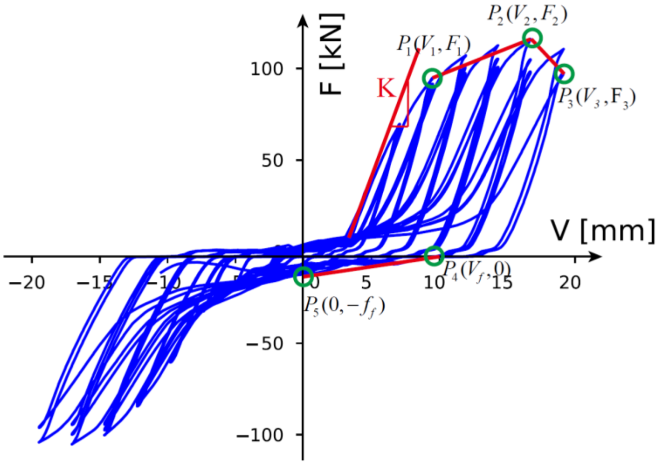

Figure 7-9 Selection of Hysteresis Curve Feature Points in Simplified Model Development

The points $P_1\left(V_1, F_1\right)$ and $P_2\left(V_2, F_2\right)$ correspond to the onset of hardening and the peak loading point, respectively, and can be roughly estimated based on the hardening segment of the hysteresis curve. The point $P_3\left(V_3, F_3\right)$, defined as the damage point, corresponds to the point where the load drops to 80% of the maximum load. Additionally, $P_4\left(V_f, 0\right)$ is defined as the intercept of the hysteresis curve on the positive x-axis, and $P_5\left(0, -f_f\right)$ is defined as the intercept on the negative y-axis; both values can be preliminarily estimated based on the unloading stage of the curve. Considering that the hysteresis response tends to stabilize after repeated loading cycles, it is recommended to determine the specific values of P_4 and P_5 based on the final loading cycle to minimize the influence of early-cycle fluctuations on parameter identification.

The proposed rough parameter identification method includes the following key steps:

(i) Initial stiffness of the model =K;

(ii) Displacement corresponding to the yielding of the bolt model $=V_y$;

(iii) Post-peak stiffness of the bolt model = slope of the line segment P_4P_3

(iv) Yield strength of the bolt model = f_{fy};

(v) The force values of the model at $V = V_1$ and $V = V_2$ should match the experimental results.

In addition, this study assumes that $G_{2+} = G_{3+} = G_{1+} + f_{cy} / k - iso_{1e+}$, $V_{2y+} = 0.5\left(V_1 + V_{y+}\right)$ and $V_{3y+} = V_1$. V_y is the experimentally obtained yielding displacement of the joint. Based on these assumptions, the material components $EP - ISO_2$ and $EP - ISO_3$ are activated immediately after the yielding of the main material $EP - ISO_1$. When the joint displacement exceeds V_1, the compressive force contribution of glubam increases linearly according to the slope $k - iso_{1p+}$. The yielding behavior of $EP - ISO_2$ and $EP - ISO_3$ effectively simulates the smooth transition from the elastic stage to the post-yield stage.

Based on the above conditions, the system parameters must satisfy the following equation constraints:

$$K_{fe}K_L / (K_{fe} + K_L) + k_{1e+}^{iso} = K$$

$$V_{fy} = V_y$$

$$K_{fp} = f_f / V_f$$

$$f_{fy} = f_f$$

$$F\left(V_1\right) = F_1$$

$$F\left(V_2\right) = F_2$$

$$F\left(V_3\right) = F_3$$

By substituting Equations (6-39), (6-45), and (6-46) into the aforementioned equations, the parameters of the bolt and glubam compression models can be calculated as follows:

For the bolt model:

$$f_{fy} = f_f$$

$$K_{fp} = f_f / \left(V_f\right)$$

$$K_L = \frac{f_{fy} K_{fe}}{K_{fe} V_y - f_{fy}}$$

For the glubam bearing model:

$$k_{1e+}^{iso} = K - f_{fy} / V_y$$

$$k_{1p+}^{iso} = \frac{F_2 - F_1}{V_2 - V_1} - K_{fp}$$

$$f_{cy} = \frac{F_2 - f_{fy} - V_2\left(k_{1p+}^{iso} + K_{fp}\right) + V_y K_{fp} + k_{1p+}^{iso} G_{1+}}{3 - k_{1p+}^{iso} / k_{1e+}^{iso}}$$

$$G_{2+} = G_{3+} = f_{cy} / k_{1e+}^{iso} + G_{1+}$$

$$k_{2e+}^{iso} = \frac{f_{cy}}{0.5(V_y + V_1) - G_{2+} - G_{1+}}$$

$$k_{3e+}^{iso} = \frac{f_{cy}}{V_1 - G_{2+} - G_{1+}}$$

It can be observed from the hysteresis curves that the initial loading stiffness is always lower than the unloading stiffness. This phenomenon can be effectively simulated by introducing the L material component into the bolt model. In the aforementioned equations, there are two undetermined parameters, K_{fe} and K_L, one of which can be estimated through assumption. Preliminary parametric studies have shown that increasing the value of K_{fe} results in a steeper unloading slope, although its effect on energy dissipation is relatively minor. This observation has also been noted in previous literature[278]. Therefore, to achieve optimal fitting of the unloading stiffness, the approximate range of K_{fe} is estimated to be 15–35 kN/mm. Table 7-7 summarizes the preliminary parameter identification results of the hysteresis model (i.e., the APD model) for the Steel Side-Clamped-plate Glubam Connectors.

Table 7-7 Preliminary Identification Results of the Hysteresis Model Parameters for the Steel Side-Clamped-plate Glubam Connectors

Parameter	k_{1e+}^{iso}	f_{cy+}	k_{1p+}^{iso}	k_{2e+}^{iso}	k_{3e+}^{iso}	G_{1+}	G_{2+}	k_{1e-}^{iso}	f_{cy-}	k_{1p-}^{iso}	k_{2e-}^{iso}	k_{3e-}^{iso}
	$\frac{kN}{mm}$	kN	$\frac{kN}{mm}$	$\frac{kN}{mm}$	$\frac{kN}{mm}$	mm	mm	$\frac{kN}{mm}$	kN	$\frac{kN}{mm}$	$\frac{kN}{mm}$	$\frac{kN}{mm}$
B10	8.4	12.1	4.5	2.4	2.2	1.5	1.45	8.4	15.2	4.5	2.93	2.7
B12	11.5	15.5	5.5	2.33	2.13	1.5	1.35	11.5	18.5	5.5	3.14	2.9
B14	13.6	6.05	8	0.6	0.4	1.5	0.44	13.6	4.4	8	0.62	0.7
B16	15.6	21.0	2	1.89	1.6	1.5	1.35	15.6	35.7	2	3.3	2.9

Table 7-7 (Continued)

Parameter	G_{1-}	G_{2-}	K_L	f_{fy}	K_{fe}	K_{fp}	F_{d+}	F_{d-}	I_{d+}	I_{d-}
	mm	mm	$\frac{kN}{mm}$	kN	$\frac{kN}{mm}$	$\frac{kN}{mm}$	kN	kN		
B10	1	1.81	1.9	8	20	0.6	70.5	92.3	0.8	0.25
B12	1	1.61	1.7	10	25	0.8	90	114	0.8	0.25
B14	1	0.32	1.6	12	30	1.1	118	132	0.8	0.25
B16	1	2.27	1.5	11	35	1.2	91	70	0.8	0.25

7. 3. 2 Parameter Identification Results Using Genetic Algorithm

Following the preliminary determination of model parameters (see Section 7.3.1), for parameters that can be directly obtained from prior knowledge or experimental observations (such as G_i), the initial estimates listed in Table 7-7 were adopted, and then multiplied by scaling factors of 7 and 0.4 to define the upper and lower bounds of the search space, respectively. For the other parameters, broader scaling factors of 20 and 0.2 were applied to ensure a wider search range, thereby covering more potential solutions.

To improve the efficiency and robustness of the identification process, the population size and number of generations were set to 30 and 50, respectively, resulting in a total of 1500 fitness evaluations throughout the optimization process.

Under these settings, the convergence history of the parameter identification for the reference model is shown in Figures 7-10 and 7-11. In particular, Figure 7-12 presents the identified individuals for B-10-J and B-12-J at several representative generations. It can be observed that the identification process stabilizes after approximately 30 generations, with convergence achieved after about 900 individual evaluations. Moreover, in the final generation, the predicted response of the proposed simplified model shows good agreement with the experimental benchmark response, validating the effectiveness of the method in parameter optimization.

This progressive optimization process is clearly illustrated by the trend of the best objective function values in Figure 7-11, where the evaluation results are computed based on Equation (7-1). A moving average curve is also plotted in the same figure to help visualize the overall convergence behavior of the optimization. In Figure 7-11, blue dots represent the best-performing individual in each generation, while red dots denote the average performance of the entire population. Notably, the convergence trend of both blue and red dots across generations is evident. As the number of generations increases, the population average gradually converges toward the optimal solution, indicating a reduction in solution variability and stabilization around a better solution—an expected outcome of the optimization process.

Figure 7-12 illustrates the predicted hysteretic responses of the best-performing individuals in all four cases after identification using the genetic algorithm. The results show that the proposed model is capable of accurately capturing pinching effects, damage characteristics, and asymmetric hysteresis behavior, while maintaining good consistency with the experimental results in terms of energy dissipation. The final identified parameters for all four cases are summarized in Table 7-8 (see Figure 7-12).

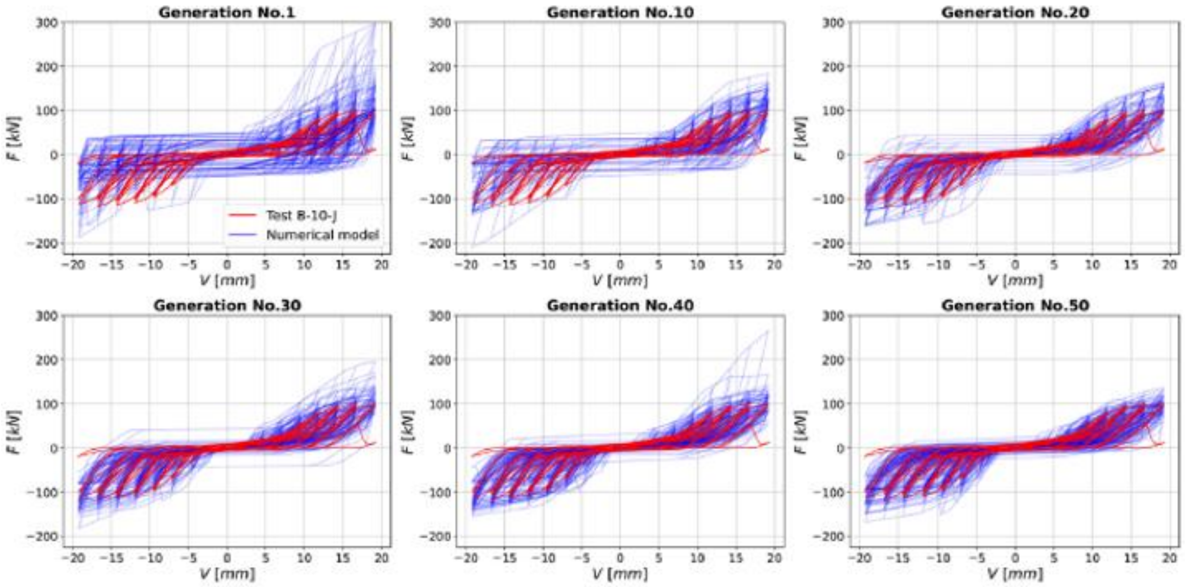

(a) B10

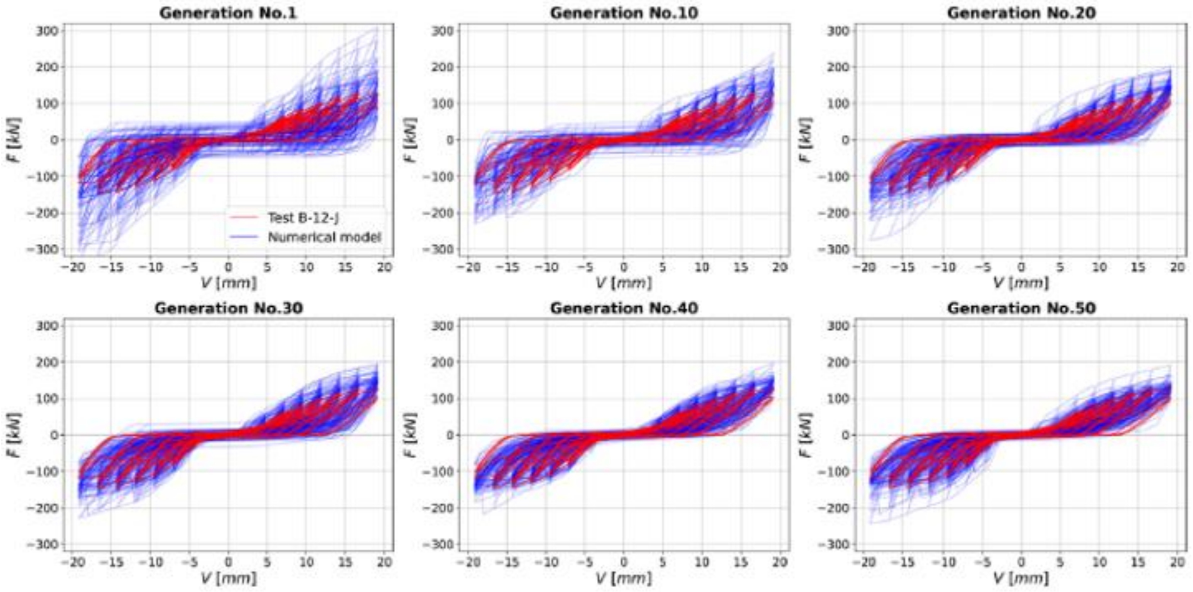

(b) B12

Figure 7-10 Predicted Results of Each Individual in Each Generation of the Genetic Algorithm: (a) B-10 and (b) B-12

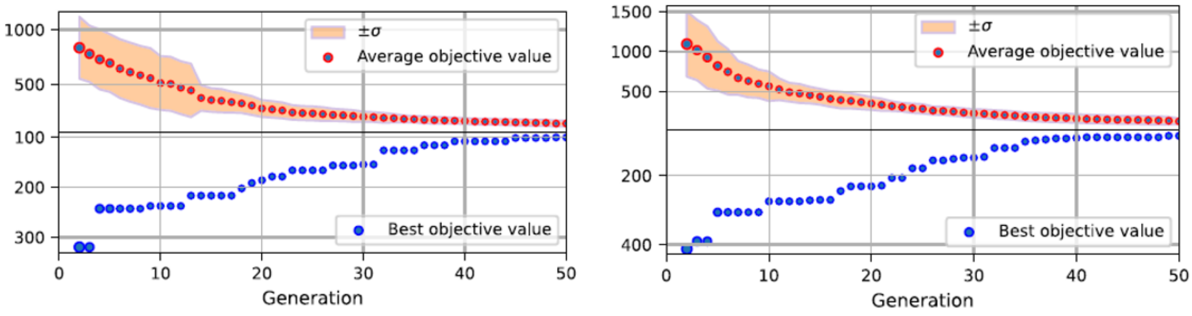

(a) B10 (b) B12

Figure 7-11 Convergence History of the Objective Function Evaluation During the Identification Process: (a) B-10 and (b) B-12

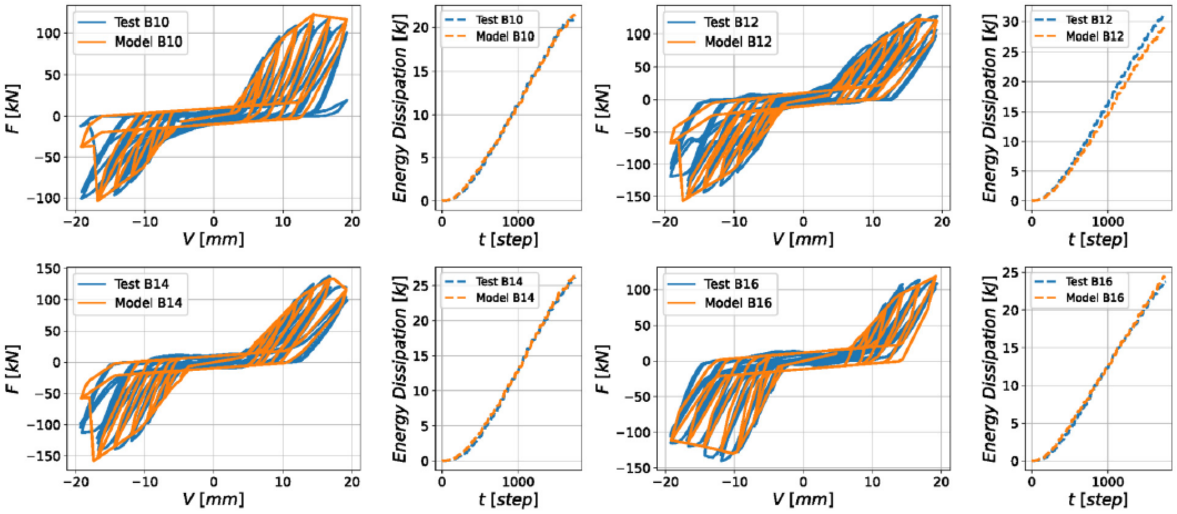

Figure 7-12 Comparison Between Experimental Hysteretic Responses and Predicted Responses by the APD Model

Table 7-8 Genetic Algorithm Identification Results of the Hysteresis Model Parameters for Steel Side-Clamped-plate Glubam Connectors

Parameter	k_{1e+}^{iso}	f_{cy+}	k_{1p+}^{iso}	k_{2e+}^{iso}	k_{3e+}^{iso}	G_{1+}	G_{2+}	k_{1e-}^{iso}	f_{cy-}	k_{1p-}^{iso}	k_{2e-}^{iso}	k_{3e-}^{iso}
	$\frac{kN}{mm}$	kN	$\frac{kN}{mm}$	$\frac{kN}{mm}$	$\frac{kN}{mm}$	mm	mm	$\frac{kN}{mm}$	kN	$\frac{kN}{mm}$	$\frac{kN}{mm}$	$\frac{kN}{mm}$
B10	16.	12.1	6.13	2.4	2.2	2.5	1.45	11.4	8.21	5.6	2.93	2.7
B12	10.	12.5	5.1	2.33	2.13	3.6	1.35	11.5	18.5	5.48	3.14	2.9
B14	10.	16.0	5.68	2.6	2.4	4.4	1.84	16.6	16.4	6.78	3.42	3.3
B16	25.	17.5	10.1	3.33	3.13	3.1	1.65	12.5	15.5	4.06	3.15	2.9

Table 7-8 (Continued)

Parameter	G_{1-} mm	G_{2-} mm	K_L $\frac{kN}{mm}$	f_{fy} kN	K_{fe} $\frac{kN}{mm}$	K_{fp} $\frac{kN}{mm}$	F_{d+} kN	F_{d-} kN	I_{d+}	I_{d-}
B10	5.5	1.81	1.5	11.3	20.6	0.60	80.5	71.3	0.85	0.32
B12	2.5	1.61	2.1	10.3	35.1	1.06	71.2	94.3	0.67	0.15
B14	3.9	1.82	2.2	10.5	25.5	0.79	81.2	105.2	0.83	0.13
B16	6.8	1.63	2.5	12	20.3	0.79	77.6	65.3	0.76	0.22

7. 3. 3 **Parameter Identification Results Using Neural Network**

Similar to other heuristic algorithms, genetic algorithms require a large number of model evaluations during the optimization process. This issue becomes particularly prominent for hysteresis models with high computational demands, making it difficult to achieve optimal efficiency. To address this challenge and improve computational efficiency while reducing overall cost, this section proposes an innovative method that integrates a Bayesian Neural Network (BNN) (Graves[279]; Blundell et al[280].) with the genetic algorithm to leverage the strengths of both approaches.

By combining Bayesian statistics with neural network architectures, BNNs not only provide a probabilistic interpretation of model predictions but also effectively quantify predictive uncertainty—an advantage not available in conventional neural networks. Leveraging the uncertainty quantification capability of BNNs enables the avoidance of reliance on large-scale training datasets, thereby significantly reducing computational burden and enhancing the practical value of the proposed method. As a result, BNNs have been increasingly applied in engineering fields such as reliability analysis and structural response prediction (Perez-Ramirez et al.[281], Dang et al.[282], Wang et al.[283]), and have demonstrated significant advantages in modeling and optimizing complex nonlinear systems.

Among the core principles of Bayesian Neural Networks, Monte Carlo Dropout (Gal and Ghahramani[284,285]) is a technique of particular practical value. This approach applies dropout not only during training to prevent overfitting, but also during inference, effectively simulating sampling from the posterior distribution. Through multiple stochastic forward passes of the network—each employing dropout to generate a randomly sampled set of weights—Monte

Carlo Dropout allows the network to estimate predictive uncertainty. Compared to other BNN implementation techniques such as Bayes by Backprop, Stochastic Gradient Langevin Dynamics (SGLD), or Kronecker-Factored Laplace Approximation, Monte Carlo Dropout offers higher operational simplicity. Its major advantage lies in its ability to be seamlessly integrated into existing neural network architectures without requiring significant structural or algorithmic changes, making it computationally efficient and well-suited for large-scale applications.

Based on these advantages, this study adopts Monte Carlo Dropout as the BNN implementation method, aiming to enhance computational efficiency in the parameter identification process and to reliably quantify the uncertainty of model predictions.

7. 3. 3. 1 **Identification Framework**

The overall framework of the coupled BNN–Genetic Algorithm (BNN–GA) is illustrated as follows and can be divided into four distinct steps:

(1) Step 1: Generation of Parameter Combinations

This step strictly follows the principles of the traditional genetic algorithm. The initial population of the first generation is randomly generated within predefined upper and lower bounds. For subsequent generations, new populations are created from selected individuals of the previous generation using processes such as crossover, recombination, and potential mutation.

(2) Step 2: BNN Training

In the process of parameter identification using the genetic algorithm, multiple iterations are typically required to systematically evaluate the impact of key parameter configurations, reduce the variability of computational results, and improve the final identification accuracy. This iterative process not only enhances parameter search efficiency but also provides a dataset for training the Bayesian Neural Network (BNN), thereby avoiding the need to generate a large dataset exclusively for BNN training. During this process, each parameter combination and its corresponding fitness value are recorded and used as the inputs (parameters) and outputs (fitness values) for BNN training. Once the BNN model is trained, it is integrated into the optimization process of the genetic algorithm to accelerate the search. In the optimization loop, the BNN performs rapid inference for each candidate parameter set, predicting the mean and standard deviation of its fitness value. These predictions are used both in the calculation of fitness and as decision-making criteria during the selection and evolution phases of the genetic algorithm, thereby significantly reducing computational cost while maintaining optimization accuracy and improving parameter identification efficiency.

(3) Step 3: Uncertainty Quantification

The uncertainty of each inference result is quantitatively assessed using the ratio of the predicted standard deviation to the mean. For results with high uncertainty, the corresponding parameter combinations are further evaluated using the ABAQUS model in parallel. In contrast, for results with low uncertainty, the fitness value is directly taken as the BNN-predicted mean. It is worth noting that in critical generations—such as the final generation—all individuals are evaluated using ABAQUS to ensure result reliability.

(4) Step 4: Fitness Evaluation and Parameter Selection

Following Step 3, the fitness values of the current population are calculated either by the mean squared error between ABAQUS simulation results and experimental data, or by the BNN-predicted fitness values. The best-performing parameter combinations are then selected as the basis for generating the next generation.

7. 3. 3. 1 **Key Settings and Evaluation of the BNN Model**

In this study, the BNN–Genetic Algorithm optimization process employed a Multilayer Perceptron (MLP) (Rosenblatt[286]; Haykin[287])—a fully connected neural network—as the base architecture, implemented using PyTorch. MLP was chosen due to its high computational efficiency during both training and inference, and its capability to effectively learn the mapping between a 20-dimensional input vector (i.e., key parameters in the numerical model) and a 1-dimensional scalar output (i.e., the predicted mean squared error, MSE, corresponding to each parameter set). Since each input dimension is treated independently, there was no need to adopt recurrent architectures such as LSTM or GRU, or iterative frameworks like Temporal Convolutional Networks (TCNs) (Hochreiter & Schmidhuber [288]; Cho et al.[289]; Xu et al.[290,291]; Gu et al.[269]).

Moreover, considering the limited size of the available training dataset and the emphasis on computational efficiency in this optimization task, more complex neural network architectures such as Transformer and its enhanced variants—Reformer, Informer, and TimesNet (Vaswani et al.[263]; Kitaev et al.[292]; Zhou et al.[293]; Wu et al.[294])—were not utilized. For theoretical details of MLP, readers are referred to the aforementioned literature and references therein.

During the training and validation stages, a systematic comparison of different network architectures was conducted, focusing on the effects of the number of hidden layers and number of neurons per layer on model performance. The key hyperparameters used in the Bayesian Neural Network (BNN) are listed in Table 7-9, and the structure of the activated BNN model—incorporating Monte Carlo Dropout—is illustrated in Figure 7-13.

Throughout the training process, both training and validation losses were continuously monitored, and an early stopping strategy was employed: training was terminated if the validation loss showed no significant improvement within a defined number of epochs (e.g., 50). The model corresponding to the minimum validation loss was retained as the final trained model.

To effectively mitigate overfitting, the following strategies were adopted:

1. Hyperparameter tuning based on cross-validation;
2. Continuous monitoring of validation loss and early termination;
3. Use of exponential learning rate decay;
4. Application of Dropout for regularization during both training and inference.

It is worth noting that, due to the inherent complexity of neural networks and the highly non-convex nature of the optimization problem, overfitting cannot be entirely avoided. However, the above measures were effective in controlling overfitting and led to acceptable outcomes, as summarized in Table 7-10.

The training dataset for the BNN model consisted of 6,500 samples generated throughout the genetic algorithm parameter identification cycle. The BNN training process was computationally efficient, with a total duration of less than 10 minutes.

The performance evaluation of the optimized BNN model is shown in Figure 7-14. Results indicate that for approximately 70% of the samples, the predicted relative error was less than 20%; however, about 7.6% of the samples exhibited relative errors exceeding 40%. After weighing the trade-off between dataset construction cost and model accuracy, the current BNN model was adopted as the final surrogate model for optimization, and no further data expansion was performed.

Table 7-9 Key hyperparameters in BNN

Name	Value	Description
Dataset size	6500	The total number of samples for BNN
Dataset separation	-	The total number of samples for BNN
Number of layer	3	The total number of samples for BNN
Dropout ratio	0.5	Dropout ratio in Monte Carlo dropout processes

Sample time	5	The number of repetitive dropout processes adopted for uncertainty quantification
Hidden unit	512	The dimension of hidden unit in BNN
Initial learning rate	0.0002	The initial learning rate adopted in BNN training

Table 7-10 BNN-PGA optimization results and comparison

Type	Threshold (Std / Mean Value)	Time （s）	Time reduction （%）	Best fitness value (MSE) in the last generation
Pure PGA (ABAQUS simulation only)	-	45382	-	86.7
	0.5	47248	-4.1	78.2
BNN-PGA	1.0	28665	36.8	100.7
	1.5	10680	76.5	164.9
BNN only	-	5257	88.4	197.7

During the optimization process of the BNN–Genetic Algorithm, if the ratio of the predicted fitness standard deviation to its mean falls below a predefined threshold (see Table 7-9), the BNN-predicted result is directly adopted as the fitness evaluation. To further enhance the reliability of the optimization, numerical simulations using ABAQUS are performed for all parameter combinations in the final generation of every 10 generations, as well as in the final evaluation generation, to ensure the accuracy of the optimization results.

The fitness evaluation metric is the Mean Squared Error (MSE). The final results of the BNN–Genetic Algorithm optimization and its comparison with the pure Genetic Algorithm are presented in Table 7-9. In this table, “Std” and “Mean Value” represent the standard deviation and mean of multiple BNN predictions, respectively; their ratio is used to quantify the uncertainty of predictions.

The results show that, although the accuracy of BNN predictions has certain limitations, the proposed BNN–Genetic Algorithm achieves comparable performance in parameter identification to that of the pure Genetic Algorithm. This success is primarily attributed to the integration of uncertainty quantification, since using only the BNN-predicted mean MSE (i.e., the “BNN only” scheme in Table 7-9) fails to reach the same level of accuracy.

In terms of optimization efficiency, when the uncertainty threshold is set to 1.0, the total computational time of the BNN–Genetic Algorithm is reduced by approximately 36.8% compared to that of the pure Genetic Algorithm. Although this approach achieves a good balance between accuracy and computational efficiency, there remains substantial room for further improvement. Notably, as the number of training samples continues to grow, the predictive accuracy of the BNN is expected to improve, potentially leading to greater computational savings.

Moreover, the proposed method exhibits significant advantages in large-scale design and simulation applications. In large-scale simulation environments, training sample accumulation occurs more rapidly, thereby enhancing the reliability of BNN predictions and further reducing computational costs. Additionally, the inference time of the BNN remains nearly constant, regardless of the simulation scale, whereas the computational cost of optimization using ABAQUS or other finite element-based genetic algorithms increases significantly with simulation complexity. Consequently, the computational efficiency advantages of the BNN–Genetic Algorithm become increasingly prominent as simulation scale expands.

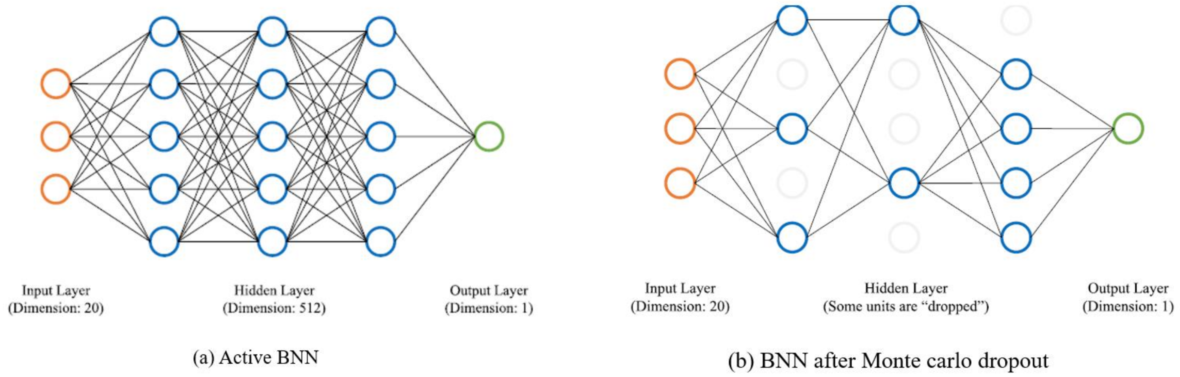

(a) Active BNN

(b) BNN after Monte carlo dropout

Figure 7-13 Types of BNN Models Before and After Applying Monte Carlo Dropout

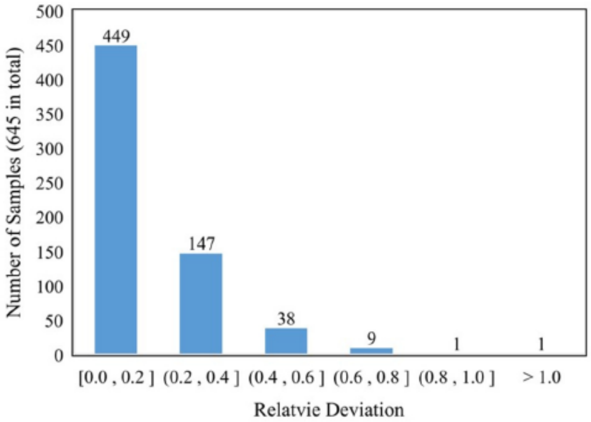

Figure 7-14 Distribution of Relative Errors on the Test Dataset

7. 3. 4 **Bayesian Parameter Identification Results**

Following the optimization procedure proposed in Section 7.1.3, this study employed the Sequential Monte Carlo (SMC) method to sample from the joint posterior distribution for parameter identification. By tempering the posterior distribution, the SMC algorithm effectively reduces the risk of convergence to local optima and enhances global convergence. This approach is particularly effective when dealing with multimodal and non-convex optimization problems, helping to obtain more robust solutions within complex parameter spaces. To mitigate the poor convergence often encountered in Bayesian inference (BI) for complex optimization tasks, informative priors were introduced to constrain the parameter space and smooth the landscape of the posterior distribution, thereby improving the convergence efficiency of the SMC algorithm. Selecting proposal distributions that are closer to the target posterior distribution significantly enhances convergence performance. In this study, we adopted truncated normal distributions as prior distributions, using the mean values obtained from the preliminary parameter estimates in Section 7.3.1. Specifically, a scaling factor of 3.0 and a reduction factor of 0.1 were applied to define the upper and lower bounds of the truncated distribution, respectively, while the standard deviation of each prior was set to 0.5 times its mean.

To further quantify the uncertainty of the parameter estimates, the response bounds of the Steel Side-Clamped-plate Glubam hysteresis model were computed based on the posterior distributions. A total of 100 parameter sets were sampled from the posterior distribution, and the corresponding standard deviation σ\sigmaσ was calculated to evaluate the uncertainty range of the estimated parameters.

These parameter sets were then input into the Steel Side-Clamped-plate Glubam hysteresis model to simulate cyclic loading responses, as shown in Figure 7-15. Statistical characteristics—including the mean and standard deviation (σ)—were computed based on the resulting responses. In Figure 7-15b, the mean response from these 100 samples is compared with the experimental data, with error bars representing the $\pm 2\sigma$ interval. Overall, the response bounds encompass the experimental data, indicating that the estimated parameters closely match the true values. Additionally, as shown in Figure 7-15a, comparisons of hysteresis loops and energy dissipation histories further demonstrate that the posterior parameter samples capture the key characteristics of the experimental results, validating both the reasonableness of the model and its predictive capability.

Figure 7-16 presents the posterior means of the SMC-sampled parameters along with the marginal posterior probability density functions (PDFs) for selected parameters, revealing their statistical distribution characteristics. Furthermore, Figure 7-17 illustrates the pairwise relationships among seven representative inferred parameters based on posterior samples obtained via SMC. The diagonal panels display kernel density estimates of each parameter's marginal PDF, while the lower triangle panels show scatter plots of joint posterior samples. The upper triangle panels depict contour plots of the joint posterior distributions. These visualizations not only verify the stability and reliability of the parameter estimation process but also provide valuable insights into inter-parameter dependencies.

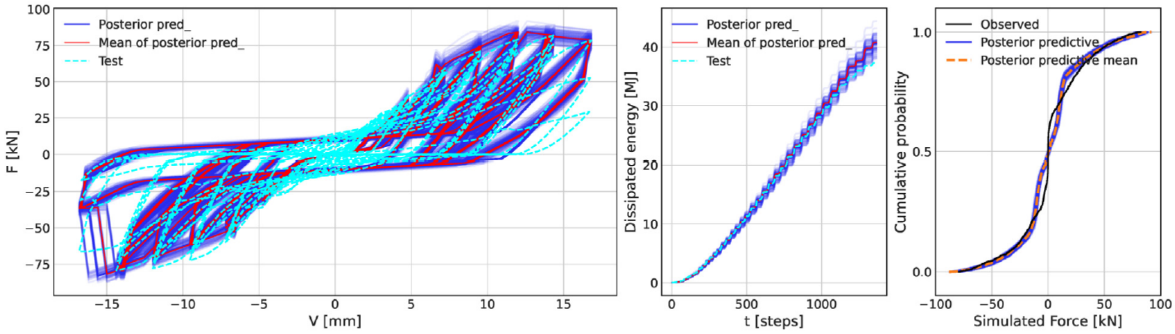

(a) Posterior prediction of hysteretic curve, energy dissipation and cumulative probability of simulated force values.

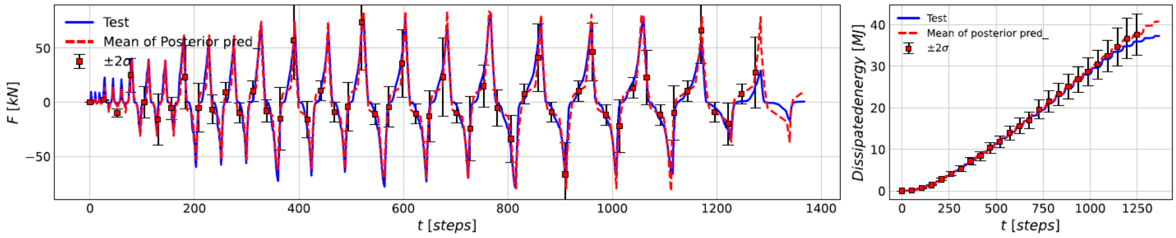

(b) Time history and standard deviation of the predicted force and energy dissipation

Figure 7-15 Comparison Between Experimental Results Under Cyclic Loading and Model Predictions

From 100 Posterior Samples

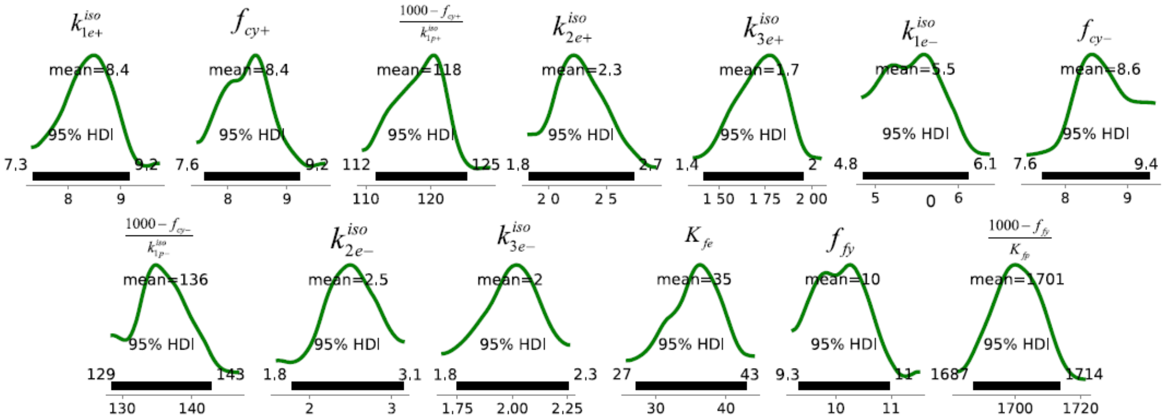

Figure 7-16 Posterior Means and Detailed Marginal Posterior Probability Density Functions (PDFs) of Each Parameter

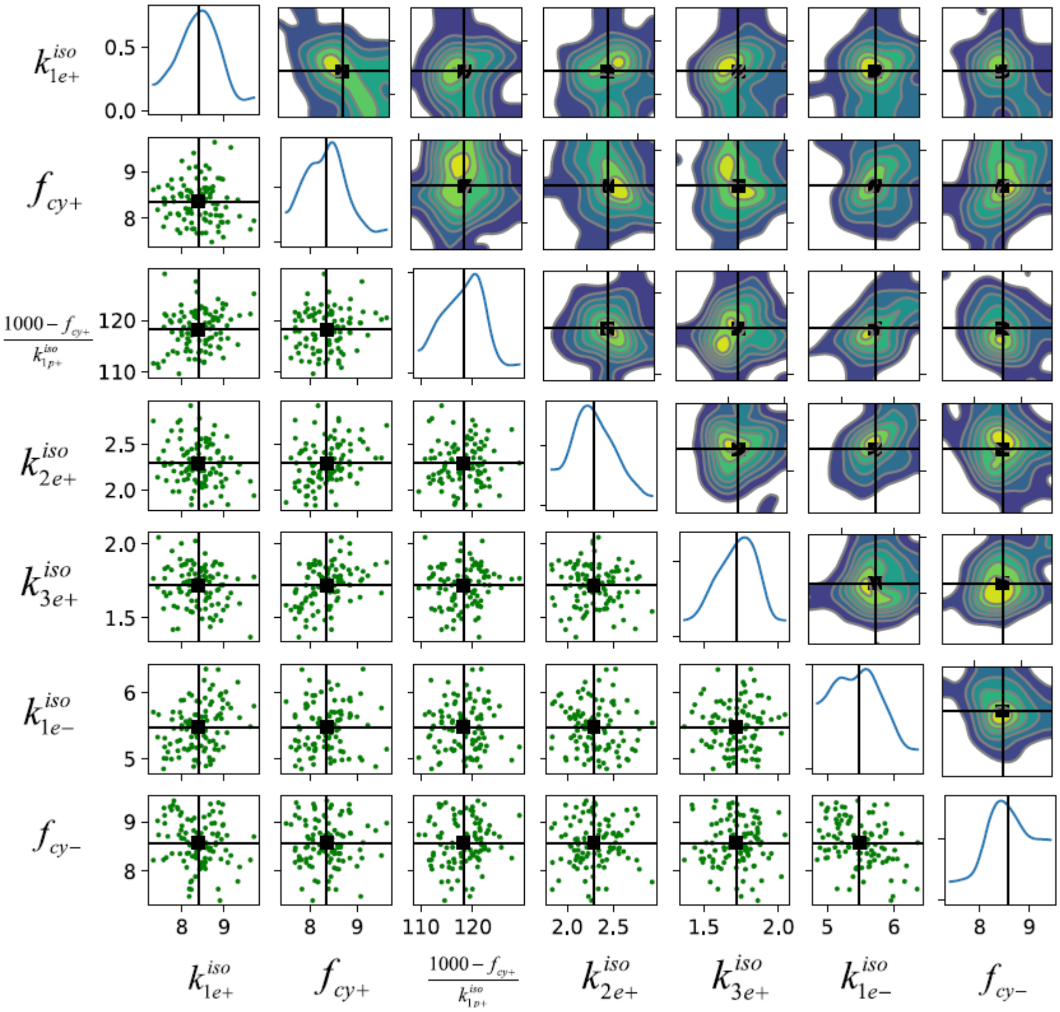

Figure 7-17 Pairwise Relationships of Posterior Samples for Seven Representative Inferred Parameters

8 Hybrid Simulation Study of Glubam Trusses and Roof Structures Based on Model Updating

In this chapter, a hybrid simulation study of glubam trusses and roof structures was conducted based on model updating techniques. Specifically, a hybrid roof model was developed by combining simplified joint models with bar elements. This modeling strategy significantly reduces computational complexity while improving simulation efficiency and effectively capturing the structural behavior of glubam roof systems.

After establishing the hybrid roof model, parameters were updated using hysteretic signals obtained from experimental tests, including node displacements and strain data from individual members. By comparing the experimental data with numerical simulation results, key model parameters were iteratively adjusted and optimized to ensure that the predicted responses more closely matched the actual mechanical behavior of the structure.

To ensure the accuracy and reliability of the updated numerical model, advanced optimization algorithms and model identification techniques were employed. The updated model accurately reflects the load-bearing characteristics of glubam roof structures. This approach not only improves prediction accuracy but also enhances the understanding of the nonlinear behavior, hysteretic characteristics, and energy dissipation mechanisms of glubam roofs, providing a solid foundation for seismic performance and durability assessment of such structural systems. The numerical modeling approach proposed in this study offers a powerful tool for the optimized design of glubam structures, while also providing valuable insights for modeling and analysis of similar timber-based systems. This contributes to the broader application of sustainable building materials in engineering practice.

8.1 Numerical Simulation and Model Updating of Steel Insert-Plate Glubam Planar Warren Trusses

8. 1. 1 Numerical Model of the Steel Insert-Plate Glubam Planar Warren Truss

The open-source finite element software OpenSees was employed to develop the numerical model used in this study. The proposed numerical model of the Steel Insert-Plate Glubam Planar Warren Truss is a phenomenological macro-model, as illustrated in Figure 8-1. This is a two-dimensional model, with each node having three degrees of freedom. As rotational behavior of the truss members is not considered, the rotational degrees of freedom at all nodes are constrained. The truss chords are modeled using truss elements with elastic uniaxial material properties, based on the assumption that damage mainly occurs at the joints, and the material properties of the beam elements are determined according to previous experimental studies.

To accurately simulate the mechanical behavior of the truss joints, all truss chords are connected using zero-length elements, and uniaxial zero-length link elements are placed between the truss elements and the joints to capture the nonlinear joint response. Each branch of the steel insert plate is connected to separate uniaxial zero-length elements, with overlapping node positions to represent the connection geometry. In the axial direction, the nonlinear mechanical behavior of the truss joints is modeled using the novel hysteresis model proposed in Section 6.1.2 of this study.

In the OpenSees model, a vertical load is applied to the midpoint node (Node 5) between the two top chords using displacement control, as shown in Figure 8-1. Meanwhile, Nodes 1 and 3 are fixed to serve as supports, ensuring that the boundary conditions are consistent with those of the experimental setup. This modeling approach effectively captures the hysteretic behavior of the truss under cyclic loading and provides a reliable numerical tool for further analysis of its nonlinear response.

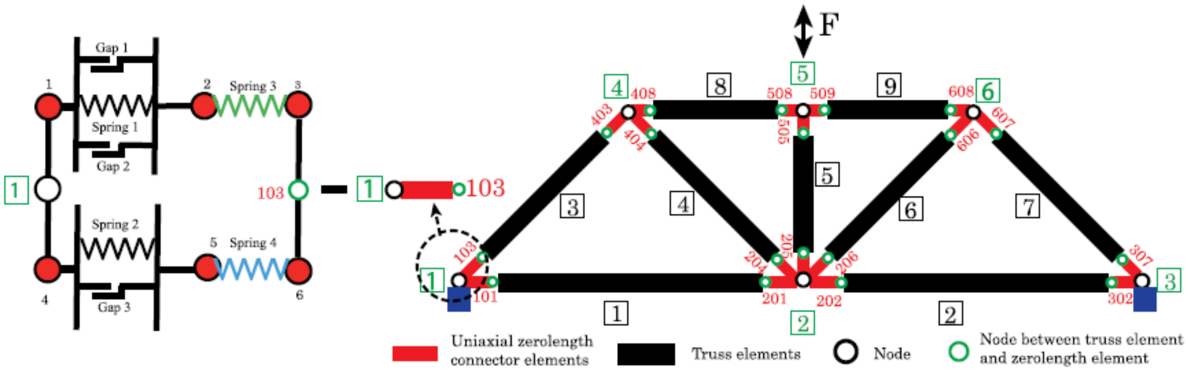

Figure 8-1 Schematic Diagram of the Planar Truss Model Proposed in OpenSees

8. 1. 2 Model Updating of the Steel Insert-Plate Glubam Planar Warren Truss

In the previous section, a numerical modeling approach for the truss structure was proposed. However, this highly idealized structural model confines nonlinear behavior to a limited number of predefined elements, which may introduce model uncertainty. Furthermore, simply incorporating the initially identified parameters from Chapter 7 into the truss model still leads to significant discrepancies between the simulated and experimental hysteretic responses. This is because the baseline identification was based solely on single-joint test behavior, which inherently contains a certain degree of uncertainty. Therefore, this section introduces a more accurate and efficient model updating approach for the truss structure. Compared with directly predicting output sequences, identifying and updating model parameters is more interpretable, and better adheres to the underlying mechanics and physical principles of the system.

The model updating presented in this section is primarily conducted within a Bayesian framework, similar to the Bayesian parameter identification process for truss joints described in Chapter 7. The updating process uses the experimental force data at Node 5 as the input response μ_k. Two levels of output responses are considered: global structural behavior and element-level behavior. The same set of parameters is applied to all joint models within the truss.

Therefore, the primary difference between the truss-level Bayesian updating framework and the joint-level Bayesian identification framework lies in the observation dataset. The truss-level model updating incorporates a comprehensive set of experimental observations, including Global behavior, such as force response at Node 5; Local behavior, such as strain measurements on the truss chords; Combined behavior, representing the integration of global and local responses. Moreover, given that the full truss model is considerably more complex than a single joint model, the number of required samples for Bayesian inference is also increased accordingly.

According to the parameter sensitivity analysis results shown in Figure 7-2, the top 20 most sensitive parameters for the two Pinching4 material models implemented in the proposed framework are as follows: For Pinching4 Material #1: eNf_4; ePd_4; ePf_2; eNf_2; eNd_4; eNf_3; ePf_3; gK_4; eNf_1; ePd_1; For Pinching4 Material #2: eNf_1; eNf_3; eNd_1; eNf_4; eNf_2; eNd_4; eNd_3; $rDispP$; $uForceN$; eNd_2. If parameter selection for model updating were based solely on sensitivity rankings, these parameters would be directly selected for updating. However, it is important to note that interdependencies exist among certain parameters. For example, parameter pairs such as (ePd_1, ePf_1), (ePd_2, ePf_2), (ePd_3, ePf_3) and (ePd_4, ePf_4) are used to define the backbone curve in the positive loading direction, and are therefore mutually dependent. These parameters should be considered jointly rather than independently. In the selection of model parameters, a balance must be struck among sensitivity, physical interpretability, and computational cost. Based on a comprehensive analysis of these factors, a total of 36 key parameters were ultimately selected for updating the hybrid roof truss model, ensuring that the model can accurately capture the mechanical behavior of the structure while maintaining computational efficiency.

8. 1. 2. 1 **Model Updating Based on Global Structural Behavior**

At the global behavior level, the force data recorded during the experiment was selected as the output response. Specifically,

$$y_k = [\text{vertical force at Node 5 at time step } \mathbf{k}]$$

was used as the response variable. The force predicted by the numerical model is regarded as the sole simulation output in the Bayesian inference process.

The prior probability density functions (PDFs) of the parameters were constructed under the assumption of mutual independence among all parameters. A truncated normal distribution was adopted, with the mean values equal to those identified from the joint-level parameter estimation (see Tables 7-3, 7-4, etc.). The upper and lower bounds of the truncated distributions were defined using scaling factors of 3.0 and 0.1, respectively, applied to the mean. The standard deviation was set to 50% of the mean.

A total of 100 sets of model parameters were generated for each truss sample. The posterior SMC samples—including both individual samples and their sample mean (i.e., the updated parameter values)—were used to simulate the response of the truss system, which was then compared with the experimentally measured response, as shown in Figure 8-2.

In addition, the cumulative distribution functions (CDFs) of the simulated and experimental responses were compared (Figure 8-2). The results clearly indicate a high level of agreement between the cumulative distribution of the simulated responses and that of the observed data, demonstrating that the Bayesian inference approach effectively captures the actual structural response at each time step kkk, thereby improving the accuracy and reliability of the model.

Figure 8-3 compares multiple global-level responses, including:

- the measured response (experimental data),
- the initial numerical model prediction (obtained using parameters identified solely from joint-level tests), and
- the final numerical model prediction (obtained after model updating).

The global responses examined include the force–displacement curve, the force–time history, and the energy dissipation profile. From the perspective of energy dissipation, the updated numerical model shows clear improvement over the initial model, resulting in significantly enhanced simulation accuracy.

In terms of the force–time history, the predicted response from the updated model aligns very closely with the experimental measurements, further validating the model's accuracy and reliability. Additionally, the force–displacement curve of the updated model effectively reproduces the strength envelope observed in the experimental data, indicating that the refined parameter identification and model updating approach can accurately capture the hysteretic behavior of the glubam truss system.

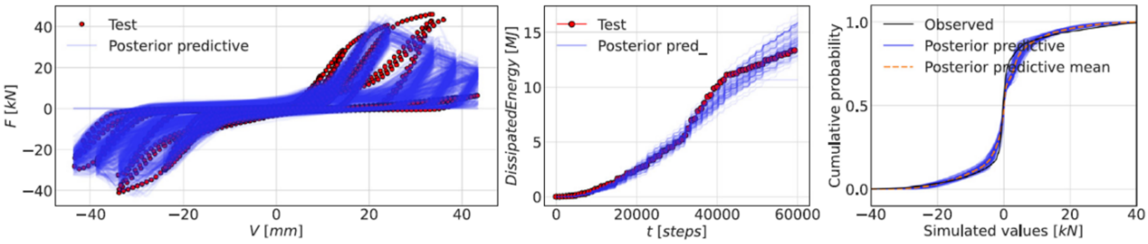

(a) G-D-8

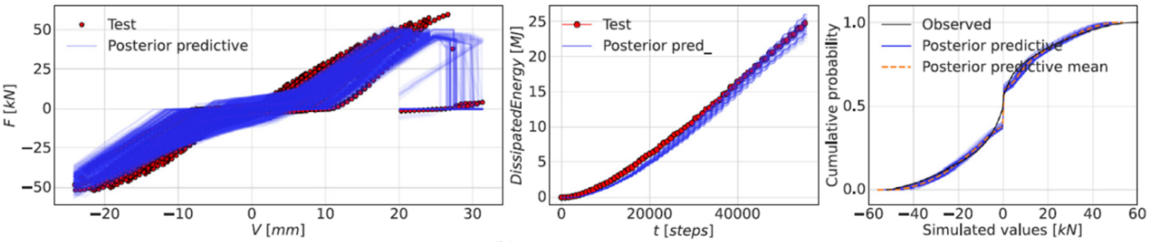

(b) G-D-10

Figure 8-2 Predicted Structural Responses Using Posterior Parameters After Model Updating

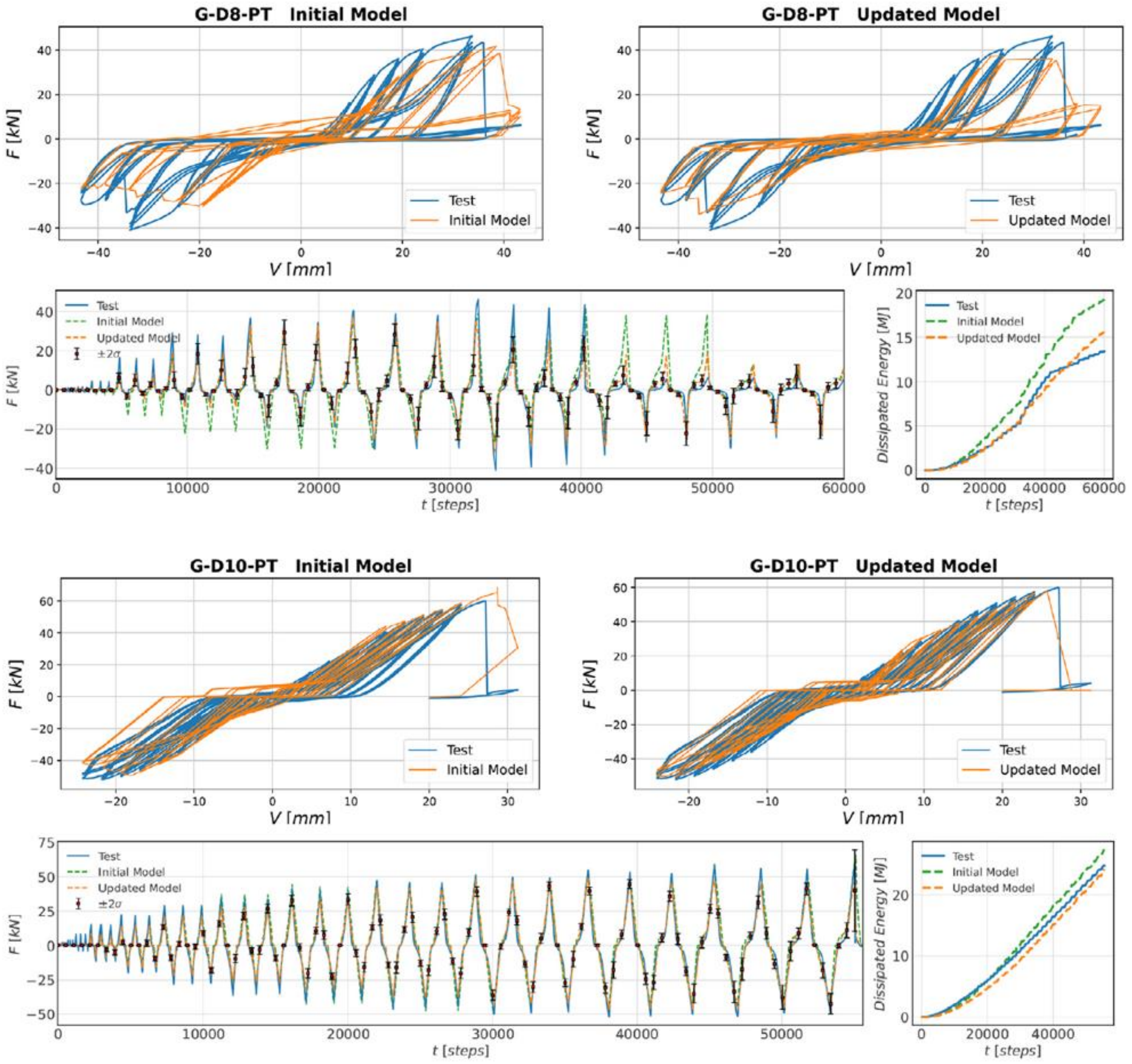

Figure 8-3 Comparison of Force–Displacement Curves Between Initial Model Prediction, Updated Model Prediction, and Experimental Records.

8. 1. 2. 2 Model Updating Based on Global and Local Structural Behavior

Although the model updating based on global behavior enables accurate prediction of force responses at certain nodes, discrepancies still remain in capturing the actual responses at the local behavior level. To develop a more robust model that can effectively represent element-level behavior, this section performs simultaneous model updating at both the global and local levels. For brevity, this section focuses only on the G-D-10 case. Specifically, the measured force at Node 5 is selected as the global output response, while the measured strain values of Truss Chords 5, 6, 7, and 9 are selected as the local output responses (refer to chord numbering in Figure 8-1). Due to the symmetry of the structure, strain data from the other chords are not included in this model updating process. Accordingly, the output responses defined in this study are as follows:

$$y_k = \begin{bmatrix} \text{Vertival force at Node 5 at time k} \\ \text{Strain Value at Chord 5,6,7,9 at time k} \end{bmatrix}$$

In the OpenSees model, the predicted forces and strains of the corresponding truss chords are regarded as the sole simulation responses in the Bayesian inference process. Similar to the model updating based solely on global behavior, the upper and lower bounds of the truncated normal distribution for all parameter means are defined using a scaling factor of 3.0 and a reduction factor of 0.1, respectively. The standard deviation is set to 10% of the mean value. For each sample, 100 sets of model parameters are generated.

The element-level responses predicted by the numerical model using the posterior SMC samples are compared with the experimentally measured responses, as illustrated in Figure 8-4. It can be observed that the prediction envelopes generally cover the experimental strain values, indicating that some of the posterior parameter sets are capable of adequately representing the true parameters of the system.

Figure 8-5 compares various responses at both the global and local (element) levels, including:

- the measured (true) responses,
- the initial numerical model predictions (prior to any model updating),
- the predictions after global-only model updating, and
- the predictions after combined global and local model updating.

The global responses include the force–displacement curve and force–time history, while the element-level responses include the strain values of Truss Chords 5, 6, 7, and 9.

It is evident that, for global responses such as the force–displacement curve and force–time history, both updating approaches yield good agreement between the predicted and measured responses. However, for the element-level responses, the predictive capabilities of the two updated finite element models differ to some extent, indicating that the inclusion of local behavior enhances the fidelity of the model at the component scale.

The test parameters and their corresponding updated values (mean and standard deviation) for each planar truss are summarized in Tables 8-2 and 8-3, respectively. These parameters were identified through model updating based on both global and local structural behavior.

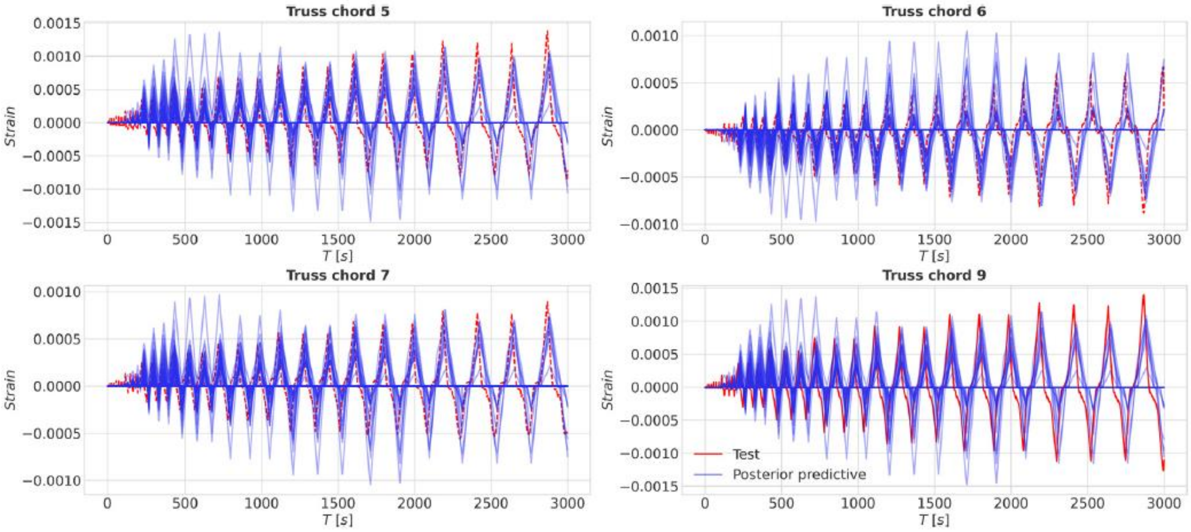

Figure 8-4 Predicted Strain Responses of Truss Chord Elements in G-D-10 After Model Updating Based on Posterior Parameters at Both Global and Element Levels.

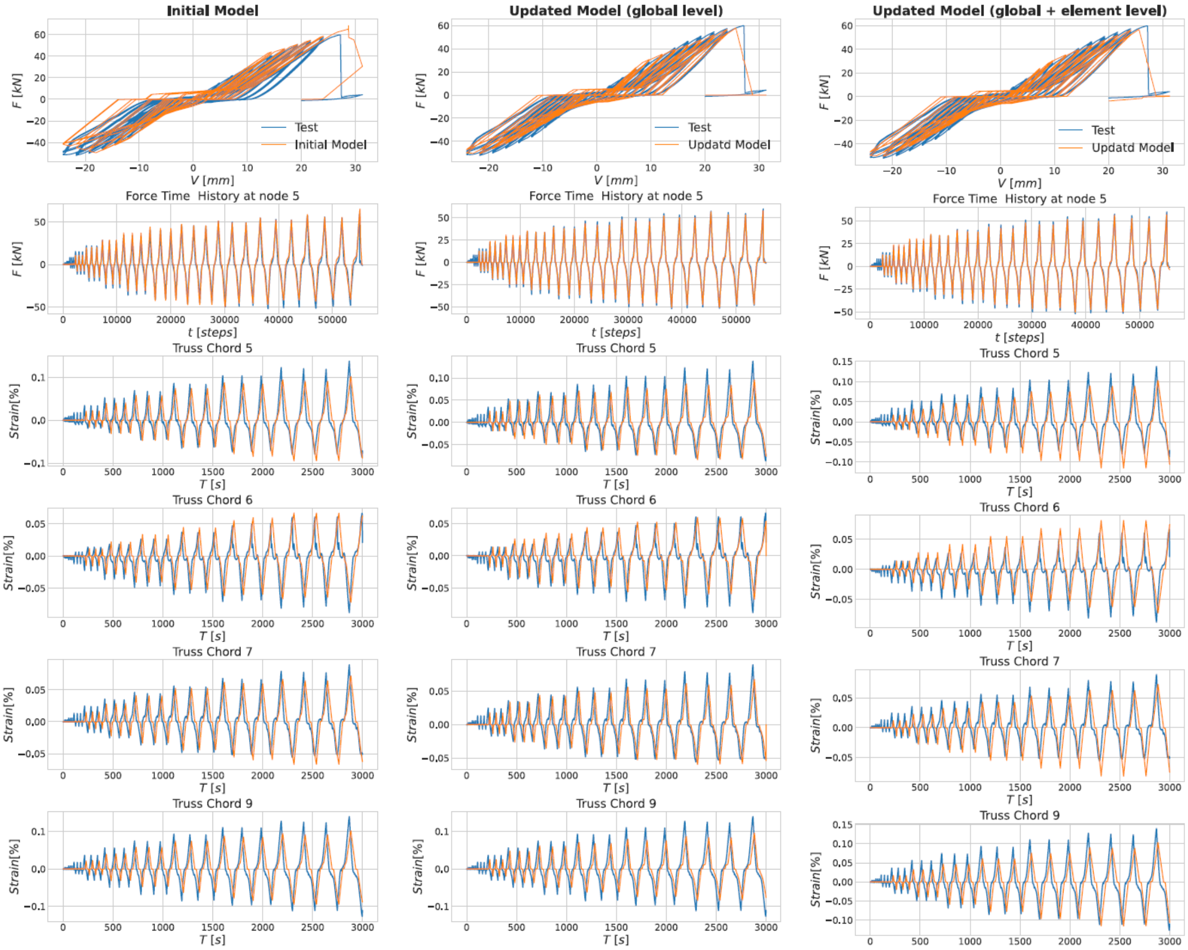

(a) (b) (c)

Figure 8-5 Comparison of Predicted Responses in the G-D-10 Case Among the Initial Model, the Model Updated at the Global Behavior Level, and the Model Updated at Both Global and Element Behavior Levels

8. 1. 2. 3 Comparison and Parameter Uncertainty Quantification

To compare the predictive capabilities of the two numerical model updating approaches, the Relative Root Mean Square Error (RRMSE) was employed to quantify the differences between the finite element (FE) predicted responses and the measured (true) responses. The RRMSE provides a normalized measure of the error between two signals and is defined as follows:

$$RRMSE(a,b)=\frac{\sqrt{\left[\frac{1}{N_s}\sum_{i=1}^{N_s}\left(a_i-b_i\right)^2\right]}}{\sqrt{\left[\frac{1}{N_s}\sum_{i=1}^{N_s}\left(a_i\right)^2\right]}}\times 100(\%) \tag{8-1}$$

Where **a** represents tested values，**b** represents predicted value， N_s represents the total number of data samples in the signal.

Table 8-1 presents the RRMSE values (see Equation (8-1)) computed for the G-D-10 case, based on the initial model parameters and the parameters updated using the two different model updating methods. Specifically, three sets of model parameters were used in the numerical simulations:

1. the initially identified parameters, and
2. two sets of updated parameters corresponding to the global-only updating method and the combined global and local updating method.

These parameter sets were used to generate predictions of the structural responses at both the global and element levels. The predicted global responses (obtained from the actuator load measurements) and element-level responses (obtained from strain gauges) were then compared to the actual measured responses, and the corresponding RRMSE values were calculated.

Table 8-1 For the G-D-10 case, the Relative Root Mean Square Error (RRMSE) between the observed responses and the corresponding predicted responses from the initial and updated numerical models was calculated based on the initially identified parameters and the two sets of updated parameters (see Eq 8-1).

Signal input type					
Global response			Element response		
Initial model	Updated model （Global level）	Updated model (Global+elemental level)	Initial model	Updated model （Global level）	Updated model (Global+elemental level)
18.56%		10.68%	29.35%	22.35%	16.69%

In terms of both global and element-level responses, the RRMSE values of the initial (unupdated) numerical model remain consistently below 30%, indicating that the parameters identified at the joint level can still provide reasonably accurate estimates of the overall truss behavior when applied to the truss model. Even without any model updating, these parameters result in relatively low RRMSE values (less than 30%). However, after model updating based solely on global behavior, the fitting error between the actual response and the model-predicted response is significantly reduced, with the final model achieving RRMSE values of less than 10%. While this global model updating approach enhances the overall prediction accuracy, only slight improvements are observed at the element response level. In contrast, when the model is updated simultaneously at both the global and element levels, the RRMSE values between the observed and predicted element-level responses are substantially reduced, eventually falling below 20%. This finding demonstrates that combined global and local model updating can significantly improve the predictive accuracy of the numerical model in capturing local structural behavior.

This analysis further confirms the effectiveness of the model updating strategy, especially when both global and local behaviors are considered. Such an approach greatly enhances the consistency between the predicted responses and the experimental observations.

Figure 8-6 presents a coefficient of variation (COV) analysis for the 36 connection parameters used in the hybrid truss model for the G-D-10 case. The figure compares the initially identified joint parameters with the two sets of updated parameters, corresponding to the global-only updating and the global + element-level updating strategies. This visual analysis offers key insights into how different model updating strategies influence the calibration of connection parameters in the hybrid truss model, highlighting the parameter adjustments that lead to improved connection performance. It also reveals how each updating method enhances the model’s accuracy and applicability in simulating real structural behavior. The results show that, compared to the initially identified parameters, the COV values of parameters updated at the global level are mainly concentrated in the range of 0.2 to 0.3, suggesting a moderate level of parameter uncertainty. Furthermore, when the model updating is extended to the global + element level, the COV values of several key parameters further decrease, indicating that this extended updating strategy can effectively reduce parameter uncertainty and improve the model's ability to represent the actual structural behavior. However, when the model updating process is expanded to incorporate element-level local responses, the overall parameter uncertainty increases significantly. In this case, the COV values are generally higher, typically ranging between 0.5 and 0.6. This increase in uncertainty reflects the greater complexity involved in parameter estimation when local response calibration is introduced. Transitioning from a global-only update to a multi-level update makes the calibration process more comprehensive—capturing both overall structural behavior and detailed local responses.

Although this enhanced calibration strategy improves the representational accuracy of the model for real structural systems, its increased complexity leads to broader parameter distributions and elevated uncertainty. This phenomenon underscores the need for a careful trade-off between model accuracy and complexity in the model updating process. Controlling the level of parameter variability is essential to ensure predictive reliability and practical applicability, while avoiding excessive computational burden or instability.

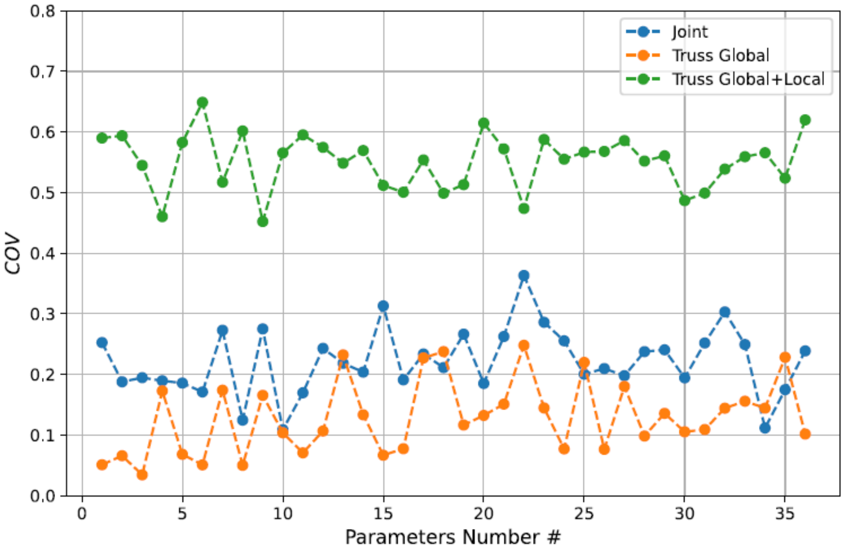

Figure 8-6 Coefficient of Variation (COV) of the 36 Joint Model Parameters in the G-D-10 Case: Comparison Between Joint-Level Identified Parameters and Updated Parameters in the Integrated Truss Model (Global-Level and Global + Element-Level Updating)

Table 8-2 Updated and Fixed Parameter Values of Pinching4 Material #1 (Spring 3)

	Specimen	G-D-8		G-D-10	
	Parameter	mean	std	mean	std
Updated Parameter	ePf_1	73.26	5.88	72.14	3.67
	ePd_1	0.80	0.12	1.27	0.08
	ePf_2	43.35	13.47	73.36	2.51
	ePd_2	4.05	1.35	0.58	0.10
	ePf_3	22.53	4.82	67.67	4.61
	ePd_3	7.42	2.18	6.40	0.32
	ePf_4	4.06	0.60	2.07	0.36
	ePd_4	7.47	2.67	12.26	0.61
	eNf_1	-85.10	14.26	-93.19	15.41
	eNd_1	-2.27	0.37	-1.70	0.17
	eNf_2	-62.34	10.78	-78.70	5.56
	ePd_2	-1.79	0.37	-1.05	0.11
	eNf_3	-52.40	13.93	-37.49	8.70
	eNd_3	-2.28	1.15	-9.27	1.23
	eNf_4	-12.15	1.82	-18.17	1.21
	eNd_4	-6.32	1.49	-18.55	1.43
	rDispP	0.69	0.18	0.49	0.11
	fForceP	0.27	0.09	0.22	0.05
	uForceP	0.23	0.04	0.11	0.01
	rDispN	0.47	0.04	0.74	0.10
	fForceN	0.15	0.06	0.68	0.10
	uForceN	0.04	0.01	0.22	0.05

Table 8-2 (Continued)

	Specimen	G-D-8		G-D-10	
	Parameter	mean	std	mean	std
Fixed Parameter	gK_1	0.48	-	0.34	-
	gK_2	0.22	-	0.47	-
	gK_3	0.23	-	0.04	-
	gK_4	0.03	-	0.08	-
	$gK_{\lim}$	0.41	-	0.37	-
	gD_1	0.65	-	0.03	-
	gD_2	0.10	-	0.19	-
	gD_3	0.27	-	0.35	-
	gD_4	0.09	-	0.21	-
	$gD_{\lim}$	0.06	-	0.44	-
	gF_1	0.44	-	0.44	-
	gF_2	0.60	-	0.41	-
	gF_3	0.10	-	0.31	-
	gF_4	0.33	-	0.25	-
	$gF_{\lim}$	0.47	-	0.35	-
	gE	19.99	-	26.6	-

Table 8-3 Updated and Fixed Parameter Values of Pinching4 Material #2 (Spring 4)

	Specimen	G-D-8		G-D-10	
	Parameter	mean	std	mean	std
Updated Parameter	$eN\ f_1$	-18.30	3.96	-19.28	-2.79
	$eN\ d_1$	-1.23	0.21	-1.06	-0.08
	$eN\ f_2$	-27.61	5.72	-7.18	-1.58
	$eP\,d_2$	-3.98	0.83	-11.74	0.90
	$eN\ f_3$	-48.90	24.21	-98.52	-17.74
	$eN\ d_3$	--6.67	1.29	-9.04	-0.89
	$eN\ f_4$	-23.34	9.84	-40.19	-5.45
	$eN\ d_4$	-24.75	9.64	-42.75	-4.50
	rDispP	0.46	0.11	0.28	0.03
	fForceP	0.79	0.13	0.34	0.05
	uForceP	0.14	0.04	0.15	0.02
	rDispN	1.24	0.13	1.80	0.26
	fForceN	0.07	0.01	0.27	0.06
	uForceN	0.02	0.003	0.04	0.03

Table 8-3 (Continued)

	Specimen	G-D-8		G-D-10	
	Parameter	mean	std	mean	std
Fixed Parameter	ePf_1	1.2	-	46.18	-
	ePd_1	20	-	0.76	-
	ePf_2	2	-	64.4	-
	ePd_2	24	-	0.83	-
	ePf_3	1.5	-	100.33	-
	ePd_3	26	-	2.62	-
	ePf_4	1	-	1.78	-
	ePd_4	30	-	4.82	-
	gK_1	0.48	-	0.34	-
	gK_2	0.22	-	0.47	-
	gK_3	0.23	-	0.04	-
	gK_4	0.03	-	0.08	-
	gK_{lim}	0.41	-	0.37	-
	gD_1	0.65	-	0.03	-
	gD_2	0.10	-	0.19	-
	gD_3	0.27	-	0.35	-
	gD_4	0.09	-	0.21	-
	gD_{lim}	0.06	-	0.44	-
	gF_1	0.44	-	0.44	-
	gF_2	0.60	-	0.41	-
	gF_3	0.10	-	0.31	-
	gF_4	0.33	-	0.25	-
	gF_{lim}	0.32	-	0.35	-
	gE	19.99	-	26.6	-

8.2 Numerical Simulation and Model Updating of Steel Side-Clamped-Plate Glubam Roof Structures

8. 2. 1 Numerical Model of the Steel Side-Clamped-Plate Glubam Roof Structure

As shown in Figure 8-7, a simplified hybrid roof model was developed by combining the proposed joint connector model (see Figure 6-20) with line elements representing the roof chords in ABAQUS. The connector model is placed between the nodes and the line elements, with its length set to 150 mm, corresponding to the actual connection region length of the roof joints (see Figure 5-2). Multiple axial connector elements are linked to the truss elements using the translation-type connection available in ABAQUS. The line elements are assigned roof beam properties, with an elastic modulus of 13 GPa[252] and a cross-sectional dimension of 140 mm × 52 mm. All joints are assumed to be pinned, and supports are modeled as hinged, to match the actual boundary conditions. The model updating process is based on the cyclic loading test results of four full-scale roof assemblies, with the experimental loading setup illustrated in Figures 5-6 and 8-7. Displacement-controlled cyclic loads are applied at Nodes 4 and 5 to simulate the actual loading conditions and optimize the numerical model parameters.

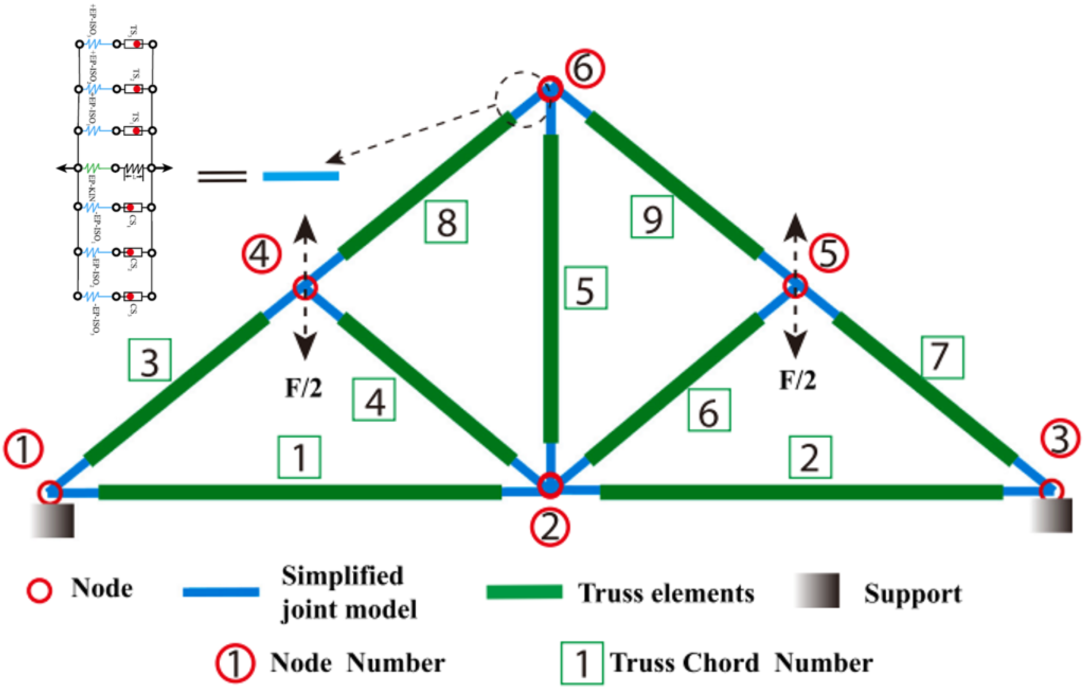

Figure 8-7 Simplified Roof Model Developed in Abaqus

8. 2. 2 Model Updating of the Steel Side-Clamped-Plate Glubam Roof Structure

In the previous two chapters, several key parameters within the joint model were preliminarily identified based on joint-level experimental data. However, it should be noted that when the joint model is integrated into the roof structure model, the highly idealized nature of the structural model causes nonlinear behavior to be restricted to a limited number of specified elements. This may introduce potential model uncertainty. Furthermore, the initial parameter identification was conducted at the single-joint level and based on only one experimental test, which inherently leads to certain uncertainties.

Therefore, to reduce model uncertainty and develop a more accurate and robust structural model, this section proposes a genetic algorithm (GA)-based model updating framework for the glubam roof structure.

This updated framework extends the genetic algorithm previously applied at the joint level, with modifications to both the parameterized model and the GA settings. Given that the roof model is more complex than a single-joint model, the number of generations and population size were set to 50 and 40, respectively, resulting in 2,000 evaluations in total. Additionally, 30 slave threads were deployed to perform the model updating tasks in parallel.

The scaling and reduction factors for the initial joint parameter values were set to 5.0 and 0.5, respectively. These were used to define the upper and lower bounds of the search space in the structural model updating process, ensuring both efficiency and stability during optimization.

8. 2. 3 Model Updating Results of the Steel Side-Clamped-Plate Glubam Roof Structure

The initial joint model parameter values identified from joint-level experiments and the final updated parameter values at the roof structure level are summarized in Table 8-4. As shown in the table, the most sensitive parameters are G_1 and G_2 in the STOP material model, which describe the initial slip behavior caused by manufacturing tolerances between bolts and bolt holes. Since the planar roof truss is composed of multiple chord members and such tolerances are difficult to maintain uniformly across all joints, these two parameters exhibit the largest relative deviation between their initially identified and final updated values.

The convergence history of the model updating process for the B-10 roof case is illustrated in Figure 8-9, where the objective function evaluations are recorded. Meanwhile, Figure 8-8 shows the predicted responses of all individuals in the population at various representative generations during the updating process. It can be observed that the optimization converges to a stable solution after approximately 40 generations (i.e., 1600 individual evaluations), and the final generation yields a model response that closely matches the experimental data. Furthermore, the strain field results of each chord member under selected loading cycles can be obtained from the best-performing updated roof model, as shown in Figures 8-10 and 8-11. However, compared to the identification results obtained at the joint level, the parameter variance at the truss (roof) level is noticeably larger. This increase in variance is attributed to the greater number of observation data points used in the model updating process, which inherently increases the complexity and difficulty of accurate parameter identification.

To further improve parameter identification accuracy and reduce error, future research may consider strategies such as optimizing the population size and adjusting the number of generations during the optimization process.

Table 8-4 Comparison Between Initially Identified Parameters at the Joint Level and Updated Parameters at the Roof Structure Level

Parameter		k_{1e+}^{iso}	f_{cy+}	k_{1p+}^{iso}	k_{2e+}^{iso}	k_{3e+}^{iso}	G_{1+}	G_{2+}	k_{1e-}^{iso}	f_{cy-}	k_{1p-}^{iso}	k_{2e-}^{iso}
		$\frac{kN}{mm}$	kN	$\frac{kN}{mm}$	$\frac{kN}{mm}$	$\frac{kN}{mm}$	mm	mm	$\frac{kN}{mm}$	kN	$\frac{kN}{mm}$	$\frac{kN}{mm}$
B10	Initial	16.4	12.19	6.13	2.4	2.2	2.5	1.45	11.4	8.21	5.6	2.93
	Updated	7.6	10.19	3.5	2.6	2.5	3.5	2.45	9.2	111.3	7.5	3.9
B12	Initial	10.5	12.52	5.1	2.33	2.13	3.6	1.35	11.5	18.51	5.48	3.14
	Updated	10.3	14.32	4.31	3.25	3.01	4.5	2.43	10.2	16.43	4.4	3.2
B14	Initial	10.6	16.05	5.68	2.6	2.4	4.4	1.84	16.6	16.42	6.78	3.42
	Updated	13.4	7.56	7.25	0.48	0.32	3.68	2.44	8.56	8.64	6.54	2.83
B16	Initial	25.5	17.52	10.13	3.33	3.13	3.1	1.65	12.5	15.51	4.06	3.15
	Updated	14.3	15.63	2.53	1.83	1.32	3.76	2.93	14.32	30.26	1.86	3.82

Table 8-4 (Continued)

Parameter		k_{3e-}^{iso} $\frac{kN}{mm}$	G_{1-} mm	G_{2-} mm	K_L $\frac{kN}{mm}$	f_{fy} kN	K_{fe} $\frac{kN}{mm}$	K_{fp} $\frac{kN}{mm}$	F_{d+} kN	F_{d-} kN	I_{d+}	I_{d-}
B10	Initial	2.7	5.5	1.81	1.5	11.3	20.6	0.60	80.5	71.3	0.85	0.32
	Updated	2.4	3.68	2.42	1.4	5.6	18.3	2.5	71	83	0.81	0.34
B12	Initial	2.9	2.5	1.61	2.1	10.3	35.1	1.06	71.2	94.3	0.67	0.15
	Updated	3.1	3.4	2.81	1.83	9.6	20.6	0.95	75.6	110.3	0.72	0.22
B14	Initial	3.3	3.9	1.82	2.2	10.5	25.5	0.79	81.2	105.2	0.83	0.13
	Updated	2.1	3.93	2.54	1.89	15.3	28.23	0.86	112.	122.2	0.76	0.19
B16	Initial	2.9	6.8	1.63	2.5	12	20.3	0.79	77.6	65.3	0.76	0.22
	Updated	3.6	3.1	2.13	1.86	13.5	28	2.8	96.3	78.4	0.72	0.32

\

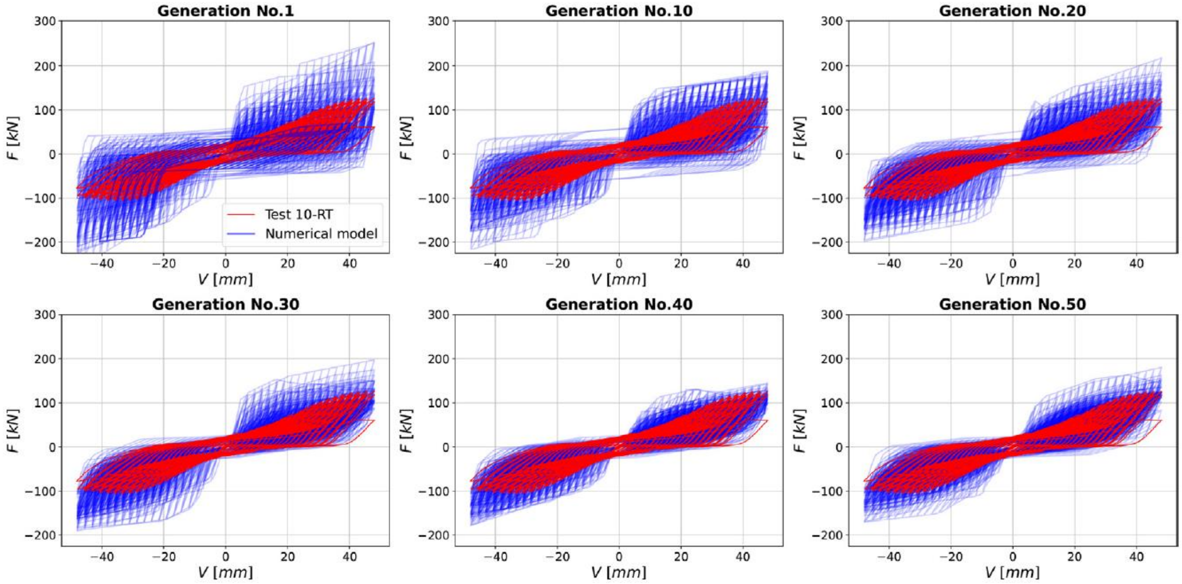

Figure 8-8 Predicted Responses of All Individuals in Selected Generations During the Model Updating Process for Roof Case B-10

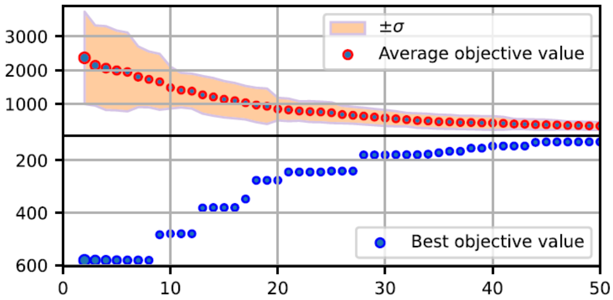

Figure 8-9 Convergence History of Objective Function Evaluations During the Model Updating Process for Roof Case B-10

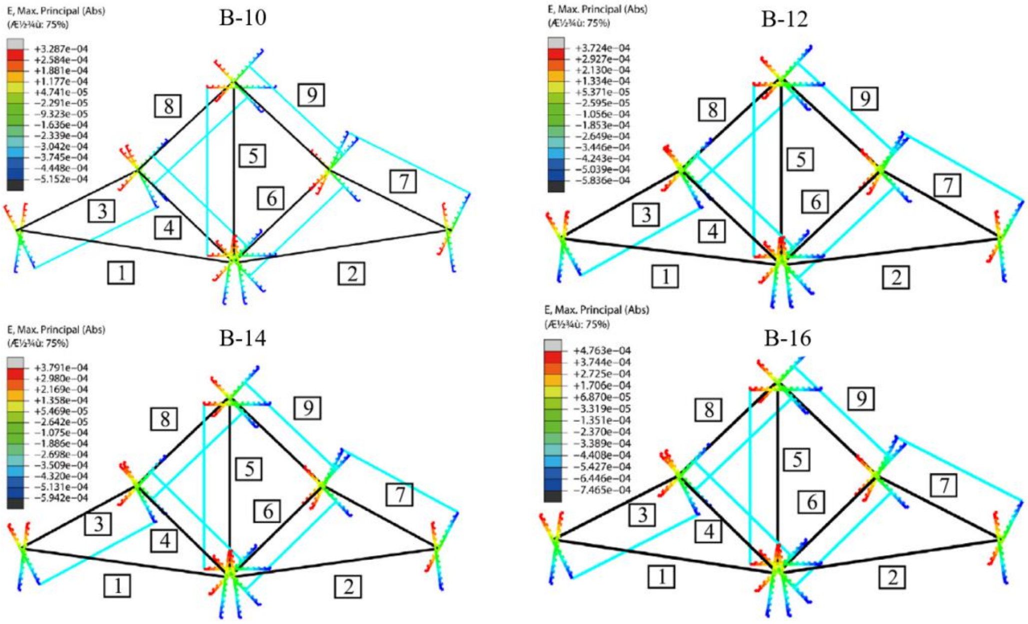

Figure 8-10 Strain Field on Each Chord Member at the 25th Loading Cycle Obtained from the Updated Optimal Individual

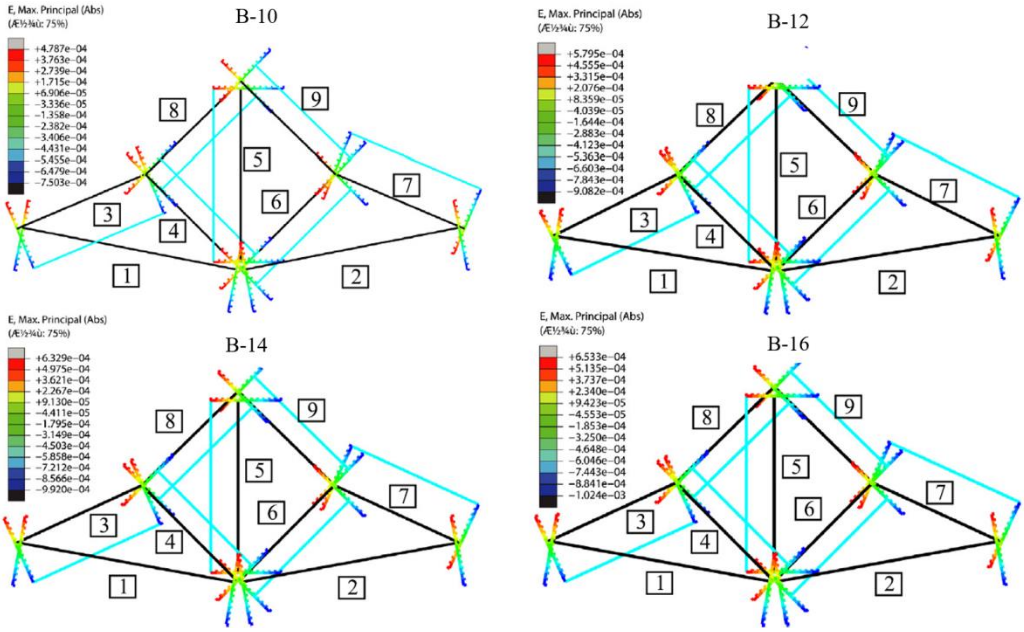

Figure 8-11 Strain Field on Each Chord Member at the 60th Loading Cycle Obtained from the Updated Optimal Individual

8. 2. 4 **Validation of the Updated Roof Model**

In the previous section, parameter updating was performed for four roof truss models using a genetic algorithm. This section further validates the updated models by comparing the force–time history at Node 2, the mid-span deflection time series, and the measured strain time series of the chord members.

Specifically, the joint model parameters identified through the genetic algorithm were used as inputs to the constructed roof model. Based on these inputs, the corresponding output responses were calculated, including:the force–time history at Node 2, the time series of mid-span deflection, and the strain time series of each chord member. These simulated responses were then compared with the experimental test data to assess the accuracy and reliability of the updated model.

8. 2. 4. 1 **Comparison of Force–Time Histories**

Figure 8-12 presents the force–time histories generated by the updated roof model alongside the corresponding experimental results. The results demonstrate that the model is capable of accurately capturing the force–time response, particularly in representing the initial slip behavior and damage evolution, as evidenced by the force trends during both the initial loading cycles and the final cycles. Overall, the developed roof model successfully reproduces the pinching effect and failure behavior of the glubam roof system, validating its effectiveness in simulating the nonlinear dynamic characteristics of the structure.

8. 2. 4. 2 Comparison of Mid-Span Deflection at Node 2 Over Time

Figure 8-13 presents the measured mid-span deflection at Node 2 over time, obtained using LVDT sensors, and compares it with the predicted results from the numerical model. Overall, the numerical simulation shows a high degree of agreement with the experimental data, further validating the accuracy of the updated model. It is worth emphasizing that, as defined in GB50005[218], mid-span deflection is a critical parameter for evaluating structural reliability under the Serviceability Limit State. Therefore, the model proposed in this study can be used not only for analyzing the mechanical performance of glubam roof structures, but also as a reliable foundation for structural reliability assessment, which will be explored in future research.

8. 2. 4. 3 Comparison of Strain–Time Histories for Each Chord Member

As an example, Figure 8-14 presents the strain–time curves of each chord member in the glubam roof structure, where the experimental data were precisely recorded using strain gauges. To comprehensively evaluate the predictive accuracy of the numerical model, the measured strain responses were compared with those computed by the model. Overall, the absolute error in strain remained within 2×10^{-4}, indicating a high level of agreement between the model predictions and experimental results. Moreover, the comparative analysis of strain responses across the chord members reveals that Chord 3 consistently experiences the highest internal force, and failure often initiates from this member—a trend that matches experimental observations and further confirms the accuracy and reliability of the proposed model.

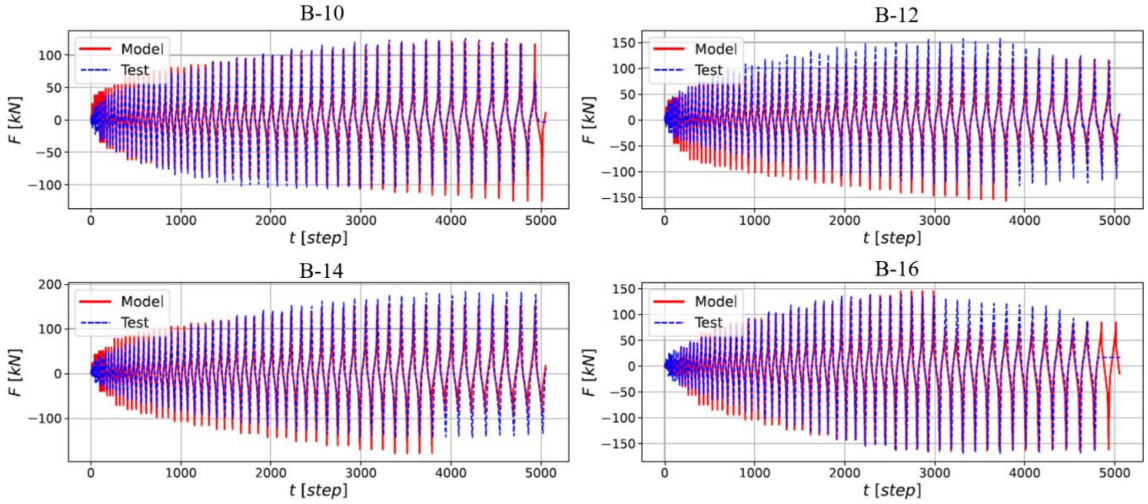

Figure 8-12 Comparison of Force–Time Histories Between the Updated Model Predictions and Experimental Tests

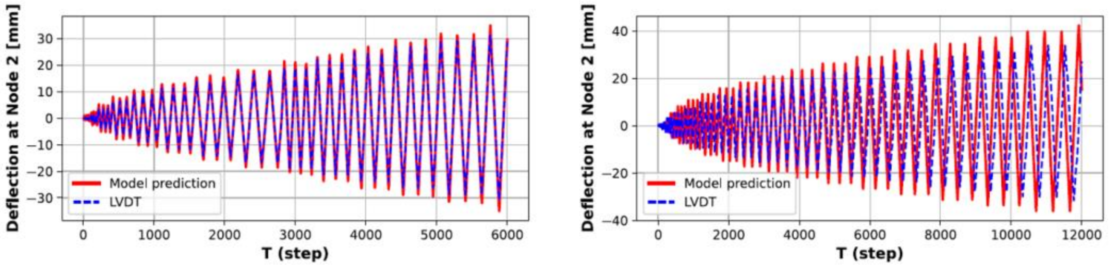

(a) B-10 (b) B-12

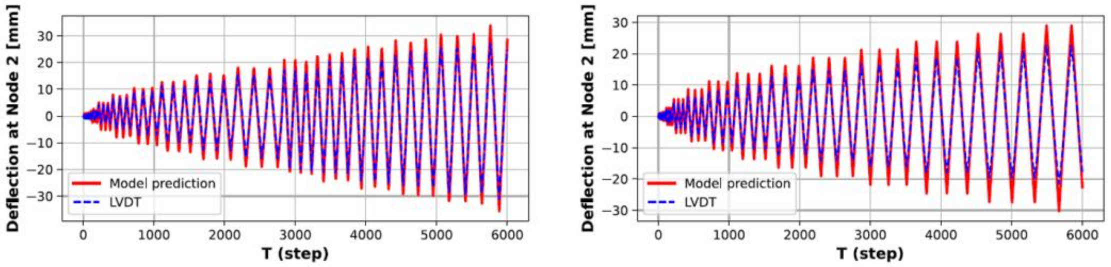

(c) B-14 (d) B-16

Figure 8-13 Comparison of Mid-Span Deflection at Node 2 Between the Updated Model Predictions and Experimental Tests

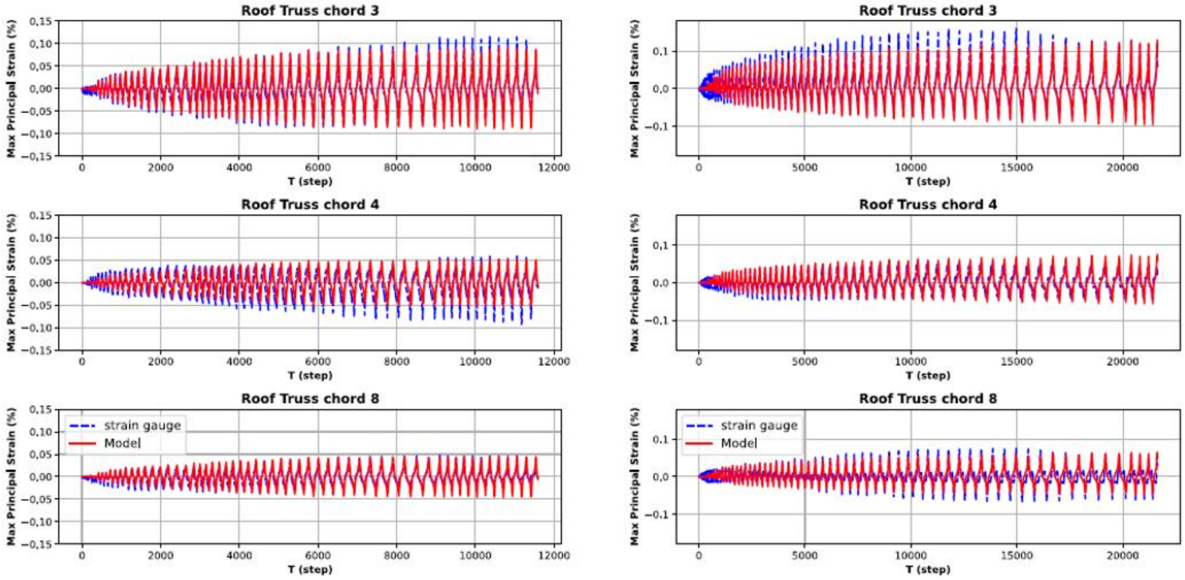

(a) **B-10** (b) **B-12**

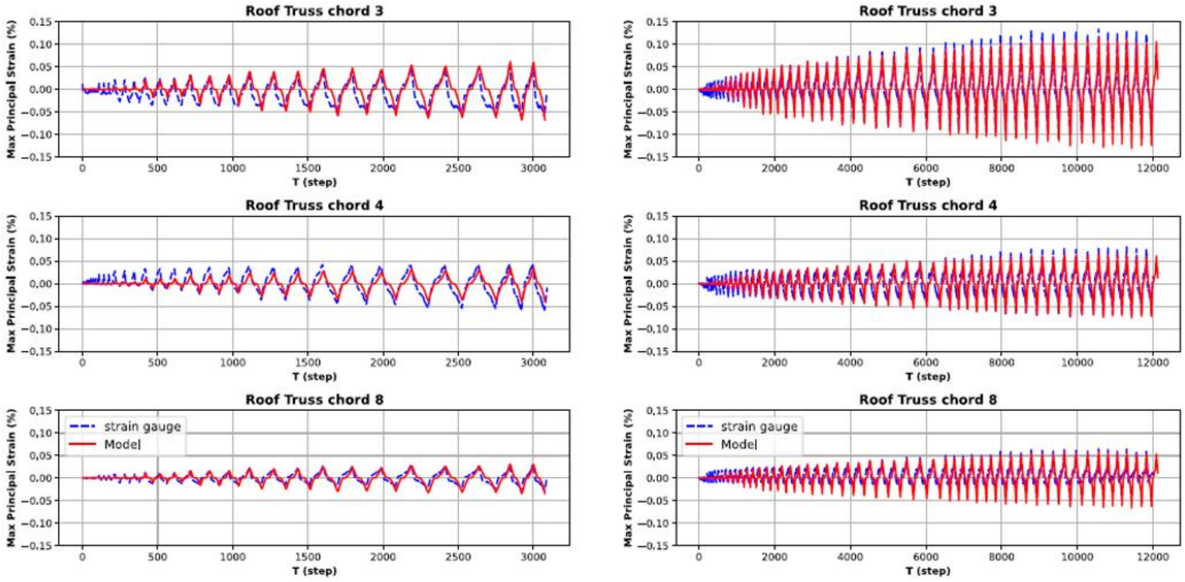

(c) **B-14** (d) **B-16**

Figure 8-14 Comparison of Strain–Time Histories on Chords 3, 4, and 8 Between the Updated Model Predictions and Experimental Measurements

9 Conclusions and Outlook

Against the backdrop of a global push for green and sustainable development in the construction industry, glue-laminated bamboo (glubam) has emerged as a promising new construction material due to its excellent mechanical properties, lightweight yet high strength, and environmentally friendly and renewable characteristics. It is increasingly becoming a research focus in the field of structural engineering. This study employed a combination of experimental investigation and numerical simulation to systematically explore the mechanical performance of glubam joints and truss structures, with an emphasis on their seismic performance, including hysteretic behavior, energy dissipation capacity, and earthquake resistance.

In the experimental research, quasi-static tests were conducted on two types of glubam joints and their corresponding truss structures to evaluate their hysteretic behavior. The results indicate that the proposed glubam joints and trusses exhibit excellent energy dissipation capacity and demonstrate ductile failure modes, thereby meeting the seismic design requirements for structural systems.

In the numerical simulation, both high-fidelity finite element models and low-fidelity simplified hysteresis models were developed for the two types of joints. Notably, the high-fidelity 3D finite element model innovatively integrates element deletion techniques and the Hill yield criterion, enabling accurate simulation of the orthotropic behavior and cracking mechanisms of glubam. For the simplified models, two separate hysteresis models were developed for the Steel Insert-Plate Glubam Connectors and the Steel Side-Clamped-Plate Glubam Connectors, respectively. A series of optimization-based parameter identification methods were also proposed to enhance the robustness and accuracy of the hysteresis models. Furthermore, a hybrid simulation method based on hysteresis model updating was proposed for the numerical analysis of glubam truss structures. Using this method, a highly robust numerical model of integrated trusses was constructed, which can accurately predict the structural response under seismic loading. This provides a solid theoretical foundation and technical support for the application of glubam in structural engineering.

1. Hysteretic Performance of Glubam Joints

As the key structural components governing both load-bearing capacity and ductility in glubam structures, the hysteretic performance of glubam joints plays a decisive role in the overall seismic performance of the system. In this study, quasi-static cyclic loading tests were systematically conducted on two typical types of glubam joint connections to comprehensively evaluate their hysteretic behavior, stiffness degradation, energy dissipation capacity, and failure modes under repeated loading.

The test results demonstrate that the proposed glubam joint connectors not only possess strong load-bearing capacity but also exhibit excellent ductility and stable energy dissipation performance. The hysteresis curves of the joints display favorable plastic deformation capacity, maintaining high energy dissipation efficiency over multiple loading cycles, thus satisfying the current seismic design code requirements for ductility and energy dissipation.

In terms of failure modes, the glubam joints primarily exhibited ductile failure characteristics. Specifically:

- The Steel Insert-Plate Glubam Connectors predominantly failed due to shear failure and splitting failure in the glubam material.
- The Steel Side-Clamped-Plate Glubam Connectors mainly experienced shear failure of the glubam or shear failure at the bolt heads.

These observed failure modes further validate the high safety redundancy and energy dissipation potential of these connection types under seismic loading, laying a solid foundation for the application of glubam structures in earthquake-resistant engineering.

2. Seismic Performance of Glubam Truss Structures

Given the excellent hysteretic performance demonstrated by the glubam joint connectors, their application as critical connection components in truss structures shows significant potential. Building on the two typical types of glubam joints, this study further designed and constructed two types of planar truss/roof systems, and conducted quasi-static cyclic loading tests to systematically investigate the overall hysteretic response, energy dissipation capacity, and seismic performance of glubam truss structures. The test results indicate that under cyclic loading, glubam truss structures exhibit good ductility, stable deformation capacity, and high energy dissipation efficiency. The overall performance meets the relevant requirements of current seismic design standards. Even after multiple reversed loading cycles, the truss systems maintained favorable mechanical performance and hysteretic stability, further confirming the feasibility and applicability of glubam as a seismic structural material. Additionally, the experiments revealed that the geometric dimensions of joint fasteners significantly influence the overall performance of the truss. It was found that using larger-diameter bolts generally resulted in higher load-bearing capacity and greater initial stiffness, but sometimes led to reduced ductility. In contrast, smaller-diameter bolts were more effective in mobilizing the deformation capacity and hysteretic energy dissipation of the joints, demonstrating superior ductility performance and energy dissipation efficiency. These findings not only validate the effectiveness of glubam joints in truss applications but also provide theoretical guidance and practical references for the seismic design and connection optimization of other glubam structural systems.

3. Development of a Constitutive Model for Glubam Joints

Building upon the experimental investigation of further conducted numerical simulations to gain deeper insights into the mechanical behavior glubam joints, this study and failure mechanisms of joints under different connection configurations. For the two typical types of joints, high-fidelity three-dimensional finite element (FE) models were developed. A key innovation lies in the integration of the element deletion technique with the Hill yield criterion, allowing simultaneous representation of the orthotropic behavior of glubam and the crack evolution process. The proposed constitutive model was implemented into Abaqus via a user-defined material subroutine (UMAT) and successfully applied to the 3D finite element analysis of the Steel Insert-Plate Glubam Connector. The simulation results showed excellent agreement with the experimentally obtained load–displacement curves, fully validating the model’s accuracy and applicability in capturing the nonlinear response and failure behavior of glubam joints.

4. Development and Parameter Identification of Hysteresis Models for Glubam Joints

To support efficient numerical analysis at the structural system level, two simplified hysteresis constitutive models were developed for the two typical types of glubam joint connections. These models are parameterized and characterized by a clear structure, high computational efficiency, and strong integrability, making them well-suited for integration into complex structural systems.

The proposed hysteresis models are capable of accurately capturing key nonlinear behaviors of glubam joints under cyclic loading, including pinching effects, asymmetric responses, and strength degradation. To ensure prediction accuracy and stability under various loading conditions, a series of optimization algorithms—including genetic algorithms, Bayesian inference, and neural networks—were employed to systematically identify and calibrate the model parameters.

By comparing the simulation results with experimental data, the optimal parameter identification strategy was selected. The calibrated models demonstrated excellent agreement with experimental results in terms of force–displacement hysteresis behavior and energy dissipation characteristics. The study shows that the identified hysteresis models exhibit strong applicability and accuracy, enabling effective prediction of the hysteretic behavior of glubam joints under diverse loading paths. This modeling framework not only provides a theoretical basis for the application of glubam structures in seismic design, but also offers a methodological reference for the development and parameter optimization of hysteresis models for other types of structural joints.

5. Numerical Simulation and Model Updating of Glubam Trusses

This study conducted a hybrid simulation of glubam truss and roof structures based on model updating techniques. By embedding hysteresis constitutive models of the joints into a macro-scale truss model, a numerical framework was developed that effectively captures the interaction between local joint behavior and global structural response. By concentrating nonlinear behavior within connection elements, the model significantly reduces computational complexity while maintaining simulation accuracy.

Numerical models of Steel Insert-Plate Glubam Warren Trusses and Steel Side-Clamped-Plate Glubam Roof Structures were developed on the OpenSees and ABAQUS platforms, respectively. Building on these models, advanced optimization techniques such as Bayesian inference and genetic algorithms were employed for parameter identification and model updating, using experimental data as a reference.

The proposed updating framework incorporates both global responses (e.g., nodal forces and displacements) and local responses (e.g., chord member strains), thereby enhancing the model’s ability to capture both overall structural behavior and local deformation mechanisms. The results show that the updated numerical models can accurately reproduce the force–displacement hysteresis, energy dissipation history, and joint deformation characteristics under cyclic loading. Notably, in the joint updating framework that includes local response data, prediction errors were significantly reduced, and the stability and physical interpretability of the model were markedly improved.

Furthermore, the coefficient of variation (COV) analysis provided insights into the uncertainty behavior of various model parameters under different updating strategies, offering theoretical guidance for future studies on model complexity control and reliability assessment.

The proposed hybrid simulation framework based on model updating offers a feasible and effective approach for the seismic performance evaluation and design optimization of glubam structures. It also provides a new methodology and technical foundation for efficient and interpretable numerical simulation of bamboo structural systems in real-world engineering applications.

6. Innovations and Contributions

This study focuses on improving the joint behavior and modeling accuracy of glubam structural systems through a comprehensive framework that integrates experimental investigation, numerical simulation, and artificial intelligence-based optimization for parameter identification and model updating. A complete research pathway is established—from joint detailing and experimental validation to model development and parameter calibration. The main innovations and theoretical contributions of this research are summarized as follows:

1). Development of a High-Fidelity Modeling Method for the Hysteretic Behavior of Glubam Joints

For the first time, this study integrates the element deletion technique with the Hill yield criterion to develop a high-fidelity finite element model capable of simulating both the orthotropic characteristics and crack propagation behavior of glubam material. The model is implemented via a UMAT subroutine in Abaqus, enabling accurate capture of the nonlinear failure behavior of joints under various loading conditions. This significantly enhances the physical credibility and simulation performance of the finite element analysis.

2). Development of Two Low-Fidelity Hysteresis Models for Glubam Joints and Their Parameter Identification Framework

Low-fidelity hysteresis models were constructed for Steel Insert-Plate and Steel Side-Clamped-Plate Glubam Connectors, designed for seamless integration into macro-scale structural simulations. These models employ serial–parallel combinations of elastic and nonlinear material elements to reproduce essential nonlinear features such as pinching, stiffness degradation, and response asymmetry under cyclic loading. To overcome the limitations of traditional parameter identification methods in terms of accuracy and efficiency, this study introduces a multi-strategy optimization framework based on genetic algorithms, Bayesian inference, and neural networks, offering a new paradigm for the calibration of complex hysteresis models.

3). Establishment of a Multi-Level Response-Based Hybrid Modeling and Updating Framework for Trusses and Roof Structures

At the structural level, a hybrid modeling strategy is proposed that combines the low-fidelity joint hysteresis model with beam–truss elements, improving the efficiency and scalability of large-scale glubam structural modeling. By incorporating multi-level response data, including nodal forces, mid-span deflections, and member strains, and applying Bayesian inference and genetic algorithms, a dual-scale feedback updating mechanism ("global behavior + local behavior") is established. Results demonstrate that this approach significantly enhances the model's predictive capacity and simulation accuracy across different structural scales.

4). Provision of Theoretical and Technical Foundations for Sustainable Structural Design

From hysteretic behavior analysis to model identification and optimization-based updating, this study comprehensively explores the seismic application potential of glubam in structural systems. A full modeling and performance evaluation strategy suitable for green building design is proposed, offering both theoretical value and practical significance for the application of glubam and other bio-based materials in modern structural engineering.

In summary, this research not only advances the numerical modeling theory for glubam joints and truss systems but also innovatively incorporates intelligent optimization algorithms into structural parameter identification and model updating. It establishes a modeling and design methodology characterized by high accuracy, high efficiency, and broad applicability, providing a solid foundation for the engineering application of novel green construction materials in seismic structural design.

7. Future Research Directions and Outlook

Although this study provides a solid theoretical foundation and technical support for the application of glubam joints and truss structures in seismic design, several challenges and open questions remain in the pursuit of wider adoption in engineering practice. Future research can be extended in the following directions:

1). Design Optimization of Glubam Joints

Joint design is a critical aspect of glubam structural systems. Future studies should further explore the optimization of various joint types, especially under high-intensity seismic loading, focusing on enhancing seismic performance and long-term durability to meet increasingly complex engineering demands.

2). Enhancement of Glubam Material Properties

Despite the excellent mechanical properties of glubam, its long-term stability and durability remain key research concerns. Future work may investigate material treatment techniques such as thermal modification, chemical modification, or laminate process improvement, to enhance performance under complex environmental conditions and extend its applicability in seismic engineering.

3). Application of Intelligent Optimization Algorithms

With the advancement of artificial intelligence, future studies may integrate deep learning and other intelligent optimization algorithms for more refined performance-based design of glubam structures, thereby further improving their mechanical efficiency and seismic resilience.

4). Standardization and Code Development

Currently, the standardization of glubam materials and structures is still in its early stages. There is a pressing need for the development of design codes, material standards, and testing protocols to promote the mainstream adoption of glubam in engineering applications globally.

5). Integration of Glubam into Green Building Systems

As the demand for sustainable architecture continues to grow, glubam—being a renewable and environmentally friendly material—holds great potential in green building applications. Future research may explore its integration with other green technologies, such as energy-efficient glazing or solar energy systems, to develop more energy-saving and eco-friendly building systems.

In summary, as a sustainable construction material, glubam is expected to play an increasingly important role in the future of the building industry. With continued research and technological advancement, glubam will offer diversified solutions to support the goals of low-carbon construction and sustainable development.

References

[1] Xiao Y, Li Z, Wang R, et al. Novel and Non-Conventional Materials and Technologies for Sustainability[M]. 2011.

[2] Das M C, Nath A, Das A. Indigenous traditional knowledge in conservation and management of bamboos of Barak valley, Assam[J]. Journal of Traditional and Folk Practices, 2016, 4: 185-192.

[3] Archila-Santos H F, Ansell M P, Walker P. Low Carbon Construction Using Guadua Bamboo in Colombia[J]. Key Engineering Materials, 2012, 517: 127 - 134.

[4] Gonzalez G G. Plybamboo wall-panels for housing : structural design[C], 2003.

[5] Sharma B, Gatóo A, Bock M, et al. Engineered bamboo for structural applications[J]. Construction and Building Materials, 2015, 81: 66-73.

[6] Echeverry J S, Correal J F. Cyclic behavior of Laminated Guadua Mat sheathing-to-framing connections[J]. Construction and Building Materials, 2015, 98: 69-79.

[7] Okubo K, Fujii T, Yamamoto Y. Development of bamboo-based polymer composites and their mechanical properties[J]. Composites Part A-applied Science and Manufacturing, 2004, 35: 377-383.

[8] Baharuddin N, Abdul Karim S R, Kassim A S, et al.: Global Bamboo Industries: An Overview, Md Tahir P, Lee S H, Osman Al-Edrus S S, Uyup M K A, editor, Multifaceted Bamboo: Engineered Products and Other Applications, Singapore: Springer Nature Singapore, 2023: 15-41.

[9] Pradhan Nischal P N, Dimitrakopoulos Elias G. Pilot Study on Capacity-Based Design of Multiculm Bamboo Axial Members with Dowel-Type Connections[J]. Journal of Structural Engineering, 2021, 147(5): 04021040.

[10] Wang Y, Jia S, Ling Z, et al. Balancing the strength and toughness in delignified bamboo through the changing of silicon composition[J]. Materials & Design, 2024, 247: 113408.

[11] Zhang K, Liu Y, Huang D. Behavior of glued laminated bamboo in compression perpendicular to the grain at elevated temperature[J]. Construction and Building Materials, 2023, 409: 134081.

[12] Kang W, Ni K, Su H, et al. Glued-bamboo composite based on a highly cross-linked cellulose-based adhesive and an epoxy functionalized bamboo surface[J]. International Journal of Biological Macromolecules, 2024, 270: 132500.

[13] Chen Z, Du H, Wang L, et al. Embedment Performance of Glued Laminated Bamboo and

Timber Composite Joints[J]. Buildings, 2024, 14(12): 4043.

[14] Liu W, Xu H, Hu X, et al. Strengthening and repairing of engineered bamboo-steel epoxy adhesive joints with carbon nanotube on the basis of resin pre-coating method[J]. European Journal of Wood and Wood Products, 2020, 78(2): 313-320.

[15] Quaranta G, Demartino C, Xiao Y. Experimental dynamic characterization of a new composite glubam-steel truss structure[J]. Journal of Building Engineering, 2019, 25: 100773.

[16] Shi D, Marano G C, Demartino C. Modeling of glubam roof truss, parameter identification and updating based on parallel genetic algorithm[J]. Engineering Structures, 2024, 316: 118520.

[17] Shi D, Xu Y, Demartino C, et al. Glubam roof truss with riveted glubam connections adopting thin-walled steel tube: Experiment, modeling, and model-updating[J]. Journal of Building Engineering, 2024, 96: 110550.

[18] Xiao Y, Chen G, Feng L. Experimental studies on roof trusses made of glubam[J]. Materials and Structures, 2014, 47(11): 1879-1890.

[19] Wu Y, Xiao Y. Steel and glubam hybrid space truss[J]. Engineering Structures, 2018, 171: 140-153.

[20] Li Z, Yang G-S, Zhou Q Y, et al. Bending performance of glubam beams made with different processes[J]. Advances in Structural Engineering, 2018, 22: 535 - 546.

[21] Chen G, Yu Y, Li X, et al. Mechanical behavior of laminated bamboo lumber for structural application: an experimental investigation[J]. European Journal of Wood and Wood Products, 2020, 78(1): 53-63.

[22] Li H-T, Zhang Q-S, Huang D-S, et al. Compressive performance of laminated bamboo[J]. Composites Part B: Engineering, 2013, 54: 319-328.

[23] 徐德良, 刘伟庆, 杨会峰, et al. 木材-钢填板螺栓连接的承载能力试验研究[J]. 南京工业大学学报：自然科学版, 2009, 31(1): 6.

[24] He M, Luo J, Tao D, et al. Rotational behavior of bolted glulam beam-to-column connections with knee brace[J]. Engineering Structures, 2020, 207: 110251.

[25] Leng Y, Xu Q, Harries K A, et al. Experimental study on mechanical properties of laminated bamboo beam-to-column connections[J]. Engineering Structures, 2020, 210: 110305.

[26] Chen C J, Lee T L, Jeng D S. Finite element modeling for the mechanical behavior of dowel-type timber joints[J]. Computers & Structures, 2003, 81(30): 2731-2738.

[27] Hong J-P, Barrett D. Three-Dimensional Finite-Element Modeling of Nailed Connections in Wood[J]. Journal of Structural Engineering, 2010, 136(6): 715-722.

[28] Izzi M, Rinaldin G, Polastri A, et al. A hysteresis model for timber joints with dowel-type fasteners[J]. Engineering Structures, 2018, 157: 170-178.

[29] Xu J, Dolan J D. Development of Nailed Wood Joint Element in ABAQUS[J]. Journal of Structural Engineering-asce, 2009, 135: 968-976.

[30] Cao J, Xiong H, Chen L. Procedure for parameter identification and mechanical properties assessment of CLT connections[J]. Engineering Structures, 2020, 203: 109867.

[31] Di Gangi G, Demartino C, Quaranta G. Bamboo Lightweight Shear Walls: Modeling and Identification of Sheathing-to-Framing Connections for Seismic Response Analysis[J]. International Journal of Structural Glass and Advanced Materials Research, 2020, 3: 149-159.

[32] Cao J, Xiong H, Wang J, et al. Model updating for timber-framed construction using the full-scale test[J]. Engineering Structures, 2020, 213: 110560.

[33] 内奥米·斯汤戈. 新型木建筑[M]. 北京: 中国轻工业出版社, 2002.

[34] 喻汝青. 浅谈日本大跨木穹顶设计[J]. 建筑技艺, 2014(04): 118-121.

[35] 谢桥军, 肖岩. 大跨度胶合竹结构屋架受力性能研究[J]. 建筑结构学报, 2016, 37(04): 47-53.

[36] Li Z, Li T, Wang C, et al. Experimental study of an unsymmetrical prefabricated hybrid steel-bamboo roof truss[J]. Engineering Structures, 2019, 201: 109781.

[37] Yang, Won-Jik. Substructure Online Test Using Real-Time Hysteresis Modeling with Neural Network[J]. JOURNAL OF THE ARCHITECTURAL INSTITUTE OF KOREA Structure & Construction, 2008, 24(3): 53-60.

[38] Hashemi M J, Masroor A, Mosqueda G. Implementation of online model updating in hybrid simulation[J]. Earthquake Engineering & Structural Dynamics, 2014, 43(3): 395-412.

[39] Elnashai A. Application of In-Test Model Updating to Earthquake Structural Assessment[J]. Journal of Earthquake Engineering, 2015, 20: 1-18.

[40] 陈凡. 框架结构离线模型更新混合试验方法研究[D]. 湖南大学, 2020.

[41] Zhong W, Chen Z. Model updating method for hybrid simulation based on global sensitivity analysis[J]. Earthquake Engineering & Structural Dynamics, 2021, 50(14): 3792-3813.

[42] Lewis D J, Clever J, Meckes C, et al. An Updated Tribal and Subtribal Classification of the Bamboos (Poaceae : Bambusoideae) Bamboo Phylogeny Group[C], 2012.

[43] Sungkaew S S C, Salamin N, Hodkinson Tr. Non-monophyly of the woody bamboos (Bambuseae; Poaceae): a multi-gene region phylogenetic analysis of Bambusoideae[J]. J Plant Res, 2009, 122: 95-108.

[44] Group G, Barker N, Clark L, et al. Phylogeny and Subfamilial Classification of the Grasses (Poaceae)[J]. Annals of the Missouri Botanical Garden, 2002, 88: 373.

[45] Thomas W. American bamboos. By Emmet J. Judziewicz, Lynn G. Clark, Ximena Londoño, and Margaret J. Stern[J]. Brittonia, 1999, 51(2): 158-158.

[46] Lobovikov M, Paudel S R, Piazza M, et al. World bamboo resources. A thematic study prepared in the framework of the Global Forest Resources Assessment 2005[C], 2007.

[47] Roslan S a H, Rasid Z A, Hassan M Z. Bamboo reinforced polymer composite - A comprehensive review[J]. IOP Conference Series: Materials Science and Engineering, 2018, 344(1): 012008.

[48] Zhang Q, Jiang S, Tang Y. Industrial Utilization on Bamboo[M]. International Network for Bamboo and Rattan, 2002.

[49] Chaowana P. Bamboo: An Alternative Raw Material for Wood and Wood-Based Composites[J]. Journal of Materials Science Research, 2013, 2: 90.

[50] Wegst U G K. Bending efficiency through property gradients in bamboo, palm, and wood-based composites[J]. Journal of the Mechanical Behavior of Biomedical Materials, 2011, 4(5): 744-755.

[51] Ashby M F, Gibson L J, Wegst U G K, et al. The mechanical properties of natural materials. I. Material property charts[J]. Proceedings of the Royal Society of London. Series A: Mathematical and Physical Sciences, 1995, 450: 123 - 140.

[52] Rao K M M, Rao K M. Extraction and tensile properties of natural fibers: Vakka, date and bamboo[J]. Composite Structures, 2007, 77(3): 288-295.

[53] Song J, Utama Surjadi J, Hu D, et al. Fatigue characterization of structural bamboo materials under flexural bending[J]. International Journal of Fatigue, 2017, 100: 126-135.

[54] Palombini F L, Kindlein W, Oliveira B F D, et al. Bionics and design: 3D microstructural characterization and numerical analysis of bamboo based on X-ray microtomography[J]. Materials Characterization, 2016, 120: 357-368.

[55] Grosser D, Liese W. On the anatomy of Asian bamboos, with special reference to their vascular bundles[J]. Wood Science and Technology, 1971, 5(4): 290-312.

[56] Zhenhua J. Bamboo and Rattan in the World[C], 2007.

[57] 田黎敏，靳贝贝，郝际平. 现代竹结构的研究与工程应用[J]. 工程力学, 2019, 36(5): 1-18,27.

[58] Palombini F L, Kindlein W, De Oliveira B F, et al. Bionics and design: 3D microstructural characterization and numerical analysis of bamboo based on X-ray microtomography[J]. Materials Characterization, 2016, 120: 357-368.

[59] Wang X-Q, Keplinger T, Gierlinger N, et al. Plant material features responsible for bamboo's excellent mechanical performance: a comparison of tensile properties of bamboo and spruce at the tissue, fibre and cell wall levels[J]. Annals of botany, 2014, 114 8: 1627-35.

[60] Li Z, Jiang Z, Fei B, et al. Comparison of bamboo green, timber and yellow in sulfite, sulfuric acid and sodium hydroxide pretreatments for enzymatic saccharification[J]. Bioresource technology, 2013, 151C: 91-99.

[61] Sun Z-Y, Tang Y-Q, Iwanaga T, et al. Production of fuel ethanol from bamboo by concentrated sulfuric acid hydrolysis followed by continuous ethanol fermentation[J]. Bioresource Technology, 2011, 102(23): 10929-10935.

[62] Chaowana P, Barbu M C, Frühwald A. BAMBOO - A FUNCTIONALLY GRADED COMPOSITE MATERIAL[C], 2014.

[63] Guan M, Huang Z, Zeng D. Shear Strength and Microscopic Characterization of a Bamboo Bonding Interface with Phenol Formaldehyde Resins Modified with Larch Thanaka and Urea[J]. Bioresources, 2016, 11: 492-502.

[64] Nugroho N, Ando N. Development of structural composite products made from bamboo I: fundamental properties of bamboo zephyr board[J]. Journal of Wood Science, 2000, 46(1): 68-74.

[65] Zheng Y, Yi B-L, Tong Y-Q, et al. Influence of assemble patterns on bonding strength of glued bamboo[J]. Journal of Wood Science, 2020, 66(1): 60.

[66] Nkeuwa W N, Zhang J, Semple K E, et al. Bamboo-based composites: A review on fundamentals and processes of bamboo bonding[J]. Composites Part B: Engineering, 2022, 235: 109776.

[67] Spencer R R, Akin D E. Rumen Microbial Degradation of Potassium Hydroxide-treated Coastal Bermudagrass Leaf Blades Examined by Electron Microscopy[J]. Journal of Animal Science, 1980, 51(5): 1189-1196.

[68] Siró I, Plackett D. Microfibrillated cellulose and new nanocomposite materials: a review[J]. Cellulose, 2010, 17(3): 459-494.

[69] Scheller H V, Ulvskov P. Hemicelluloses - Annual Review of Plant Biology, 61(1):263[J].

[70] Popper Z A. Evolution and diversity of green plant cell walls[J]. Current Opinion in Plant Biology, 2008, 11(3): 286-292.

[71] Yue P-P, Fu G-Q, Hu Y-J, et al. Changes of Chemical Composition and Hemicelluloses Structure in Differently Aged Bamboo (Neosinocalamus affinis) Culms[J]. Journal of Agricultural and Food Chemistry, 2018, 66(35): 9199-9208.

[72] Dinwoodie J M. Timber: Its Nature and Behaviour[M]. CRC Press, 2000.

[73] Hillis D W E. Heartwood and Tree Exudates[C]. Springer Series in Wood Science, 1987.

[74] Huang Y, Fei B, Wei P, et al. Mechanical properties of bamboo fiber cell walls during the culm development by nanoindentation[J]. Industrial Crops and Products, 2016, 92: 102-108.

[75] Crow E, Murphy R J. Microfibril orientation in differentiating and maturing fibre and parenchyma cell walls in culms of bamboo ((Carr.) Riv. & Riv.)[J]. Botanical Journal of the Linnean Society, 2000, 134(1): 339-359.

[76] Liese W. The Anatomy of Bamboo Culms[C], 2002.

[77] Parameswaran N, Liese W. Ultrastructural aspects of bamboo cells[J]. Cellulose Chemistry and Technology, 1980.

[78] Batchelor W J, Conn A B, Parker I. Measuring the fibril angle of fibres using confocal microscopy[J]. Appita Journal, 1997, 50: 377-380.

[79] Bai Z, Lv Z, Rao J, et al. The effect of bamboo (Phyllostachys pubescens) cell types on the structure of hemicelluloses[J]. Industrial Crops and Products, 2022, 187: 115464.

[80] Dungani R, Sulaeman A, Nurudin N, et al. Review on Quality Enhancement of Bamboo Utilization: Preservation, Modification and Applications[J]. Asian Journal of Plant Sciences, 2017, 17: 1-18.

[81] Schmidt O, Wei D, Liese W, et al. Fungal degradation of bamboo samples[J]. Holzforschung, 2011, 65: 883–888.

[82] Archila H, Kaminski S, Trujillo D, et al. Bamboo reinforced concrete: a critical review[J]. Materials and Structures, 2018, 51.

[83] Liese W. Bamboos - Biology, silvics, properties, utilization[C], 1985.

[84] Nandiyanto A B D, Fiandini M, Ragadhita R, et al. Mechanical and biodegradation properties of cornstarch-based bioplastic material[C], 2020.

[85] Sun F, Bao B, Ma L, et al. Mould-resistance of bamboo treated with the compound of chitosan-copper complex and organic fungicides[J]. Journal of Wood Science, 2012, 58(1):

51-56.

[86] Hanim A R, Zaidon A, Anwar U M K, et al. Effects of Chemical Treatments on Durability Properties of Gigantochloa scortechinii Strips and Ply-bamboo[J]. Asian Journal of Biological Sciences, 2013, 6: 153-160.

[87] Qi J Q, Xie J L, Huang X Y, et al. Influence of characteristic inhomogeneity of bamboo culm on mechanical properties of bamboo plywood: effect of culm height[J]. Journal of Wood Science, 2014, 60(6): 396-402.

[88] Wang Z, Li H, Yang D, et al. Bamboo node effect on the tensile properties of side press-laminated bamboo lumber[J]. Wood Science and Technology, 2021, 55(1): 195-214.

[89] Xuan Y, Li H, Bei Z, et al. Nodes Effect on the Bending Performance of Laminated Bamboo Lumber Unit[J]. Journal of Renewable Materials, 2021.

[90] Liu C, Liu M, Liu W, et al. Interlaminar fracture property of Moso bamboo strips influenced by fiber distributions in bamboo internode and node[J]. Composite Structures, 2022, 294: 115777.

[91] Tan T, Rahbar N, Allameh S M, et al. Mechanical properties of functionally graded hierarchical bamboo structures[J]. Acta Biomaterialia, 2011, 7(10): 3796-3803.

[92] Cheng D, Li T, Smith G D, et al. The properties of Moso bamboo heat-treated with silicon oil[J]. European Journal of Wood and Wood Products, 2018, 76(4): 1273-1278.

[93] Zhu R, Zhang Y, Yu W. Changes in the Chemical Properties of Phyllostachys iridescens Bamboo with Steam Treatment[J]. BioResources, 2015, 10.

[94] He Z, Wang Z, Zhao Z, et al. Influence of ultrasound pretreatment on wood physiochemical structure[J]. Ultrasonics Sonochemistry, 2017, 34: 136-141.

[95] Guan M, Zhou M, Yong C. Antimold Effect of Ultrasonic Treatment on Chinese Moso Bamboo[J]. Forest Products Journal, 2013, 63: 288-291.

[96] Nussbaum R M, Sutcliffe E J, Hellgren A-C. Microautoradiographic studies of the penetration of alkyd, alkyd emulsion and linseed oil coatings into wood[J]. Journal of Coatings Technology, 1998, 70: 49-57.

[97] Piao X, Zhao Z, Guo H, et al. Improved properties of bamboo by thermal treatment with wood wax oil[J]. Colloids and Surfaces A: Physicochemical and Engineering Aspects, 2022, 643: 128807.

[98] Gan J, Chen M, Semple K, et al. Life cycle assessment of bamboo products: Review and harmonization[J]. Science of The Total Environment, 2022, 849: 157937.

[99] Ma X, Cai L, Chen L, et al. Bamboo grid versus polyvinyl chloride as packing material

in cooling tower: Energy efficiency and environmental impact assessment[J]. Journal of Environmental Management, 2021, 286: 112190.

[100] Pardo C A. A COMPARATIVE LIFE CYCLE ASSESSMENT OF A SOCIAL INTEREST HOUSING BUILDING: BAMBOO VS. CONCRETE[C], 2014.

[101] Shi S Q, Cai L, Weng Y, et al. Comparative life-cycle assessment of water supply pipes made from bamboo vs. polyvinyl chloride[J]. Journal of Cleaner Production, 2019, 240: 118172.

[102] Vogtländer J, Van Der Lugt P, Brezet H. The sustainability of bamboo products for local and Western European applications. LCAs and land-use[J]. Journal of Cleaner Production, 2010, 18(13): 1260-1269.

[103] Bonilla S H, Guarnetti R L, Almeida C M V B, et al. Sustainability assessment of a giant bamboo plantation in Brazil: exploring the influence of labour, time and space[J]. Journal of Cleaner Production, 2010, 18(1): 83-91.

[104] Panda H. Bamboo Plantation and Utilization Handbook: Bamboo products manufacturing process, Bamboo Products Processing, Bamboo Products, Bamboo properties, Bamboo pulp manufacturing process, Bamboo Pulp, Bamboo pulp-Making process, Bamboo resources and their utilization, Bamboo Shoots, Bamboo Small Business Manufacturing, Bamboo Technology, Bamboo Used For Paper Manufacture, Bamboo Utilization, Bamboo: properties and utilization[M]. Asia Pacific Business Press, 2011.

[105] Ramirez A D, Torres D, Peña P, et al. Life Cycle Assessment Of Greenhouse Gas Emissions Arising From The Production Of Glued And Pressed Wall Panels Derived From Guadua Angustifolia Kunth (bamboo) In Ecuador[C]. International Workshop on Applied Reconfigurable Computing, 2014.

[106] Salcido J C, Raheem A A, Ravi S. Comparison of embodied energy and environmental impact of alternative materials used in reticulated dome construction[J]. Building and Environment, 2016, 96: 22-34.

[107] Ge S, Ma N L, Jiang S, et al. Processed bamboo as a novel formaldehyde-free high-performance furniture bio-composite[J]. ACS applied materials & interfaces, 2020.

[108] Laleicke P F, Cimino-Hurt A, Gardner D N A, et al. COMPARATIVE CARBON FOOTPRINT ANALYSIS OF BAMBOO AND STEEL SCAFFOLDING[J]. Journal of Green Building, 2015, 10: 114-126.

[109] Lugt P V D, Vogtländer J G, Vegte J H V D, et al. Environmental Assessment of Industrial Bamboo Products: Life Cycle Assessment and Carbon Sequestration[C], 2015.

[110] Phuong V, Việt N. INBAR Working Paper Technical Paper Life Cycle Assessment for Key Bamboo Products in Viet Nam[M]. 2020.

[111] Liese W, Kumar S, Rattan N D E. Bamboo preservation compendium[C], 2003.

[112] Switzerland I O S. ISO 19624:2018 (E). Bamboo structures -Grading of bamboo culms - Basic principles and procedures", 20118.

[113] Ding J, Wang X, Ge Y, et al. Experimental and nonlinear analytical investigation of the flexural performance of single-box double-chamber steel–bamboo composite beams[J]. Thin-Walled Structures, 2023, 183: 110424.

[114] Li Y, Zhang J, Zhang X, et al. Two-dimensional analysis method of bonding stress at steel-bamboo interface[J]. Structures, 2022, 37: 723-734.

[115] Davies I. Sustainable construction timber sourcing and specifying local timber[C], 2016.

[116] Wang M, Harries K A, Zhao Y, et al. Variation of mechanical properties of P. edulis (Moso) bamboo with moisture content[J]. Construction and Building Materials, 2022, 324: 126629.

[117] 基 太, Ota M. Studies on the Properties of Bamboo Stem (Part 10) : On the Relation between the Tensile Strength Parallel to the Grain and the Moisture Content of Bamboo Splint[J]. Bulletin of the Kyushu University Forests, 1954, 23: 155-164.

[118] Limay V D. Strength of Bamboo (Dendrocalamus strictus)[J]. The Indian Forester, 1952, 78: 558-575.

[119] Vetter R, Sá Ribeiro R, Sá Ribeiro M, et al. Studies on drying of imperial bamboo[J]. Holz als Roh- und Werkstoff - European Journal of Wood and Wood Products, 2015, 73.

[120] Leite Neta M T S, De Jesus M S, Da Silva J a C, et al. Effect of spray drying on bioactive and volatile compounds in soursop (Annona muricata) fruit pulp[J]. Food research international, 2019, 124: 70-77.

[121] Yan J-K, Wu L-X, Qiao Z-R, et al. Effect of different drying methods on the product quality and bioactive polysaccharides of bitter gourd (Momordica charantia L.) slices[J]. Food Chemistry, 2019, 271: 588-596.

[122] China M O C P R. JG/T 199-2007. Testing methods for physical and mechanical properties of bamboo used in building[J], 2007.

[123] Switzerland I O F S. ISO 22157:2019. Bamboo structures-Determination of physical and mechanical properties of bamboo culms-Test methods, 2019.

[124] Saha N, Fillerup E, Thomas B, et al. Improving bamboo's fuel and storage properties

with a net energy export through torrefaction paired with catalytic oxidation[J]. Chemical Engineering Journal, 2022, 440: 135750.

[125] Li Z, Xiao Y, Monti G, et al. Lightweight Woodframe Shear Walls with Ply-Bamboo Sheathings[J]. Applied Mechanics and Materials, 2016, 847: 529 - 536.

[126] Xiao Y, Shan B, Yang R, et al. Glue Laminated Bamboo (GluBam) for Structural Applications[C], 2014.

[127] Wei D, Schmidt O, Liese W. Durability test of bamboo against fungi according to EN standards[J]. European Journal of Wood and Wood Products, 2013, 71.

[128] Ridley-Ellis D J, Moore J C, Lyon A J, et al. Strategic Integrated Research in Timber: Getting the most out of the UK's timber resource[C], 2009.

[129] Switzerland I O F S. ISO 22156:2021. Bamboo Structures - Bamboo Culms - Structural Design, 2021.

[130] Bahtiar E T, Imanullah A P, Hermawan D, et al. Structural grading of three sympodial bamboo culms (Hitam, Andong, and Tali) subjected to axial compressive load[J]. Engineering Structures, 2019, 181: 233-245.

[131] (Cen) T E C F S. BS EN 388: Protective gloves against mechanical risks.

[132] Lefevre B, West R, O'reilly P, et al. A new method for joining bamboo culms[J]. Engineering Structures, 2019, 190: 1-8.

[133] Villegas L, Morán R, García J J. Combined culm-slat Guadua bamboo trusses[J]. Engineering Structures, 2019, 184: 495-504.

[134] Nugroho N, Bahtiar E T, Karlinasari L, et al.: Structural Design of Round Bamboo, 2023: 145-191.

[135] Nurmadina, Nugroho N, Bahtiar E T. Structural grading of Gigantochloa apus bamboo based on its flexural properties[J]. Construction and Building Materials, 2017, 157: 1173-1189.

[136] Trujillo D, Jangra S, Gibson J. Flexural properties as a basis for bamboo strength grading[J]. Proceedings of the Institution of Civil Engineers - Structures and Buildings, 2016, 170: 284-294.

[137] Paraskeva T, Pradhan N P N, Stoura C D, et al. Monotonic loading testing and characterization of new multi-full-culm bamboo to steel connections[J]. Construction and Building Materials, 2019, 201: 473-483.

[138] Pradhan N P N, Paraskeva T S, Dimitrakopoulos E G. Simulation and experimental verification of an original full-scale bamboo truss[J]. Engineering Structures, 2022, 256: 113965.

[139] Shan B, Qiu J, Xu H, et al. Experimental research on standardized bamboo culm components for developing prefabricated bamboo building[J]. Structures, 2023, 50: 272-285.

[140] Puri V, Chakrabortty P, Anand S, et al. Bamboo reinforced prefabricated wall panels for low cost housing[J]. Journal of Building Engineering, 2017, 9: 52-59.

[141] Li H, Wei Y, Yan L, et al. Structural behavior of steel dowel-reinforced cross-laminated bamboo and timber beams[J]. Composite Structures, 2023, 318: 117111.

[142] Dong W, Wang Z, Chen G, et al. Bonding performance of cross-laminated timber-bamboo composites[J]. Journal of Building Engineering, 2023, 63: 105526.

[143] Li H, Wang L, Wang B J, et al. Study on in-plane compressive performance of cross-laminated bamboo and timber (CLBT) wall elements[J]. European Journal of Wood and Wood Products, 2023, 81(2): 343-355.

[144] Wei P, Wang B, Wang L, et al. An exploratory study of composite cross-laminated timber (CCLT) made from bamboo and hemlock-fir mix[J]. BioResources, 2019, 14: 2160-2170.

[145] Rowell R. Chemical modification of wood: A short review[J]. Wood Material Science and Engineering, 2007, 1.

[146] Huang Y, Zhang Y, Qi Y, et al. Identification of odorous constituents of bamboo during thermal treatment[J]. Construction and Building Materials, 2019, 203: 104-110.

[147] Shangguan W, Gong Y, Zhao R, et al. Effects of heat treatment on the properties of bamboo scrimber[J]. Journal of Wood Science, 2016, 62(5): 383-391.

[148] Yun H, Li K, Tu D, et al. Effect of heat treatment on bamboo fiber morphology crystallinity and mechanical properties[J]. Wood research, 2016, 61: 227-234.

[149] Yu Y, Zhu R, Wu B, et al. Fabrication, material properties, and application of bamboo scrimber[J]. Wood Science and Technology, 2015, 49(1): 83-98.

[150] Meng F-D, Yu Y-L, Zhang Y-M, et al. Surface chemical composition analysis of heat-treated bamboo[J]. Applied Surface Science, 2016, 371: 383-390.

[151] Fengel D, Wegener G. Wood: Chemistry, Ultrastructure, Reactions[C], 1983.

[152] Sivonen H, Maunu S L, Sundholm F, et al. Magnetic Resonance Studies of Thermally Modified Wood[C], 2002.

[153] Li Y, Huang C, Wang S, et al. The effects of thermal treatment on the nanomechanical behavior of bamboo (Phyllostachys pubescens Mazel ex H. De Lehaie) cell walls observed by nanoindentation, XRD, and wet chemistry[J]. Holzforshung, 2016, 71.

[154] Zhang Y M, Yu Y L, Yu W J. Effect of thermal treatment on the physical and mechanical

properties of phyllostachys pubescen bamboo[J]. European Journal of Wood and Wood Products, 2013, 71(1): 61-67.

[155] Zhao R, Jiang Z H, Hse C-Y, et al. Effects of steam treatment on bending properties and chemical composition of moso bamboo (Phyllostachys pubescens)[J]. Journal of Tropical Forest Science, 2010, 22: 197-201.

[156] Wang X, Yao Y, Xie X, et al. Investigation of the microstructure, chemical structure, and bonding interfacial properties of thermal-treated bamboo[J]. International Journal of Adhesion and Adhesives, 2023, 125: 103400.

[157] Fabiani M, Greco S, Mentrasti L, et al. Thermal treatment of bamboo with flame: influence on the mechanical characteristics[J]. Advances in Bamboo Science, 2023.

[158] Correal J F: 14 - Bamboo design and construction, Harries K A, Sharma B, editor, Nonconventional and Vernacular Construction Materials: Woodhead Publishing, 2016: 393-431.

[159] Gauss C, Kadivar M, Savastano Jr H. Effect of disodium octaborate tetrahydrate on the mechanical properties of Dendrocalamus asper bamboo treated by vacuum/pressure method[J]. Journal of Wood Science, 2019, 65(1): 27.

[160] Caldeira F. Boron in wood preservation: a review in its physico-chemical aspects[C], 2010.

[161] Khadiran T, Lipeh S, Uyup M K A: Chemical Preservation of Bamboo for Structural Application, Md Tahir P, Lee S H, Osman Al-Edrus S S, Uyup M K A, editor, Multifaceted Bamboo: Engineered Products and Other Applications, Singapore: Springer Nature Singapore, 2023: 67-84.

[162] Liese W, Tang T K H. Preservation and Drying of Bamboo[C], 2015.

[163] Donmez Cavdar A, Mengeloğlu F, Karakus K. Effect of boric acid and borax on mechanical, fire and thermal properties of wood flour filled high density polyethylene composites[J]. Measurement, 2015, 60: 6-12.

[164] Kaur P. Bamboo availability and utilization potential as a building material[J]. Forestry Research and Engineering: International Journal, 2018, 2.

[165] Zhou Z, Yao X, Du C, et al. Effect of hygroscopicity of fire retardant on hygroscopicity of fire retardant bamboo chips[J]. Wood Research, 2018, 63: 373-382.

[166] Ninez K, Prinindya N, Ardiansyah L. The Effect of Chemical Substance and Imm ersion Time ofDendrocalamus asper as Chemical Preservation Treatment[C], 2014.

[167] Janssen J J A. Designing and building with bamboo[J]. CTIT technical reports series,

1997, 20.

[168] Jayanetti D L, Follett P R, Development G B D F I, et al. Bamboo in Construction: An Introduction[M]. TRADA Technology, Limited, 1998.

[169] Chen Y, Ye X-Y, Wang D-W, et al. Stepwise modification with 2,3-epoxypropyltrimethylammonium chloride cationization and rosin acid impregnation to improve water repellency and mold-proof property of bamboo[J]. Industrial Crops and Products, 2023, 193: 116248.

[170] Dong Y, Yan Y, Wang K, et al. Improvement of water resistance, dimensional stability, and mechanical properties of poplar wood by rosin impregnation[J]. European Journal of Wood and Wood Products, 2016, 74(2): 177-184.

[171] Su N, Fang C, Yu Z, et al. Effects of rosin treatment on hygroscopicity, dimensional stability, and pore structure of round bamboo culm[J]. Construction and Building Materials, 2021, 287: 123037.

[172] Klejdysz T, Łęgosz B, Czuryszkiewicz D, et al. Biobased Ionic Liquids with Abietate Anion[J]. ACS Sustainable Chemistry & Engineering, 2016, 4(12): 6543-6550.

[173] Li W, Liu M, Zhai H, et al. Preparing highly durable bamboo materials via bulk furfurylation[J]. Construction and Building Materials, 2020, 262: 120726.

[174] Liu M, Li W, Guo F, et al. Dimensionally stable and highly durable bamboo material prepared through a simple surface furfurylation[J]. Construction and Building Materials, 2021, 276: 122156.

[175] Peng C, Huang A, Ma X, et al. Transparent and flame-retardant hybrid protective coating with high surface hardness, yet foldability[J]. Progress in Organic Coatings, 2023, 175: 107346.

[176] Wang K, Tao Z, Xiao X, et al. Nature-Inspired Phytic Acid-Based Hybrid Complexes for Fabricating Green and Transparent Superhydrophobic and Anti-Mildew Coating on Bamboo Surface[J]. Colloids and Surfaces A: Physicochemical and Engineering Aspects, 2022.

[177] Wang F, Shao J. Modified Weibull Distribution for Analyzing the Tensile Strength of Bamboo Fibers[J]. Polymers, 2014, 6: 3005-3018.

[178] Dauletbek A, Li H, Lorenzo R. A review on mechanical behavior of laminated bamboo lumber connections[J]. Composite Structures, 2023, 313: 116898.

[179] 肖岩 -, 佘立永 -, 单波 -, et al. - 装配式竹结构房屋的设计与研究[J]. - 工业建

筑, 2009, - 39(- 1): - 56.

[180] Xiao Y, Chen G, Shan B, et al. Two-by-four house construction using laminated bamboos[J], 2010, 2.

[181] Hashemi A, Bagheri H, Yousef-Beik S M M, et al. Enhanced Seismic Performance of Timber Structures Using Resilient Connections: Full-Scale Testing and Design Procedure[J]. Journal of Structural Engineering-asce, 2020, 146: 04020180.

[182] Vengala J, Mohanthy B, Raghunath S. Seismic performance of Bamboo housing-an overview[M]. 2015.

[183] Michiels T, Lu L, Archer R, et al. Design of Three Hypar Roofs Made of Guadua Bamboo[J]. Journal of the International Association for Shell and Spatial Structures, 2017, 58: 95-104.

[184] Oliva J G T, Magdalena; Ezeta, Susana; Abud, Ramón; Verhulst, María I. Bamboo gridshells for rural housing in mexico[C], 2022.

[185] Svatoš-Ražnjević H, Orozco L, Menges A. Advanced Timber Construction Industry: A Review of 350 Multi-Storey Timber Projects from 2000–2021[J]. Buildings, 2022, 12: 404.

[186] Wang X, Li Z, Xie P, et al. Seismic assessment of glulam frames with dual-tube self-centering buckling-restrained braces[J]. Journal of Building Engineering, 2024, 97: 110753.

[187] Blomgren H-E, Koppitz J-P, Valdes A. THE HEAVY TIMBER BUCKLING-RESTRAINED BRACED FRAME AS A SOLUTION FOR COMMERCIAL CONSTRUCTION IN REGIONS OF HIGH SEISMICITY[C], 2015.

[188] Xiao Y, Cai H, Dong S Y. A Pilot Study on Cross-Laminated Bamboo and Timber Beams[J]. Journal of Structural Engineering-asce, 2021, 147: 06021002.

[189] Liu K, Demartino C, Li Z, et al.: The 2019 International Bamboo Construction Competition, Liu K, Demartino C, Li Z, Liu Q, Xiao Y, editor, 2019 International Bamboo Construction Competition: From the Concepts to the Realized Pavilions, Cham: Springer International Publishing, 2022: 1-13.

[190] Wang R, Xiao Y, Li Z. Lateral Loading Performance of Lightweight Glubam Shear Walls[J]. Journal of Structural Engineering-asce, 2017, 143: 04017020.

[191] Han T, Liu Y, Lu Y, et al. Design and numerical analysis of Cross-Laminated bamboo (CLB) buildings with different rocking wall configurations[J]. Structures, 2023, 56: 105011.

[192] Blomgren H-E, Pei S, Jin Z, et al. Full-Scale Shake Table Testing of Cross-Laminated Timber Rocking Shear Walls with Replaceable Components[J]. Journal of Structural

Engineering, 2019.

[193] Ji X-D, Molina Hutt C. Seismic design and application of hybrid coupled walls with replaceable steel coupling beams in high-rise buildings[J]. The Structural Design of Tall and Special Buildings, 2020, 29.

[194] Moerman B, Li M, Palermo A, et al. Cyclic Testing and Repair of Coupled CLT Walls with Steel Link Beams[J]. Journal of Structural Engineering, 2024.

[195] Thai H-T, Ngo T, Uy B. A review on modular construction for high-rise buildings[J]. Structures, 2020, 28: 1265-1290.

[196] Bhandari S, Riggio M, Jahedi S, et al. A review of modular cross laminated timber construction: Implications for temporary housing in seismic areas[J]. Journal of Building Engineering, 2023, 63: 105485.

[197] Ramage M, Foster R, Smith S, et al. Super Tall Timber: design research for the next generation of natural structure[J]. The Journal of Architecture, 2017, 22: 1-19.

[198] Jorissen A, Fragiacomo M. General notes on ductility in timber structures[J]. Engineering Structures, 2011, 33(11): 2987-2997.

[199] Leng Y, Xu Q, Harries K A, et al. Experimental study on mechanical properties of laminated bamboo beam-to-column connections[J]. Engineering Structures, 2020, 210: 110305.

[200] Sarkisian M, Mathias N, Garai R, et al. Improving Seismic Resilience Using Structural Systems with Friction-Based Fuses[M]. 2017: 591-602.

[201] Wang R, Wei S Q, Li Z, et al. Performance of connection system used in lightweight glubam shear wall[J]. Construction and Building Materials, 2019, 206: 419-431.

[202] Lu Y, Lv Q, Liu Y. Experimental and numerical study on seismic performance of CLB rocking wall with bending-friction coupled dampers[J]. Journal of Building Engineering, 2022, 45: 103622.

[203] Zhengyao L, Tsavdaridis K. Design for Seismic Resilient Cross Laminated Timber (CLT) Structures: A Review of Research, Novel Connections, Challenges and Opportunities[J]. Buildings, 2023, 13.

[204] Ottenhaus L-M, Jockwer R, Van Drimmelen D, et al. Designing timber connections for ductility – A review and discussion[J]. Construction and Building Materials, 2021, 304: 124621.

[205] GB/T50329-2002. Standard for testing methods of timber structures., 2002.

[206] ASTM. ASTM D143–09: standard test methods for small clear specimens of

timber, 2009.

[207] ASTM. ASTM D5764–97a (2013) standard test method forevaluating dowel-bearing strength of wood and wood-based products, 2013.

[208] ASTM. ASTM F1575-03: Standard test method for determining bending yield moment of nails[J], 2008.

[209] Boccadoro L, Zweidler S, Steiger R, et al. Bending tests on timber-concrete composite members made of beech laminated veneer lumber with notched connection[J]. Engineering Structures, 2017, 132: 14-28.

[210] Jockwer R, Fink G, Köhler J. Assessment of the failure behaviour and reliability of timber connections with multiple dowel-type fasteners[J]. Engineering Structures, 2018, 172: 76-84.

[211] Pilon D S, Palermo A, Sarti F, et al. Benefits of multiple rocking segments for CLT and LVL Pres-Lam wall systems[J]. Soil Dynamics and Earthquake Engineering, 2019, 117: 234-244.

[212] Li Z, He X, Cai Z, et al. Mechanical Properties of Engineered Bamboo Boards for Glubam Structures[J]. Journal of Materials in Civil Engineering, 2021, 33: 04021058.

[213] Tang G, Yin L, Li Z, et al. Structural behaviors of bolted connections using laminated bamboo and steel plates[J]. Structures, 2019, 20: 324-339.

[214] Tang Z, Shan B, Li W G, et al. Structural behavior of glubam I-joists[J]. Construction and Building Materials, 2019, 224: 292-305.

[215] Gonzalez G G. Determination of the embedding strength of plybamboo[C], 2000.

[216] Daloglu A, Vallabhan C. Values of k for Slab on Winkler Foundation[J]. Journal of Geotechnical and Geoenvironmental Engineering - J GEOTECH GEOENVIRON ENG, 2000, 126.

[217] Riley M, Sadek F. Experimental Testing of Roof to Wall Connections in Wood Frame Houses: NIST Interagency/Internal Report (NISTIR), National Institute of Standards and Technology, Gaithersburg, MD, 2003.

[218] GB50005. Code for design of timber structures, 2017.

[219] E E C F S C. Timber structures-test methods-cyclic testing of joints made withmechanical fasteners. Brussels, Belgium., 2001.

[220] Cao J, Xiong H, Liu Y. Experimental study and analytical model of bolted connections under monotonic loading[J]. Construction and Building Materials, 2021, 270: 121380.

[221] Cao J, Xiong H, Chen J, et al. Bayesian parameter identification for empirical model of

CLT connections[J]. Construction and Building Materials, 2019, 218: 254-269.

[222] Liu Y, Wang Y, Zhang Y, et al. Force–displacement relations of bolted timber joints with slotted-in steel plates parallel to the grain[J]. Journal of Wood Science, 2020, 66(1): 83.

[223] Awaludin A, Hirai T, Hayashikawa T, et al. Load-carrying capacity of steel-to-timber joints with a pretensioned bolt[J]. Journal of Wood Science, 2008, 54(5): 362-368.

[224] Macrae G, Clifton G, Mackinven H, et al. The Sliding Hinge Joint Moment Connection[J]. Bulletin of the New Zealand Society for Earthquake Engineering, 2010, 43.

[225] Lam F, Closen M, Gehloff M. Moment-resisting bolted timber connections[J]. Proceedings of The Institution of Civil Engineers-structures and Buildings - PROC INST CIVIL ENG-STRUCT B, 2010, 163: 267-274.

[226] Tao H, Yang H, Ju G, et al. Elastic stiffness of timber joints with dowel-type fasteners and slotted-in steel plate based on the theory of beam on elastic foundation[J]. Construction and Building Materials, 2021, 294: 123569.

[227] Hassanieh A, Valipour H R, Bradford M A. Load-slip behaviour of steel-cross laminated timber (CLT) composite connections[J]. Journal of Constructional Steel Research, 2016, 122: 110-121.

[228] Hassanieh A, Valipour H R, Bradford M A, et al. Modelling of steel-timber composite connections: Validation of finite element model and parametric study[J]. Engineering Structures, 2017, 138: 35-49.

[229] Sawata K. Strength of bolted timber joints subjected to lateral force[J]. Journal of Wood Science, 2015, 61(3): 221-229.

[230] Reynolds T, Sharma B, Harries K, et al. Dowelled structural connections in laminated bamboo and timber[J]. Composites Part B: Engineering, 2016, 90: 232-240.

[231] Ding C, Xia Y, Li Z, et al. Strength of Bolted Lap Shear Connections with Advanced High-Strength Steel Sheets[J]. Journal of Structural Engineering, 2024, 150(1): 04023208.

[232] Cabrero J M, Yurrita M. Performance assessment of existing models to predict brittle failure modes of steel-to-timber connections loaded parallel-to-grain with dowel-type fasteners[J]. Engineering Structures, 2018, 171: 895-910.

[233] Xu B H, Taazount M, Bouchaïr A, et al. Numerical 3D finite element modelling and experimental tests for dowel-type timber joints[J]. Construction and Building Materials, 2009, 23(9): 3043-3052.

[234] Yurrita M, Cabrero J M. New design model for brittle failure in the parallel-to-grain direction of timber connections with large diameter fasteners[J]. Engineering Structures, 2020,

217: 110557.

[235] Li Z, Wang C, Wang R. Application of screw reinforcement in the slotted-in bamboo-steel-bamboo connections[J]. Structures, 2021, 33: 4112-4123.

[236] Mai B V, Pham C H, Hancock G J, et al. Block shear strength and behaviour of cold-reduced G450 steel bolted connections using DIC[J]. Journal of Constructional Steel Research, 2019, 157: 151-160.

[237] Ghosh R, Gupta S, Dickinson A, et al. Experimental Validation of Finite Element Models of Intact and Implanted Composite Hemipelvises Using Digital Image Correlation[J]. Journal of biomechanical engineering, 2012, 134: 081003.

[238] Hong C, Li H, Xiong Z, et al. Axial compressive behavior of laminated bamboo lumber columns with a chamfered section[J]. Structures, 2021, 33: 678-692.

[239] Xu B-H, Bouchair A, Racher P. Mechanical Behavior and Modeling of Dowelled Steel-to-Timber Moment-Resisting Connections[J]. Journal of Structural Engineering, 2014, 141: 04014165.

[240] Hill R. A theory of the yielding and plastic flow of anisotropic metals[J]. Proceedings of the Royal Society of London. Series A. Mathematical and Physical Sciences, 1948, 193: 281 - 297.

[241] Jalilifar E, Koliou M G, Pang W. Experimental and Numerical Characterization of Monotonic and Cyclic Performance of Cross-Laminated Timber Dowel-Type Connections[J]. Journal of Structural Engineering, 2021.

[242] Xu B-H, Taazount M, Bouchair A, et al. Numerical 3D finite element modelling and experimental tests for dowel-type timber joints[J]. Construction and Building Materials - CONSTR BUILD MATER, 2009, 23: 3043-3052.

[243] Guan Z W, Zhu E C. Finite element modelling of anisotropic elasto-plastic timber composite beams with openings[J]. Engineering Structures, 2009, 31(2): 394-403.

[244] Wen H, Mahmoud H. Strength Determination and Fracture Characteristics of Bolted Connections[J]. Journal of Structural Engineering, 2021, 147.

[245] Wen H, Mahmoud H. Block Shear Strength of Coped Beam Connections with Double Bolt Lines[J]. Journal of Structural Engineering, 2021, 148.

[246] Aicher S, Gustafsson P J, Haller P, et al. Fracture Mechanics Models for Strength Analysis of Timber Beams with a Hole or a Notch - A Report of RILEM TC-133[C], 2002.

[247] Yurrita M, Cabrero J M. On the need of distinguishing ductile and brittle failure modes in timber connections with dowel-type fasteners[J]. Engineering Structures, 2021, 242:

112496.

[248] Zhang J, He M, Li Z. Mechanical Performance Assessment of Bolted Glulam Joints with Local Cracks[J]. Journal of Materials in Civil Engineering, 2018, 30: 04018094.

[249] Shi D, Huang H, Li N, et al. Bolted steel to laminated timber and glubam connections: Axial behavior and finite-element modeling[J]. International Journal of Mechanical Sciences, 2023, 252: 108364.

[250] Hong J-P, Barrett D. Three-Dimensional Finite-Element Modeling of Nailed Connections in Wood[J]. Journal of Structural Engineering-asce - J STRUCT ENG-ASCE, 2010, 136.

[251] Xu B-H, Bouchaïr A, Taazount M, et al. Numerical 3D finite element modelling and experimental tests of rounded dovetail connection[J]. European Journal of Environmental and Civil Engineering, 2013, 17: 564 - 578.

[252] Shi D, Demartino C, Li Z, et al. Axial load–deformation behavior and fracture characteristics of bolted steel to laminated timber and glubam connections[J]. Composite Structures, 2023, 305: 116486.

[253] Dong H, He M, Wang X, et al. Development of a uniaxial hysteretic model for dowel-type timber joints in OpenSees[J]. Construction and Building Materials, 2021, 288: 123112.

[254] Xu B H, Bouchaïr A, Taazount M, et al. Numerical and experimental analyses of multiple-dowel steel-to-timber joints in tension perpendicular to grain[J]. Engineering Structures, 2009, 31(10): 2357-2367.

[255] Yang J-Q, Smith S T, Wang Z, et al. Modelling of hysteresis behaviour of moment-resisting timber joints strengthened with FRP composites[J]. International Journal of Mechanical Sciences, 2020, 179: 105593.

[256] Chan N, Hashemi A, Zarnani P Z, et al. Pinching-Free Connector for Timber Structures[J]. Journal of Structural Engineering-asce, 2021, 147: 04021036.

[257] Shi D, Marano G C, Demartino C. Bio-based connections and hybrid planar truss: A parallel genetic algorithm approach for model updating[J]. Computers & Structures, 2024, 301: 107463.

[258] Stewart W G. The seismic design of plywood sheathed shear walls[C], 1987.

[259] Folz B, Filiatrault A. Seismic Analysis of Woodframe Structures. I: Model Formulation[J]. Journal of Structural Engineering-asce - J STRUCT ENG-ASCE, 2004, 130.

[260] Lowes L N, Mitra N. A Beam-Column Joint Model for Simulating the Earthquake Response of Reinforced Concrete Frames[C], 2004.

[261] Dennis J J E, Moré J J. Quasi-Newton Methods, Motivation and Theory[J]. SIAM Review, 1977, 19(1): 46-89.

[262] Ehrlich L W. A modified Newton method for polynomials[J]. Commun. ACM, 1967, 10: 107-108.

[263] Vaswani A, Shazeer N M, Parmar N, et al. Attention is All you Need[C]. Neural Information Processing Systems, 2017.

[264] Au S-K. Operational Modal Analysis[M]. 2017.

[265] Chatfield C. Model uncertainty, data mining and statistical inference[J]. Journal of The Royal Statistical Society Series A-statistics in Society, 1995, 158: 419-444.

[266] Sartori T, Tomasi R. Experimental investigation on sheathing-to-framing connections in wood shear walls[J]. Engineering Structures, 2013, 56: 2197-2205.

[267] Seim W, Kramar M, Pazlar T, et al. OSB and GFB As Sheathing Materials for Timber-Framed Shear Walls: Comparative Study of Seismic Resistance[J]. Journal of Structural Engineering-asce, 2016, 142.

[268] Verdret Y, Faye C, Elachachi S M, et al. Experimental investigation on stapled and nailed connections in light timber frame walls[J]. Construction and Building Materials, 2015, 91: 260-273.

[269] Gu Y, Lu X, Xu Y. A deep ensemble learning-driven method for the intelligent construction of structural hysteresis models[J]. Computers & Structures, 2023, 286: 107106.

[270] Luo H, Paal S G. Data-driven seismic response prediction of structural components[J]. Earthquake Spectra, 2021, 38: 1382 - 1416.

[271] Mckay M D, Beckman R J, Conover W J. A Comparison of Three Methods for Selecting Values of Input Variables in the Analysis of Output From a Computer Code[J]. Technometrics, 2000, 42: 55 - 61.

[272] Xu Y, Fei Y, Huang Y, et al. Advanced corrective training strategy for surrogating complex hysteretic behavior[J]. Structures, 2022, 41: 1792-1803.

[273] Raissi M, Perdikaris P, Karniadakis G E. Physics-informed neural networks: A deep learning framework for solving forward and inverse problems involving nonlinear partial differential equations[J]. Journal of Computational Physics, 2019, 378: 686-707.

[274] Liu F, Li J, Wang L. PI-LSTM: Physics-informed long short-term memory network for structural response modeling[J]. Engineering Structures, 2023, 292: 116500.

[275] Zhang R, Liu Y, Sun H. Physics-informed multi-LSTM networks for metamodeling of nonlinear structures[J]. Computer Methods in Applied Mechanics and Engineering, 2020, 369:

113226.

[276] Gu Q, Ding Y-S, Zhang T-L. An ensemble classifier based prediction of G-protein-coupled receptor classes in low homology[J]. Neurocomputing, 2015, 154: 110-118.

[277] Liu Y, Lin Y, Chen Y. Ensemble Classification Based on ICA for Face Recognition[J]. 2008 Congress on Image and Signal Processing, 2008, 3: 144-148.

[278] Izzi M, Polastri A, Fragiacomo M. Investigating the Hysteretic Behavior of Cross-Laminated Timber Wall Systems due to Connections[J]. Journal of Structural Engineering, 2018, 144.

[279] Graves A. Practical Variational Inference for Neural Networks[C]. Neural Information Processing Systems, 2011.

[280] Blundell C, Cornebise J, Kavukcuoglu K, et al. Weight Uncertainty in Neural Networks[J]. ArXiv, 2015, abs/1505.05424.

[281] Perez-Ramirez C A, Amezquita-Sanchez J P, Valtierra-Rodriguez M, et al. Recurrent neural network model with Bayesian training and mutual information for response prediction of large buildings[J]. Engineering Structures, 2019, 178: 603-615.

[282] Dang H V, Trestian R, Bui-Tien T, et al. Probabilistic method for time-varying reliability analysis of structure via variational bayesian neural network[J]. Structures, 2021, 34: 3703-3715.

[283] Wang T, Li H, Noori M, et al. Probabilistic Seismic Response Prediction of Three-Dimensional Structures Based on Bayesian Convolutional Neural Network[J]. Sensors, 2022, 22: 3775.

[284] Gal Y, Ghahramani Z. Bayesian Convolutional Neural Networks with Bernoulli Approximate Variational Inference[J]. ArXiv, 2015, abs/1506.02158.

[285] Gal Y, Ghahramani Z. Dropout as a Bayesian Approximation: Representing Model Uncertainty in Deep Learning[C]. International Conference on Machine Learning, 2015.

[286] Rosenblatt F. The perceptron: a probabilistic model for information storage and organization in the brain[J]. Psychological review, 1958, 65 6: 386-408.

[287] Haykin S S. Neural Networks: A Comprehensive Foundation[C], 1998.

[288] Hochreiter S, Schmidhuber J. Long Short-Term Memory[J]. Neural Computation, 1997, 9: 1735-1780.

[289] Cho K, Merrienboer B V, Gülçehre Ç, et al. Learning Phrase Representations using RNN Encoder–Decoder for Statistical Machine Translation[C]. Conference on Empirical Methods in Natural Language Processing, 2014.

[290] Xu Y, Lu X, Fei Y, et al. Iterative self-transfer learning: A general methodology for response time-history prediction based on small dataset[J]. ArXiv, 2023, abs/2306.08700.

[291] Yongjia X, Lu X, Fei Y, et al. Hysteretic behavior simulation based on pyramid neural network: Principle, network architecture, case study and explanation[J]. Advances in Structural Engineering, 2023, 26: 2359–2374.

[292] Kitaev N, Kaiser L, Levskaya A. Reformer: The Efficient Transformer[J]. ArXiv, 2020, abs/2001.04451.

[293] Zhou H, Zhang S, Peng J, et al. Informer: Beyond Efficient Transformer for Long Sequence Time-Series Forecasting[M]. 2020.

[294] Wu H, Hu T, Liu Y, et al. TimesNet: Temporal 2D-Variation Modeling for General Time Series Analysis[J]. ArXiv, 2022, abs/2210.02186.

Research Achievements During the Doctoral Program

[1] **Da Shi** ,Yongjia Xu, Cristoforo Demartino, Yan Xiao, Billie F. Spencer. Cyclic behavior of laminated bio-based connections with slotted-in steel plates: Genetic algorithm, deterministic neural network-based model parameter identification, and uncertainty quantification. ***Engineering structures**,* 310, 2024, 118114.

[2] **Da Shi**, Giuseppe Carlo Marano, Cristoforo Demartino. Modeling of glubam roof truss, parameter identification and updating based on parallel genetic algorithm. ***Engineering structures**,* 316,2024,118520.

[3] **Da Shi**, Zhi Li, Cristoforo Demartino. Bio-based hybrid planar truss: Experimental testing, FE modeling and Bayesian model updating. ***Engineering structures**,* 308, 2024, 117987.

[4] **Da Shi**, Haonan Huang, Yiwei Liu, Ning Li, Cristoforo Demartino. Bolted steel to laminated timber and glubam connections: Axial behavior and finite-element modeling. ***International Journal of Mechanical Sciences**,* 252,2023,108364.

[5] **Da Shi** ,Yongjia Xu, Yan Xiao, Billie F. Spencer. Bio-based laminated truss structures with bolted steel connections: Experiment, modeling, and model-updating.***Earthquake Engineering and structural Dynamics***, 2023;1-17.

[6] **Da Shi**, Cristoforo Demartino, Giuseppe Carlo Marano, Yongjia Xu. An asymmetric pinching damaged hysteresis model for glubam members: Parameter identification and model comparison. ***Computers and Structures**,* 305,2024,107574.

[7] **Da Shi**, Giuseppe Carlo Marano, Cristoforo Demartino. Bio-based connections and hybrid planar truss: A parallel genetic algorithm approach for model updating. ***Computers and Structures**,* 301,2024,107463.

[8] **Da Shi**, Cristoforo Demartino, Zhi Li, Yan Xiao. Axial load–deformation behavior and fracture characteristics of bolted steel to laminated timber and glubam connections. ***Composite Structures**,* 305,2023,116486.

[9] **Da Shi**, Yongjia Xu, Guoshan Lu, Zhi Li, Cristoforo Demartino. Glubam roof truss with riveted glubam connections adopting thin-walled steel tube: Experiment, modeling, and model-updating. ***Journal of Building Engineering**,* 2024, 110550.